Deformation of Granular Materials under Multi-Directional Loading

DEFORMATION OF GRANULAR MATERIALS UNDER MULTI-DIRECTIONAL LOADING

BY

XING LI, M.A.sc., B.Eng.

A THESIS

SUBMITTED TO THE DEPARTMENT OF CIVIL ENGINEERING

AND THE SCHOOL OF GRADUATE STUDIES

OF MCMASTER UNIVERSITY

IN PARTIAL FULFILMENT OF THE REQUIREMENTS

FOR THE DEGREE OF

DOCTOR OF PHILOSOPHY

Doctor of Philosophy (2018) McMaster University
(Civil Engineering) Hamilton, Ontario, Canada

TITLE:	Deformation of Granular Materials under Multi-Directional Loading
AUTHOR:	Xing Li M.A.sc., B.Eng., (Civil Engineering) Southwest Jiaotong University, Chengdu, China
SUPERVISOR:	Dr. Peijun Guo
NUMBER OF PAGES:	xxi, 220

Abstract

The deformation and failure properties of granular soils largely affect the stability of upper structures built on or in such soils. Owing to its discrete nature as well as the randomness of particle shape and inter-particle connectivity, the internal structure of a granular material usually exhibits a certain level of anisotropy. In addition, the microstructure of a granular material evolves following certain patterns, which are influenced by the initial fabric, void ratio, stress level, as well as the stress or deformation history. It has been a major challenge to properly describe the deformation of anisotropic granular materials in constitutive models especially when the materials are subjected to cyclic loading. The existing constitutive models usually have limited capabilities in describing the behaviour of granular materials subjected to repeated loading with principal stress rotation. How to quantify the microstructure change and how to consider the changing microstructure in constitutive models have been two missing links for building a comprehensive model framework.

This research aimed at developing a constitutive model that can properly describe the deformation of granular soils under repeated multi-directional loading. To achieve this goal, a systematic study was performed, including a comprehensive experimental study and a theoretical development of a stress-strain model with proper consideration of the influence of fabric. The developed model was verified with experimental results

and then implemented into a finite element code to solve boundary-valued problems.

In the first part of this study, a comprehensive experimental study was carried out to investigate the behaviours of granular materials under both monotonic and cyclic loading to investigate the influence of the intermediate principal stress and the major principal stress direction on soil responses. The results of monotonic loading tests showed that both the strength and dilatancy of sand decreased notably with an increase of either the intermediate principal stress or the inclination angle of the major principal stress direction relative to the major principal fabric direction. The stress states at failure from the tests suggested that the benchmarked Matsuoka-Nakai and Lade-Duncan failure criteria are only valid under certain conditions. From the cyclic loading tests, it was observed that, in addition to the increased intermediate principal stress, varied cyclic loading direction caused a significant increase in accumulative volumetric compaction.

To consider the microstructural dependencies of granular materials, a more general mathematical formulation of stress-dilatancy was developed based on the assumption of the existence of a critical state fabric surface that is expressed as a function of the invariants of the fabric tensor. This assumption was also used to establish the fabric evolution law. The implementation of the resulting stress-dilatancy formulation and the fabric evolution law in elasto-plasticity theory produced interesting modelling results consistent with experimental observations with respect to the microstructural aspects of granular materials. The developed constitutive model was further extended to cyclic loading within the framework of hypo-plasticity with kinematic hardening. The model was capable of describing the behaviour of sand subjected cyclic loading under various conditions including the variation of loading directions.

Finally, the constitutive model was implemented into a commercial software package ABAQUS via the subroutine UMAT. The capacity of the proposed stress-strain model in solving boundary value problems was examined. Six series of elements tests were designed to examine the proposed model under different initial void ratios, degrees of anisotropy, loading directions, and stress paths. Furthermore, a series of simulations were performed for the settlement of footing on sands with different bedding plane orientations. Results from the simulations were found to be consistent with experimental observations.

Acknowledgements

I would like to express my deepest gratitude to my supervisor, Dr. Peijun Guo, whose extensive knowledge, excellent guidance and unceasing encouragement supported me throughout the past years. My sincere appreciation is extended to Dr. Dieter Stolle, Dr. Michael Tait and Dr. John Emery for giving me great advice during my research.

I would like to thank Mr. Peter Koudys for helping me with the experimental setups. Additional thanks go to Dr. Yaqian Liu for his help during my experimental study.

The China Scholarship Council supported this research. My supervisor, Dr. Peijun Guo, also provided partial financial assistance. I would like to express gratitude to them for funding my research. Sincere thanks also go to Ms. Joanne Gadawski and Ms. Sarah Sullivan, for giving me much help during my work at Civil Engineering Department of McMaster University.

I would also like to thank my friends and family, who supported me unconditionally during the past years.

Notation and abbreviations

a	hardening parameter
b	intermediate principal stress ratio, $b = (\sigma_2 - \sigma_3)/(\sigma_1 - \sigma_3)$
e, e_{cr}	void ratio and critical state void ratio, respectively
e_{max}, e_{min}	maximum and minimum void ratio, respectively
e_{ij}	deviatoric strain tensor
f	yield function
g	plastic potential function
n_{ij}^F	unit-norm tensor of deviatoric fabric tensor F_{ij}
n_{ij}^s	unit-norm tensor of deviatoric stress tensor s_{ij}
$n_{ij}^{\dot{s}}$	unit-norm tensor of deviatoric incremental stress tensor $\dot{s}_{ij}$
p	mean stress, $p = \frac{1}{3}I_1$
q	deviatoric stress, $q = \sqrt{3J_2}$
q^{test}	deviator stress measure used in test control, $q^{test} = \frac{1}{2}(\sigma_z - \sigma_\theta)$
$q^\star$	deviator stress measure used in cyclic conditions, $q^\star = \pm\sqrt{3J_2}$
r	a Haigh-Westergaard stress invariant of the deviatoric stress tensor, $r = \sqrt{2J_2}$
r^F	a Haigh-Westergaard stress invariant of the deviatoric fabric tensor, $r^F = \sqrt{2J_2^F}$
s_{ij}	deviatoric stress tensor
A	measure of the non-coaxility between the deviatoric fabric tensor and the deviatoric stress tensor, $A = n_{ij}^F n_{ij}^s$
A'	measure of the non-coaxility between the deviatoric fabric tensor and the deviatoric incremental stress tensor, $A' = n_{ij}^F n_{ij}^{\dot{s}}$
B	bulk modulus
D	dilatancy equation
D_r	relative density, $D_r = (e_{max} - e) / (e_{max} - e_{min})$
F_{ij}	deviatoric fabric tensor
G	shear modulus

I_1, I_2, I_3	three invariants of stress tensor σ_{ij}
I_1^ε, I_2^ε, I_3^ε	three invariants of strain tensor ε_{ij}
J_1, J_2, J_3	three invariants of deviatoric stress tensor s_{ij}
J_1^F, J_2^F, J_3^F	three invariants of deviatoric fabric tensor F_{ij}
J_1^ε, J_2^ε, J_3^ε	three invariants of deviatoric strain tensor e_{ij}
K_{MN}, λ_{MN}, ω_{MN}	material constants in the Matsuoka-Nakai's failure criterion
K_{LD}, λ_{LD}, ω_{LD}	material constants in the Lade-Duncan's failure criterion
K_c	first joint invariant of the deviatoric stress and fabric tensors
α	angle between direction of the major principal stress and the normal direction of the bedding plane
$\alpha_{d\sigma}$	angle between direction of the major principal incremental stress and the normal direction of the bedding plane
β	softening parameter
$\gamma^\star$	shear strain, $\gamma^\star = \pm\sqrt{3J_2^\varepsilon}$
γ_{oct}	octehedral shear strain, $\gamma_{oct} = \frac{2}{3}\sqrt{6J_2^\varepsilon}$
$\gamma_{z\theta}$	torsional shear strain
δ	angle between directions of the major principal stress and the major principal fabric (for cross anisotropic material, α is used instead)
ε_1, ε_2, ε_3	major, intermediate, and minor principal strains, respectively
ε_{ij}	strain tensor
ε_z, ε_r, ε_θ	vertical, radial, and circumferential strains, respectively
ε_q	deviatoric strain, $\varepsilon_q = \pm\frac{2}{3}\sqrt{3J_2^\varepsilon}$
ε_v	volumetric strain, $\varepsilon_v = I_1^\varepsilon$
η	stress ratio, $\eta = q/p$
η_{ij}	deviatoric stress ratio tensor, $\eta_{ij} = s_{ij}/p$
θ	a Haigh-Westergaard stress invariant of the deviatoric stress tensor, also known as the Lode angle, $\theta = \frac{1}{3}\sin^{-1}(\frac{3\sqrt{3}}{2}\frac{J_3}{J_2^{\frac{3}{2}}}), \theta \in [-\frac{\pi}{6}, \frac{\pi}{6}]$
$\theta_{\dot{\sigma}}$	Lode angle corresponding to the incremental deviatoric stress tensor
ν	Possion's ratio
σ_1, σ_2, σ_3	major, intermediate, and minor principal stresses, respectively
σ_{ij}	stress tensor
σ_z, σ_r, σ_θ	vertical, radial, and circumferential stresses, respectively
$\tau_{z\theta}$	torsional shear stress
φ_{cv}	friction angle at critical state, $sin\varphi_{cv} = (\sigma_1 - \sigma_3)/(\sigma_1 + \sigma_3)$
Φ_{ij}	fabric tensor
ξ	a Haigh-Westergaard stress invariant, the distance from the origin to the deviatoric plane, $\xi = \frac{I_1}{\sqrt{3}}$
ψ	dilatancy angle, $sin\psi = -d\varepsilon_v/d\gamma_{oct}$
Ω	measure of initial degree of anisotropy, $\Omega = \frac{2}{3}\sqrt{3J_2^F}$

superscript e	elastic component
superscript p	plastic component
subscript 0	initial value
subscript ref	reference value
subscript cv	critical state value (same for superscript cv)
overhead dot($\cdot$)	rate of quantities
overhead bar(-)	average of quantities
prefix d	infinitesimal increment of quantities
prefix Δ	finite change in quantities
DEM	discrete element method
FEM	finite element method
HCA	hollow cylinder apparatus
LD	Lade-Duncan
MC	Mohr-Coulomb
MN	Matsuoka-Nakai

Contents

List of Figures

Chapter 1

Introduction

1.1 Background

Sand and other granular materials formed by natural sedimentation tend to have cross-anisotropic structures and possess inherent anisotropy, which is mainly caused by interparticle connectivity and preferred alignment of the major axes of particles along the bedding plane perpendicular to gravity. It has long been recognized that the inherent anisotropy has significant influence on the strength and deformation properties of sand (Arthur and Menzies, 1972; Meyerhof, 1978; Tatsuoka, 2000; Siddiquee *et al.*, 2001). Studies also suggest that even initially isotropic materials can exhibit anisotropy associated with the applied load. This type of anisotropy is normally termed as induced anisotropy (Casagrande and Carillo, 1944; Arthur *et al.*, 1977; Wong and Arthur, 1985; Oda, 1993). It is well-recognized that the directional dependency of granular material behaviour is induced by both types of anisotropy; i.e., the inherent and induced anisotropy. During the past few decades, numerous studies, both experimental and theoretical, have been carried out to investigate the anisotropic behaviour of granular materials.

1.2 Experimental study on anisotropy of granular materials

To investigate the directional dependency of granular material behaviour, extensive studies have been undertaken using various experimental techniques, including the plane strain test (Alshibli and Sture, 2000; Oda *et al.*, 1978; Tatsuoka *et al.*, 1990; Wanatowski and Chu, 2006), the directional shear test (Arthur and Menzies, 1972; Oda and Konishi, 1974a,b; Wong and Arthur, 1985; Guo, 2008), the conventional triaxial test (Oda, 1972a, 1981; Tatsuoka and Ishihara, 1974; Ishihara and Okada, 1978; Finge *et al.*, 2006; Hareb and Doanh, 2012), the true triaxial test(Lade and Duncan, 1975a; Yamada and Ishihara, 1979; Haruyama, 1981; Ochiai and Lade, 1983; Miura and Toki, 1984a,b; Abelev and Lade, 2004), and hollow cylinder apparatus tests (Hight *et al.*, 1983; Tatsuoka *et al.*, 1986; Shibuya and Hight, 1987; Symes *et al.*, 1988; Vaid *et al.*, 1990; Sãyao and Vaid, 1996; Chaudhary *et al.*, 2002; Toyota *et al.*, 2003; Georgiannou *et al.*, 2008; Cai *et al.*, 2012; Lade *et al.*, 2014a; Kandasami and Murthy, 2015; Yang *et al.*, 2016).

When describing the effect of inherent anisotropy on soil strength, the inclination angle α between the major principal stress direction and the normal direction of the bedding plane is usually used. Guo (2008) developed a modified direct shear box to investigate the directional dependency of the shear strength of sand. He observed that with the increase of the inclination angle α, the friction angle decreases first and reaches its minimum value when α is approximately 65°. A further increase of

α induces slight increases of the friction angle. The results by the modified direct shear box, although interesting, are limited since the inclination angle α is the only variable in these tests. The limitations of the direct shear box test are due to its lack of capacity to characterize the stress-strain behaviour and investigate induced anisotropy of granular materials. Plane strain tests and hollow cylinder apparatus tests have been used extensively to study the inherent anisotropic deformation and strength characteristics of granular materials (Tatsuoka *et al.*, 1986; Lam and Tatsuoka, 1988; Park and Tatsuoka, 1994).

The induced anisotropy originates from particle arrangements induced by applied stresses or material deformation. It depends on the stress states together with the loading path, which is usually quantified by the Lode angle θ or the intermediate principal stress ratio b defined as $b = (\sigma_2 - \sigma_3)/(\sigma_1 - \sigma_3)$. At a given deviator stress level, these two quantities reflect the relative amplitude of the intermediate principal stress σ_2. The effect of σ_2 was largely neglected in early studies, mainly because of two reasons. Firstly, the widely used Mohr-Coulomb failure criterion is formulated only regarding the major and the minor principal stresses, σ_1 and σ_3. Secondly, most laboratory and in-situ testing methods do not permit independent control of σ_2 (Sayão 1996). However, with the emerging of advanced soil testing techniques, extensive studies have shown that the influence of σ_2 on the mechanical response of sand can also be significant.

The hollow cylinder apparatus (HCA) can provide independent control of the three principal stress components, including the b value and the inclination angle α between the major principal stress direction and the normal direction of the bedding plane. Therefore, it is widely chosen in studies on the behaviour of granular material under generalized stress conditions. Starting from the 1980's, the hollow cylinder apparatus has become increasingly popular in investigating the anisotropic behaviour of soils, with many phenomenological observations on anisotropic material behaviour being made. However, owing to the influence of stress non-uniformity, tests have often been performed under the special condition $b = sin^2\alpha$ with relatively limited attention being given to the combined effects of α and b; i.e., the direction of the major principal stress and the magnitude of the intermediate principal stress.

1.3 Theoretical and numerical modelling of anisotropy of granular materials

Based on experimental investigation and theoretical studies, different constitutive model frameworks have been developed for granular materials, including models based on, for example, non-linear elasticity and hypo-elasticity, the classical theory of plasticity, endochronic theory, and hypo-plasticity (Guo, 2000). State-dependent parameters were introduced in the models to quantify the internal structure or material anisotropy (Wroth and Bassett, 1965; Been and Jefferies, 1985), with the evolution of the state-dependent parameters being related to the internal structure, which was characterized by either scalar or tensorial quantities or both (Wan and Guo, 1997; Manzari and Dafalias, 1997).

It was assumed in early studies that the material anisotropy remains unchanged during the loading process. Later studies made efforts to better quantify the current and critical state void ratio by incorporating the effect of stress dilatancy (Wan and Guo, 1997, 1998; Manzari and Dafalias, 1997; Gajo and Wood, 1999). However, the proper description and consideration of both inherent and induced anisotropy are still missing.

Various methods were used to investigate the internal structure and anisotropy of granular materials on the micromechanics level, including the use of advanced equipment such as X-ray computer tomopraphy (Bésuelle *et al.*, 2006; Takemura *et al.*, 2007), special laboratory tests such as photo-elastic tests dealing with granular assemblies (Oda and Konishi, 1974a,b; Allersma, 1982; Oda *et al.*, 1985) and tests on transparent soils (Iskander *et al.*, 1994; Iskander, 1997; Allersma, 1998; Sadek *et al.*, 2002), as well as numerical simulations using the discrete element methods (DEM) (Cundall and Strack, 1979). With the enormous progress of computer capacity, DEM simulation has become a powerful numerical approach to explore the micromechanics feature of granular materials. Recent DEM studies simulated the spatial arrangement of particles during loading and unloading processes (Antony *et al.*, 2004; Maeda *et al.*, 2006; Suzuki and Kuhn, 2013; Sazzad, 2014). Given the results of the experiments and numerical simulations, efforts have been made to develop evolution laws for the fabric structure, which is usually expressed by a second-order tensor.

With a sophisticated fabric evolution law that can properly describe fabric change under generalized stress conditions, it is possible to develop a constitutive model in which the material anisotropy is quantified by fabric tensor. However, a well-acknowledged fabric evolution law is yet to be developed. Nevertheless, the existing studies have provided methods of incorporating such a fabric tensor in a constitutive model framework.

1.4 Objectives of the research

The primary objective of this thesis was to develop a constitutive model that could properly describe the deformation of granular soils under multi-directional loading. The modelling results were expected to help understand the behaviour of granular soils under generalized stress conditions, in particular for anisotropic materials in which the microstructure plays a significant role in the mechanical behaviour of the material.

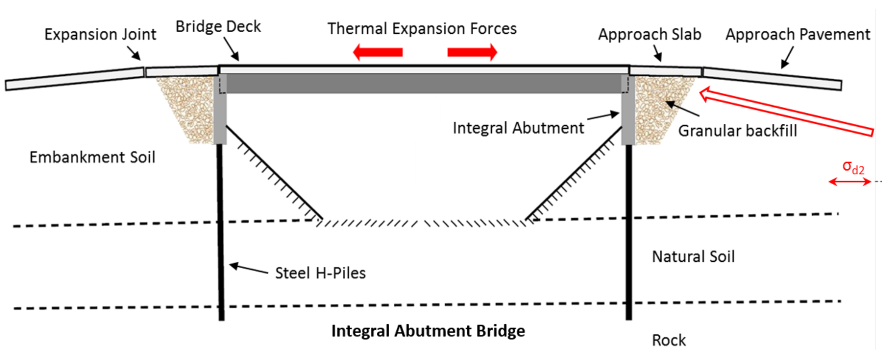

(a) Backfill of integral abutment bridge

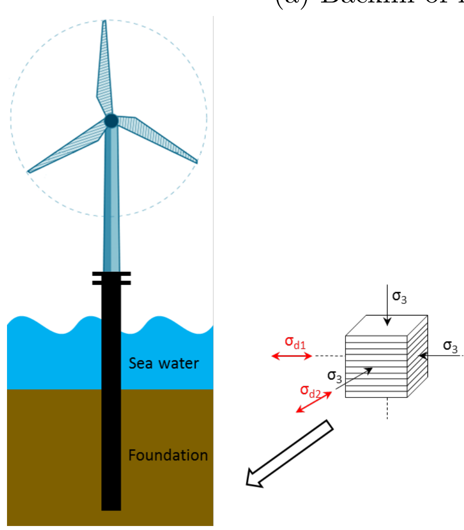

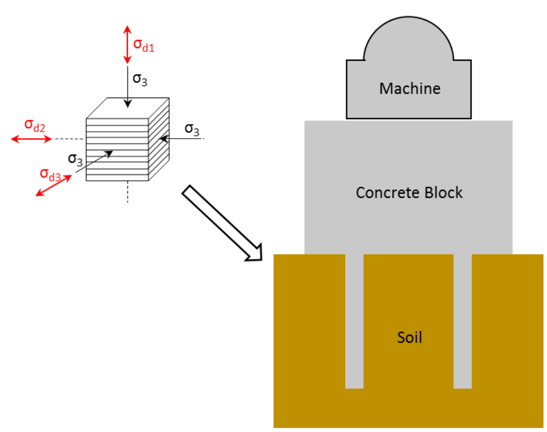

(b) Offshore wind power plant (c) Machine foundation

Figure 1.1: Examples of multi-directional loading problem

On the practical side, this study is to provide an approach for the analysis of engineering problems that involve cyclic or vibratory loading applied from multiple directions, such as an approach embankment of integral abutment bridge (IAB) (Figure 1.1a) where the granular backfill is subject to cyclic loading from both vertical (traffic loads) and horizontal directions (loading induced by cyclic thermal expansion of the bridge structure). Similar circumstances can be found in coastal structures, the foundation of offshore wind power plants (Figure 1.1b), machine foundations (Figure 1.1c), compaction, etc.

This study mainly focused on the following aspects:

(1) Experimental study of granular material behaviour under generalized stress conditions.

A comprehensive experimental study was carried out to investigate the effects of loading direction and intermediate principal stress ratio on the behaviour of sand subjected to both monotonic and cyclic loading. Three series of monotonic loading tests and one series of cyclic loading tests were performed. The test results provided benchmark and calibration for the development of constitutive models.

(2) Mathematical description of material anisotropy and development of a constitutive model.

It is not new to use second-order fabric tensors to describe the microstructure of granular materials. However, how these tensorial measures evolve during deformation processes and how they are considered in constitutive models had been two missing links for incorporating the concept of fabric tensor into a stress-strain model. Based on the concept of ultimate fabric state, a fabric evolution law was developed and incorporated into the constitutive model framework through proper methods.

(3) Numerical implementation of the developed stress-strain model in FEM for boundary-valued problems.

The incorporation of a fabric tensor in a constitutive model has brought challenges to the implementation of the model into FEM analysis, especially under generalized stress conditions. An effort was made to develop a proper algorithm to incorporate the constitutive framework in the FEM software package ABAQUS to solve boundary-valued problems.

1.5 Outline

An outline of the rest of the thesis is as follows.

Chapter 2 presents a comprehensive literature review, which mainly focuses on areas regarding experimental studies and constitutive models of granular soils. Based on the literature review, the need and significance of the work in this thesis are discussed.

Chapter 3 presents the details of the experimental study as well as the analyses of the experimental results. The objective of the experimental study was to investigate the influence of the intermediate principal stress and the major principal stress direction relative to the principal direction of fabric on the behaviour of an inherently anisotropic granular material.

Chapter 4 develops a constitutive model for monotonic loading, in which a fabric tensor is used to describe the anisotropic behaviour of granular materials under generalized stress conditions. An evolution law of fabric tensor is proposed based on the concept of the ultimate fabric surface, and a modified stress-dilatancy formulation is proposed based on the relation between the fabric and the stress states. Then a constitutive model is developed by incorporating the proposed stress-dilatancy equation into the theory of plasticity as a flow rule.

Chapter 5 extends the constitutive model to account for cyclic loading conditions by adopting a kinematic hardening law. Seven loading modes are designed to verify the extended stress-strain model, all starting from isotropic consolidation condition with constant confining pressure. Four of the loading modes simulate one-way loading conditions, and the other three represent two-way loading conditions.

The proposed constitutive model is implemented in Chapter 6 into the commercial software ABAQUS via a user-defined subroutine (UMAT) to solve boundary-value problems. Six series of element tests are designed to examine the proposed model under different initial void ratios, degrees of anisotropy, loading directions, and stress paths. Furthermore, a series of simulations are performed to determine the settlement induced by uniformly applied stresses on sands with different bedding plane orientations.

Finally, Chapter 7 gives the conclusions as well as suggestions for the future work.

Chapter 2

Literature Review

This chapter briefly reviews the basic behaviour, continuum modelling as well as the microstructure consideration of granular materials.

2.1 Basic behaviour of granular materials

The most important mechanical properties of a granular material are its shear strength and deformation characteristics. These two properties are affected by many factors, including void ratio, internal structure (or fabric), particle shape, stress state, stress level, loading directions and loading paths, etc.. This section summarizes the basic mechanical characteristics of cohesionless granular materials such as sand.

2.1.1 Void ratio and stress level

For granular materials, the basic contributions to strength are the frictional resistance between particles in contact and the internal kinematic constraints of particles associated with particle rearrangement, interlocking and fabric change. The magnitude of these contributions depends on Terzaghi's effective stress, the volume change tendencies, and the internal structure. The tendency of volume change is usually controlled by density or the void ratio of the material. For a loose sand with a high void ratio, voids in a soil skeleton tend to reduce under shear, which is termed as the shear-induced contraction. On the other hand, for a dense sand with a relatively small void ratio, shear tends to cause an increase in volume or dilation. In addition to void ratio, the applied confinement level also has a significant influence on shear-induced volume change of granular materials.

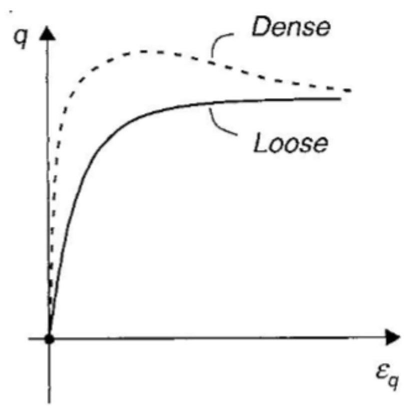

(a) stress-strain curves

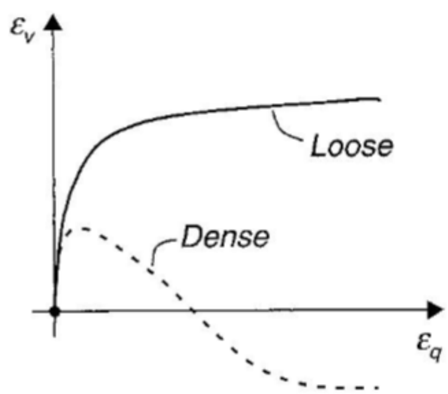

(b) volumetric-shear strain curves

Figure 2.1: Typical responses of granular materials under drained triaxial compression (Pietruszczak, 2010)

Figure 2.1 illustrates the ideal responses of granular materials (both dense and loose) when sheared under drained conditions at the same confining stress level. For a loose specimen with a high void ratio, the deviator stress increases monotonically with shear strain, accompanied by continuous volume contraction. The specimen eventually reaches the critical state at which no further change occurs in stresses or volumetric strain as shearing continues. For a dense specimen of the same material at a low void ratio, shear-induced contraction initially takes place as the deviator stress increases. With an increase of shear strain, dilation develops, and a distinct peak deviator stress is observed on the stress-strain curve. Continued shearing induces a reduction in the shear resistance, which is termed as strain-softening. A critical state is assumed to be reached at large shear strains.

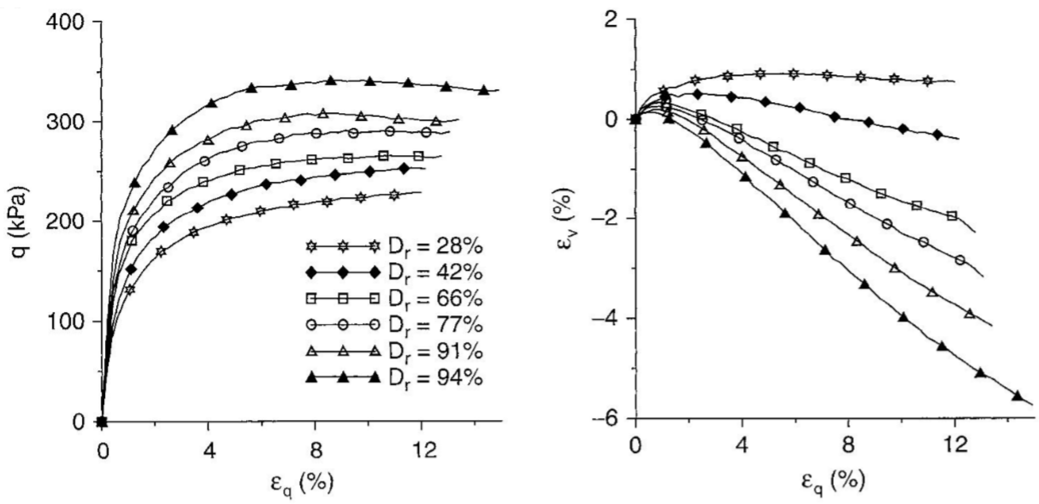

(a) stress-strain curves (b) volumetric-shear strain curves

Figure 2.2: Triaxial tests on Karlsruhe sand at $p'_0 = 100$ kPa and different initial densities (Kolymbas and Wu, 1990)

Figure 2.2 shows the experimental triaxial test results of Karlsruhe sand with different initial void ratios under the same confining pressure (Kolymbas and Wu, 1990). D_r is the relative density, which is related to the void ratio e by $D_r = (e_{max} - e)/(e_{max} - e_{min})$. A specimen with a larger value of D_r means it is denser and has a smaller void ratio.

In addition to density, the frictional resistance of granular materials is also affected by the mean effective stress level. Figures 2.3 and 2.4 show the drained triaxial compression test results of loose and dense specimens of Karlsruhe sand at different

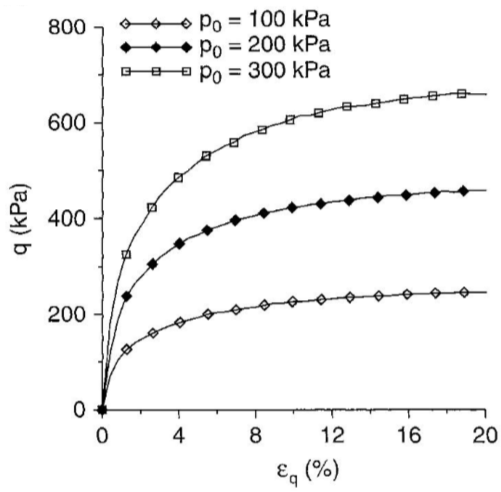

(a) stress-strain curves

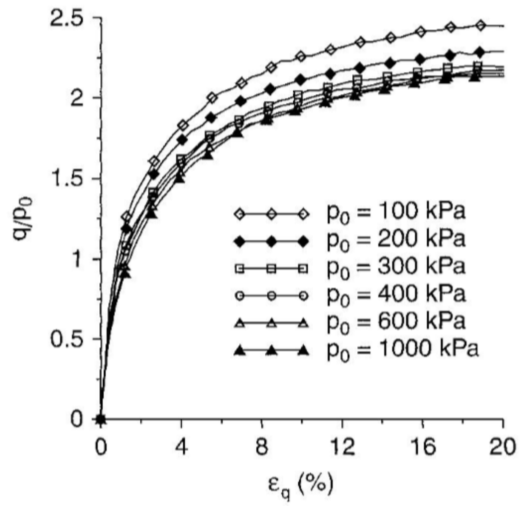

(b) normalized stress-strain curves

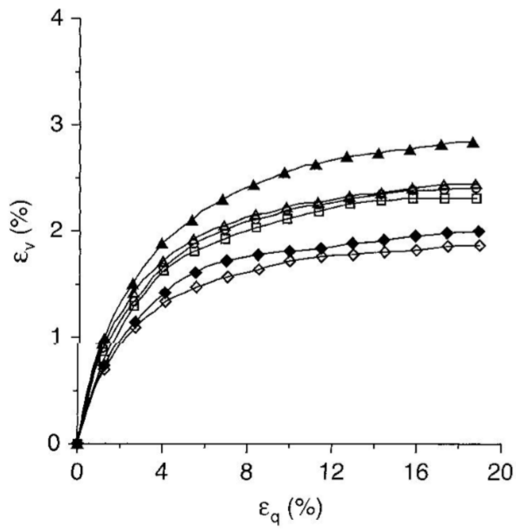

(c) volumetric-shear strain curves

Figure 2.3: Triaxial tests on loose Karlsruhe sand at different confining pressures ($D_r = 16\%$) (Kolymbas and Wu, 1990)

confining pressure levels (Kolymbas and Wu, 1990). With an increase of the confining pressure, the maximum deviatoric stress increases, as shown in Figure 2.3a. However, the peak stress ratio, or the mobilized friction angle, tends to decrease as the confining pressure increases. In other words, specimens of the same density have higher friction angle under lower confining pressure. At the same time, shear-induced volume contraction increases with the confining pressure as shown in Figures 2.3b and 2.3c. On the other hand, for dense sand specimens, significant post-peak strain softening may take place at low confining pressure, while monotonic hardening is observed at high confining pressures; as shown in Figures 2.4a and 2.5a. The dilatancy characteristics of dense sand are also affected by the confining pressure. The higher the confining pressure, the lower the tendency of dilation. In other words, increased confining pressure tends to suppress dilation of dense sand, as shown in Figures 2.4b and 2.5b.

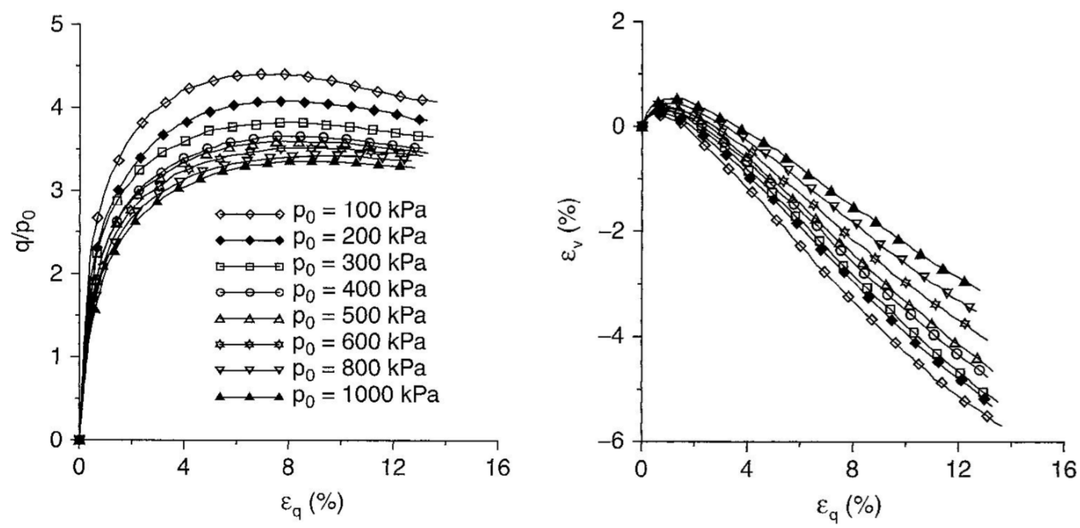

(a) normalized stress-strain curves (b) volumetric-shear strain curves

Figure 2.4: Triaxial tests on dense Karlsruhe sand at different confining pressures ($D_r = 98\%$) (Kolymbas and Wu, 1990)

The behaviour of sand under drained conditions provides implications on the undrained behaviour of the same material when it is fully saturated. The tendency to compact under drained conditions leads to a buildup of the excess pore pressure for undrained conditions. The trend of dilation results in the generation of negative

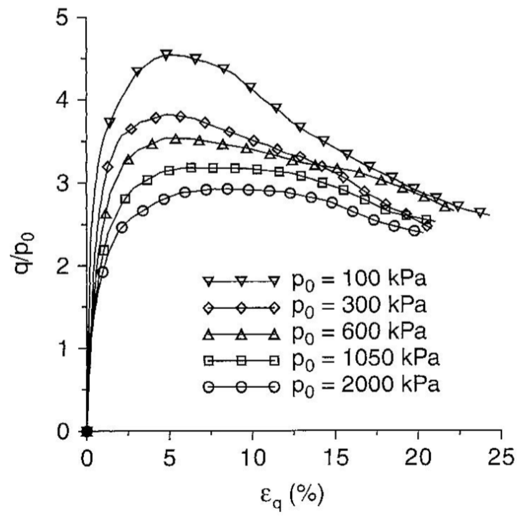

(a) normalized stress-strain curves

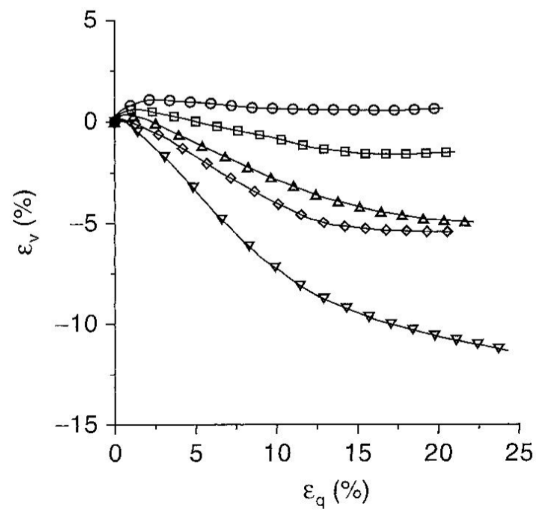

(b) volumetric-shear strain curves

Figure 2.5: Triaxial tests on dense Sacramento river sand at different confining pressures ($D_r = 100\%$) (Lade, 1977)

excess pore pressure owing to the constraint of constant volume enforced by the undrained condition. Figure 2.6 illustrates the idealized effective stress trajectories of saturated sand with different densities under the undrained constraint. For a dense specimen, at the very beginning of shearing, the tendency of compaction causes a decrease in the effective stress due to a buildup of the excess pore pressure, so the stress trajectory moves left slightly as the deviator stress increases. With an increase of deviator stress (or shear strain), the tendency of dilation (as shown in Figure 2.1) triggers a decrease in excess pore pressure and an increase of the mean effective stress. As a result, the effective stress trajectory changes direction and gradually approaches the ultimate state, as shown in Figure 2.6. For a very loose specimen, shearing induces a significant generation of pore pressure with the effective stress decreasing continuously, owing to the high tendency of shear-induced volume contraction. As the mean effective stress decreases with shear strain, the mobilized deviator stress first increases to its peak, followed by a continuous decline. At a certain point, the stability is lost with the deviator stress decreasing intensely with continuing deformation. In the end, both the effective mean stress and the deviator stress reduce to near-zero, accompanied by the continuous flow of the material, which is termed as steady state. During this process, the mobilized effective friction angle monotonically increases. The trajectories for loose/medium dense samples lie between the two extreme cases.

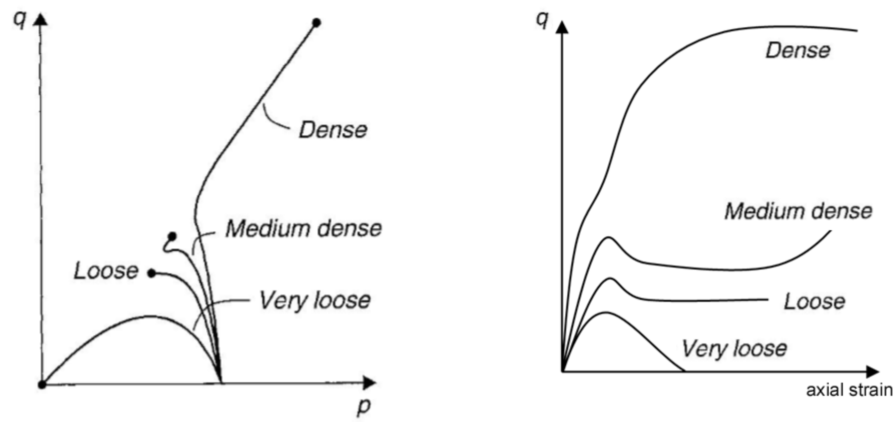

(a) q-p curves (b) stress-strain curves

Figure 2.6: Typical effective stress trajectories for saturated sand specimens under undrained constraint (Pietruszczak, 2010)

2.1.2 Concept of the critical state

The critical state soil mechanics was originally developed by the Cambridge soil mechanics group in the late 1950's and early 1960's, beginning with Roscoe *et al.* (1958), to emphasize the effect of volume change and effective stresses when characterizing the soil behaviour. The critical state is defined as a state at which the material undergoes continuous deformation without further change in stress and volume (Schofield and Wroth, 1968). The basic concept is that, under sustained shearing at failure, there is a unique combination of void ratio e, effective mean pressure p' and deviator stress q. The friction angle at critical state is independent of stress history and the original structure. The experimental studies of Desrues *et al.* (1985) confirmed that the achievement of a critical state is associated with a unique critical void ratio, which is a function of the mean effective stress only.

The critical state concept has been used in developing stress-strain models for different types of soils. The first model based on this concept is the well-known Cam-Clay model for clay. To consider the effect of void ratio, adopting the concept of critical state void ratio, Wroth and Bassett (1965) used the 'distance' between the current state on the $e - log\sigma$ space and the imaginary point at critical state as the control variable of soil deformation. Been and Jefferies (1985) suggested a state parameter $\psi = e - e_{cr}$, with e and e_{cr} being the current void ratio and imaginary critical state void ratio, respectively.

While the critical state theory is well established in the geotechnical research community, it ignores the possible influences of fabric and stress path. Hardin (1989) found that, at very low confining pressures, the void ratio at large deformation is not unique given different initial densities. Through undrained tests, Yoshimine and Ishihara (1998) also found that the steady state is fabric dependent. Studies on the microstructure of soil found without exception that an intense fabric formation is present at critical state (Oda, 1972a,b; Masson and Martinez, 2001; Li and Li, 2009). Such fabric may be described in different ways, but invariably involving the preferred orientations of some tensor-valued quantities (Li and Dafalias, 2012). As such, a missing link exists between the classical critical state theory and a generalized model framework that includes the notion of fabric and its evolution. More discussion about fabric consideration is presented in the section on the microstructure of soil.

2.1.3 Loading direction and stress path dependency

Chapter 1 pointed out that the mechanical responses of a granular soil are strongly influenced by its microstructure, the loading direction, and stress paths. Systematic studies on the effect of inherent anisotropy on the behaviour of granular materials can be dated back to Arthur (Arthur and Menzies, 1972; Arthur *et al.*, 1977; Wong and Arthur, 1985), Oda (Oda, 1972a,b; Oda *et al.*, 1978; Oda and Koishikawa, 1979) and Tatsuoka (Tatsuoka *et al.*, 1986; Lam and Tatsuoka, 1988; Tatsuoka *et al.*, 1990; Park and Tatsuoka, 1994). Herein some important observations from the experimental studies are reviewed.

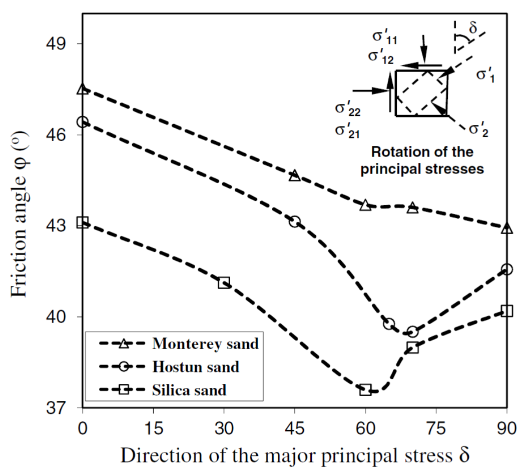

Figure 2.7: Peak strength variation of different sands under different principal stress directions from plane strain tests (Park and Tatsuoka, 1994)

The strength of cohesionless soil is traditionally quantified through the friction angle φ, which is defined as $\sin\varphi = (\sigma_1 - \sigma_3)/(\sigma_1 + \sigma_3)$. The friction angle φ, however, does not consider the influence of σ_2 or the direction of σ_1 by definition. Figure 2.7 illustrates the plane strain test results for three types of sand at different principal stress directions (Park and Tatsuoka, 1994). Being prepared by using air or water pluviation method, the samples have a cross-anisotropic structure with the direction perpendicular to the bedding plane being the axis of axisymmetry and the material being isotropic within the bedding plane. The direction of major principal stress σ_1 is characterized by angle δ, which is defined as the angle between the major principal stress direction and the normal of the bedding plane, as shown in Figure 2.7. With an increase of δ starting from zero, the peak friction angle tends to decrease. The maximum peak strength is observed at $\delta = 0$ when σ_1 is applied perpendicular to the bedding plane, while the minimum strength takes place in the range of $\delta = 60^\circ - 90^\circ$. Similar observations are found from results of plane strain tests by Tatsuoka *et al.* (1990), modified direct shear tests by Guo (2008) and HCA tests by Tatsuoka *et al.* (1986), Lam and Tatsuoka (1988) among others.

Studies of Tatsuoka *et al.* (1986) and Lam and Tatsuoka (1988) find that the friction angle of sand is influenced not only by the direction of the major principal stress σ_1 but also the intermediate principal stress σ_2. Figure 2.8 shows the failure envelope obtained from a series of true triaxial tests in Kirkgard and Lade (1993) corresponding to different Lode angles. Herein the Lode angle, which is defined as $\theta = \frac{1}{3}\sin^{-1}(\frac{3\sqrt{3}}{2}\frac{J_3}{J_2^{\frac{3}{2}}})$, reflects the magnitude of σ_2 relative to the major and the minor principal stresses. The same pattern in the variation of peak strength has been consistently reported thereafter (Lam and Tatsuoka, 1988; Callisto and Calabresi, 1998; Leroueil and Hight, 2003), as shown in Figure 2.9.

In recent years, experimental studies using HCA have further proven that both the loading direction relative to the bedding plane and stress path have a significant influence on the peak strength of granular materials. In general, the loading direction

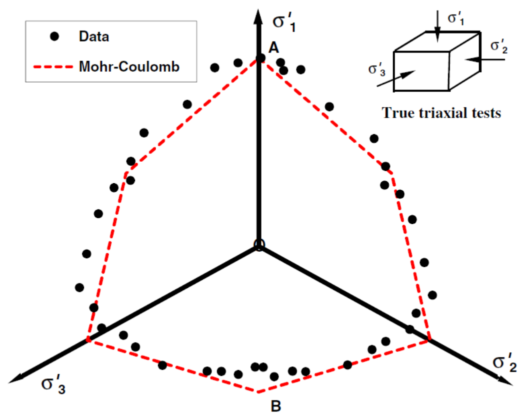

Figure 2.8: Failure stresses of natural San Franciso Bay mud (Kirkgard and Lade, 1993)

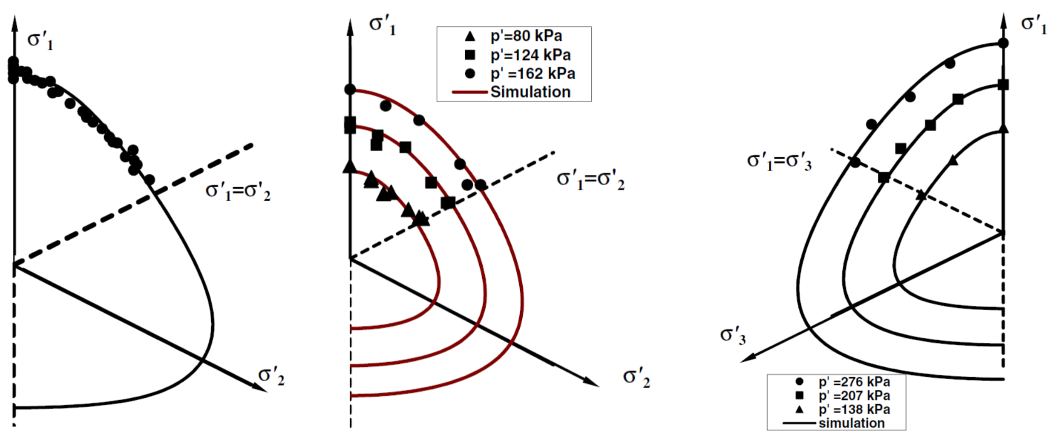

(a) Trachyte rock (Mogi, 1971)

(b) grundite clay (Lade and Musante, 1978)

(c) Monterey sand (Reddy and Saxena, 1993)

Figure 2.9: Failure stresses compared with simulations (Liu and Indraratna, 2010)

is characterized by α that is the angle between σ_1 and the normal of the bedding plane with the stress path being characterized either by the Lode angle θ or the intermediate principal stress ratio b, which is defined as $b = \frac{\sigma_2 - \sigma_3}{\sigma_1 - \sigma_3}$.

Using HCA, Symes *et al.* (1984, 1988) conducted both undrained and drained tests on Ham River sand to investigate the effect of the initial anisotropy and principal stress rotation during shear. Miura *et al.* (1986) studied the anisotropic behaviour of dense Toyoura sand using HCA. These studies both found a strong dependence of failure strength on the principal stress direction. Extensive studies using HCA were carried out thereafter, focusing on both the effects of loading direction and stress path (Hight *et al.*, 1983; Tatsuoka *et al.*, 1986; Shibuya and Hight, 1987; Vaid *et al.*, 1990; Sãyao and Vaid, 1996; Chaudhary *et al.*, 2002; Toyota *et al.*, 2003; Georgiannou *et al.*, 2008). In what follows, some recent HCA experimental studies are reviewed.

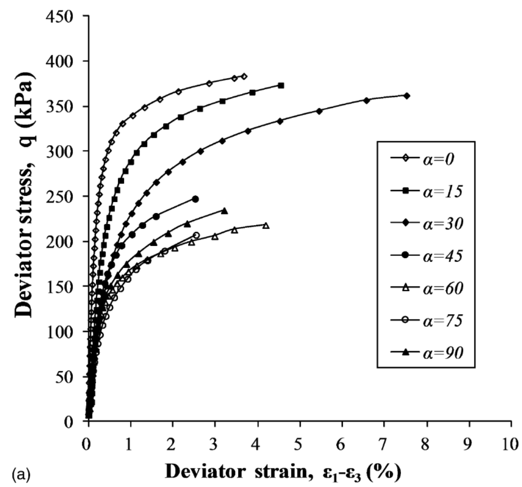

Figure 2.10: Stress-strain curves under different loading directions as well as stress paths with $b = sin^2\alpha$ (Cai *et al.*, 2012)

Figure 2.10 shows the results from Cai *et al.* (2012). In this study, the two parameters, α and b, are not independently controlled. Instead, all the tests are conducted under the condition $b = sin^2\alpha$, which is a very common constraint in experimental studies using the HCA. More discussion regarding this constraint is presented in Chapter 3. The results show that the shear resistance decreases with an increase of α and b under the coupled effects of α and b.

Kandasami and Murthy (2015) investigated the influence of loading direction and stress path with α and b being controlled independently. Their test results are summarized in Figure 2.11. According to Figure 2.11a, for a given α, the deviator stress at failure tends to decline when the value of b increases. On the other hand, when the intermediate principal stress factor b is fixed, the variation of α alone has a significant influence on the peak friction angle. As shown in Figure 2.11b, the peak friction angle generally decreases as α increases, with the minimum friction angle appearing at $\alpha = 60° - 75°$. The same observations were also made by Miura *et al.* (1986).

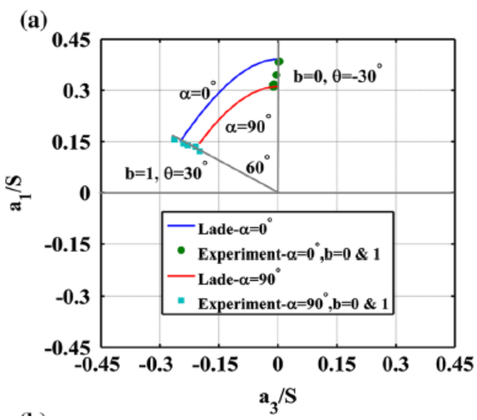

(a) Variation of failure stress obtained along different loading directions and loading paths

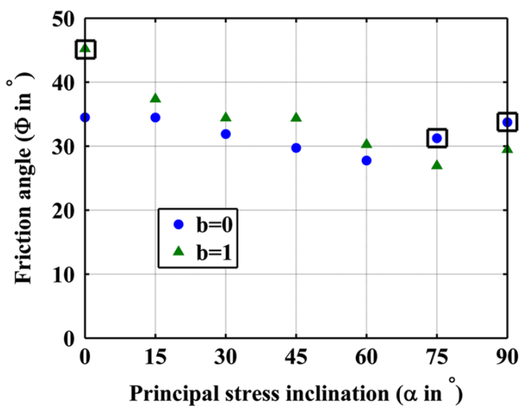

(b) Variation of peak friction angle with loading direcition α

Figure 2.11: Failure stresses on π-plane and variation of peak friction angle ($p' = 300kPa$) (Kandasami and Murthy, 2015)

Yang *et al.* (2016) investigated the influence of the major principal stress direction and the intermediate stress, which is quantified by b, on the strength of sand. In Figure 2.12a, the strength of soil is characterized by the peak stress ratio, which is defined as $\eta = \frac{q}{p} = \frac{\sqrt{3J_2}}{I_1/3}$. The peak stress ratio tends to decrease with an increase of α. For a select value of α, the peak stress ratio decreases with an increase of b. These results show that both inherent anisotropy and the intermediate principal stress influence the shear strength of sand. The test results in Figure 2.12a are alternatively presented in Figure 2.12b by using the peak friction angle φ_p as the strength measure. The peak friction angle decreases with an increase of α. However, with an increase of the intermediate stress factor b, the peak friction angle increases first and decreases after $b = 0.5$.

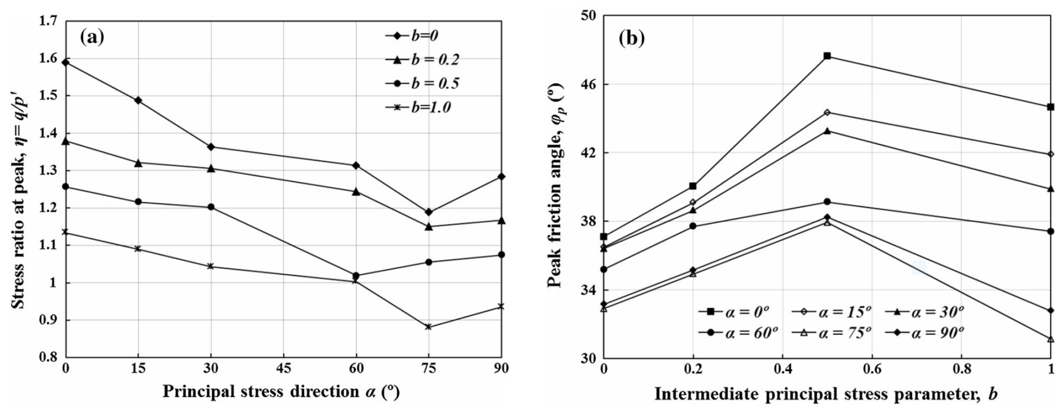

(a) Variation of failure stress ratio under different loading directions

(b) Variation of peak friction angle under different loading directions

Figure 2.12: Variation of stress state at failure with principal stress direction (Yang *et al.*, 2016)

Some advanced failure criteria have incorporated the effect of σ_2, such as the Lade-Duncan criterion (Lade and Duncan, 1975b; Lade, 1977) with $I_1^3/I_3 = constant$ and the Matsuoka-Nakai criterion (Matsuoka, 1974; Matsuoka and Nakai, 1974, 1977) with $I_1 I_2/I_3 = constant$. While constitutive models based on these failure criteria can account for the effect of σ_2, the effects of material's inherent anisotropy are not considered.

Kandasami and Murthy (2015) and Yang *et al.* (2016) examined the effects of major principal stress direction and intermediate principal stress on the deformation properties of sand. As shown in Figure 2.13 and Figure 2.14, the tendency of dilation decreases with an increase of either α or b. Based on these experimental results, it can be concluded that a comprehensive modelling framework needs to be capable of considering the effects of both factors.

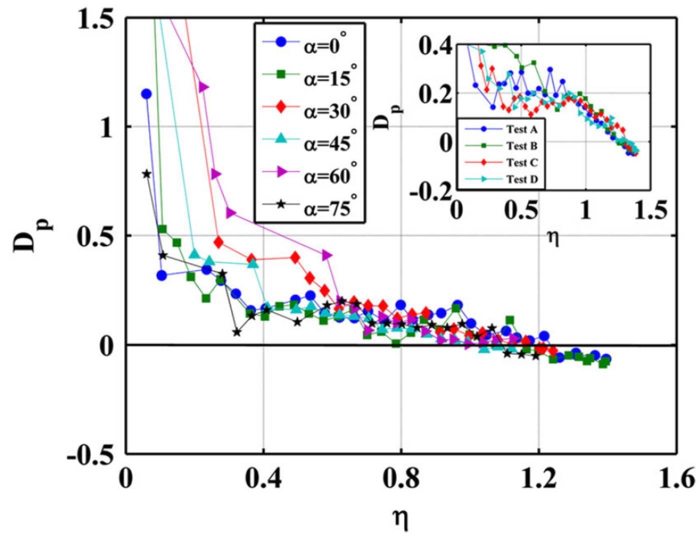

Figure 2.13: Stress-dilatancy relationship under different major principal stress directions (Kandasami and Murthy, 2015)

2.2 Continuum modelling of cohesionless soils

A classical elastoplasticity model has the following basic components: a failure criterion characterizing the strength of the materials; a yield function and the associated hardening law defining the domain of elastic deformation; and a flow rule to characterize the direction of plastic flow. These aspects of constitutive modelling are discussed in this section.

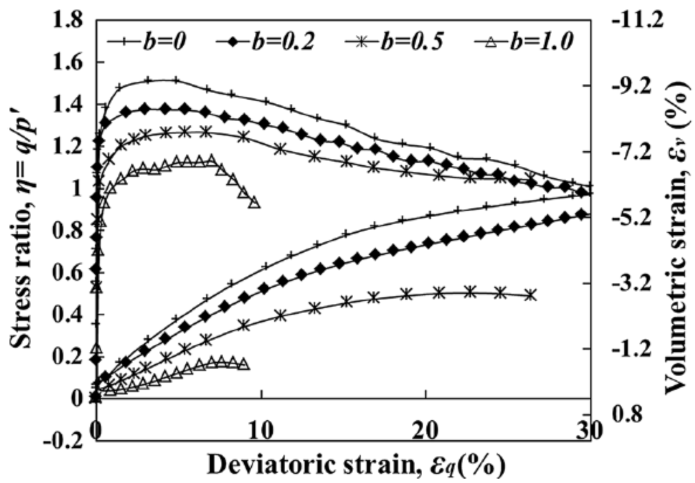

Figure 2.14: Stress-strain behaviour at $\alpha = 0°$ with different b (Yang *et al.*, 2016)

2.2.1 Yield criteria and hardening rules

A yield surface defines the boundary of the current elastic region in stress space. A stress state that lies inside the yield surface is an elastic state, while a stress state that lies on the surface is referred to as a plastic state. For a strain-hardening material at a plastic state, if the stress state tends to move out of the yield surface, loading takes place. On the other hand, if the stress state tends to move into the yield surface, it is an unloading progress. Another possibility is that the stress state moves along the current yield surface, and this process is referred to as a neutral loading. Both unloading and neutral loading are associated with elastic deformation, while the loading progress at plastic state is associated with elastic-plastic deformation. For a hardening material, when describing a yield surface by a yield function f, the loading criteria, which are shown schematically in Figure 2.15, are expressed mathematically as follows:

$f < 0$: elastic state

$f = 0$ and $\frac{\partial f}{\partial \sigma_{ij}} d\sigma_{ij} > 0$: loading

$f = 0$ and $\frac{\partial f}{\partial \sigma_{ij}} d\sigma_{ij} = 0$: neutral loading

$f = 0$ and $\frac{\partial f}{\partial \sigma_{ij}} d\sigma_{ij} < 0$: unloading

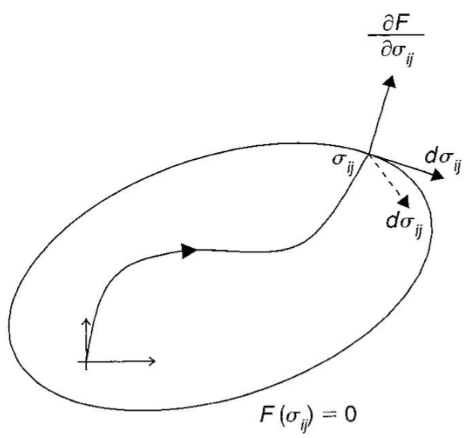

(a) elastic-perfectly plastic material

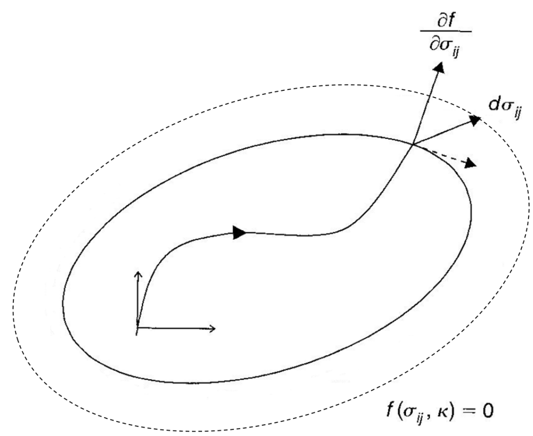

(b) isotropic-hardening material

Figure 2.15: Loading criteria for elastic-perfectly plastic material and isotropic-hardening material

The hardening rule is a major component in the hardening theory of plasticity. It is referred to as the rule that governs the evolution of yield surface. Depending on the mechanism of material deformation, different hardening rules have been developed, including isotropic hardening rules, kinematic hardening rules, and mixed hardening rules. Figure 2.15b shows the simplest, and the most frequently used isotropic hardening rule in geomechanics. The loading function, which defines the current yield surface, is written as

$$f(\sigma_{ij}, \kappa) = \bar{f}(\sigma_{ij}) - g(\kappa) = 0 \tag{2.1}$$

where κ is the hardening parameter that depends on the plastic deformation and

$g(\kappa)$ is a monotonically increasing function of κ. Depending on the type of plastic deformation that is used to quantify κ, the isotropic hardening rules can further be divided into the volumetric hardening rule, the deviatoric hardening rule, and the combined volumetric-deviatoric hardening rule (Pietruszczak, 2010).

Depending on the material's sensitivity to hydrostatic pressure, isotropic materials can be divided into two categories, the hydrostatic-pressure-independent materials, and the hydrostatic-pressure-dependent materials. In general, metallic materials fall into the first category, referred to as frictionless materials, while geo-materials usually fall into the second category and are called frictional materials. Consequently, two types of yield functions are used for these materials owing to the different considerations for hydrostatic pressure.

For hydrostatic-pressure-independent metallic materials, the most important yield functions are the Tresca function (Tresca, 1864) and the von Mises function (Mises, 1913). The Tresca function defines the yield surface so that the maximum shear stress is restrained by a certain value, see Equation (2.2). On the other hand, the von Mises function defines the surface by using the second deviatoric stress invariant J_2 instead of the maximum shear stress, see Equation (2.3).

$$f = |\tau_{\max}| - k = \max(\frac{|\sigma_1 - \sigma_2|}{2}, \frac{|\sigma_1 - \sigma_3|}{2}, \frac{|\sigma_2 - \sigma_3|}{2}) - k = 0 \tag{2.2}$$

$$f = \sqrt{J_2} - k = 0 \tag{2.3}$$

Using stress invariants, the Tresca and von Mises formulations are both independent of the first stress invariant I_1 (or the mean stress, $p = I_1/3$).

For frictional materials (particularly granular materials), however, the influence of the mean stress cannot be neglected. Therefore, yield functions for frictional materials should contain term I_1, such as the Mohr-Coulomb function (Mohr, 1900) and the Drucker-Prager function (Drucker and Prager, 1952). The Drucker-Prager function is simply a modification of von Mises function, with the influence of hydrostatic pressure included. Mathematically, the Drucker-Prager function is expressed as

$$f(I_1, J_2) = \alpha I_1 + \sqrt{J_2} - k = 0 \tag{2.4}$$

where α and k are material constants. When $\alpha = 0$, Equation (2.4) is reduced to Equation (2.3), thus the Drucker-Prager criterion is also called extended von Mises criterion.

In 1900, Mohr presented a theory for rupture in materials that a material fails through a critical combination of normal and shear stresses. The functional relationship between the shear stress and normal stress on the failure plane is expressed as

$$\tau_f = f(\sigma) \tag{2.5}$$

For most soil, it is sufficient to approximate the relationship between the shear and normal stresses on the failure plane by a linear function, which leads to the Coulomb failure criterion (Coulomb, 1773):

$$\tau_f = c + \sigma \tan \varphi_0 \tag{2.6}$$

where c is cohesion, and φ_0 is the internal friction angle of the material. For frictionless materials, φ_0 becomes zero and Equation (2.6) is reduced to Equation (2.2).

Therefore, the Coulomb function can be regarded as a generalization of Tresca function considering the normal stress on the failure plane.

When the stress states at failure are concerned, by assuming shear failure takes place when the stress Mohr circle is tangent to the line representing the Coulomb failure criterion, one obtaines the Mohr-Coulomb function in the form of

$$\frac{1}{2}(\sigma_1-\sigma_3)\cos\varphi_0 = c + \left[\frac{1}{2}(\sigma_1+\sigma_3) - \frac{1}{2}(\sigma_1-\sigma_3)\sin\varphi_0\right]\tan\varphi_0 \tag{2.7}$$

The Haigh-Westergaard invariants (ξ, r and θ) are normally used to standardize the expression of yield functions in terms of stress invariants. These invariants are defined as

$$\begin{aligned} \xi &= \frac{I_1}{\sqrt{3}} \\ r &= \sqrt{2J_2} \\ \theta &= \frac{1}{3}\sin^{-1}\left(\frac{3\sqrt{3}}{2}\frac{J_3}{J_2^{\frac{3}{2}}}\right), \theta \in [-\frac{\pi}{6}, \frac{\pi}{6}] \end{aligned} \tag{2.8}$$

where ξ is the distance from the origin to the current deviatoric plane, r is distance from current stress state point to the hydrostatic axis on the deviatoric plane, and θ is the Lode angle. (ξ, r and θ) can uniquely define the stress state and represent the relative position of current stress point in the principal stress space. Note that by the current definition, the Lode angle is $\pi/6$ for the classical triaxial compression condition ($\sigma_1 > \sigma_2 = \sigma_3$), and is $-\pi/6$ under triaxial extension condition ($\sigma_1 = \sigma_2 > \sigma_3$). The Lode angle is related to the intermediate principal stress coefficient b by $b = \frac{1}{2} - \frac{\sqrt{3}}{2}\tan\theta$.

One of the advantages of using the Haigh-Westergaard coordinates is that all the invariants have clear physical meanings. In the circular yield surfaces of von Mises function or Drucker-Prager function, the yield function is independent of the Lode angle and takes a simple form as

$$r = f(\xi)$$

The Mohr-Coulomb equation can be alternatively expressed in the form of

$$r(\xi,\theta) = \frac{\sqrt{2}\xi \sin\varphi_0}{\sqrt{3}\cos\theta - \sin\theta\sin\varphi_0} \tag{2.9}$$

or

$$f(\xi,r,\theta) = \xi sin\varphi_0 - \frac{r}{\sqrt{2}}(\sqrt{3}cos\theta - sin\theta sin\varphi_0) = 0 \tag{2.10}$$

Although the above equation includes the Lode angle θ, the Mohr-Coulomb equation isn't designed for generalized stress conditions. The experimental basis of the Mohr-Coulomb equation can only hold under triaxial compression ($\theta = 30°$) and triaxial extension ($\theta = -30°$) conditions. A linear segment is assumed for stress paths that lie between $\theta = 30°$ and $\theta = -30°$ and results in a hexagonal yield surface. Such a yield surface contains corners, which may cause numerical difficulty in its application to plasticity theory (Chen *et al.*, 2005). On the other hand, although the circular yield surface of the Druck-Prager function on the $\pi-$plane is smooth, it fails to properly address the effect of the intermediate principal stress σ_2, which has been shown to be significant (Tatsuoka *et al.*, 1986; Lam and Tatsuoka, 1988; Kirkgard and Lade, 1993; Lam and Tatsuoka, 1988; Callisto and Calabresi, 1998; Leroueil and Hight, 2003; Kandasami and Murthy, 2015; Yang *et al.*, 2016).

Two well-established yield functions that satisfy the requirements of both smoothness and consider the effect of the intermediate principal stress σ_2 are the Matsuoka-Nakai criterion (Matsuoka, 1974; Matsuoka and Nakai, 1974, 1977) and Lade-Duncan criterion (Lade and Duncan, 1975b; Lade, 1977). Based on the concept of spatially mobilized plane (SMP), the Matsuoka-Nakai criterion assumes that failure takes place on the SMP plane with the relation between the shear stress τ_{SMP} and the normal stress σ_{SMP} being described by the Coulomb relation. When using the stress invariants (I_1, I_2, I_3), the Matsuoka-Nakai criterion is normally expressed as

$$I_1 I_2 - K_{MN} I_3 = 0 \tag{2.11}$$

where K_{MN} is a material constant, which can be related to the triaxial compression friction angle φ_0 as

$$K_{MN} = \frac{9 - sin^2\varphi_0}{1 - sin^2\varphi_0} = 9 + 8tan^2\varphi_0 \tag{2.12}$$

The Lade-Duncan criterion, which is purely based on laboratory test results, was originally expressed as

$$I_1^3 - K_{LD} I_3 = 0 \tag{2.13}$$

in which the material constant K_{LD} can be related to the triaxial compression friction angle φ_0 as

$$K_{LD} = \frac{(3 - sin\varphi_0)^3}{(1 + sin\varphi_0)(1 - sin\varphi_0)^2} \tag{2.14}$$

Using the Haigh-Westergaard invariants, a unique expression for both Matsuoka-Nakai and Lade-Duncan criteria can be writen as

$$r = \frac{\xi}{\lambda}[sin(\frac{\pi - sin^{-1}(\omega sin3\theta)}{3})]^{-1} \tag{2.15}$$

The expressions of λ and ω are listed in Table 2.1.

Table 2.1: Equations for λ and ω

Yield criterion	λ	ω
Matsuoka-Nakai	$\lambda_{MN} = \sqrt{2}\sqrt{\frac{K_{MN}-3}{K_{MN}-9}}$	$\omega_{MN} = \frac{K_{MN}}{K_{MN}-3}\sqrt{\frac{K_{MN}-9}{K_{MN}-3}}$
Lade-Duncan	$\lambda_{LD} = \sqrt{\frac{2K_{LD}}{K_{LD}-27}}$	$\omega_{LD} = \sqrt{\frac{K_{LD}-27}{K_{LD}}}$

Figure 2.16 illustrates the Matsuoka-Nakai, Lade-Duncan and Mohr-Coulomb surfaces on the $\pi-$plane. The three criteria have the same yield stress under the triaxial compression condition.

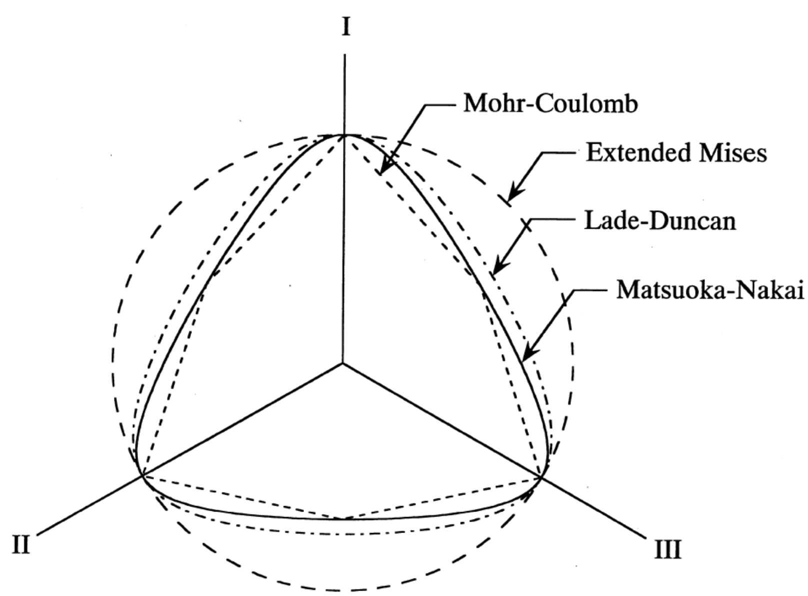

Figure 2.16: Comparison of yield surfaces on the π-plane

2.2.2 Dilatancy and flow rule

Dilatancy is a specific feature of granular material deformation. Owing to the discrete nature of granular materials, individual particles tend to ride over one another when sheared, which in turn induces volume change of the material. In the framework of classical plasticity theory, dilatancy can be described through a flow rule, which is defined by a plastic potential function in such a way that the outward normal to the plastic potential surface specifies the direction of plastic flow. When the plastic potential function is identical with the yield function, the flow rule is called an associated flow rule. Otherwise, it is referred to as a non-associate flow rule.

In the early work of Taylor (1948), the dilatancy in simple shear was quantified as $D = -d\varepsilon_n/d\gamma$, with $d\varepsilon_n$ and $d\gamma$ being the normal and shear strain increments on the shear plane respectively. Under triaxial stress conditions, Rowe (1962) quantified dilatancy of granular materials by the ratio of plastic volumetric strain increment to plastic deviatoric strain increment in the triaxial space $D = -d\varepsilon_v^p/d\gamma^{\star p}$ or the angle of dilation ψ_m defined as $\sin\psi_m = D$. The second law of thermodynamics shows that the stress ratio η and the angle of dilation ψ_m are interrelated at a fundamental level (Vardoulakis and Sulem, 1995). Based on the hypothesis that there is a constant effective friction coefficient, Taylor (1948) proposed a over-simplified relationship $\eta + D = const.$ for simple shear conditions. In a more rigious work based on the hypothesis of minimum energy ratio, under triaxial stress conditions Rowe (1962) correlated a dilatancy factor D_0 and a stress ratio σ_1/σ_3 via the interparticle friction angle φ_μ as

$$\begin{aligned} &\frac{\sigma_1}{\sigma_3} = KD_0 \\ &K = tan^2(45^\circ + \varphi_\mu) \\ &D_0 = 1 - \frac{d\varepsilon_3^p}{d\varepsilon_1^p} \end{aligned} \tag{2.16}$$

where $d\varepsilon_1^p$ is the increment of axial plastic strain, and σ_1 and σ_3 are the major and minor principal stresses, respectively. It should be noted that D_0 is different from $D = \sin\psi_m$. Rowe's dilatancy formulation can be alternatively expressed as

$$sin\psi_m = \frac{sin\varphi_m - sin\varphi_\mu}{1 - sin\varphi_m sin\varphi_\mu} \tag{2.17}$$

in which φ_m and φ_μ are the mobilized friction angle and dilatancy angle, respectively. Even though having different functional forms, the equations proposed by Taylor (1948) and Rowe (1962) both make the dilatancy $D = sin\psi_m$ a function of stress ratio and some intrinsic material properties, such that

$$D = D(\eta, C) \tag{2.18}$$

where C is a set of intrinsic material constants. Dilatancy formulations of this type can also be derived from the Cam-clay model as $D = M - \eta$ and from the Modified Cam-Clay model as $D = (M^2 - \eta^2)/2\eta$, where M is a material constant defined as the stress ratio η at the critical state; i.e., $M = \eta_{cr}$. In the different dilatancy formulations, $D = 0$ always holds true at the critical state.

For granular soils, however, experimental evidences show that dilatancy is significantly affected by density (Li and Dafalias, 2000) and stress level (Kolymbas and Wu, 1990), as shown in Figure 2.1b and Figure 2.2b. Based on experimental studies, Manzari and Dafalias (1997) showed that $D+\eta$ increases as the shear strain increases.

Wan and Guo (1998) assumed that the effect of density and stress level on dilatancy can be described by $(e/e_{cr})^{\alpha}$, where α is a material constant and the critical void ratio e_{cr} is a function of the mean effective stress. They proposed a modifed Rowe's dilatancy formulation

$$sin\psi_m = \frac{sin\varphi_m - \sin\varphi_f}{1 - \sin\varphi_f \sin\varphi_{cv}} \tag{2.19}$$

in which φ_f is a characteristic friction angle expressed as

$$\sin\varphi_f = (e/e_{cr})^{\alpha} sin\varphi_{cv}$$

Equation (2.19) was modified by Wan and Guo (2004, 2014) to account for the effect of microstructure by assuming

$$sin\varphi_f = \frac{\alpha_f + \gamma^p}{\alpha_0 + \gamma^p}(\frac{e}{e_{cr}})^{n_f} sin\varphi_{cv} \tag{2.20}$$

in which α_0 and n_f are material constants, and the fabric dependency is provided through α_f that depends on the current stress and fabric states.

It is now believed that, the basic requirements for a dilatancy formulation include the consideration of barotropy (stress level), pyknotropy (void ratio) and anisotropy (micro-structure) (Guo, 2000), which are all considered in Equaiton (2.20). When considering the effect of fabric on dilatancy, a more general form of dilatancy formulation could be written as

$$D = D(\eta, e, \Omega) \tag{2.21}$$

where Ω is a term to describe the internal state variables other than void ratio e, such as the evolving tensor of anisotropy (Dafalias, 1986a). Li and Dafalias (2000) proposed a dilatancy formulation

$$D = d_0(\eta - Me^{m\psi}) \tag{2.22}$$

where d_0 and m are material constants, M is the critical state stress ratio, and ψ is a state parameter defined as $\psi = e - e_{cr}$. More recently, Li and Dafalias (2012) and Zhao and Guo (2013) proposed a modified state parameter ζ to replace ψ to allow incorporating the evolving fabric. ζ is defined as

$$\zeta = (e - e_{cr}) + f(F, \sigma, ...) \tag{2.23}$$

where F and σ are fabric and stress tensors respectively. However, the method to incorporate the fabric tensor and the evolution law of fabric tensor must be investigated.

2.3 Micromechanical understanding of soil behaviour

It is evident from the previous literature review that the microstructure strongly influences the mechanical response of granular soils. For some materials, which have homogeneous, random structures, their macro-level responses may be considered as isotropic with path-dependency. However, for most geomaterials, their microstructures exhibit apparent inherent anisotropy, which is commonly caused by the preferred orientation of particles or direction-dependent distribution of pores. For this type of materials, both the strength and deformation characteristics are orientation-dependent, and the description of fabric requires tensorial, rather than scalar descriptors. Extensive studies on the micromechanical level have revealed that the internal structure of a granular material evolves during loading and unloading, which is termed "induced anisotropy". To properly incorporate the fabric effects in constitutive modeling, it is important to develop a fabric evolution law.

Two different approaches for describing the evolution of fabric can be found in literature, namely the strain approach and the stress approach (Pietruszczak and Krucinski, 1989; Oda *et al.*, 1985; Guo, 2000). The strain approach assumes that the rate of fabric change $\dot{F}_{ij}$ can be expressed as a tensor-valued function of the current fabric tensor F_{ij}, the void ratio e as well as the rate of plastic deviator strain $\dot{e}^p_{ij}$, i.e. $\dot{F}_{ij} = f(F_{ij}, e, \dot{e}^p_{ij})$. However, as a granular material approaches critical state during a loading process, the material continues to deform without further change in stresses and volume, and the fabric may reach an ultimate state as well. This contrasts the strain-approach formulation of fabric evolution, in which the fabric change continues at the critical state.

In the stress-based approach, the fabric evolution is related to the current states and the rate of deviator stress ratio as $\dot{F}_{ij} = f(F_{ij}, e, \dot{\eta}_{ij})$. Herein the deviator stress ratio is defined as $\eta_{ij} = s_{ij}/p$. Biarez and Wiendieck (1963) studied the distribution of contact normals through biaxial compression tests, and found that the contact normal tends to concentrate towards the direction of compression. Similar observations were made by Oda (1972b) and Oda and Konishi (1974a) for natural sand in triaxial tests. Oda *et al.* (1980) concluded based on these experiments that the distribution of contact normal changes in such a manner as to produce a greater concentration of contact normals in the direction of the major principal stress. Oda (1993) summarized the previous knowledge about fabric evolution, which includes:

(a) $\dot{F}_{ij}$ should be a deviator tensor with $\dot{F}_{ii} = 0$;

(b) Change of fabric tensor $\dot{F}_{ij}$ occurs as a result of the stress anisotropy measured by $\dot{\eta}_{ij}$;

(c) The rate of fabric change should depend on the current state of fabric, especially α and $(\sqrt{J_2^F} - \sqrt{\hat{J}_2^F})$, in which α is the inclination angle of the major principal axis of $\dot{F}_{ij}$ to the major principal axis of $\dot{\eta}_{ij}$, and $\sqrt{\hat{J}_2^F}$ is a limiting value of $\sqrt{J_2^F}$, representing a certain saturated state in concentrating the contact normals.

In a series of biaxial compression tests, Oda (1993) observed a linear relationship between $\sqrt{J_2^F}/I_2^F$ and $\sqrt{J_2}/I_2$. Herein I_2^F and J_2^F are fabric invariants, while I_2 and J_2 are stress invariants.

DEM simulations have been used as a powerful means to explore fabric evolution. By simulating granular assemblies under bi-axial compression tests, Antony *et al.* (2004) observed a correlation between stress ratio and fabric ratio:

$$\frac{\sigma_1 - \sigma_2}{\sigma_1 + \sigma_2} \approx \sqrt{\frac{\phi_{22}}{\phi_{11}}}$$

which was confirmed by Maeda *et al.* (2006). Based on the results of a series of DEM simulations for cyclic biaxial compression tests, Suzuki and Kuhn (2013) and Sazzad (2014) found a correlation between the deviator stress ratio and the fabric components defined for the strong contact network as

$$\frac{\sigma_1 - \sigma_2}{\sigma_1 + \sigma_2} = \frac{H_1^S - H_2^S}{H_1^S + H_2^S}$$

in which H_1^S and H_2^S are the components of the fabric tensors defined in the strong contact network.

Recent studies have revealed that a unique ultimate state of the fabric tensor exists. Yimsiri and Soga (2010) observed that triaxial extension causes more significant fabric anisotropy at ultimate than triaxial compression. Similar observations were made by Thornton (2000) and Zhao and Guo (2013). It has now become possible to define a limit surface which quantifies the fabric state when the granular material approaches the critical state along various stress paths. By discrete element simulations, Thornton (2000) proposed a function of fabric at critical state as $(I_1^\Phi)^3/(2I_1^\Phi I_2^\Phi - 3I_3^\Phi) = \eta^\star$, in which I_1^Φ, I_2^Φ and I_3^Φ are the invariants of the fabric tensor Φ_{ij}, and $\eta^\star$ is a material constant. The fabric surface has the shape of an inverted Lade-Duncan failure criterion. Zhao and Guo (2013) proposed a relation at critical state between the mean effective stress p' and a fabric anisotropy parameter K_c, as $K_c = 0.41p'^{0.894}$, in which K_c is the first joint invariant of the deviatoric stress tensor and the deviator fabric tensor defined as $K_c = s_{ij}^{(cv)} F_{ji}^{(cv)}$, where s_{ij} is the deviatoric stress tensor.

2.4 Conclusions

Based on the above literature review, the following conclusions are made:

Firstly, based on experimental studies, the influences of the major principal stress direction and the intermediate principal stress on the granular material behaviour are significant. These influences are reflected not only in the peak strength properties but also on the deformation properties. Few previous studies have focused on the combined effects of the two factors.

Furthermore, a proper description of the evolution of fabric tensor during the loading process was missing. However, computer simulation tools have made it possible for such an evolution law to be developed.For a given fabric evolution law, the method of incorporating a fabric tensor in the framework of plasticity is required.

In the following chapters, attempts are made to explore the properties of a granular material under generalized stress conditions. Thereafter a fabric evolution law is developed based on observations from DEM studies, with the model framework being developed and verified.

Chapter 3

Experimental Study

This chapter presents an experimental study on soil behaviour under different loading conditions using a hollow cylinder apparatus. The primary objective of the experimental study was to investigate the influence of the intermediate principal stress and the major principal stress direction relative to the principal direction of fabric on the behaviour of an inherently anisotropic granular material subjected to monotonic loading. The behaviour, particularly the accumulative deformation, of the same material under cyclic loading along different stress paths, with or without change of principal stress direction, were also explored. A detailed description of the experimental equipment, tested material, sample preparation method, sample installation process and testing procedures are presented in this chapter. The test results are analyzed focusing on the effect of loading direction and stress path on the behaviour of sand.

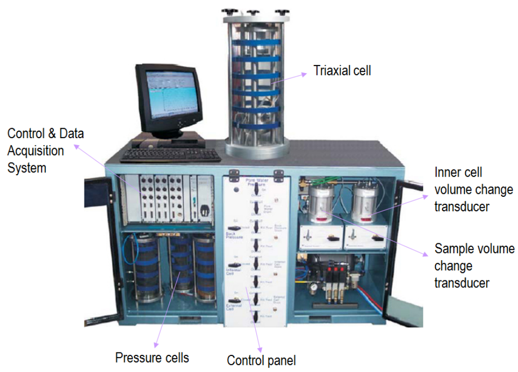

(a) Apparatus

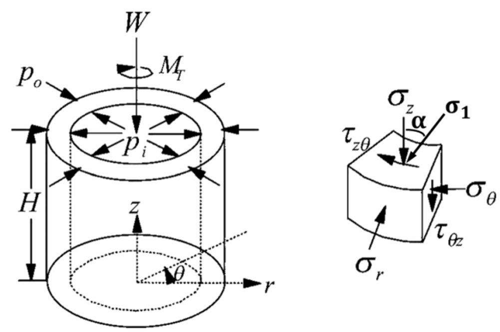

(b) Stress components

Figure 3.1: Hollow Cylinder Apparatus (HCA)

3.1 Test equipment

3.1.1 Hollow Cylinder Apparatus

The Hollow Cylinder Apparatus (HCA) at McMaster University was used in this study. The dimensions of the specimens adopted for the study were 100 mm for the outer diameter (O.D.), 60 mm for the inner diameter (I.D.), and 200 mm for the height. Schematic diagrams of the equipment and the stress state of the specimen are shown in Figure 3.1. Four independent stress components, the axial stress σ_z, radial stress σ_r, circumferential stress σ_θ, and shear stress $\tau_{z\theta}$, were applied to a specimen by independently controlled axial load W, torque M_T, inner cell pressure p_i, and outer cell pressure p_o. The axial and torsional movements were controlled by two servo motors individually, and the outer and inner cell pressures were controlled through air-driven pressure cells in which the applied air pressure was converted to water pressure.

3.1.2 Calculation of stresses and strains

The effective principal stresses σ_1', σ_2' and σ_3' were computed from σ_z, σ_r, σ_θ, $\tau_{z\theta}$ and the pore pressure, with the strains being calculated from the readings of two volume change transducers and the vertical displacement transducer. The average stresses and strains in the specimen were calculated using equations listed in Table 3.1. Two parameters, b and α, are used herein to describe the stress states. The intermediate principal stress parameter b, defined as $b = (\sigma_2 - \sigma_3)/(\sigma_1 - \sigma_3)$, is a measure of the relative magnitude of the intermediate principal stress σ_2. The parameter α is defined as the angle between the direction of the major principal stress σ_1 and the normal direction of the bedding plane. Since the bedding plane of the specimen was horizontal in the test, α can be calculated by $\tan 2\alpha = 2\tau_{z\theta}/(\sigma_z - \sigma_\theta)$ when the radial stress is a principal stress.

3.1.3 Stress non-uniformity

In the experimental study of soil behaviour, it is important to ensure uniform distribution of stresses in the specimen. In this study, the main sources of stress non-uniformity include the end restraint effect, application of the torque and the difference between the inner and outer cell pressures. To minimize stress non-uniformity in HCA tests, it is important to choose proper specimen geometry. To reduce the non-uniformity of stresses and strains in the radial direction, Hight *et al.* (1983) suggested a specimen with 203 mm inner diameter, 254 mm outer diameter, and 254 mm height. Tatsuoka *et al.* (1986) used large height/radius ratio to reduce the influence of end restraint, with the dimension of 60 mm I.D., 100 mm O.D. and 200 mm height. Vaid *et al.* (1990) developed a hollow cylinder apparatus and examined

Table 3.1: Equations for stress and strain calculation of HCA

	Stresses	Strains
Axial stress/strain	$\sigma_z = \frac{W}{\pi(r_o^2-r_i^2)} + \frac{p_o r_o^2 - p_i r_i^2}{r_o^2-r_i^2}$	$\varepsilon_z = \frac{\Delta H}{H}$
Radial stress/strain	$\sigma_r = \frac{p_o r_o + p_i r_i}{r_o + r_i}$	$\varepsilon_r = -\frac{\Delta r_o - \Delta r_i}{r_o - r_i}$
Circumferential stress/strain	$\sigma_\theta = \frac{p_o r_o - p_i r_i}{r_o - r_i}$	$\varepsilon_\theta = -\frac{\Delta r_o + \Delta r_i}{r_o + r_i}$
Shear stress/strain	$\tau_{z\theta} = \frac{3M_T}{2\pi(r_o^3-r_i^3)}$; $\tau_{zr} = \tau_{r\theta} = 0$	$\gamma_{z\theta} = 2\varepsilon_{z\theta} = \frac{2\theta(r_o^3-r_i^3)}{3H(r_o^2-r_i^2)}$; $\varepsilon_{zr} = \varepsilon_{r\theta} = 0$
Major principal stress/strain	$\sigma'_1 = \frac{\sigma_z+\sigma_\theta}{2} + \sqrt{(\frac{\sigma_z-\sigma_\theta}{2})^2 + \tau_{z\theta}^2}$	$\varepsilon_1 = \frac{\varepsilon_z+\varepsilon_\theta}{2} + \sqrt{(\frac{\varepsilon_z-\varepsilon_\theta}{2})^2 + \varepsilon_{z\theta}^2}$
Intermediate principal stress/strain	$\sigma'_2 = \sigma_r$	$\varepsilon_2 = \varepsilon_r$
Minor principal stress/strain	$\sigma'_3 = \frac{\sigma_z+\sigma_\theta}{2} - \sqrt{(\frac{\sigma_z-\sigma_\theta}{2})^2 + \tau_{z\theta}^2}$	$\varepsilon_3 = \frac{\varepsilon_z+\varepsilon_\theta}{2} - \sqrt{(\frac{\varepsilon_z-\varepsilon_\theta}{2})^2 + \varepsilon_{z\theta}^2}$
Effective Mean stress/Volumetric strain	$p' = \sigma'_{oct} = \frac{\sigma'_1+\sigma'_2+\sigma'_3}{3}$	$\varepsilon_v = \varepsilon_1 + \varepsilon_2 + \varepsilon_3$
Deviator stress/Octahedaral strain	$q = \frac{1}{\sqrt{2}}\sqrt{(\sigma'_1-\sigma'_2)^2 + (\sigma'_2-\sigma'_3)^2 + (\sigma'_1-\sigma'_3)^2}$	$\gamma_{oct} = \frac{2}{3}\sqrt{(\varepsilon_1-\varepsilon_2)^2 + (\varepsilon_2-\varepsilon_3)^2 + (\varepsilon_1-\varepsilon_3)^2}$

the stress non-uniformity across the wall of the hollow cylinder specimen, using a dimension of 102 mm I.D., 152 mm O.D. and 302 mm height. Sãyao and Vaid (1991) made the following recommendations for the geometry of HCA specimens: (1) The wall thickness $(r_o - r_i) = 20 - 60mm$, (2) the ratio of the inner radius to the outer radius $0.65 \leq r_i/r_o \leq 0.82$, and (3) the height $1.8 \leq H/(2r_o) \leq 2.2$. The geometry of specimens used in this study meets the recommendations (1) and (3), while the r_i/r_o ratio (0.6) is only slightly smaller than that from Recommendation (2). Nevertheless, the dimension of specimens used in this study is considered acceptable.

Another way of reducing the stress non-uniformity across the wall of the specimen is to minimize the difference between the inner and outer cell pressures. When the material is elastic and $\tau_{z\theta} = 0$, the radial stress σ_r and circumferential stress σ_θ in the specimen are derived as

$$\begin{aligned}\sigma_r &= \frac{p_o r_o^2 - p_i r_i^2}{r_o^2 - r_i^2} - \frac{(p_o - p_i)\, r_o^2 r_i^2}{(r_o^2 - r_i^2)\, r^2} \\ \sigma_\theta &= \frac{p_o r_o^2 - p_i r_i^2}{r_o^2 - r_i^2} + \frac{(p_o - p_i)\, r_o^2 r_i^2}{(r_o^2 - r_i^2)\, r^2}\end{aligned}$$

One observes that the stress non-uniformity across the wall of the specimen increases with the $(p_o - p_i)$. σ_r and σ_θ are uniform only when $p_i = p_o$. For cases with $\alpha \neq 0°$ and $\alpha \neq 90°$, $p_i - p_o$ can be expressed as

$$p_i - p_o = \frac{b - \sin^2\alpha}{2\sin\alpha\cos\alpha}\frac{r_o^2 - r_i^2}{r_o r_i}\tau_{z\theta}$$

If the parameters b and α satisfy $b = \sin^2\alpha$, the internal and external pressures will remain identical during the loading process. Therefore, the stress non-uniformity across the wall of the hollow cylindrical specimen vanishes.

For cases with $\alpha = 0°$ or $\alpha = 90°$, the shear stress $\tau_{z\theta}$ and hence the torque are zero. $p_i - p_o$ can be expressed as

$$\begin{aligned} p_i - p_o &= \frac{3b}{2(2-b)}\frac{r_o^2 - r_i^2}{r_o r_i}(\sigma_z - p) \quad \text{for} \quad \alpha = 0° \\ p_i - p_o &= \frac{3(1-b)}{2(2-b)}\frac{r_o^2 - r_i^2}{r_o r_i}(\sigma_z - p) \quad \text{for} \quad \alpha = 90° \end{aligned}$$

It can be shown that the condition of $p_i = p_o$ is satisfied when $b = \sin^2\alpha$ for these two cases as well. Consequently, it can be concluded that $b = \sin^2\alpha$ is of great importance in reducing stress non-uniformity. However, to fully understand the effects of both the principal stress direction and the intermediate principal stress, the two parameters of α and b need to be individually controlled. In this study, tests with $b = \sin^2\alpha$ and $b \neq \sin^2\alpha$ were both carried out.

3.2 Test material and test programme

3.2.1 Test material

The test material used in this research was Ottawa sand C109. It is a uniform quartz sand of rounded and subrounded particles. The particle size distribution curve is shown in Figure 3.2a and the scanning electron micrograph of typical particles is shown in Figure 3.2b. The maximum and minimum void ratios of the sand are 0.811 and 0.503, respectively. To obtain specimens with a constant initial fabric, the water pluviation technique was used to fabricate the specimens (Vaid and Negussey, 1984; Cresswell *et al.*, 1999; Saada *et al.*, 2000). The void ratios of specimens after consolidation fell into the range of 0.59 ± 0.02, with the relative densities in the range of $D_r = 72\% \pm 5\%$.

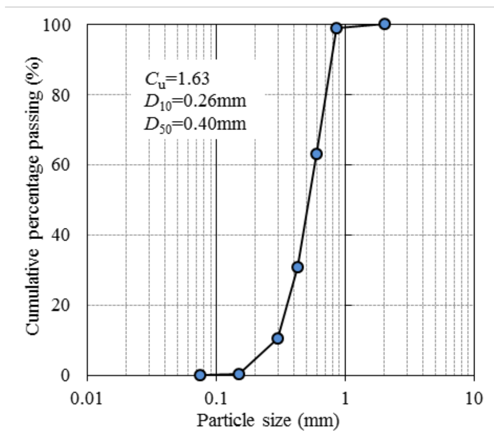

(a) Grain size distribution

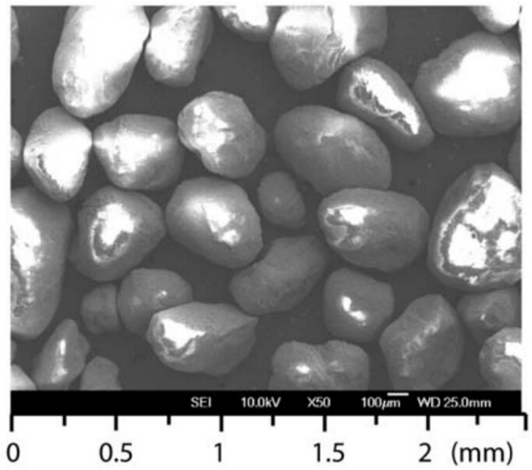

(b) Scanning electron micrograph (Guo, 2008)

Figure 3.2: Test material: Ottawa Sand

3.2.2 Specimen preparation

Figure 3.3 shows the details of specimen preparation by the water-pluviation method. Firstly, take approximately 2kg of oven-dried sand, measure the weight, and put into a specially designed bottle. Fill the bottle with distilled water until the sand is completely submerged. Seal the bottle and apply vacuum pressure of -80kPa for at least 12 hours, during which the bottle should be pitched back and forth several times to help the trapped air bubbles to escape. A water tank was also set up to produce de-aired water for use in the tests, see Figure 3.3a. Before fabricating the specimen, all tubes connected to the top or the bottom of the specimen should be flushed by water. After setting up the base pedestal, assembling the inner and outer moulds and membranes, the space between the inner and outer moulds was filled with de-aired water (see Figure 3.3b). Then the bottle with de-aired water-sand mixture is

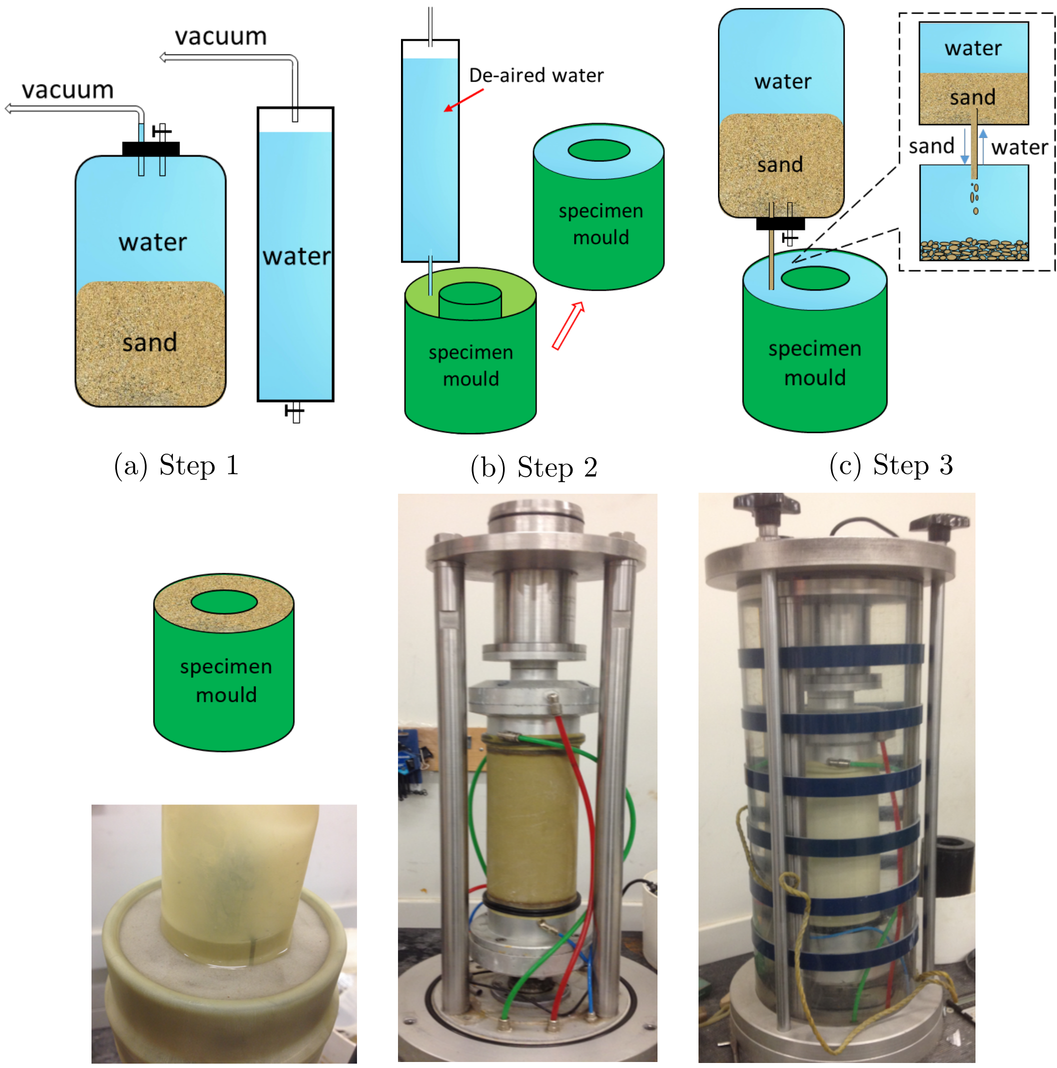

(a) Step 1 (b) Step 2 (c) Step 3

(d) Step 4 (e) Step 5 (f) Step 6

Figure 3.3: Specimen preparation precedure

placed upside down on a shelf. The valve on the bottle is then opened while the lower end of the pipe was put beneath the water between the inner and outer moulds. As illustrated in Figure 3.3c, the sand settles while the water replaces the sand in the bottle. In case the sand becomes jammed, the bottle is gently tapped.The mould is filled until the surface of the sand is approximately 3mm beneath the top edge of the mould so that the top cap can be properly mounted; as shown in Figures 3.3d and 3.3e. When mounting the top cap, care must be taken so that no air is trapped in the specimen.

Before removing the inner and outer moulds, a negative pressure of 15 kPa is applied to the specimen so it can stand by itself. Figure 3.3e shows a completed specimen with the top cap in place and all tubing connected. The next step is to mount the cell of the apparatus in the loading frame, as shown in Figure 3.3f. By properly adjusting the valves that control the flows as shown in Figure 3.4, de-aired water is added into the inside and outside cells of the specimen at the same time.

3.2.3 Saturation and consolidation

Before saturating a specimen, the applied negative water pressure is firstly removed by applying a pressure of 20kPa in both the inner and outer cells and releasing the applied negative pressure. Water is flushed from the de-aired water tank through the specimen using the back pressure lines shown in Figure 3.4. Flush continues for 30 minutes. The propose of this step is to drive out residual air bubbles trapped in the specimen.

Afterward, the water supply and the drainage valves are closed. Simultaneously, the inner and outer cell pressures are increased by 50kPa in 5 seconds. The change on the pore pressure transducer is recorded. Then the back pressure is increased until the pressure increment within the specimen is also 50kPa. Based on the change of pore pressure Δu and the increased cell pressure $\Delta \sigma_c$, the Skempton's pore pressure B-coefficient is calculated as $\Delta u / \Delta \sigma_c$. A value of 0.95 was considered acceptable for the requirement of saturation. During the saturation stage, the cell pressures and the

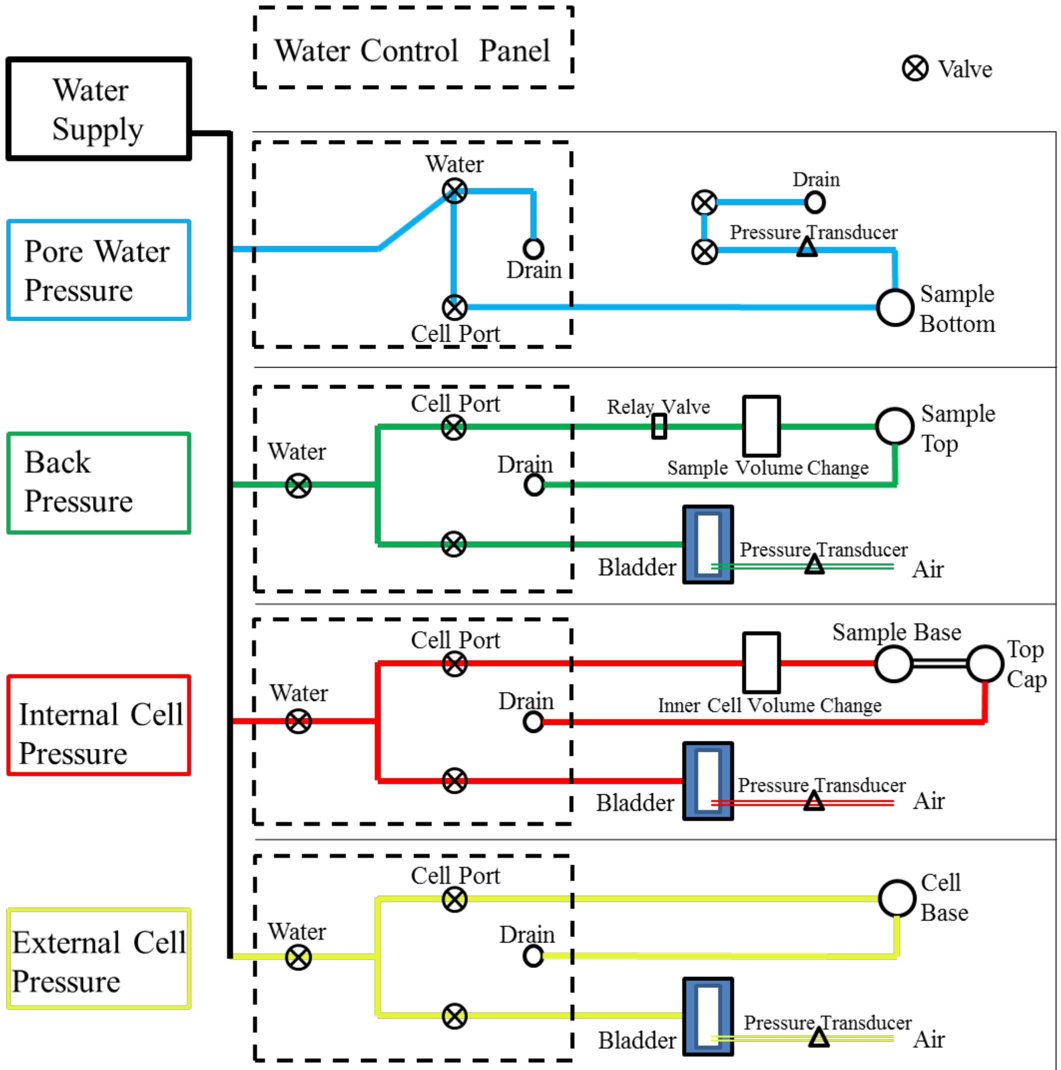

Figure 3.4: System flow chart of HCA

back pressure must be applied incrementally. All the tests of this study satisfied the criterion of $B \geq 0.95$ with the back pressure in the range of 250-300kPa.

All specimens were consolidated under a hydrostatic effective stress of 100kPa. During consolidation and shearing, the volume changes of the specimen and the inner cell of the hollow cylindrical specimen were measured by the volume change transducers. The vertical displacement and the rotation of the specimen were measured by an axial displacement transducer and a radial displacement transducer respectively. The outer circumferential displacement of the specimen was measured by an LVDT mounted on the specimen. The data gathered by these transducers were recorded for the corrections of loading control as well as the calculation of strains using the equations in Table 3.1.

3.2.4 Testing Programme

To investigate the influence of the intermediate principal stress and the major principal stress direction relative to the principal direction of fabric on the behaviour of inherently anisotropic granular material as well as the fabric evolution during shearing, four series of tests were carried out. The major principal stress direction was characterized by α, the angle between the major principal stress direction and the normal of the bedding plane (see Figure 3.1). The intermediate principal stress was characterized by the intermediate principal stress parameter b, defined as $b = (\sigma_2 - \sigma_3)/(\sigma_1 - \sigma_3)$. On the π-plane (see Figure 3.5), b can be related to the Lode angle via

$$\theta = \tan^{-1}\left(\frac{1-2b}{\sqrt{3}}\right) = \tan^{-1}\left[\frac{1}{\sqrt{3}}\left(1 - 2\frac{\sigma_2 - \sigma_3}{\sigma_1 - \sigma_3}\right)\right]$$

For all the tests of the four series, the mean effective stress was kept constant (p'=100kPa).

Test Series A: monotonic loading with $b = sin^2\alpha$

The objective of Series A tests was to determine the deformation and strength properties of the sand subjected to monotonic loading at select values of b and α. To

Table 3.2: Test matrix for test Series A

Test No.	α	$b = sin^2\alpha$	Lode angle $\theta(°)$
A1	0	0	30
A2	30	0.25	16.1
A3	45	0.5	0
A4	60	0.75	-16.1
A5	90	1	-30

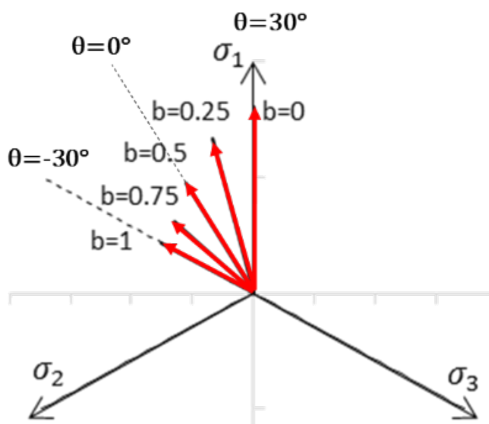

Figure 3.5: Monotonic loading stress paths on π-plane (Series A)

minimize the non-uniformity of stresses in the hollow cylindrical specimens, the internal and external pressures were kept identical during monotonic shear; i.e., $p_i = p_o$. This requirement was satisfied by adjusting the applied stresses continuously to satisfy $b = \sin^2\alpha$. The test matrix for this series of tests is given in Table 3.2, with the stress paths on the π-plane being shown in Figure.3.5.

All specimens were saturated until B-value of 0.95 was attained. The back pressures fell into the range of 250kPa-300kPa. Following saturation, the specimens were isotropically consolidated to a mean effective stress of $p' = 100kPa$. During the shearing process, a deviator stress measure, defined as $q^{test} = (\sigma_z - \sigma_\theta)/2$, was increased monotonically at a rate of 2kPa/min until failure.

Test Series B and C: monotonic loading with independent α and b

Table 3.3: Test matrix for test Series B

Test No.	α	b	$sin^2\alpha$	Lode angle $\theta(°)$
B1	0	0	0	30
B2	30	0	0.25	30
B3	60	0	0.75	30
B4	90	0	1	30

Table 3.4: Test matrix for test Series C

Test No.	α	b	$sin^2\alpha$	Lode angle $\theta(°)$
C1	0	1	0	-30
C2	30	1	0.25	-30
C3	60	1	0.75	-30
C4	90	1	1	-30

The objective of tests in Series B and C was to investigate the influence of loading direction on soil behaviour at select values of intermediate principal stress coefficient b. More specifically, tests in Series B were carried out at $b = 0$, which corresponds to conventional triaxial compression. In Series C, all tests were performed at $b = 1$. In each test of Series B and C, α was kept constant in the range of $0°$ to $90°$. Table 3.3 and Table 3.4 present the test matrixes of test Series B and C, respectively.

The stress paths in test Series A to C are shown graphically in Figure 3.6. The three shaded surfaces represent the stress paths in these three test series, respectively. By comparing results from tests B1 to B4, and from tests C1 to C4, the influence of the loading direction α can be obtained. Also, the effect of stress paths corresponding to different b values can be observed by comparing the results from tests B1 and C1 at $\alpha = 0°$, A2, B2 and C2 at $\alpha = 30°$, A4, B3 and C3 at $\alpha = 60°$ and B4 and C4 at $\alpha = 90°$, respectively.

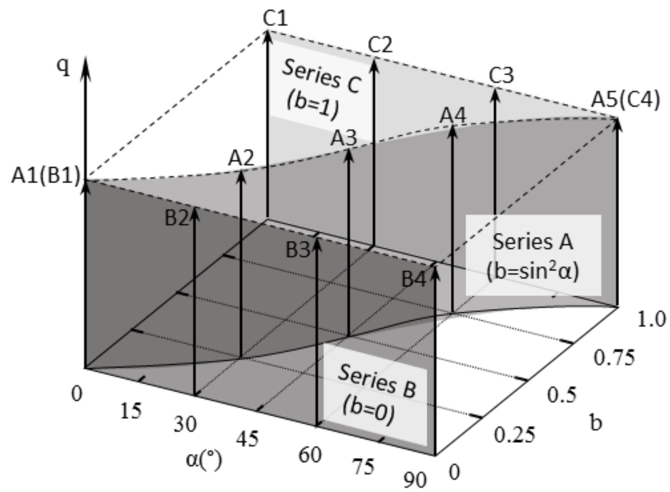

Figure 3.6: Loading paths for test series A, B and C in $\alpha - b - q$ space

Test Series D: cyclic loading

In addition to monotonic loading tests, a series of cyclic loading tests were performed to investigate the effects of principal stress direction and the intermediate principal stress on the mechanical behaviour of sand. The specimens were isotropically consolidated to a mean effective stress of $p' = 100kPa$, which was the same as that for the monotonic loading tests. Then cyclic stresses were applied while keeping p' constant. Different sequences of cyclic loading with different values of intermediate stress coefficient b were used in these tests, as summarized in Table 3.5. During the cyclic loading, the inner and outer cell pressures were allowed to vary to maintain a constant mean effective stress. To understand the effect of cyclic loading direction and stress path on the accumulative deformation, the applied stresses were alternated between two modes: mode 1 with $b = 0$, and mode 2 with $b = 1$. For each loading mode, the cyclic stress was applied for a certain number of times.

The stress paths for cyclic loading are shown in Figures 3.7. Figures 3.7a and

Table 3.5: Testing matrix for cyclic shear tests - series D

Test No.	Loading sequence		$q^{test} = (\sigma_z - \sigma_\theta)/2$
	value of b	number of cycles	kPa
D1	$0 \to 1 \to 0 \to 1$	50×8	(-40,40)
D2	0	200×2	(-40,40)
D3	$0 \to 1$	100×4	(-40,40)
D4	$1 \to 0 \to 1 \to 0$	50×8	(-40,40)
D5	1	200×2	(-40,40)
D6	$1 \to 0$	100×4	(-40,40)

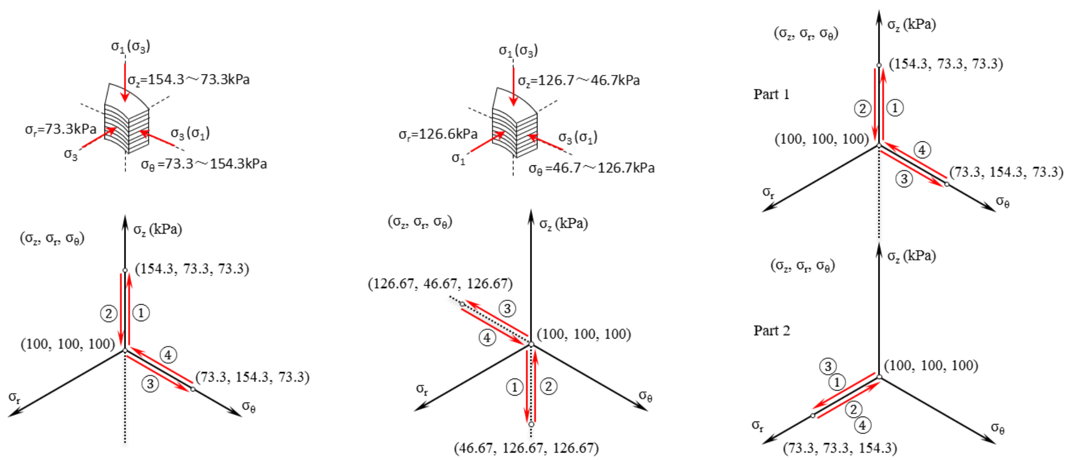

(a) mode 1 ($b = 0$) (b) mode 2 ($b = 1$) (c) Decomposed mode 2

Figure 3.7: Cyclic loading stress paths on π-plane in Series D tests

Figure 3.7b represent the cyclic loading stress paths at $b = 0$ (mode 1) and $b = 1$ (mode 2), respectivley. The circled numbers ①②③④ denote the order of the loading paths in one cycle.

To better understand the role of the loading path during cyclic loading, the loading Mode 2 with $b = 1$ can be decomposed into two parts as shown in Figure 3.7c. Part 1 is the same as that of loading Mode 1 with $b = 0$, and Part 2 can be interpreted as a one-way repeated loading in the radial direction of the specimen within the bedding plane. To simplify notation in the rest of this chapter, σ_{ij} and p are used to represent the effective stresses instead of σ'_{ij} and p' in the rest of the thesis.

3.3 Accuracy of stress control and repeatability of tests

3.3.1 Accuracy of stress control

Stress and strain components in monotonic loading tests (Series A)

We first examine the accuracy of stress control in monotonic tests. As outlined earlier, in each monotonic loading test, the mean effective stress was kept constant at 100 kPa with a selected combination of b and α that were both constant during the loading process.

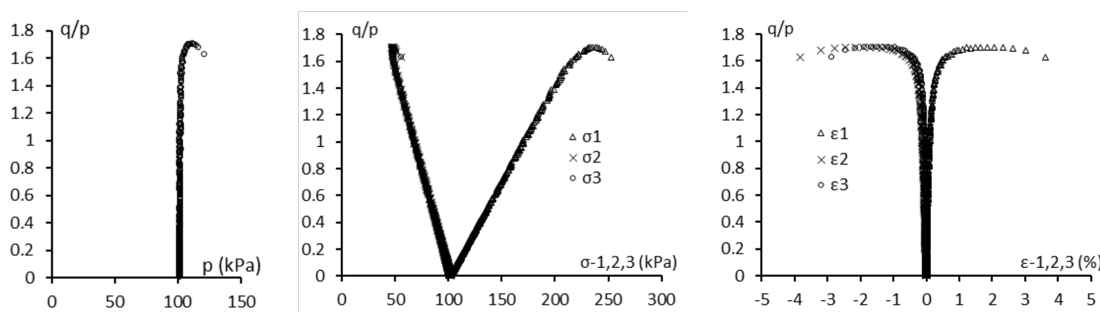

(a) $q/p - p$ (b) $q/p - \sigma$ (c) $q/p - \varepsilon$

Figure 3.8: Stress and strain components at $b = 0$

Figures 3.8 to 3.12 present typical stress and strain histories along different stress paths. The vertical axis represents q/p, where $q = \sqrt{3J_2}$ and $p = I_1/3$. Figure 3.8a shows the variation of the mean effective stress during a loading process with $b = 0$ and $\alpha = 0°$. It is observed that the mean effective stress was kept constant for the majority of the loading process. When the stress level was close to failure, the mean stress

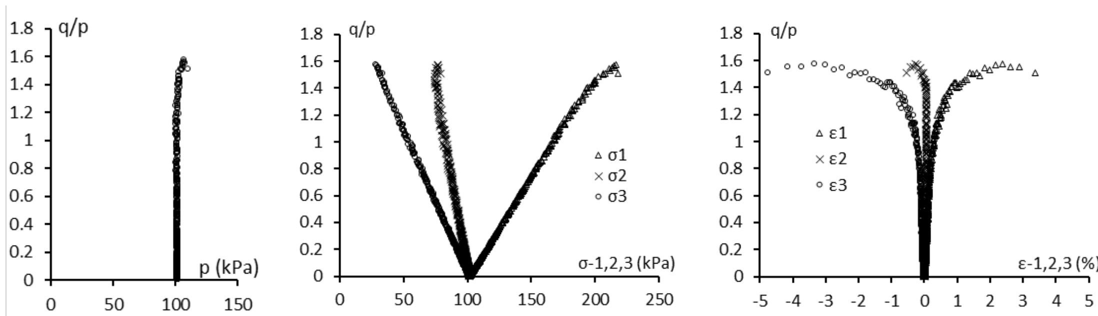

(a) $q/p - p$ (b) $q/p - \sigma$ (c) $q/p - \varepsilon$

Figure 3.9: Stress and strain components at $b = 0.25$

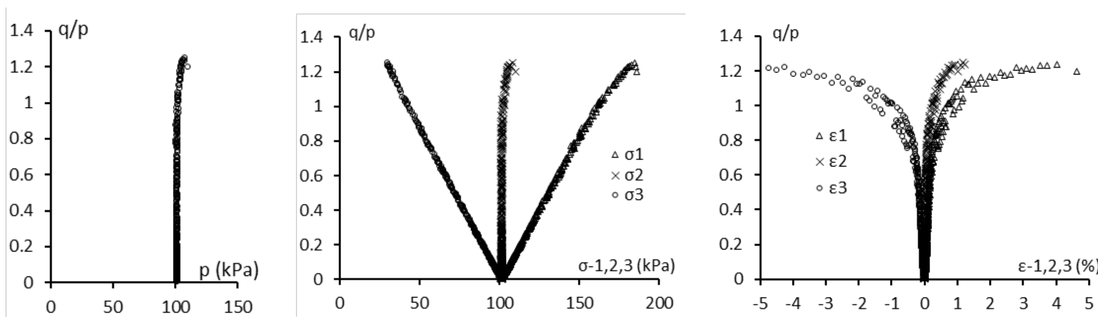

(a) $q/p - p$ (b) $q/p - \sigma$ (c) $q/p - \varepsilon$

Figure 3.10: Stress and strain components at $b = 0.5$

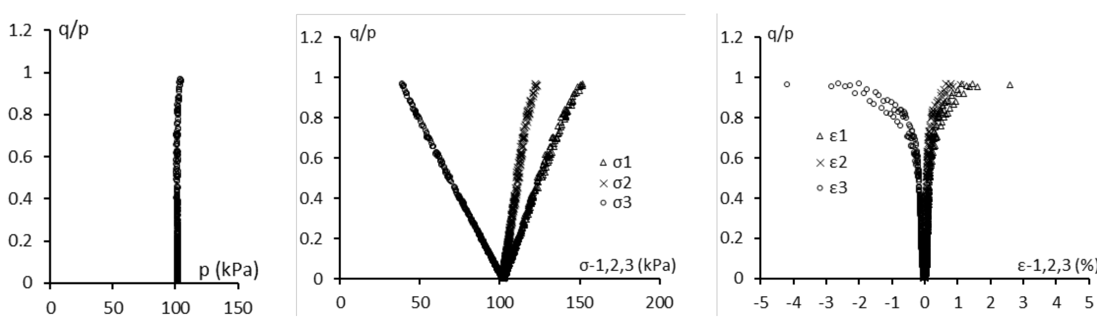

(a) $q/p - p$ (b) $q/p - \sigma$ (c) $q/p - \varepsilon$

Figure 3.11: Stress and strain components at $b = 0.75$

started to increase, which was related to the insufficient stress control capacity of the system. Since the shearing process was controlled by increasing the deviator stress

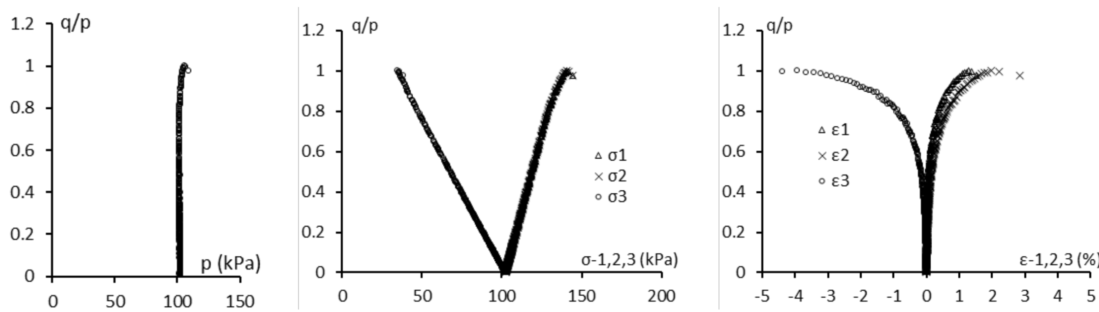

(a) $q/p - p$ (b) $q/p - \sigma$ (c) $q/p - \varepsilon$

Figure 3.12: Stress and strain components at $b = 1$

q^{test} monotonically at a rate of 2kPa/min, such a loading rate could not be maintained when deformation was close to failure without increasing the mean effective stress. Figure 3.8b shows the evolution of three principal stresses during loading. Starting from the initial value of 100 kPa, during the loading process, σ_1 increased while σ_2 and σ_3 both decreased at the same rate so that $b = 0$, $dq^{test}/dt = 2kPa/min$ and $p = 100kPa$ were achieved. Figure 3.8c shows the measured three principal strain components during loading. Because of the initial cross-anisotropy condition under $b = 0$ and $\alpha = 0°$, ε_2 and ε_3 should increase at the same rate during the test. However, a small divergence was observed between ε_2 and ε_3 at large strains ($\varepsilon_1 > 1\%$), which is very likely caused by strain localization. The hollow cylindrial geometry renders the specimen to be more deformable in the radial direction (ε_2=ε_r according to Table 3.1) than in the circumferential direction (ε_3=ε_θ in this case). Therefore at large strains, the specimen tends to bulge in the $r-$direction (Zdravkovic and Jardine, 1997) and the shear plane tends to develop in the $r - z$ plane (Lade *et al.*, 2014b), resulting in a larger rate of $\varepsilon_2(\varepsilon_r)$. By the same reason, a larger rate of ε_2 was observed for $b = 1$ ($\alpha = 90°$). Figures 3.9 to 3.12 show the history of stress and strain components in tests with $b = 0.25$ ($\alpha = 30°$) to $b = 1$ ($\alpha = 90°$), respectively.

Figure 3.13 shows the variation of the major principal stress direction during the monotonic loading tests. For tests where $b = 0$ and $b = 1$, the control of major principal stress direction was stable for $\alpha = 0°$ and $\alpha = 90°$. Small perturbations were observed in tests with $\alpha = 30°$, $\alpha = 45°$ and $\alpha = 60°$, especially at the very beginning. However, the errors were in the range of $\pm 3°$. It is concluded that the stresses were properly controlled for the proposed monotonic loading tests.

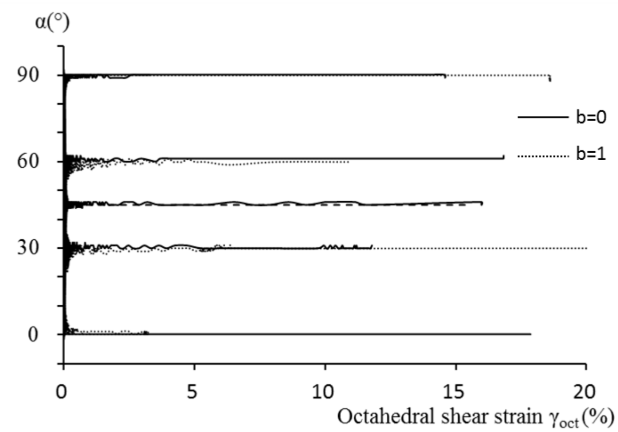

Figure 3.13: Variation of major principal stress direction under tests with $b = 0$ and $b = 1$

Stress control in cyclic loading tests

Figure 3.14 shows the variations of the stress components in the cyclic loading test with $b = 0$. Three full cycles are presented in the figure, each containing four stages of loading (as shown in Figure 3.7a). The starting points of the three stress components were $100kPa$. At stage ①, σ_z increased while σ_r and σ_θ decreased. The deviator stress q^{test} was increased to $40kPa$. At stage ②, σ_z decreased and σ_r and σ_θ increased. By the end of stage ②, the deviator stress was $0kPa$. At stage ③, σ_z continued to decrease while σ_r and σ_θ continued to increase until the deviator stress reached -40kPa. Finally, at stage ④, σ_z increased and σ_r and σ_θ decreased until the deviator stress became zero again. It is observed that at stage ① and ②, the axial direction was the major principal stress direction, while at stage ③ and ④, the circumferential direction became the major principal stress direction. While a minor difference between σ_2 and σ_3, is observed, the value of b throughout the whole procedure was kept at $b = 0$, and the variation in the mean effective stress was less than 5%.

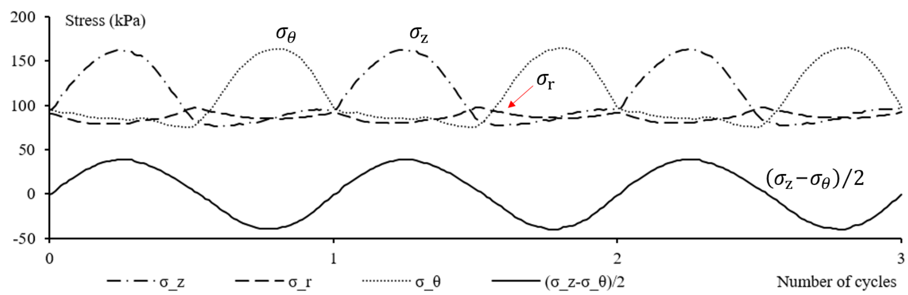

Figure 3.14: Cyclic stress compontents at $b = 0$

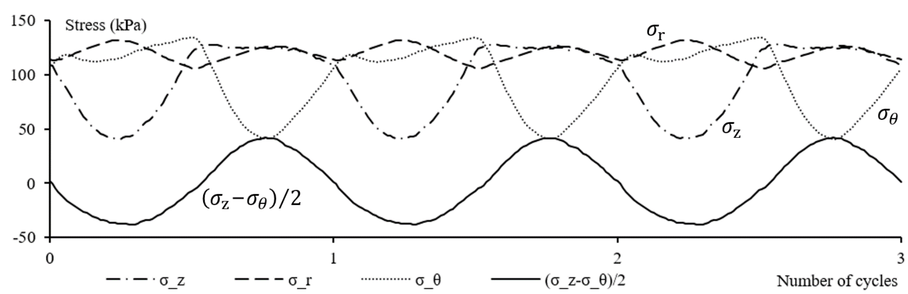

Figure 3.15: Cyclic stress compontents at $b = 1$

Figure 3.15 shows the variations of the stress components during cyclic loading at $b = 1$. The radial stress σ_r was the intermediate principal stress during the test, and the axial and circumferential stresses alternated between σ_1 and σ_3. Again, the measured data confirmed $b = 1$. The mean effective stress was observed to have a variation of ±8% around the expected value of 100kPa. As discussed in Section 3.1.3, the stress non-uniformity across the wall of the specimen when $b \neq \sin^2 \alpha$ tended to increase, particularly at $b = 1$.

3.3.2 Repeatability of test results

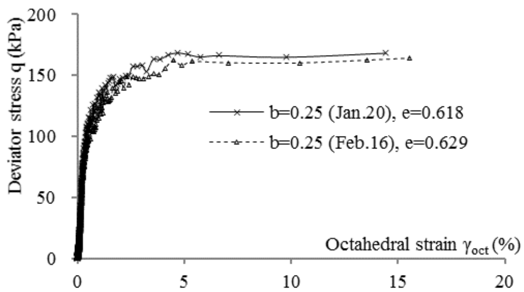

(a) $b = 0.25$

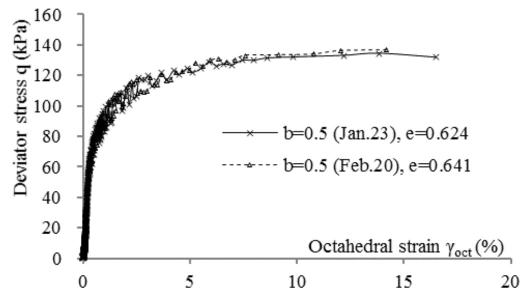

(b) $b = 0.5$

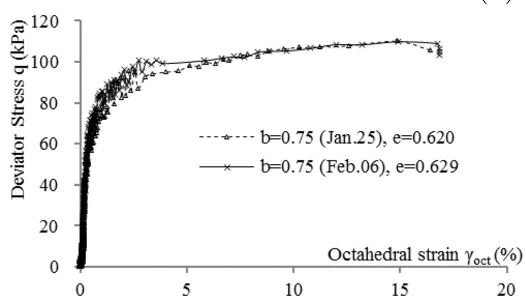

(c) $b = 0.75$

Figure 3.16: Repeatability of tests in terms of stress-strain curves

Figure 3.16 shows the repeatability of tests in terms of the stress-strain relations in monotonic loading tests. Tests at $b = 0.25$, $b = 0.5$ and $b = 0.75$ were repeated to examine the repeatability of tests. As shown in the figure, for the same intermediate principal stress coefficient and the same principal stress direction, the stress-strain curves obtained from replicated tests were close to one another. For the tests at $b = 0.25$, the difference between the obtained peak stress values was less than 2.5%, while for tests at $b = 0.5$ and $b = 0.75$, the difference was less than 1%.

3.3.3 Effect of membrane penetration

Membrane penetration effect is important on the measure of excess pore-water pressure in undrained tests and its influence increases with the increase of grain size. For drained tests, membrane penetration has a minor effect on the volume change. Since the current experimental study was carried out under a drained condition using a material with relatively small particles, the effect of membrane penetration was neglected.

3.4 Results and discussion

3.4.1 Monotonic loading test results-Series A, B and C

(a) Combined effect of loading direction and stress path-Series A with $b = sin^2\alpha$

The stress-strain curves from tests in Series A are shown in Figure 3.17. The mean effective stress was kept $p = 100kPa$ and $b = \sin^2\alpha$ was maintained in all these tests. The octahedral shear strain is defined as $\gamma_{oct} = \frac{2}{3}\sqrt{6J_2^{\varepsilon}}$. In general, the deviator stress at failure gradually decreased when the value of α varied from $\alpha = 0°$ (Test A1) to $\alpha = 90°$ (Test A5). Herein the deviator stress is defined as $q = \sqrt{3J_2}$. The highest deviator stress at failure, q_{peak}, was obtained in Test A1 ($b = 0$, $\alpha = 0°$). The lowest deviator stress at failure was obtained from Test A5 ($b = 1$, $\alpha = 90°$), which is only slightly smaller than that in Test A4 ($b = 0.75$, $\alpha = 60°$). A significant decrease of q_{peak} was observed between Test A2 ($b = 0.25$, $\alpha = 30°$) and Test A3 ($b = 0.5$, $\alpha = 45°$).

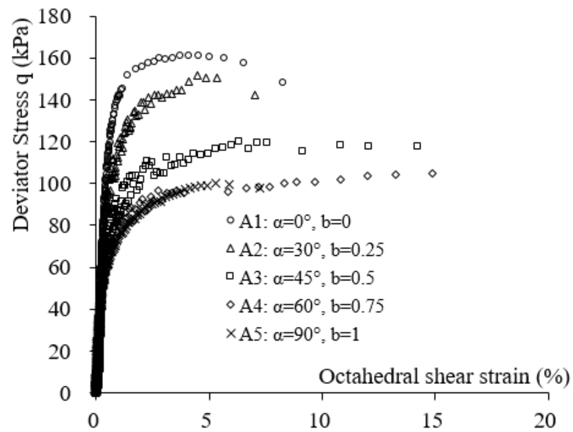

Figure 3.17: Stress-strain curves from Series A with $b = sin^2\alpha$ ($p = 100kPa$)

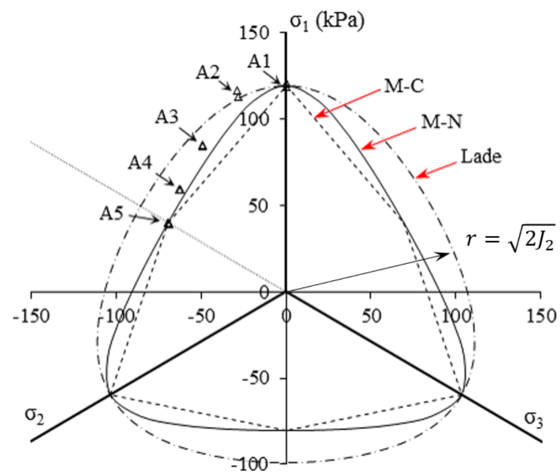

Figure 3.18: Failure states of Series A on π plane with $b = sin^2\alpha$ ($p = 100kPa$)

Figure 3.18 shows the failure envelope on the octahedral plane (π-plane) based on the stress states at failure in Tests A1 to A5. Repeated tests were performed under the same conditions to confirm the reliability of the test results. The benchmarked

Lade, Matsuoka-Nakai (M-N) and Mohr-Coulomb (M-C) failure criteria are also plotted in the figure. The stress states at failure all fell into the range between curves representing the Matsuoka-Nakai and Lade failure criteria.

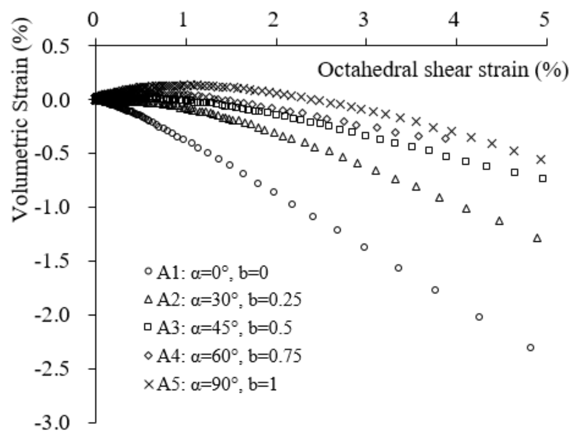

Figure 3.19: Volumetric strain against octahedral shear strain plots from Series A tests

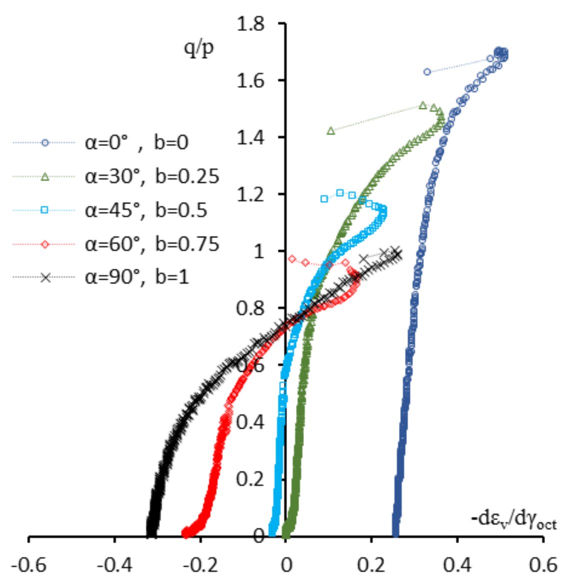

Figure 3.20: Stress-dilatancy plots from Series A tests

Figure 3.19 presents the volumetric strain against the octahedral shear strain plot for each test. In this figure, a positive volumetric strain is referred as volumetric compression. Since the mean effective stress was kept constant during shearing, the volume change of the specimen was considered to be induced by shearing. In general, regardless of the principal stress direction relative to the bedding plane, shearing tended to induce volume contraction at the beginning of shearing prior to dilation. With an increase of b and α, the dilatancy tended to decrease while shear-induced volume contraction became more pronounced. More specifically, at the octahedral shear strain of $\gamma_{oct} = 5\%$, in Tests A1 ($b = 0$ and $\alpha = 0°$) and A5 ($b = 1$ and $\alpha = 90°$), the dilatant volumetric strains were -2.3% and -0.5%, respectively. The corresponding maximum shear-induced volume contraction was 0% and 0.1% in these two tests. In addition, the octahedral shear strain at which the maximum volume contraction occurred tended to be larger at higher b and α values.

Figure 3.20 shows the relations between the mobilized stress ratio q/p and the strain increment ratio $-d\varepsilon_v/d\gamma_{oct}$ for Tests A1 to A5. It is observed that the initial dilatancy decreased significantly as the values of b and α increased. For each test, the dilatancy increased during the loading process, and the rate of dilatancy increased for Tests A1 to A5. The minimum peak dilatancy was observed in Test A4. In all five tests, the dilatancy started to decrease after it reached the peak value and approached zero as the loading approaching critical states.

In this series of tests, since b varies with α following $b = \sin^2\alpha$, no solid conclusions can be made about the effect of each factor on the behaviour of sand. However, as mentioned previously, the non-uniformity across the wall of the hollow cylindrical specimen was minimized by keeping $b = \sin^2\alpha$. Results from this series of tests were reliable and can provide a benchmark when comparing with results obtained from

Series B ($b = 0$ with varying α) and C ($b = 1$ with varying α).

(b) Effect of major principal stress direction

Tests of Series B and C were carried out to explore the influence of the major principal stress direction on soil behaviour at select intermediate principal stress factor b. Figures 3.21 and 3.22 present the stress-strain curves from tests in Series B ($b = 0$) and C ($b = 1$) , respectively. For both series of tests, the deviator stress at failure, q_{peak}, decreased as the value of α increased. For tests with $b = 0$, the value of q_{peak} dropped from $148kPa$ at $\alpha = 0°$ to $127kPa$ at $\alpha = 90°$; for tests with $b = 1$, q_{peak} decreased from $137kPa$ at $\alpha = 0°$ to $98kPa$ at $\alpha = 90°$.

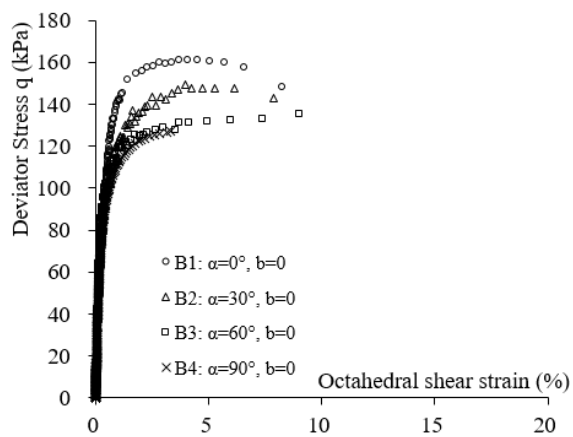

Figure 3.21: Stress-strain curves from Series B tests with $b = 0$ ($p = 100kPa$)

Figure 3.23 summarizes the stress states at failure on the π-plane, based on results obtained from tests in Series B and C. For comparison purposes, the results obtained from tests in Series A are also plotted, together with the failure envelopes corresponding to the Lade, Matsuoka-Nakai (M-N) and Mohr-Coulomb (M-C) criteria. The circular markers represent the results from tests B1 to B4, the square makers represent the results of tests C1 to C4 and the triangle makers represent results from

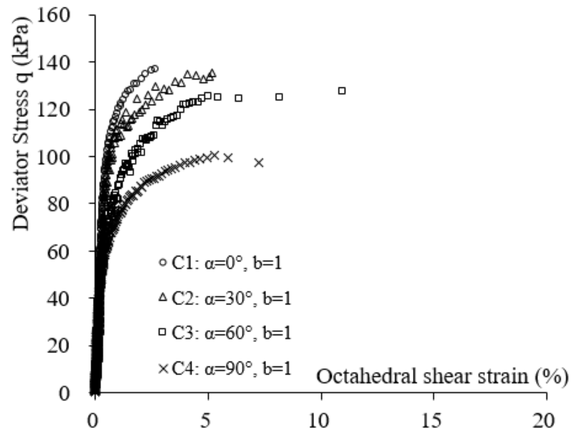

Figure 3.22: Stress-strain curves from Series C tests with $b = 1$ ($p = 100kPa$)

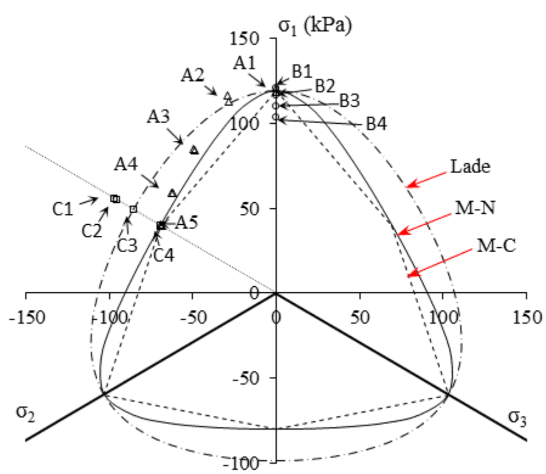

Figure 3.23: Failure states on π-plane from Series A , B and C ($p = 100kPa$)

tests of Series A. It should be noted that Tests A1 and A5 duplicate Tests B1 and C4.

The test results of C1 to C4 presented in Figures 3.22 and 3.23 show that the strength decreased with an increase of α. However the deviator stresses at failure obtained from tests C1, C2 and C3 were notably larger than predictions of the benchmarked failure envelopes. The main reason is that for tests C1, C2, and C3, $b \neq sin^2\alpha$ ($p_o \neq p_i$), the non-uniformity across the wall of the hollow cylinder specimen tended to cause a large experimental error. According to Table 3.1, in Series C with $b = 1$ ($\sigma_2 = \sigma_1$), the radial stress σ_r became one of the two major principal stresses. The radial stress σ_r, which was calculated as $\sigma_r = \frac{p_o r_o^2 - p_i r_i^2}{r_o^2 - r_i^2} - \frac{(p_o - p_i) r_o^2 r_i^2}{(r_o^2 - r_i^2) r^2}$, became non-uniform under $p_o \neq p_i$. With σ_r being a major principal stress, the influence of non-uniformity became important. As a result, the deviator stresses at failure for tests C1-C3 were larger than their actual values.

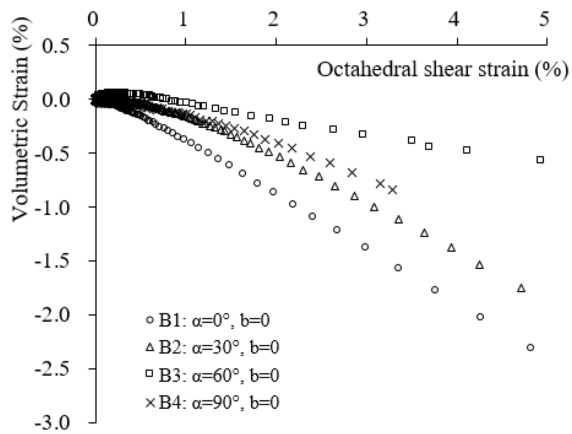

Figure 3.24: Volumetric strain against octahedral shear strain plots from Series B tests

Figures 3.24 and 3.25 present plots of the volumetric strain against the octahedral shear strain γ_{oct} and the stress-dilatancy plots for tests of Series B, respectively. As shown in Figure 3.24, at the same shear strain, the magnitude of shear-induced dilation was significantly affected by angle α. The maximum dilation took place at $\alpha = 0°$ (both b=0 and b=1) when the major principal stress was applied perpendicular to the bedding plane. The minimum dilation occurred at $\alpha = 60°$, which is different from the results in Figure 3.19 for tests in Series A.

Physically, the minimum dilation in the test with $\alpha = 60°$ can be interpreted as follows (see Figure 3.26). According to the Mohr-Coulomb criterion, the normal

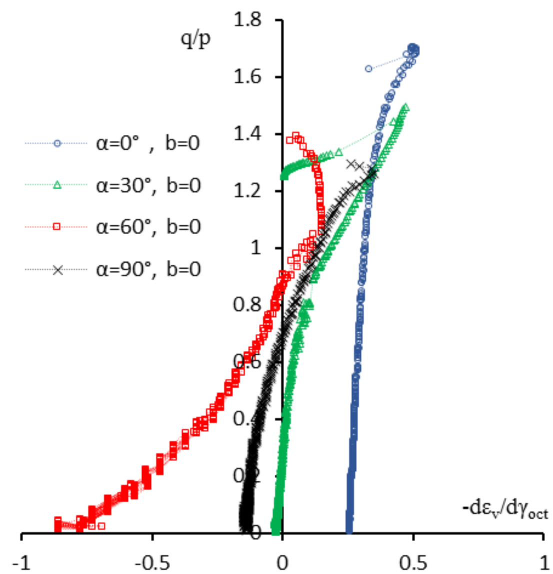

Figure 3.25: Stress-dilatancy plots from Series B tests

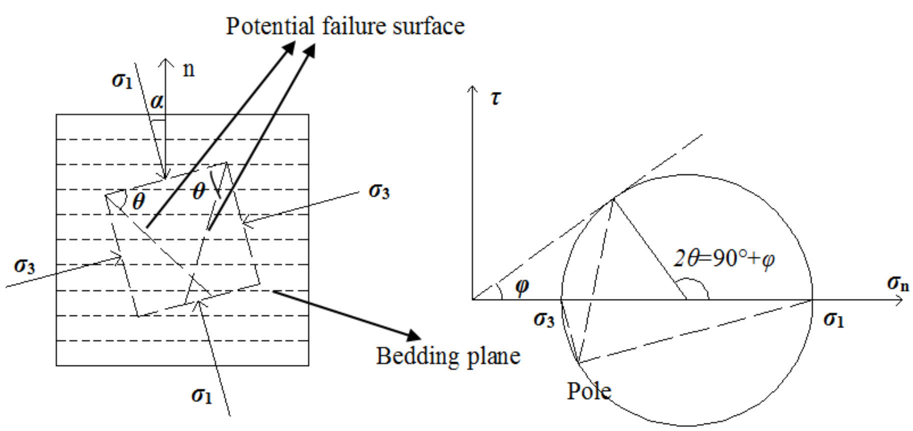

Figure 3.26: Geometry description of the direction of shear plane, principal stress and the bedding plane

of the failure plane makes an angle of approximately $\theta = \pi/4 + \varphi/2$ to the major principal stress direction. When $\alpha = 60°$, the failure plane was nearly parallel to the bedding plane for the friction angle $\varphi \approx 30°$, which implied relatively small overriding of particles along the failure plane and hence small dilation. It should be noted that in Series A tests the minimum dilation took place in the test of $\alpha = 90°$ rather than

$\alpha = 60°$. This difference was related to the different stress paths in Series A.

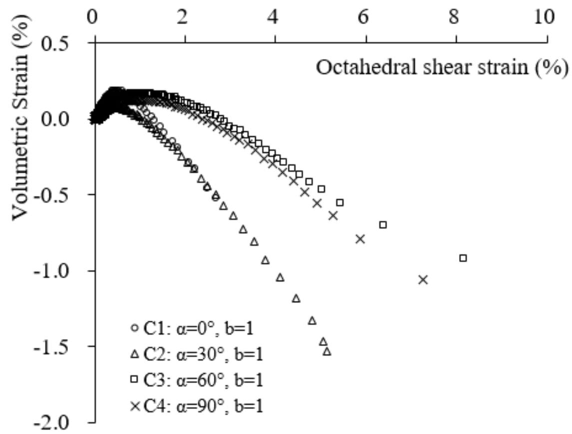

Figure 3.27: Volumetric strain against octahedral shear strain plots from Series C tests

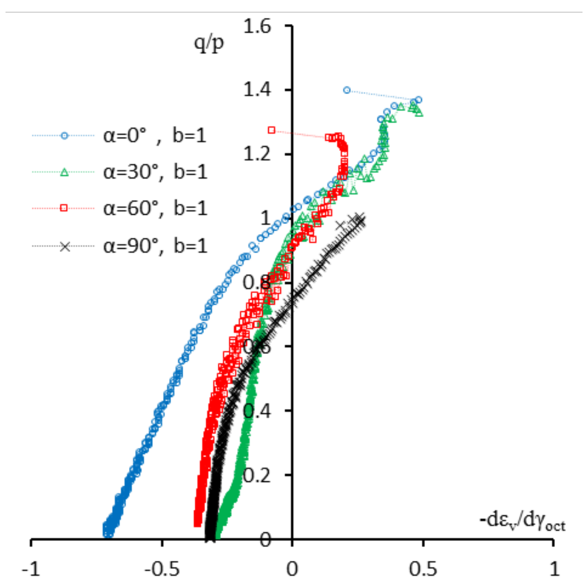

Figure 3.28: Stress-dilatancy plots from Series C tests

Figures 3.27 and 3.28 show the volumetric strain against octahedral shear strain and the stress-dilatancy plots in Series C tests. From Figure 3.27, the volumetric strain curves from tests C1 with $\alpha = 0°$ and C2 with $\alpha = 30°$ are quite similar, and so are the volumetric strain curves from tests C3 with $\alpha = 60°$ and C4 with $\alpha = 90°$. However, similar to Series B, the rate of dilatancy generally decreased with an increase of α, with the minimum value being reached at $\alpha = 60°$. From Figure 3.28, the initial rate of dilatancy did not show a clear pattern, but the rate of dilatancy at failure was larger in tests C1 and C2 than in tests C3 and C4, which is consistent with the observation from Series B tests.

(c) Effect of intermediate principal stress parameter b

The effect of b on the behaviour of Ottawa sand can be identified from tests in series A, B and C having the same α but different values of b. Figure 3.29 compares the experimental stress-strain curves at $\alpha = 0°$, $\alpha = 30°$, $\alpha = 60°$ and $\alpha = 90°$ with different b values.

According to Figure 3.29, the deviatoric stress at failure generally decreased with an increase of b, which was clear in Figures 3.29a, 3.29b and Figure 3.29d. The only exception is Figure 3.29c at $\alpha = 60°$, in which the lowest deviator stress at failure was found at $b = 0.75$ while the shear strength in test with $b = 1$ was slightly smaller than that in test with $b = 0$. As discussed earlier, because of the non-uniformity of stress when $b \neq sin^2\alpha$, the failure stresses obtained from tests C1, C2 and C3 were believed to be larger than their real values.

Figure 3.30 presents the variation of volumetric strain against octahedral shear strain in tests with $\alpha = 0°$, $30°$, $60°$ and $90°$ at different b. The four groups of tests show that for a given direction of the major principal stress, with an increase of b, the potential of shear-induced volume dilation decreased significantly. In other words, increased intermediate principal stress tended to suppress dilation of a granular

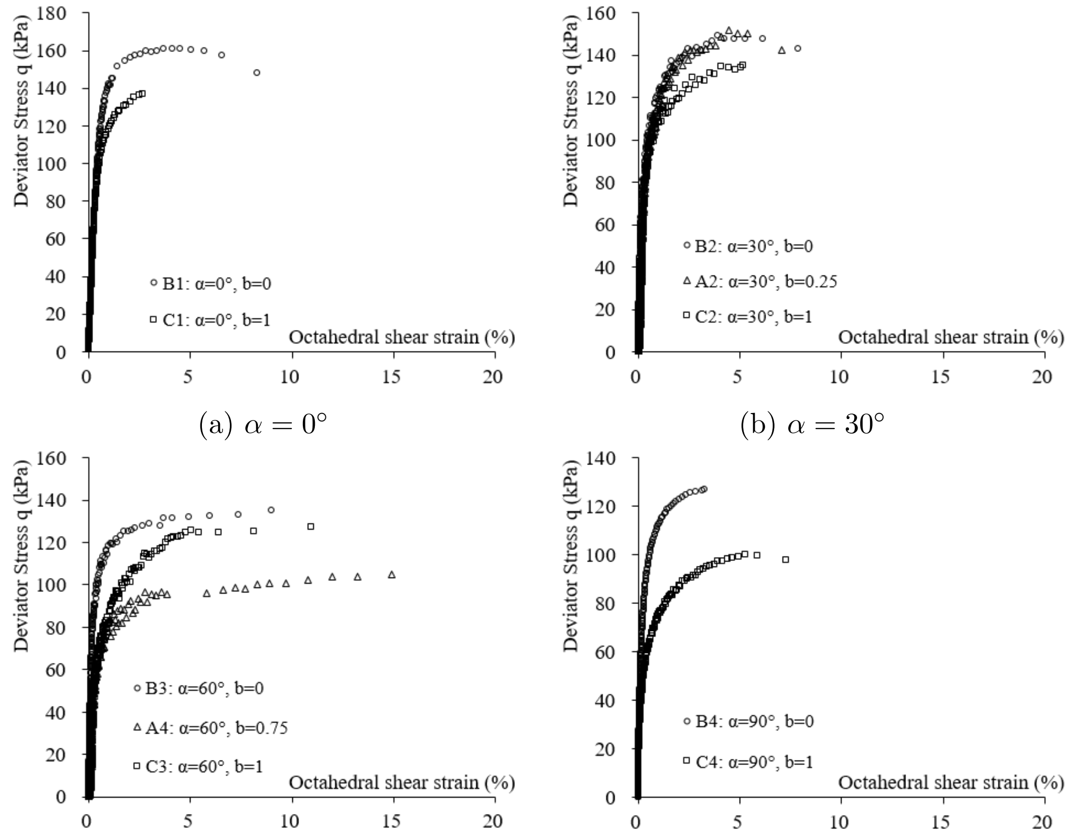

(a) $\alpha = 0°$ (b) $\alpha = 30°$

(c) $\alpha = 60°$ (d) $\alpha = 90°$

Figure 3.29: Stress-strain curves from Series A, B and C-cross comparison

material, even under the same mean effective stress. The dilatancy plots presented in Figure 3.31 reveal that an increase of b value tended to induce low rate of dilatancy $-d\varepsilon_v/d\gamma_{oct}$ at the same q/p ratio. At the failure states corresponding to the peak q/p ratios, the dilatancy in tests with the same α angle approached a similar value. In other words, the peak dilatancy was not largely influenced by the intermediate principal stress coefficient.

Figure 3.32 shows the dependency of peak dilatancy angle $\psi_{\max}$ on the major principal stress direction α and the intermediate principal stress ratio b in Series A, B and C. Herein the angle of dilation is defined as $\sin\psi = -d\varepsilon_v/d\gamma_{oct}$. According to

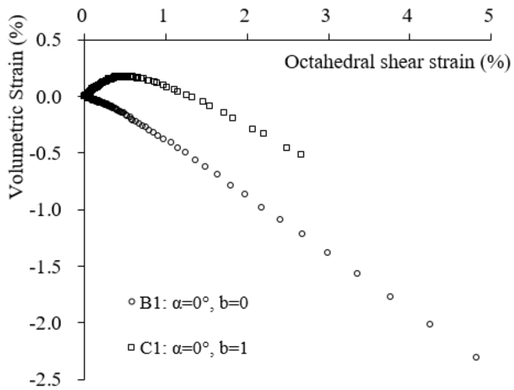

(a) $\alpha = 0°$

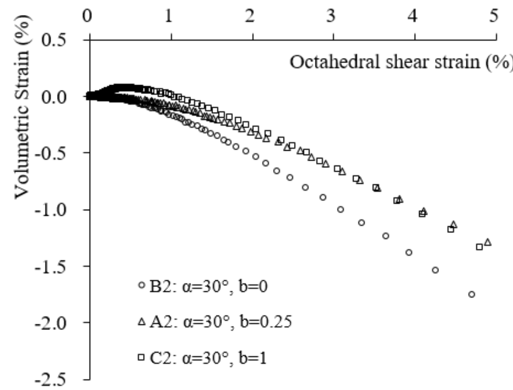

(b) $\alpha = 30°$

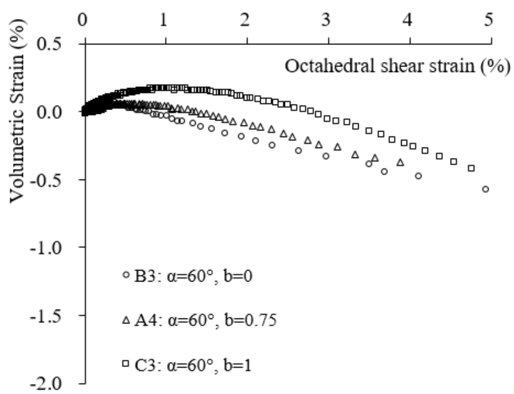

(c) $\alpha = 60°$

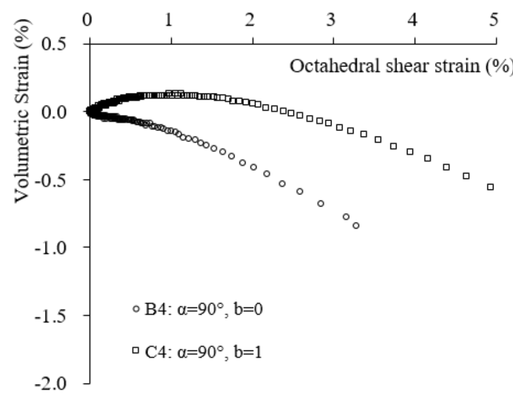

(d) $\alpha = 90°$

Figure 3.30: Volumetric strain against octahedral shear strain plots from Series A, B and C-cross comparison

Figure 3.32a, the maximum value of $\psi_{\max}$ was at $\alpha = 0°$. With the increase of α, $\psi_{\max}$ decreased and reached its minimum at approximately $\alpha = 60°$. A further increase of α resulted in a regain of $\psi_{\max}$. Comparing with the effect of loading direction, the influence of the intermediate principal stress coefficient on the peak dilatancy angle was less significant (see Figure 3.32b).

The different dilatancy properties of Ottawa sand observed in tests along different loading directions and stress paths imply that, if the loading direction and/or the stress path changes in a test involving cyclic loading, the accumulated deformation

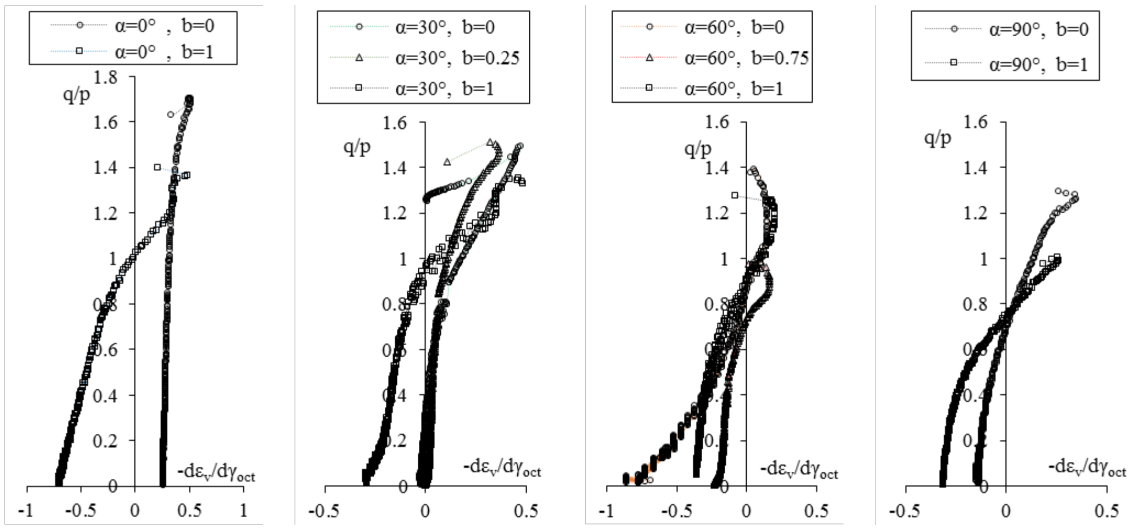

(a) $\alpha = 0°$ (b) $\alpha = 30°$ (c) $\alpha = 60°$ (d) $\alpha = 90°$

Figure 3.31: Stress-dilatancy plots from test series A, B and C- cross comparison

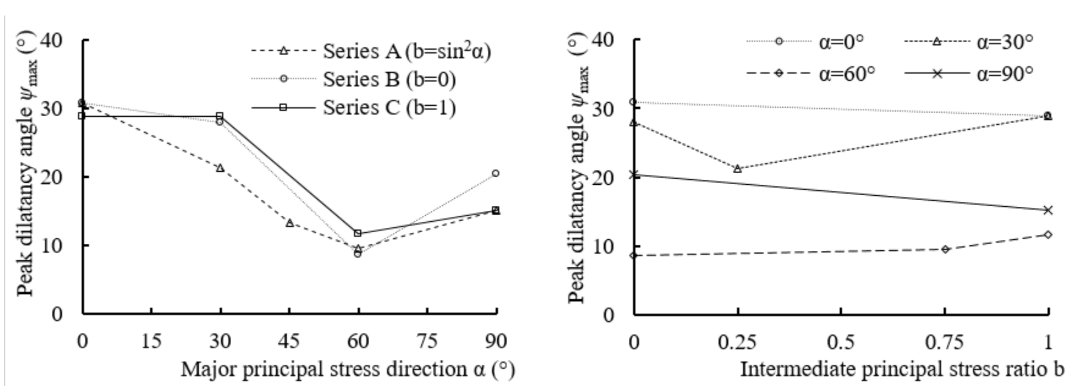

(a) Peak dilatancy angle against major principal stress direction α

(b) Peak dilatancy angle against intermediate principal stress coefficient b

Figure 3.32: Variation of peak dilatancy angle

may change accordingly. This was investigated in detail through a series of cyclic loading tests, which are discussed in the following section.

3.4.2 Cyclic loading tests along different stress paths-Series D

As observed from the results of the monotonic loading tests on the Ottawa sand, both the loading direction and the stress path had significant influences on both the strength and deformation characteristics of the material. This is attributed to inherent and induced anisotropy as well as the different fabric evolutions under different conditions. In the cyclic loading tests reported in this section, cyclic loads were applied to specimens with altered loading sequences along stress paths having different values of b, with the major principal stress in different directions. For comparison purposes, two tests with constant value of b, Test D2 ($b = 0$) and Test D5 ($b = 1$), were carried out as references. For the other tests, D1 and D3, started with $b = 0$, and altered between $b = 0$ and $b = 1$. Tests D4 and D6 started with $b = 1$, and altered between $b = 1$ and $b = 0$. Referring to Table 3.5, cyclic loading was applied with the amplitude being controlled as $q^{cyc} = 40kPa$ corresponding to a frequency of 0.2Hz. The amplitude of the cyclic stress ratio was $q^{cyc}/p = 0.4$. In the following discussions, the focus is placed on the development of accumulative deformation during cyclic loading.

Figure 3.33 presents the volumetric strains against the number of stress cycles obtained from Tests D1 to D6. From the figure, the following observations are made:

(a) After 200 cycles, the accumulative volumetric strains in tests D2 ($b = 0$) and D5 ($b = 1$) were 0.2% and 1.2%, respectively. The latter was five times larger, which

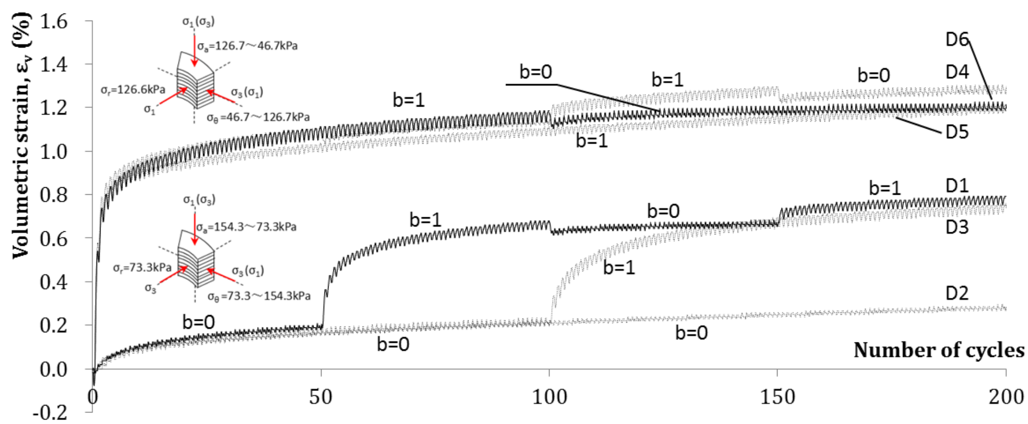

Figure 3.33: Volumetric strain against number of loading cycles plot ($p = 100kPa$)

means even under the same cyclic stress amplitude, the specimen subjected to cyclic loading with $b = 1$ had much larger contraction than that with $b = 0$. The reasons follow.

According to the results of the monotonic loading tests presented in Figure 3.31, at the beginning of the loading, the specimen at $b = 1$ had a higher rate of volumetric compaction than that at $b = 0$. For cyclic loading where the amplitude of the stress ratio was 0.4, it corresponded to the starting part of the dilatancy curve in Figure 3.31. Therefore, a larger contraction was expected in Test D5 with $b = 1$. Consequently, cyclic loading in Test D5 with $b = 1$ resulted in larger accumulative volume compaction.

As is shown in Figure 3.7c, the cyclic loading Mode 2 ($b = 1$) can be decomposed into Mode 1 ($b = 0$) and an additional one-way cyclic load applied in the radial direction within the bedding plane. With σ_r being a major principal stress, this part of cyclic loading corresponded to $\alpha = 90°$. For the equivalent Mode loading 1 with $b = 0$, the major principal stress direction rotated between $\alpha = 0°$ and $90°$. As such, the difference between Tests D2 and D5 could also be attributed to a larger contraction at $\alpha = 90°$ than that at $\alpha = 0°$, as shown in Figures 3.24, 3.25, 3.27 and 3.28.

(b) For the first 50 cycles, Test D1 to D3 had the same loading condition ($b = 0$), as did Tests D4 to D6 ($b = 1$). The results showed good agreement with one another. By the end of the first 50 cycles, the accumulative volumetric strain was around 0.18% for tests with $b = 0$ (D1 to D3) comparing with approximately 1.1% in tests with $b = 1$ (D4 to D6).

(c) In Tests D1 and D3, for the first time when the value of b was changed from 0 to 1, a sudden increase in the volumetric strain was observed. For example, in Test D3, the accumulated volumetric strain at $b = 0$ was 0.18% after 50 cycles and was 0.2% after 100 cycles. If the value of b was changed to 1 after the first 50 cycles of loading with $b = 0$, as in Test D1, the volumetric strain reached 0.68% after another 50 cycles with $b = 1$. However, the strains were still apparently lower than those obtained by firstly apply cyclic loading with $b = 1$ on an original sample (Tests D4 to D6) at the same number of stress cycles. The reason is that the preceding sequences of loading densified the sample, which reduced the potential of particle rearrangement and the influence of fabric.

(d) A small decrease in the volumetric strain occurs when the value of b changed from 1 to 0 (i.e. Test D1 after 100 cycles), indicating that dilation may have happened when b decreased from 1 to 0. This was consistent with the results presented in Figure 3.31, which showed more pronounced dilation at $b = 0$.

(e) When comparing tests starting with $b = 0$ (Tests D1 to D3), the more often the value of b changed, the larger the final accumulative volumetric strain became. The accumulative volumetric strain after 200 cycle was 0.3% when the b value was kept at $b = 0$ (Test D2, N=200), 0.75% if b value changed once (Test D3, N=100×2, 100 at b=0, and 100 at $b = 1$), and was 0.80% if b value changed three times (Test D1, N=50×4). For tests starting with $b = 1$ (Tests D4 to D6), the accumulative volumetric strain after 200 cycle was 1.20% if b value was kept at $b = 1$ (Test D5), 1.22% if b value changed once (Test D6), and was 1.30% if b value changed three times (Test D4). In order to verify this observation, tests D4 and D6 were performed at N=50×8 and N=100×4, respectively by alternatively changing the b value, as shown in Figure 3.34.

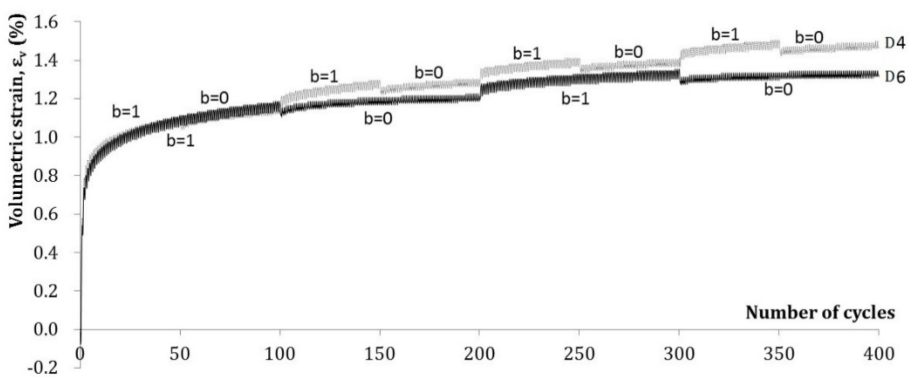

Figure 3.34: Volumetric strain of groups D4 and D6 with N=400 ($p = 100kPa$)

The deviation between tests D4 and D6 after the total number of 400 cycles became more apparent than that after 200 cycles. The volumetric strain was 1.48% for Test D4 (50×8) with the b value changing seven times, and was 1.32% for Test D6 (100×4) with the b value changing three times. The former was 12% larger than the latter.

Figure 3.35 shows the volumetric strain against shear strain curves for all cyclic tests. Figure 3.36 presents the evolution of cyclic stress-strain curves from Tests D1 and D4. The stress-strain curves from tests starting with $b = 0$ (Tests D1 to D3) were similar. Therefore only the curves from Test D1 are presented here, as shown

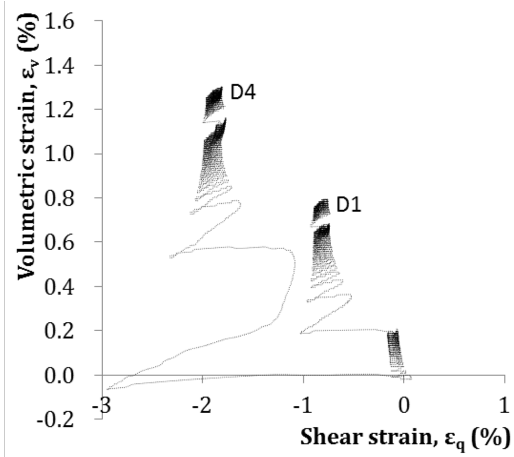

(a) D1, D4

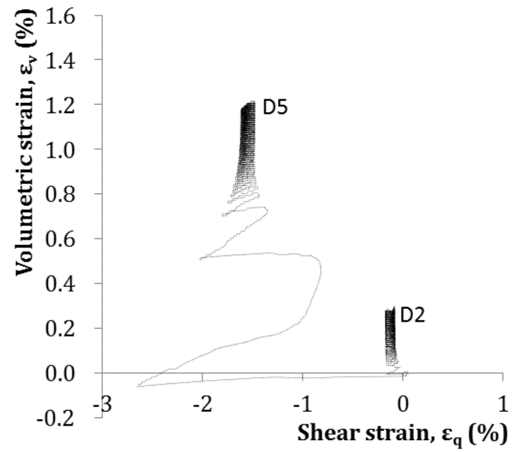

(b) D2, D5

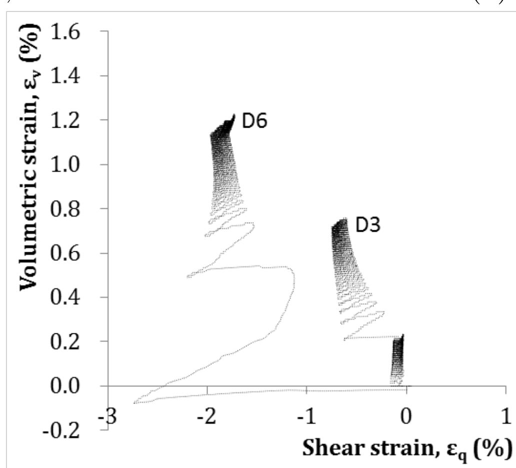

(c) D3, D6

Figure 3.35: The volumetric strain against the shear strain for the cyclic tests-Series D

in Figure 3.36a. Similarly, the stress-strain curves from Test D4 are presented as representative results of tests starting with $b = 1$ (Tests D4 to D6), as shown in Figure 3.36b.

Both test series contained four stages, each of which had 50 cycles (50×4). In Test D1, the absolute value of the shear strain grew slowly in the first 50 cycles with $b = 0$ and increased rapidly during the next 50 cycles with $b = 1$. For the following 50 cycles

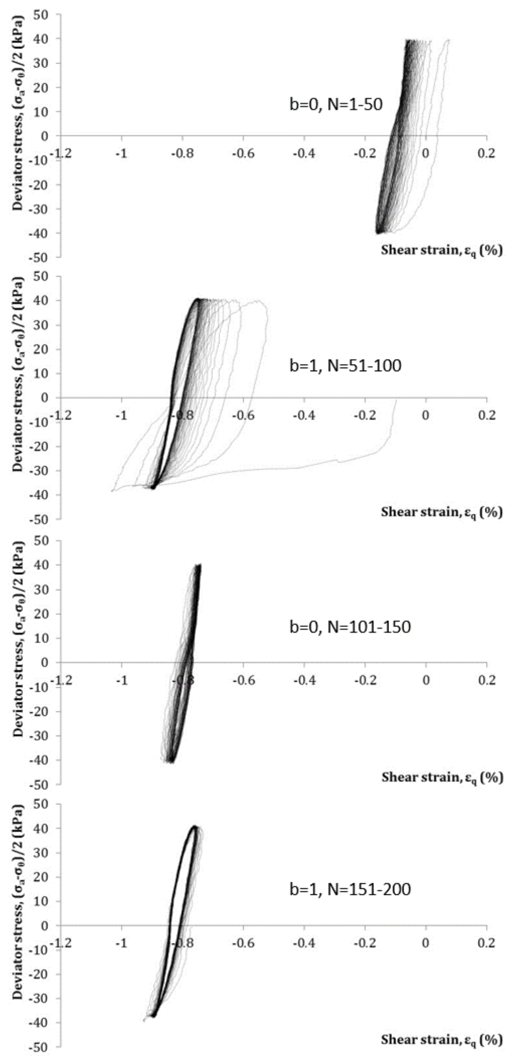

(a) Test D1, $0 \to 1 \to 0 \to 1$

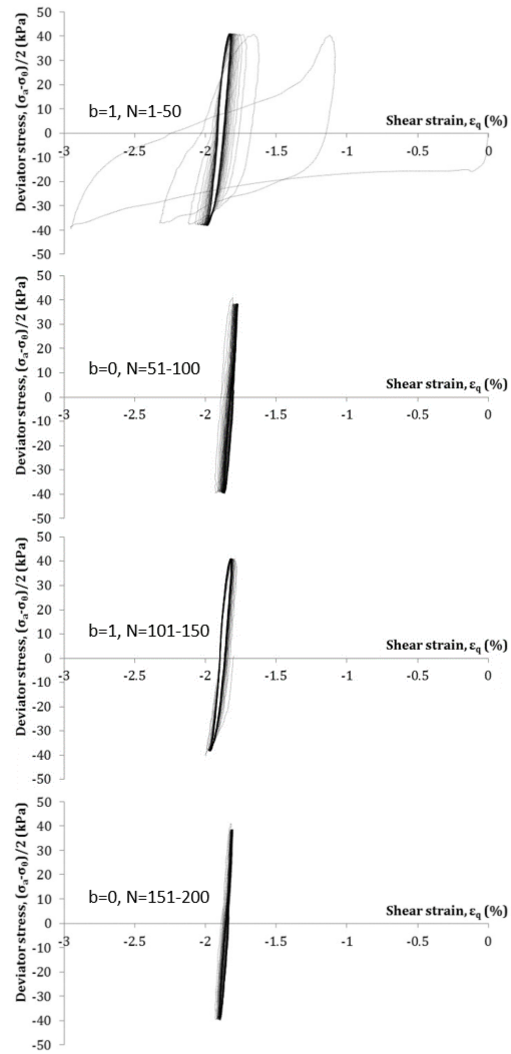

(b) Test D4, $1 \to 0 \to 1 \to 0$

Figure 3.36: Cyclic stress-strain relation from tests D1 and D4

with $b = 0$, the shear strain decreased slightly, and in the final 50 cycles with $b = 1$, another slight increase occurred (see Figures 3.35a and 3.36a). In Test D4, as shown in Figure 3.36b, the absolute value of the shear strain increased rapidly to 1.8% in the first 50 cycles with $b = 1$ and slightly decreased during the next 50 cycles with $b = 0$. In the following 100 cycles, the evolution of the volumetric strain was the same as in Test D1. For cyclic loading with $b = 1$, the shear strain amplitude increased with the number of stress cycles, while in tests with $b = 0$, the strain amplitude decreased. However, after the first 100 cycles, the shear strain was relatively stable, and the influences of the b variation were not significant. The stress-strain curves approached stable by the end of each loading stage.

Based on the last five cycles of each stage, the resilient shear modulus was calculated and is listed in Table 3.6, as well as shown in Figure 3.37. Note that, when calculating shear modulus, the data from tests D2-D6 were extended to a total number of 400 cycles with the test matrix shown in Table 3.6. One finds that (1) Resilient shear modulus is 50% $\sim$ 60% larger for $b = 0$ than $b = 1$ ($G_r^{b=0} > G_r^{b=1}$), meaning that, during cyclic loading at the stabilized stage, a higher b value was associated with lower stiffness. The reason is that under $b = 1$, one of the major principal stress was applied parallel to the bedding plane with minimum resistance between particles. (2) Both $G_r^{b=0}$ and $G_r^{b=1}$ increased with the increases of cycle numbers. This can be explained by the densification effects of the cyclic loads. The tendency to increase shall slow down and eventually stop if the loading cycles increased to larger values since the material's density has limits.

Table 3.6: Resilient shear modulus from cyclic loading tests

Test No.	Loading sequence		$G_r = q/\varepsilon_q$ (MPa)			
	value of b	number of cycles	$G_r^{b=0}$	$G_r^{b=1}$	$G_r^{b=0}$	$G_r^{b=1}$
D1	$0 \to 1 \to 0 \to 1$	50×4	75.0	54.6	85.7	60.0
D2	0	200×2	85.7	66.7		
D3	$0 \to 1$	100×4	80.0	52.2	92.3	57.1
			$G_r^{b=1}$	$G_r^{b=0}$	$G_r^{b=1}$	$G_r^{b=0}$
D4	$1 \to 0 \to 1 \to 0$	50×8	50.0	80.0	57.1	85.7
			57.1	92.3	57.1	100.0
D5	1	200×2	57.1	85.7		
D6	$1 \to 0$	100×4	48.0	75.0	52.2	85.7

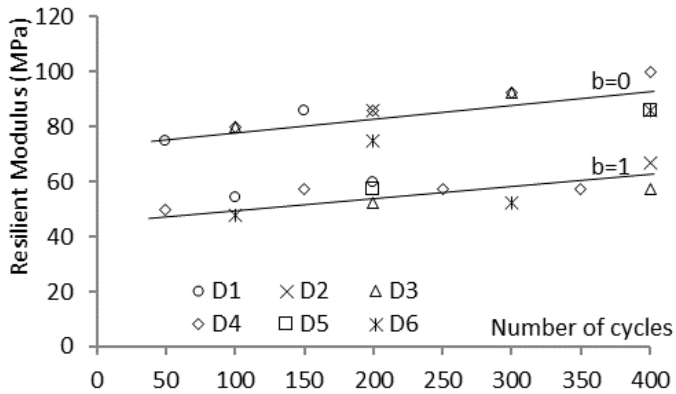

Figure 3.37: Resilient shear modulus from cyclic loading tests

3.5 Concluding remarks

The present study shows the importance of principal stress direction and intermediate principal stress on both monotonic and cyclic behaviour of sand.

The monotonic strength of sand decreased with the principal stress direction α increasing and reached a minimum when the major principal stress was parallel to the bedding plane at $\alpha = 90°$ under both $b = 0$ and $b = 1$. However, when $b = 0$, the variation of strength in tests with α larger than 60° was very small. For $b = 1$, the decrease of strength remained notable even for $\alpha \geq 60°$. With the increase of intermediate principal stress coefficient b, the strength of sand decreased steadily. The only exception was that for tests with $b = 0.75$ and $\alpha = 60°$. The non-uniformity had a certain influence on the latter group, which results in an over-predicted strength. The initial dilatancy decreased with an increase of both the principal stress direction α and the intermediate principal stress coefficient b. Compared with b, the influence of α was more significant on the peak dilatancy of sand.

From cyclic loading tests, larger accumulative volumetric deformation was found from tests with two-directional loading ($b = 1$) than tests with one directional loading ($b = 0$). When the loading mode was changed from $b = 0$ to $b = 1$ for the first time, which meant a second cyclic loading was applied in an orthogonal direction without changing the total deviator stress, a significant increase in the accumulative volumetric strain was observed. Furthermore, the resilient shear modulus was $50\% \sim 60\%$ larger under one directional loading ($b = 0$) than under two-directional loadings ($b = 1$).

Chapter 4

A constitutive model for granular materials with fabric consideration

Owing to its discrete nature, the behaviour of granular materials is significantly affected by the geometrical arrangement of particles and the interaction forces between particles. Shear-induced volume change, or dilatancy, can be viewed as the result of internal constraints to particle movements imposed by discrete particles (Goddard and Didwania, 1998). The anisotropic behaviour and the influence of loading direction on soil behaviour as observed from the experimental study in Chapter 3 all originate from fabric and its evolution induced by applied stresses.

Various stress-strain models based on different assumptions have been developed for granular materials. However, models with proper consideration for fabric and clear physical meanings are rare. In this chapter, an effort is made to describe the anisotropic behaviour of granular material based on a number of simple physical concepts. The model was built within the framework of elasto-plasticity, with the assumption of the existence of a critical fabric surface characterizing the fabric state of sand at its critical state.

In this Chapter, the mean effective stress is represented by p instead of p' for convenience.

4.1 Fabric and its evolution: an introduction

To describe the fabric or internal structure of a granular assembly, various definitions of fabric tensors have been proposed (Oda, 1982; Oda *et al.*, 1985; Satake, 1982; Ken-Ichi, 1984; Bagi, 1996; Zhao and Guo, 2013). For granular materials, tensorial measures of fabric based on the contact normal distribution are considered to be appropriate. The fabric tensor defined by Satake (1982) and Oda (1982) is adopted in this study.

Consider two particles in contact, let $\mathbf{n}$ be the unit vector normal to the contact surface. The fabic tensor of a granular assembly can be defined as

$$\Phi_{ij} = \frac{1}{N_C} \sum_{k=1}^{N_C} n_i^{(k)} n_j^{(k)}, (i, j = 1, 2, 3) \tag{4.1}$$

in which N_C is the total number of contacts within a unit sphere that is considered to be representative element volume, and $n_i^{(k)}$ defines the direction cosines of the k-th contact normal with respect to the i-th coordinate axis. Φ_{ij} satisfies $\Phi_{ii} = 1$. The directional distribtuion of the contact normals can be described by a probability density function (PDF) $E(\mathbf{n})$, which mathematically satisfies

$$\int_\Omega E(\mathbf{n}) d\Omega = 1 \tag{4.2}$$

in which Ω is the solid angle corresponding to the whole surface of a unit sphere. $E(\mathbf{n})d\Omega$ gives the estimate of $\Delta N_C(\Omega)/N_c$ with $\Delta N_C(\Omega)$ being the number of contact normals whose directions are within a small solid angle $d\Omega$. The fabric tensor can then be expressed as a continuous function

$$\Phi_{ij} = \int_{\Omega} E(\mathbf{n}) n_i n_j d\Omega \tag{4.3}$$

In general, $E(\mathbf{n})$ can be expressed as

$$E(\mathbf{n}) = \frac{1}{4\pi}(1 + F_{ij} n_i n_j + G_{ijkl} n_i n_j n_k n_l + ...)$$

which can be simplified to a second-order approximation(Ouadfel and Rothenburg, 2001) in the form of

$$E(\mathbf{n}) = \frac{1}{4\pi}(1 + F_{ij} n_i n_j) \tag{4.4}$$

By taking into account Equation (4.3), one has

$$F_{ij} = \frac{15}{2}(\Phi_{ij} - \frac{1}{3}\delta_{ij}) \tag{4.5}$$

The two tensors Φ_{ij} and F_{ij} can be interchangeably used to represent the internal structure or fabric of a granular assembly. In this study, Φ_{ij} is referred to as the fabric tensor with $\Phi_{ii} = 1$. F_{ij} is a deviatoric measure of Φ_{ij} with $F_{ii} = 0$. It should be noted that F_{ij} is different from the conventional deviatoric tensor of Φ_{ij}, which is $\Phi_{ij} - \frac{\Phi_{kk}}{3}\delta_{ij}$. However, for convenience, F_{ij} is referred to as the deviatoric fabric tensor in the rest of this thesis.

4.2 Fabric evolution law based on a limit fabric surface

4.2.1 Limit surface of fabric state

Within the framework of the critical state soil mechanics, when a granular material reaches its critical state, the stress state can be characterized by a unique surface in the stress space, while the void ratio and the internal structure all reach a steady state as the shear strain continues increasing. Here we assume that the fabric of a granular material at the critical state can be quantified by a unique function or a limit surface in the principal fabric space. Evidence for the existence of such a limit fabric surface is provided as follows.

Based on the test results of 2D granular materials, Satake (1982, 2007) suggested that the fabric tensor defined by contact normals can be used to characterize the induced anisotropy, satisfying

$$\Phi_1 : \Phi_2 : \Phi_3 = \sigma_1^\alpha : \sigma_2^\alpha : \sigma_3^\alpha \tag{4.6}$$

with $\alpha \simeq 0.5$. This relation was further elucidated by Chowdhury and Nakai (1998) using the concept of spatially mobilized plane (SMP) and the t_{ij}-concept. When taking Nakai's criterion as the function of stress states at the critical state, Equation (4.6) yields in the deviatoric plane a critical state fabric surface, which has a shape similar to that of Nakai's or Lade's curve for the critical stress states as shown in Figure 2.16. It should be noted, for an initially isotropic specimen, the induced anisotropy during the course of deformation is the same as the overall anisotropy.

However, Yimsiri and Soga (2010) observed larger ultimate fabric anisotropy under triaxial extension than that under triaxial compression. Moreover, the results of DEM simulations for shearing along stress paths of constant Lode angles or equivalently constant intermediate principal stress ratio $b = (\sigma_2 - \sigma_3)/(\sigma_1 - \sigma_3)$ show that a critical state fabric surface in the deviatoric plane can be described by an inverted Lade's curve in the form of (Thornton, 2000; Thornton and Zhang, 2010)

$$\eta^* = \frac{(I_1^\Phi)^3}{2I_1^\Phi I_2^\Phi - 3I_3^\Phi} \tag{4.7}$$

in which I_1^Φ, I_2^Φ and I_3^Φ are the invariants of fabric tensor Φ_{ij}, and η^* is a material constant. For a dense polydisperse system of elastic spheres with sizes ranging from 0.25 mm to 0.33 mm and interparticle friction coefficient μ =0.5, Thornton and Zhang (2010) found $\eta^* = 1.810 \pm 0.001$ at a mean effective stress $p = 100$ kPa. It should be noted that $\eta^* = 1.8$ corresponds to an isotropic state. Using spherical particles, Barreto and O'Sullivan (2012) showed that η^* at the peak stress state tended to increase with interparticle friction, $\eta^* = (5.488/3)\mu^{0.0034}$.

In a series of DEM simulations with interparticle friction coefficient $\mu = 0.5$ under different mean effective stresses (from $p = 80$ kPa to 2000 kPa), Zhao and Guo (2013) showed $\eta_F^* = 1.805 \pm 0.0025$. However, they argued that "although the use of an invariant function in the form of Equation (4.7) considerably reduces the range of variation for all data, it still cannot unify all cases uniquely". Alternatively, they defined a fabric anisotropy parameter K_c that is the first joint invariant of the deviatoric stress tensor and the deviator fabric tensor expressed as $K_c = s_{ij}^{(cv)} F_{ji}^{(cv)}$. They further proposed a relation between K_c and the mean effective stress p at critical state as

$$K_c = s_{ij}^{(cv)} F_{ij}^{(cv)} = \alpha\,(p)^{\zeta} \tag{4.8}$$

in which $\alpha = 0.41 \pm 0.01$ and $\zeta = 0.894$, which were determined for an assembly of polydisperse spherical particles.

While both relations in Equations (4.7) and (4.8) can describe the fabric tensor at the critical state by functions of fabric invariants, the latter relates the fabric and stress surfaces more directly. Moreover, both studies suggest that the critical fabric surface is represented by an inverted Lade's failure surface. In the following section, different fabric surfaces are represented using the equation by Zhao and Guo (2013). The convexity of fabric surfaces is discussed.

4.2.2 Fabric surfaces based on different failure criteria

In this study, the relationship between the deviatoric fabric tensor F_{ij} and the deviatoric stress tensor s_{ij} is assumed at the critical state to be

$$s_{ij}^{(cv)} F_{ji}^{(cv)} = K_c \tag{4.9}$$

where K_c is a given by Equation (4.8).

As discussed in the literature review, using the Haigh-Westergaard invariants, the expressions for Matsuoka-Nakai and Lade-Duncan criteria can be written as

$$r_{cv} = \frac{\xi}{\lambda}[sin(\frac{\pi - sin^{-1}(\omega sin3\theta)}{3})]^{-1} \tag{4.10}$$

where $\xi = \frac{I_1}{\sqrt{3}}$ and $r = \sqrt{2J_2}$. λ and ω are determined using the equations in Table

4.1.

Table 4.1: Equations for λ and ω

Yield criterion	λ	ω
Matsuoka-Nakai	$\lambda_{MN} = \sqrt{2}\sqrt{\frac{K_{MN}-3}{K_{MN}-9}}$	$\omega_{MN} = \frac{K_{MN}}{K_{MN}-3}\sqrt{\frac{K_{MN}-9}{K_{MN}-3}}$
Lade-Duncan	$\lambda_{LD} = \sqrt{\frac{2K_{LD}}{K_{LD}-27}}$	$\omega_{LD} = \sqrt{\frac{K_{LD}-27}{K_{LD}}}$

where $K_{MN} = \frac{9-sin^2\varphi_0}{1-sin^2\varphi_0} = 9 + 8tan^2\varphi_0$ and $K_{LD} = \frac{(3-sin\varphi_0)^3}{(1+sin\varphi_0)(1-sin\varphi_0)^2}$, in which φ_0 is the friction angle under triaxial compression stress conditions. The Mohr-Coulomb equation can be expressed in the form of

$$r_{cv} = \frac{\sqrt{2}\xi \sin\varphi_0}{\sqrt{3}\cos\theta - \sin\theta\sin\varphi_0} \tag{4.11}$$

Referring to Oda (1993) and Zhao and Guo (2013), s_{ij} and F_{ij} can be considered as coaxial at critical state. As a result, $s_{ij}^{(cv)}F_{ji}^{(cv)}$ can be related to the stress invariant r and the fabric invariant r^F at the crtical state via $r_{cv}r_{cv}^F = s_{ij}^{cv}F_{ji}^{cv}$. It follows that

$$r_{cv}^F = \frac{s_{ij}F_{ij}}{r_{cv}} = \frac{K_c}{r_{cv}} \tag{4.12}$$

which defines the critical fabric surface on the $\pi-$plane. Figure 4.1 shows the stress and fabric surfaces on the $\pi-$plane at critical state when using Matsuoka-Nakai (MN), Lade-Duncan (LD) and Mohr-Coulomb (MC) failure criteria, respectively, when the triaxial compression friction angle φ_0 varies from $10°$ to $55°$ and $p = 100kPa$.

As shown in Figure 4.1d, the fabric surfaces corresponding to the Mohr-Coulomb failure criterion are not convex regardless of the value of φ_0. The nonconvexity occurs not only at $b = 0$ (axes σ_1, σ_2, and σ_3) but also at $b = 1$, which is represented by the middle lines between two axes; i.e. the dashed lines in the figure. In Figure 4.1e

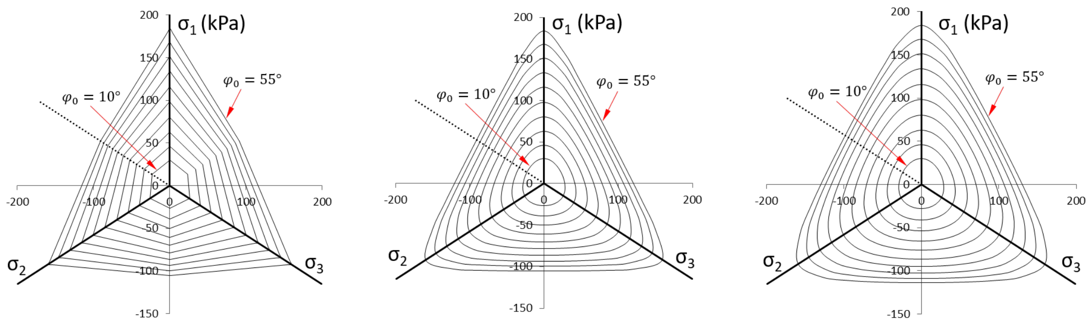

(a) Mohr-Coulomb stress surfaces

(b) Matsuoka-Nakai stress surfaces

(c) Lade-Duncan stress surfaces

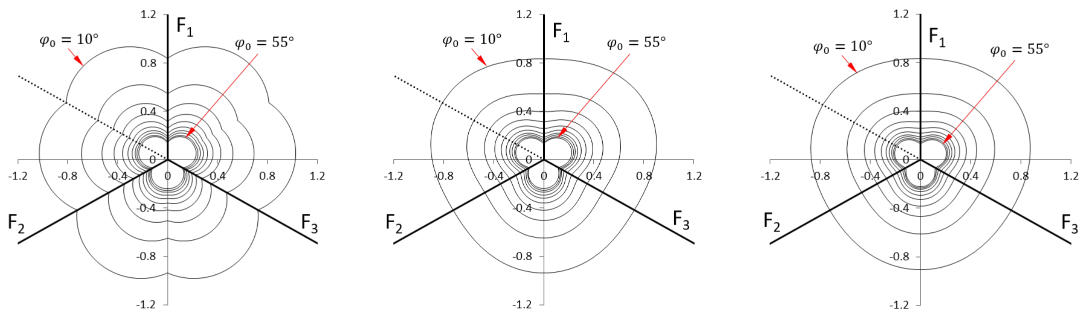

(d) Mohr-Coulomb fabric surfaces

(e) Matsuoka-Nakai fabric surfaces

(f) Lade-Duncan fabric surfaces

Figure 4.1: Comparison of stress and fabric surfaces

and Figure 4.1f that correspond to the Matsuoka-Nakai and Lade-Duncan failure criteria respectively, nonconvexity is observed when the friction angle is relatively large. Figure 4.2 compares the nonconvexity of the critical fabric surfaces associated with the three failure criteria at $\varphi_0 = 30°$. The nonconvexity of fabric surface is a little more significant when using the MN criterion than the LD criterion.

Figures 4.3a and 4.3b compare the fabric surfaces associated with the MN and LD criterion at $\varphi_0 = 30°$ with a circle for reference to demonstrate the level of nonconvexity. Note that these surfaces are plotted with similar sizes for demonstration purposes only. Figure 4.3c provides the DEM simulation results from the study of Zhao and Guo (2013).

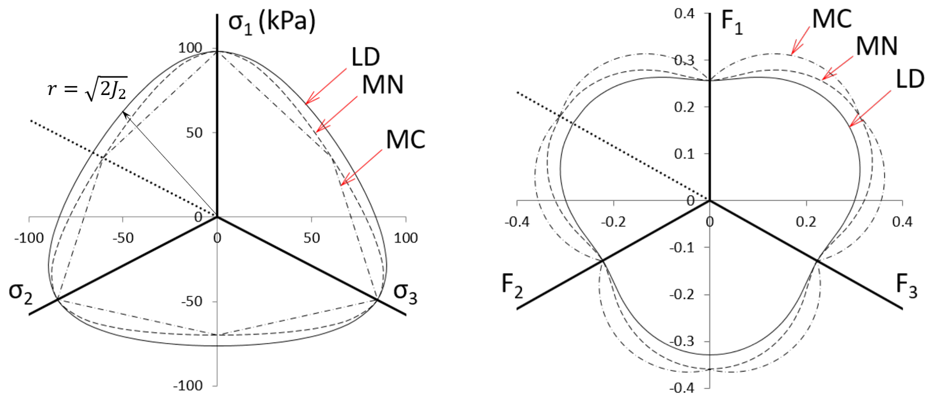

(a) Stress surfaces (b) Fabric surfaces

Figure 4.2: Stress and fabric surfaces under $\varphi_0 = 30°$, p=100kPa

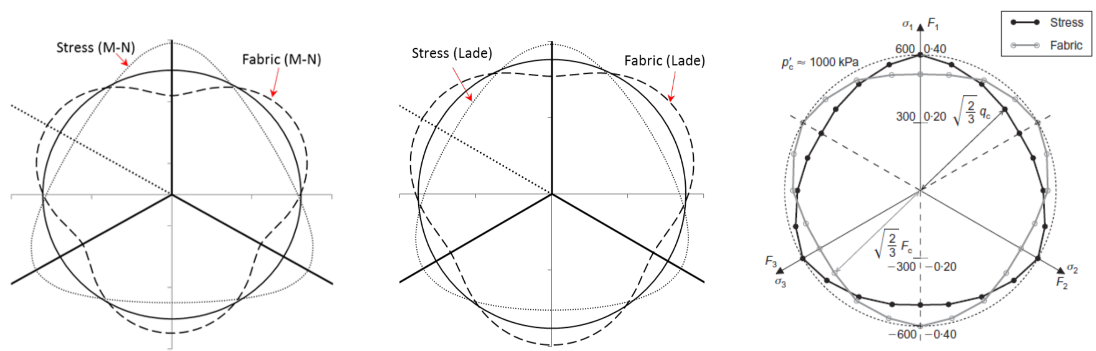

(a) MN equations (b) LD equations (c) DEM results (Zhao and Guo, 2013)

Figure 4.3: Comparison of stress and fabric surfaces when $\varphi_0 = 30°$

The convexity for the stress surface (when used as a yield surface or loading function) is of fundamental importance in setting variational inequalities for plasticity (Lions and Duvaut, 1976) and the basis of limit analysis of geomechanics problems in geotechnical engineering. It has also been supported by results of numerous experimental work and DEM simulations. One may, therefore, conclude that, in the absence of a clear and specific motivation, it is not sensible to employ a yield function that violates convexity (Bigoni and Piccolroaz, 2004). As a special case of loading surfaces, the stress surface at the critical state should be convex as well.

While the convexity of yield surfaces and the critical state stress surface are generally accepted and approved, the convexity of the critical state fabric surface has not been examined. However, the convexity of fabric surfaces at critical states has been observed from DEM simulations (Thornton, 2000; Ng, 2004, 2005; Thornton and Zhang, 2010; Barreto and O'Sullivan, 2012). Therefore, at this stage, the convexity requirement should be considered when establishing a fabric surface. From Figure 4.2b, the fabric surface obtained using the Lade-Duncan failure criterion best satisfies the requirement of convexity. To use an inverted LD surface also agrees with findings from DEM studies as discussed previously. Therefore, the LD criterion is chosen in this study in the following sections.

4.3 Fabric evolution law and assessment

The evolution of fabric is an important component of a stress-strain model for granular materials. Two different approaches have been used to describe the fabric evolution, namely strain approach and stress approach, in the literature. In the strain approach, the rate change of F_{ij} is assumed to be an isotropic tensor-valued function of the rate of plastic strain deviator e^p_{ij}, the current value of F_{ij} and the void ratio e, i.e.

$$\dot{F}_{ij} = \dot{F}(F_{ij}, \dot{e}^p_{ij}, e) \tag{4.13}$$

When further assuming that the principal axes of $\dot{F}_{ij}$ may be considered to be coaxial with the principal axes of plastic strain rate deviator $\dot{e}^p_{ij}$, the evolution of fabric may then be expressed as (Pietruszczak and Krucinski, 1989)

$$\dot{F}_{ij} = [g_1(e) + g_2(e)I_{2F}]\,\dot{e}^p_{ij} \tag{4.14}$$

where $I_{2F} = F_{kl}F_{kl}/2$. The functions $g_1(e)$ and $g_2(e)$ should reflect some basic trends in the evolution of soil fabric.

Experimental evidence shows that at very large deformation, the granular material may reach an ultimate state at which the fabric reaches a "saturated" state (i.e. $\dot{F}_{ij} = 0$), even though the plastic strain deviator is still accumulated beyond this point. Unfortunately, Equation (4.14) cannot reflect this property. Hence, the stress approach for the description of fabric evolution is introduced.

Extensive studies on the micromechanical analysis of granular materials have revealed that, regardless of the inherent internal structure, the distribution of contact normal changes in such a manner as to produce a greater concentration of contact normals in the direction of major principal stress (Biarez and Wiendieck, 1963; Oda, 1972b; Oda and Konishi, 1974a; Oda *et al.*, 1980). Oda (1993) suggests that there is a linear relationship between the fabric ratio $\sqrt{J_2^\Phi}/I_1^\Phi$ and the stress ratio $\sqrt{J_2}/I_1$ with a certain saturated state for the concentration of contact normals at large deformation. Herein I_1 and I_1^Φ are the first invariants of the stress and fabric tensors while J_2 and J_2^Φ are the second invariants of the deviatoric stress and fabric tensors respectively. The results of discrete element simulations for granular materials under different conditions also show certain correlations between the stress ratio and the fabric ratio. For example, Antony *et al.* (2004) suggested $(\sigma_1 - \sigma_2)/(\sigma_1 + \sigma_2) \approx (1/2)(\Phi_{11}/\Phi_{22})^{1/2}$ for 2D granular materials, while Maeda *et al.* (2006) proposed a different relation such that $\sigma_1/\sigma_2 \approx (\Phi_{11}/\Phi_{22})^{1/2}$. Similar findings were reported by Suzuki and Kuhn

(2013) and Sazzad (2014).

When shearing a granular material with inherent fabric, according to experimental measurements and the results of DEM simulations, contact normals tend to re-orient themselves in the direction of major principal stress so as to maintain the resistance to external forces. As a result, the direction of the major principal fabric has a tendency to follow that of the major principal stress.

In this study, the fabric evolution was established using the stress-based approach. The rate of fabric change $\dot{F}_{ij}$ was related to the rate of deviator stress ratio $\dot{\eta}$ by taking into account the current stress and fabric states; i.e., $\dot{F}_{ij} = \dot{F}(F_{ij}, \eta, \theta_{\dot{\sigma}}, \dot{\eta})$. The following assumptions were made when establishing the fabric evolution law:

(a) Regardless the initial fabric state, a granular material has an ultimate surface of fabric tensor at the critical state. This ultimate fabric state satisfies Equation (4.9);

(b) The change of fabric tensor $\dot{F}_{ij}$ is proportional to the difference between the critical state fabric tensor and the current fabric tensor $F_{ij}^{(cv)} - F_{ij}$;

(c) The deviator stress tensor s_{ij} and the deviator fabric tensor F_{ij} are coaxial at the critical state.

Based on these assumptions, the following functional form of fabric evolution law is assumed

$$\dot{F}_{ij} = \frac{\dot{\eta}}{\eta^{(cv)} - \eta}(F_{ij}^{(cv)} - F_{ij}) \tag{4.15}$$

where F_{ij} and $F_{ij}^{(cv)}$ are the current and critical state deviatoric fabric tensors, η and $\eta^{(cv)}$ are the current and critical state deviatoric stress ratios. $F_{ij}^{(cv)}$ and $\eta^{(cv)}$ are determined using a linear projection rule with the same Lode angle $\theta_{\dot{\sigma}}$. $\eta^{(cv)}$ and

$F_{ij}^{(cv)}$ can be expressed in terms of r_{cv} and r_{cv}^F as

$$\eta^{(cv)} = \frac{\sqrt{2} r_{cv}}{\xi} \tag{4.16}$$

$$F_{ij}^{(cv)} = \sqrt{\frac{2}{3}} r_{cv}^F \begin{bmatrix} sin(\frac{2}{3}\pi - \theta_{\dot{\sigma}}) & 0 & 0 \\ 0 & -sin\theta_{\dot{\sigma}} & 0 \\ 0 & 0 & sin(\frac{4}{3}\pi - \theta_{\dot{\sigma}}) \end{bmatrix} \tag{4.17}$$

where r_{cv}, r_{cv}^F are obtained from Equations (4.10) and (4.12), respectively.

While the deviatoric stress tensor s_{ij} and the deviatoric fabric tensor F_{ij} are considered coaxial at the critical state, during the deformation process, the stress and fabric tensors are not necessarily coaxial, even though $\dot{s}_{ij}$ and $\dot{F}_{ij}$ are coaxial as described by Equation (4.15). During the loading process, the major principal fabric component gradually rotates from its current direction towards the ultimate state at which it becomes coaxial with the major principal stress direction. This rotation process is generally stress-path dependent.

4.3.1 Fabric evolution in monotonic loading

In this study, the Lade's surface for critical stress states is used to generate the critical fabric surface and hence the fabric evolution law. In the following illustrations, without loss of generality, an initial deviator fabric tensor of the material is assumed as

$$F_{ij} = \begin{bmatrix} 0.05 & 0 & 0 \\ 0 & -0.025 & 0 \\ 0 & 0 & -0.025 \end{bmatrix}$$

Figure 4.4 demonstrates the fabric evolution as described by Equation (4.15) when using Lade's expression as the ultimate stress surface. The major principal stress is applied from different directions, initially making an angle δ_0 with the major principal fabric direction. The angle δ is introduced here to represent the angle between the major incremental principal stress ($\dot{\sigma}_1$) direction and major principal fabric (F_1) direction. For monotonic loading under isotropic consolidation, direction of $\dot{\sigma}_1$ is identical with that of σ_1. For cross-anisotropy materials, δ is the same as α in Figure 3.1, since the major principal fabric direction is identical with the normal of the bedding plane.

The specimen was sheared by keeping the mean effective stress p as a constant along a stress path with $b = 0$ (i.e., $\sigma_2 = \sigma_3$). Figure 4.4a and Figure 4.4b show the variation of angle δ and the magnitude of r^F for different cases.

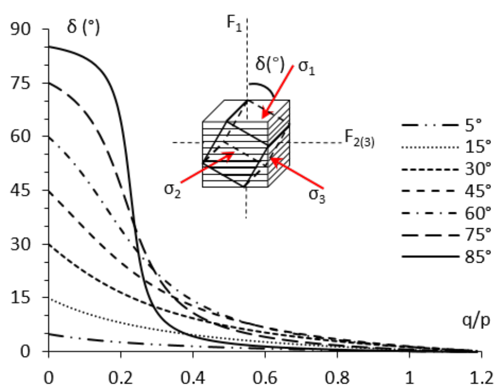

(a) Evolution of δ

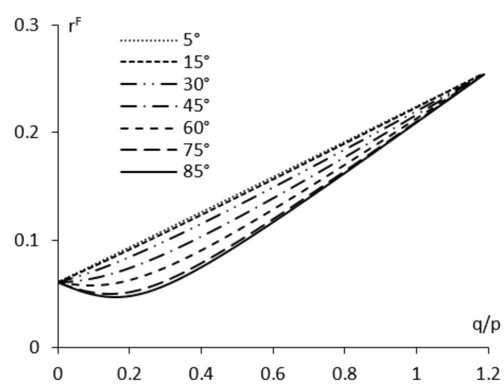

(b) Anisotropic fabric measure r^F

Figure 4.4: Fabric evolution at different initial fabric inclination angles

Regardless of the value of δ_0 at the initial state, with the increase of q/p, δ decreases gradually and approaches a small value, indicating the fabric tensor and the stress tensor are becoming coaxial. The variation rate of δ with respect to q/p is significantly affected by δ_0. In general, with the increase of δ_0, δ decreases more dramatically when

q/p increases at the beginning of loading, which implies a dramatic rotation of the major principal fabric component direction. With the increase of q/p level, the rate of fabric rotation decreases gradually while δ approaches zero, as shown in Figure 4.4a. The evolution of the fabric deviator measured by r^F with the stress ratio q/p is affected by δ_0 as well. In the case of insignificant initial non-coaxiality (i.e. a small δ_0), r^F tends to increase monotonically with q/p, which implies that the applied stress increases the degree of anisotropy. On the other hand, for large values of δ_0, 90° for the maximum, the increased stress ratio tends to reduce the degree of fabric anisotropy initially, as shown in Figure 4.4b. However, at a higher q/p level, the induced anisotropy becomes significant in all cases.

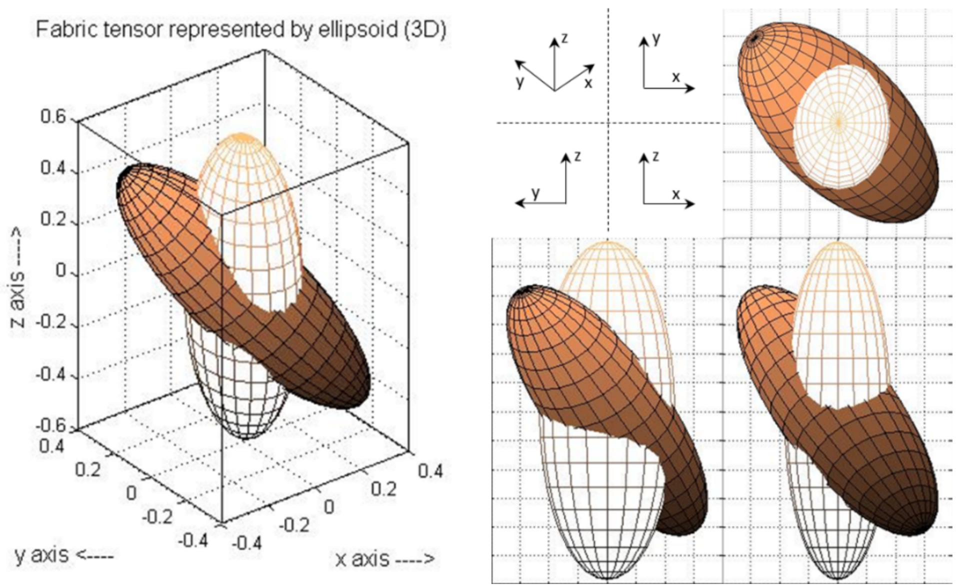

(a) 3D Representation (b) 2D orthographic projection

Figure 4.5: Demostration of fabric tensor by ellipsoid

A more intuitive way to demonstrate the variation of fabric is to use a fabric ellipsoid to represent the fabric tensor. The fabric ellipsoid is plotted by using the three principal fabric components as radii, with the rotation angle being determined by the direction of the major principal fabric component. In Figure 4.5a, the ellipsoid with the solid surface represents a fabric tensor with strong anisotropy, whose major principal fabric component makes an angle of 45° with respect to the z-axis direction. For comparison purposes, Figure 4.5a shows another fabric ellipsoid with the meshed surface that has the same principal fabric components but the major principal fabric is in the direction of the z-axis. The three views of the fabric ellipsoid are shown in Figure 4.5b.

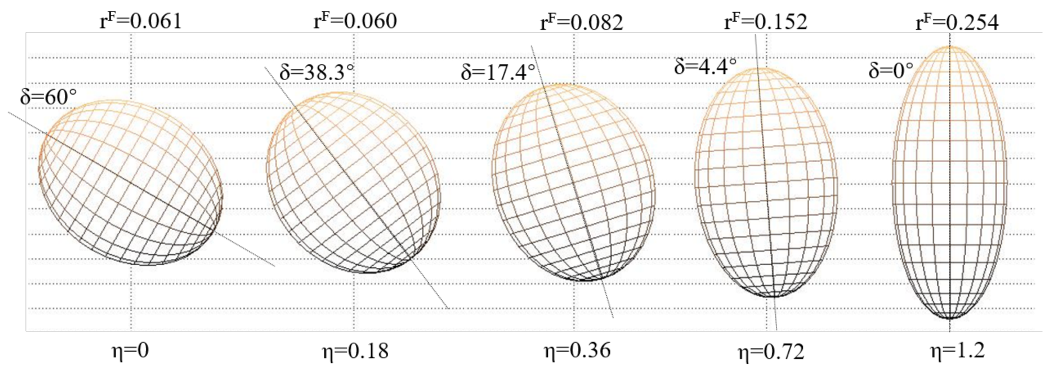

Figure 4.6: Evolution of fabric during loading

Now we examine the rotation of fabric tensor during a loading process when the major principal stress direction initially makes an angle of $\delta_0 = 60°$ with the major principal fabric direction. During the loading process, the major principal incremental stress direction is fixed, but the fabric tensor rotates owing to the evolution of fabric. For simplicity, the major principal stress direction is selected as the z-axis to illustrate the rotation of fabric ellipsoid. Figure 4.6 shows the evolution of fabric tensor corresponding to the curve in Figure 4.4 via the rotation and the change of geometry of the fabric ellipsoid.

4.3.2 Fabric evolution induced by cyclic loading

Equation (4.15) can also be used to describe fabric evolution induced by cyclic loading. For the case with $\delta_0 = 60°$, discussed previously in Figure 4.6, when cyclic loading is applied in the direction of the z-axis, the evolution of fabric is conceptually illustrated in Figure 4.7 (from the view of x-z plane). Obviously, the evolution of fabric during the loading stage is the same as that in the monotonic loading case shown in Figure 4.6. During unloading, the major incremental principal stress direction changes from vertical to horizontal. It should be noted that the values of $F_{ij}^{(cv)}$ and $\eta^{(cv)}$ are different during the loading and unloading processes because of the change on $\theta_{\dot{\sigma}}$. More details about the stress-strain model including fabric evolution will be discussed in Chapter 5.

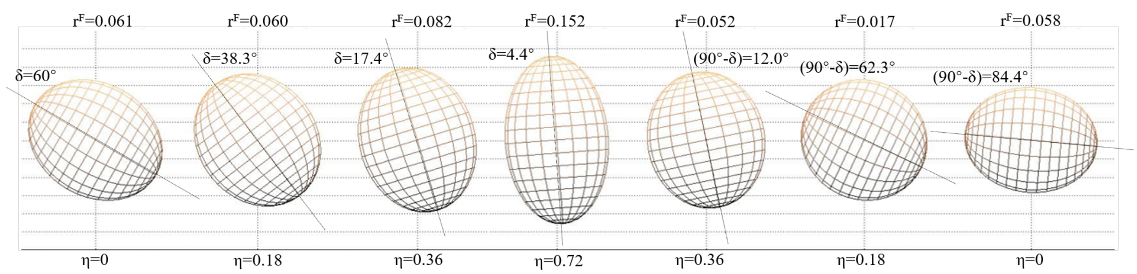

Figure 4.7: Evolution of fabric during loading and unloading

Figure 4.8 shows the rotation of the major principal fabric direction during a complete one-way loading-unloading process with the stress path being illustrated in Figure 4.8c on the π-plane. The loading stage and the unloading stage both contain 100 increments, and the maximum stress ratio is $q/p = 0.72$. The rotation of the major principal fabric direction relative to $\dot{\sigma}_1$ is illustrated in Figure 4.8a. It starts at $\delta_0 = 60°$ and decreases dramatically as soon as the loading begins. At $N = 100$ with $q/p = 0.72$, the angle δ is close to $0°$. When the unloading begins, the major

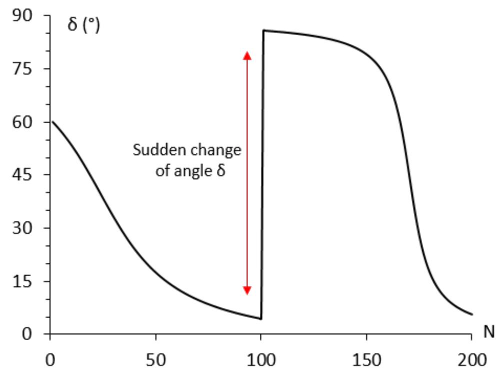

(a) Major principal fabric direction δ

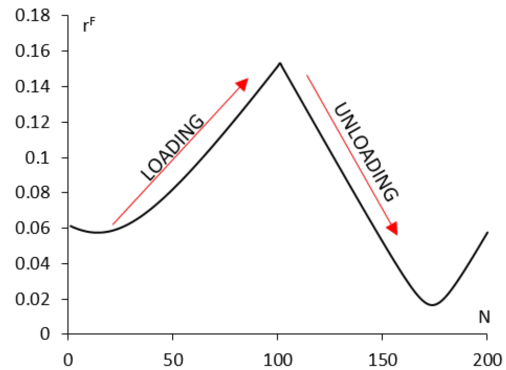

(b) Anisotropic fabric measure r^F

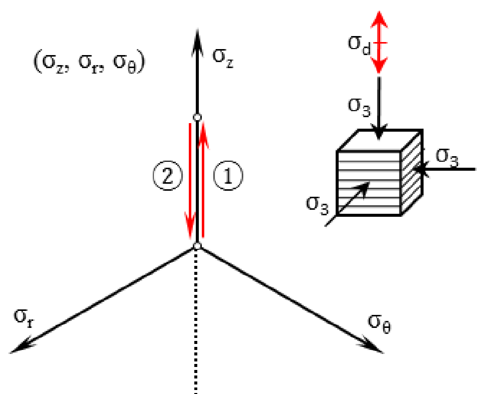

(c) One-way loading path on π-plane

Figure 4.8: Demostration of fabric rotation during one cycle of loading and unloading

principal incremental stress changes direction and a sudden change of δ is observed. It should be noted that, during unloading, the directions of the major principal stress and the major principal incremental stress are not identical. It is more convenient to compare the directions of the major principal fabric component and the major principal incremental stress. As we can see from the unloading stage of Figure 4.8a, δ decreases again, implying that the non-coaxiality between the stress and fabric tensors is decreasing. The evolution of the fabric anisotropic measure r^F is shown in Figure 4.8b. It increases during loading and decreases during unloading. However, after a cycle of loading and unloading, the final fabric measure r^F is slightly different from its initial value. This implies that continuous fabric evolution is possible during cyclic loading.

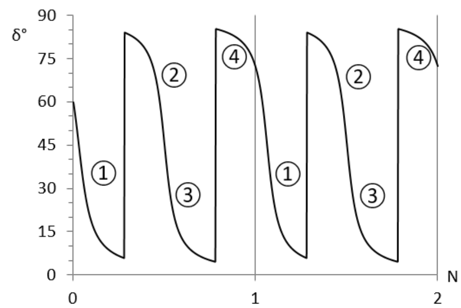

(a) Change of δ under a two-way cyclic loading

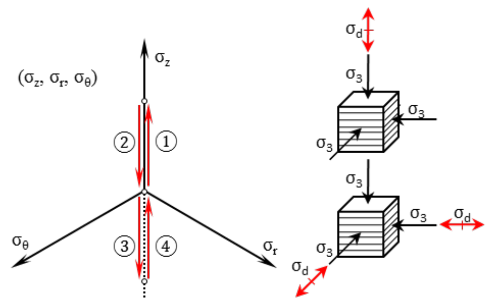

(b) Two-way stress path on π-plane

Figure 4.9: Variation of δ during a two-way cyclic loading

Figure 4.9a shows the continuous rotation of the fabric direction during a two-way cyclic loading test. Figure 4.9b shows the stress path on the π-plane. Different from the one-way cyclic loading, the cyclic stress is applied in different directions alternatively that corresponds to a 90° jump in the major principal stress direction. As a result, one expects different ways of principal fabric rotation during the cyclic loading process.

4.3.3 Modified dilatancy formulation with the effect of fabric

A proper dilatancy formulation for granular materials should consider the effect of barotropy (stress level), pyknotropy (void ratio) and anisotropy (microstructure). In general, a denser granular material tends to dilate more when sheared and the dilation tends to be suppressed under increased mean effective stress level. For granular materials with inherent anisotropy, shear tends to induce higher dilation when the major principal stress is the direction of the major principal fabric component (i.e., σ_1 is perpendicular to the bedding plane). Some of the existing dilatancy formulations can reasonably capture the stress level and void ratio dependency (Vermeer and De Borst, 1984; Wan and Guo, 1998; Li and Dafalias, 2012). However, the proper consideration of anisotropy is usually missed.

To address the effect of barotropy (stress level), pyknotropy (void ratio) and anisotropy (micro-structure) on dilatancy, in this study, the following formulation for dilatancy D is proposed:

$$D = -\frac{\dot{\varepsilon}^p_{v(s)}}{\dot{\varepsilon}^p_{q(s)}} = d[\eta - \eta_{cv}(\theta)e^{m\zeta}] \tag{4.18}$$

$$\zeta = (e - e_{cr}) + k[1 - (\frac{s_{ij}F_{ij}}{K_c})A] \tag{4.19}$$

where d, m, k are material constants, η_{cv} is the stress ratio at the projection of the current stress state onto the critical stress surface. $\dot{\varepsilon}^p_{q(s)}$ is the equivalent shear strain increment defined as $\dot{\varepsilon}^p_{q(s)} = \frac{2}{3}\sqrt{3J_2^{(\dot{\varepsilon}^p)}}$, with $J_2^{(\dot{\varepsilon}^p)}$ being the second deviator invariant of the incremental plastic strain tensor $\dot{\varepsilon}^p_{ij}$. For a convential triaxial compression test on a isotropic material, $\dot{\varepsilon}^p_{q(s)} = \frac{2}{3}(\dot{\varepsilon}^p_1 - \dot{\varepsilon}^p_3)$. A is a measure of the non-coaxiality angle $\delta_{F_{ij},s_{ij}}$ between F_{ij} and s_{ij} and is expressed as

$$A = \cos\delta_{F_{ij},s_{ij}} = n^F_{ij}n^s_{ij} \tag{4.20}$$

with

$$n^F_{ij} = \frac{F_{ij}}{\sqrt{F_{kl}F_{kl}}}, \qquad n^s_{ij} = \frac{s_{ij}}{\sqrt{s_{kl}s_{kl}}}$$

Alternatively, $\delta_{F_{ij},s_{ij}}$ can be related to the Lode angles of F_{ij} and s_{ij} via $\delta_{F_{ij},s_{ij}} =$

$\theta_F - \theta_\sigma$. The value of A varies between -1 and 1, with $A = 1$ representing a coaxial condition with $\delta_{F_{ij},s_{ij}} = 0$ between deviatoric fabric and stress tensors. It should be noted that $D > 0$ stands for dilatancy, while $D < 0$ reflects contraction (or shear induced volumetric compaction).

The effect of fabric on dilatancy reflected in the proposed formulation, Equation (4.18), is twofold. Firstly, based on the assumption used to build the fabric evolution law, the term $s_{ij}F_{ij}/K_c$ increases from 0 to 1 during a loading process. Under a condition where the fabric and stress tensors are coaxial, the term $k[1 - (\frac{s_{ij}F_{ij}}{K_c})A]$ in Equation (4.19) decreases from k to 0, meaning that dilatancy is a function of stress states and fabric evolution during the deformation process. Secondly, the term A describes the influence of the degree of non-coaxiality between the fabric and stress tensors. When F_{ij} and s_{ij} are coaxial, $A = 1$. With an increase of the non-coaxiality between F_{ij} and s_{ij}, the value of A tends to decrease with $A_{\text{min}} = -1$. As a result, variation of A from 1 to -1 may result in significant increase of $k[1 - (\frac{s_{ij}F_{ij}}{K_c})A]$ and ζ may increase significantly in Equation (4.19) and hence reduced dilation according to equation (4.18). More specifically, the value of A changes between 1 and -1 under different combination of α and b, as shown in Figure 4.10. Based on Equation (4.19), a larger value of A means a larger dilatancy. As we can see, the largest value of A is found at $\alpha = 0°$ and $b = 0$, and value of A decreases with both α and b.

During a loading process with the shear strain increasing monotonically, if the applied stresses and the fabric tensor are initially non-coaxial, the fabric tensor would rotate in such a way that the deviator fabric becomes coaxial with the stress tensor at the critical state. In other words, the value of A should approach 1 at the critical state. Figure 4.11 illustrates the variation of A, according to the proposed fabric

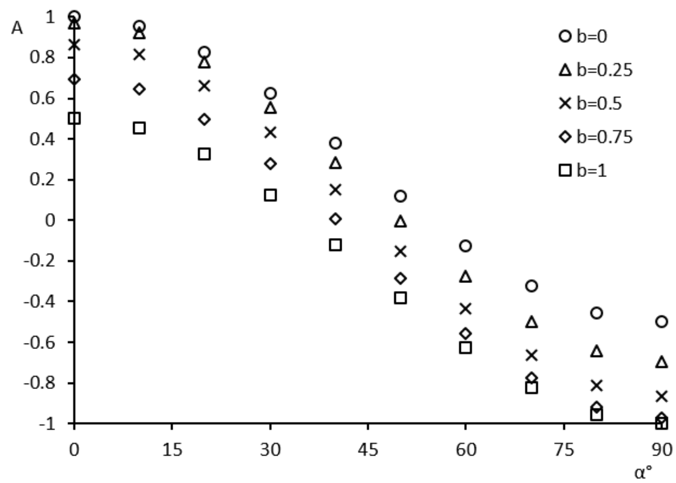

Figure 4.10: Value of A under different loading conditions

evolution law, during the loading process under different conditions with various initial non-coaxiality.

The performance of the dilatancy formulation is illustrated in Figure 4.12. The initial angle of α has a large impact on the initial dilatancy, which is consistent with laboratory observations. An increase of b is associated with a decrease of dilatancy. As the stress ratio increases, the influence of initial anisotropy on the dilatancy decreases. For the same stress path (described by b), the final dilatancy from different initial fabric conditions becomes unique. The dilatancy at critical stress approaches zero for all loading conditions.

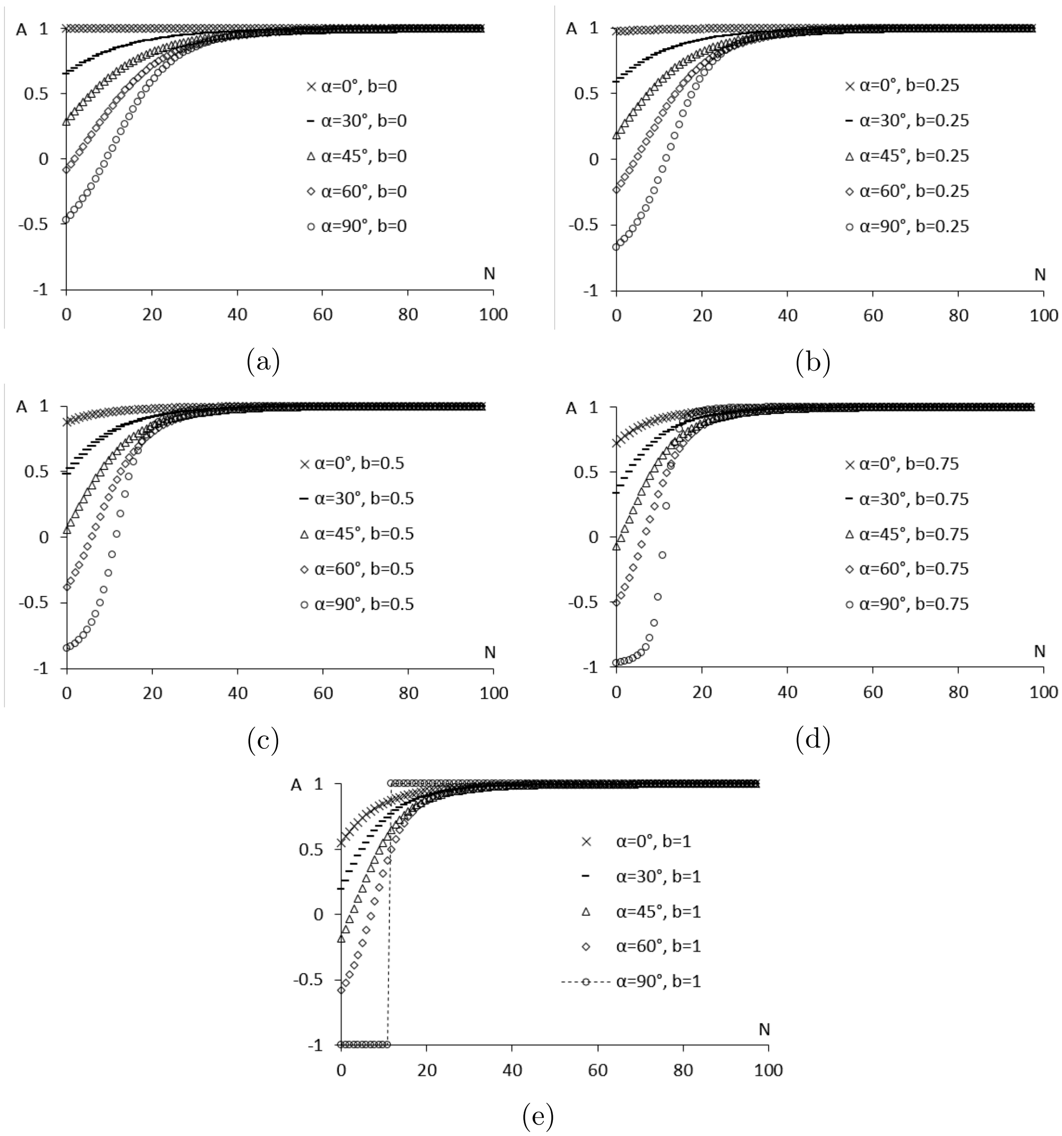

Figure 4.11: Variation of A during the loading process under different conditions

4.4 Framework of a constitutive model for granular materials

In this section, a constitutive model is developed based on the proposed stress-dilatancy equation. Since the current study focuses on the effect of fabric on shear

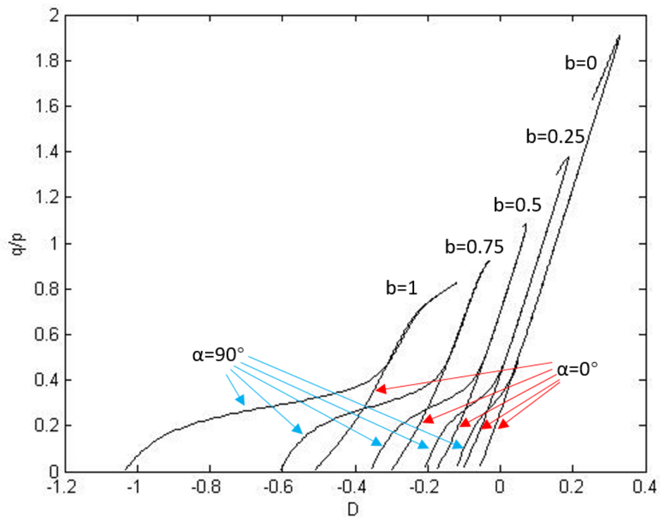

Figure 4.12: Stress-dilatancy curves under different loading conditions

strength and dilatancy characteristics, the following assumptions are made when developing the constitutive model:

(1) Plastic strain dominates the sand deformation, so the influence of elastic anisotropy, if any, is considered negligible. As a result, the effect of fabric on the elastic behaviour is neglected.

(2) Lade's criterion is used in the yield function to determine the stress and fabric surfaces at the critical state.

The framework of the stress-strain model proposed here is primarily based on the model by Guo (2000). The novel features of the proposed stress-strain model include: (1) the development of a tensor-based fabric evolution law and (2) the dilatancy equation which is incorporated with the evolving fabric tensor. The details of this model are summarized as follows.

4.4.1 Elastic strains

The total strain increment $\dot{\varepsilon}$ is composed of elastic strain increment $\dot{\varepsilon}^e$ and plastic strain increment $\dot{\varepsilon}^p$. Among them, the elastic strain increment $\dot{\varepsilon}^e$ can be determined by the generalized Hooke's law, and the plastic strain increment $\dot{\varepsilon}^p$ can be decomposed into the volumetric strain increment $\dot{\varepsilon}^p_{(c)}$ and the deviatoric strain increment $\dot{\varepsilon}^p_{(s)}$. Using the empirical equations proposed by Iwasaki *et al.* (1978), the elastic shear modulus is expressed as a function of void ratio e and the mean effective stress p:

$$G = G_0 \frac{(2.17 - e)^2}{1 + e} \sqrt{\frac{p}{p_{ref}}}$$

in which $p_{ref} = 1kPa$ and G_0 is a constant. The elastic shear strain increment and the elastic volumetric strain increment can, therefore, be expressed as

$$\dot{\varepsilon}^e_q = \frac{\dot{q}}{3G}, \quad \dot{\varepsilon}^e_v = \frac{\dot{p}}{B}$$

in which the bulk modulus B can be determined from the shear modlus G and the Poisson's ratio v as $B = \frac{2(1+v)}{3(1-2v)}G$.

4.4.2 Strains caused by compaction mechanism

The material's deformation induced by change in the mean effective stress is controlled by the compaction mechanism. An associated flow rule is assumed with the yield and the plastic potential functions being

$$g_c = f_c = p - p_c \tag{4.21}$$

in which p_c is the consolidation pressure as obtained from the virgin compression line at a given void ratio.

When the mean effective stress p varies in a relatively small range, the consolidation curve of sand is assumed to be straight line in the $e - \ln p$ plane,

$$e = e_0 - \lambda \ln(\frac{p}{p_0}) \tag{4.22}$$

The total plastic strain increments, $\dot{\varepsilon}_{(c)}$, caused by the compaction mechanism is therefore obtained as

$$\dot{\varepsilon}_{v(c)} = \dot{\varepsilon}_v^e + \dot{\varepsilon}_{v(c)}^p = \frac{\lambda}{1 + e_0} \frac{\dot{p}}{p} \tag{4.23}$$

However, if the mean effective stress p varies in a large range, the following expression for consolidation curve is more accurate (Guo, 2000):

$$e = e_0 \exp[-(\frac{p}{h_l})^{n_l}] \tag{4.24}$$

in which h_l and n_l are two material constants. The instantaneous slope λ of the $e - \ln p$ curve can be expressed as

$$\lambda = -p\frac{\dot{e}}{\dot{p}} = n_l e (\frac{p}{h_l})^{n_l} \tag{4.25}$$

4.4.3 Plastic strains caused by shearing mechanism

Assuming a combined volumetric-deviatoric strain hardening mechanism, the yield function associated with the plastic shearing mechanism is expressed as

$$f_s(p,q,\theta,\varepsilon_q^{p\star},e) = q - \eta_m(\theta,\varepsilon_q^{p\star},e)p = q - \frac{\varepsilon_q^{p\star}}{a+\varepsilon_q^{p\star}}(\frac{e}{e_{cr}})^{-\beta}\eta_{cv}(\theta)p = 0 \tag{4.26}$$

in which $\varepsilon_q^{p\star}$ is the equivalent plastic shear strain of the strain tensor factored with the fabric tensor such that $\varepsilon_{ij}^{p\star} = \varepsilon_{ik}^{p}\Phi_{kj}$. The void ratio e_{cr} at the critical state depends on the mean effective stress at the critical state by following

$$e_{cr} = e_{cr0}exp[-(\frac{p}{h_{cr}})^{n_{cr}}] \tag{4.27}$$

where e_{cr0}, h_{cr} and n_{cr} are constants.

Using the failure criteria in Equation (4.10), the critical state stress ratio η_{cv} can be determined as

$$\eta_{cv}(\theta) = \frac{\sqrt{3/2}r_{cv}}{\sqrt{3}\xi/3} = \frac{3}{\sqrt{2}\lambda_{LD}}[sin(\frac{\pi - sin^{-1}(\omega_{LD}sin3\theta)}{3})]^{-1} \tag{4.28}$$

in which λ_{LD} and ω_{LD} are calculated using the equations in Table 4.1.

The plastic strains caused by shearing mechanism is determined using a non-associated flow rule. Based on the modified dilatancy fomulation that considering the effect of fabric, the plastic potential function is written as

$$g_s = q - D(\theta)p \tag{4.29}$$

in which $D(\theta)$ is given in Equation (4.18).

4.4.4 Incremental stress-strain relations: q-p space

The total strain increments are expressed as

$$\dot{\varepsilon}_v = \dot{\varepsilon}_v^e + \dot{\varepsilon}_v^p = \dot{\varepsilon}_{v(c)}^e + \dot{\varepsilon}_{v(c)}^p + \dot{\varepsilon}_{v(s)}^p = \frac{\lambda}{1+e_0}\frac{\dot{p}}{p} + \dot{\Lambda}\frac{\partial g_s}{\partial p} \tag{4.30}$$

$$\dot{\varepsilon}_q = \dot{\varepsilon}_q^e + \dot{\varepsilon}_q^p = \frac{1}{3G}\dot{q} + \dot{\Lambda}\frac{\partial g_s}{\partial q} \tag{4.31}$$

where the value of the plastic multiplier $\dot{\Lambda}$ can be obtained from the consistency condition $f_s(p, q, \theta, \varepsilon_q^p, e) = 0$. Finally, the incremental stress-strain relation is given as

$$\begin{pmatrix} \dot{\varepsilon}_q \\ \dot{\varepsilon}_v \end{pmatrix} = \begin{pmatrix} C_{11} & C_{12} \\ C_{21} & C_{22} \end{pmatrix} \begin{pmatrix} \dot{q} \\ \dot{p} \end{pmatrix} \tag{4.32}$$

with the matrix C being the compliance operator, and its components' values are

$$\begin{array}{ll} C_{11} = \frac{1}{3G} + \frac{1}{H}\frac{\partial g_s}{\partial q}\frac{\partial f_s}{\partial q} & C_{12} = \frac{1}{H}\frac{\partial g_s}{\partial q}\frac{\partial f_s}{\partial p} \\ C_{21} = \frac{1}{H}\frac{\partial g_s}{\partial p}\frac{\partial f_s}{\partial q} & C_{22} = \frac{\lambda}{(1+e_0)p} + \frac{1}{H}\frac{\partial g_s}{\partial p}\frac{\partial f_s}{\partial p} \end{array}$$

in which

$$\begin{array}{l} H = -\dfrac{\partial f_s}{\partial \varepsilon_q^p}\dfrac{\partial g_s}{\partial q} + (1+e_0)\dfrac{\partial f_s}{\partial e}\dfrac{\partial g_s}{\partial p} \\ \dfrac{\partial f_s}{\partial q} = 1 \qquad \dfrac{\partial g_s}{\partial q} = 1 \\ \dfrac{\partial f_s}{\partial p} = -\eta_m = -\eta_{cv}\dfrac{\varepsilon_q^p}{a+\varepsilon_q^p}(\dfrac{e}{e_{cr}})^{-\beta} \end{array}$$

$$
\begin{aligned}
\frac{\partial g_s}{\partial p} &= -D = d(\eta_{cv} e^{m\zeta} - \eta) \\
\frac{\partial f_s}{\partial \varepsilon_q^p} &= \frac{\partial f_s}{\partial \eta_m}\frac{\partial \eta_m}{\partial \varepsilon_q^p} = -p[\frac{a}{(a+\varepsilon_q^p)^2}](\frac{e}{e_{cr}})^{-\beta}\eta_{cv} \\
\frac{\partial f_s}{\partial e} &= \frac{\partial f_s}{\partial \eta_m}\frac{\partial \eta_m}{\partial e} = \beta p(\frac{\varepsilon_q^p}{a+\varepsilon_q^p})(\frac{e^{-\beta-1}}{e_{cr}^{-\beta}})\eta_{cv}
\end{aligned}
$$

So the final expression of the stress-strain relation is written as

$$
\begin{pmatrix} \dot{\varepsilon}_q \\ \dot{\varepsilon}_v \end{pmatrix} = \begin{pmatrix} \frac{1}{3G} + \frac{1}{H} & -\frac{\eta_m}{H} \\ -\frac{D}{H} & \frac{D\eta_m}{H} + \frac{\lambda}{(1+e_0)p} \end{pmatrix} \begin{pmatrix} \dot{q} \\ \dot{p} \end{pmatrix} \tag{4.33}
$$

By finding the inverse of the compliance matrix in Equation (4.33), the stress-strain relationship can be alternatively expressed as

$$
\begin{pmatrix} \dot{q} \\ \dot{p} \end{pmatrix} = \begin{pmatrix} D_{11} & D_{12} \\ D_{21} & D_{22} \end{pmatrix} \begin{pmatrix} \dot{\varepsilon}_q \\ \dot{\varepsilon}_v \end{pmatrix} \tag{4.34}
$$

with

$$
\begin{pmatrix} D_{11} & D_{12} \\ D_{21} & D_{22} \end{pmatrix} = \begin{pmatrix} C_{11} & C_{12} \\ C_{21} & C_{22} \end{pmatrix}^{-1} = \frac{1}{\Pi}\begin{pmatrix} C_{22} & -C_{12} \\ -C_{21} & C_{11} \end{pmatrix} \tag{4.35}
$$

where

$$
\Pi = C_{11}C_{22} - C_{12}C_{21} = (\frac{1}{3G} + \frac{1}{H})(\frac{D\eta_m}{H} + \frac{\lambda}{(1+e_0)p}) - \frac{D\eta_m}{H^2}
$$

4.4.5 Incremental stress-strain relations: generalized stress space

From the consistency condition of the yield surface associated with the plastic shearing mechanism,

$$\dot{f}_s = \frac{\partial f_s}{\partial \sigma_{ij}}\dot{\sigma}_{ij} + \frac{\partial f_s}{\partial \varepsilon_q^p}\dot{\varepsilon}_q^p + \frac{\partial f_s}{\partial \varepsilon_v^p}\dot{\varepsilon}_v^p = 0$$

$$\frac{\partial f_s}{\partial \sigma_{ij}} D^e_{ijkl}(\dot{\varepsilon}_{kl} - \dot{\varepsilon}^p_{kl}) + \frac{\partial f_s}{\partial \varepsilon_q^p}\dot{\Lambda}\frac{\partial g_s}{\partial q} + \frac{\partial f_s}{\partial \varepsilon_v^p}\dot{\Lambda}\frac{\partial g_s}{\partial p} = 0$$

the plastic multiplier is determined as

$$\dot{\Lambda} = \frac{1}{H}\frac{\partial f_s}{\partial \sigma_{ij}} D^e_{ijkl}\dot{\varepsilon}_{kl}$$

with

$$H = \frac{\partial f_s}{\partial \sigma_{pq}} D^e_{pqrs}\frac{\partial g_s}{\partial \sigma_{rs}} - \frac{\partial f_s}{\partial \varepsilon_q^p}\frac{\partial g_s}{\partial q} + (1+e_0)\frac{\partial f_s}{\partial e}\frac{\partial g_s}{\partial p}$$

The elastic constituent tensor D^e_{ijkl} is given as

$$D^e_{ijkl} = \frac{vE}{(1-2v)(1+v)}\delta_{ij}\delta_{kl} + \frac{E}{2(1+v)}(\delta_{ik}\delta_{jl} + \delta_{il}\delta_{jk})$$

where E is related to G as $E = 2(1+v)G$. The incremental plastic strain tensor is written as

$$\dot{\varepsilon}^p_{ij} = \dot{\Lambda}\frac{\partial g_s}{\partial \sigma_{ij}} = \frac{1}{H}\frac{\partial f_s}{\partial \sigma_{rs}} D^e_{rskl}\dot{\varepsilon}_{kl}\frac{\partial g_s}{\partial \sigma_{ij}} \tag{4.36}$$

The incremental stress-strain relation can be written as

$$\dot{\sigma}_{ij} = D^{ep}_{ijkl}\dot{\varepsilon}_{kl} = D^e_{ijkl}(\dot{\varepsilon}_{kl} - \dot{\varepsilon}^p_{kl}) \tag{4.37}$$

From Equations (4.36) and (4.37), D^{ep}_{ijkl} can be obtained as

$$D^{ep}_{ijkl} = D^{e}_{ijkl} - \frac{1}{H}(D^{e}_{ijpq}\frac{\partial g_s}{\partial \sigma_{pq}}\frac{\partial f_s}{\partial \sigma_{rs}}D^{e}_{rskl}) \tag{4.38}$$

with

$$\frac{\partial f_s}{\partial \sigma_{ij}} = \frac{\partial q}{\partial \sigma_{ij}} - \frac{\varepsilon^p_q}{a+\varepsilon^p_q}(\frac{e}{e_{cr}})^{-\beta}\eta_{cv}(\theta)\frac{\partial p}{\partial \sigma_{ij}} - \frac{\varepsilon^p_q}{a+\varepsilon^p_q}(\frac{e}{e_{cr}})^{-\beta}p\frac{\partial \eta_{cv}(\theta)}{\partial \theta}\frac{\partial \theta}{\partial \sigma_{ij}}$$

$$\frac{\partial g_s}{\partial \sigma_{ij}} = \frac{\partial q}{\partial \sigma_{ij}} - D(\theta)\frac{\partial p}{\partial \sigma_{ij}} - p\frac{\partial D(\theta)}{\partial \theta}\frac{\partial \theta}{\partial \sigma_{ij}} - p\frac{\partial D(\theta)}{\partial \zeta}\frac{\partial \zeta}{\partial \sigma_{ij}}$$

where

$$\frac{\partial q}{\partial \sigma_{ij}} = \frac{3s_{ij}}{2q}$$

$$\frac{\partial p}{\partial \sigma_{ij}} = \frac{1}{3}\delta_{ij}$$

$$\frac{\partial \theta}{\partial \sigma_{ij}} = \frac{\sqrt{3}}{2J_2^{3/2}cos3\theta}(\frac{3J_3}{2J_2}s_{ij} + \frac{2}{3}\delta_{ij}J_2 - s_{ik}s_{kj})$$

$$\frac{\partial \eta_{cv}(\theta)}{\partial \theta} = \frac{3\omega cos3\theta cos(\frac{\pi - sin^{-1}(\omega sin3\theta)}{3})}{\sqrt{2}\lambda\sqrt{1-(\omega sin3\theta)^2}sin^2(\frac{\pi - sin^{-1}(\omega sin3\theta)}{3})}$$

$$\frac{\partial D(\theta)}{\partial \theta} = (-de^{m\zeta})\frac{\partial \eta_{cv}(\theta)}{\partial \theta} = \frac{-3d\omega e^{m\zeta}cos3\theta cos(\frac{\pi - sin^{-1}(\omega sin3\theta)}{3})}{\sqrt{2}\lambda\sqrt{1-(\omega sin3\theta)^2}sin^2(\frac{\pi - sin^{-1}(\omega sin3\theta)}{3})}$$

$$\frac{\partial D(\theta)}{\partial \zeta} = -dm\eta_{cv}(\theta)e^{m\zeta}$$

$$\frac{\partial \zeta}{\partial \sigma_{ij}} = -\frac{kA}{K_c}F_{ij}$$

4.5 Model assessments

4.5.1 Material constants used in the constitutive model

In this section, the stress-strain responses of Ottawa sand under different stress conditions were simulated using the proposed constitutive model. The proposed constitutive model is subsequently accessed by comparing the model results with test results presented in Chapter 3. The mean effective stress was kept constant at $p = 100kPa$ in all the laboratory tests and constitutive simulations.

Table 4.2: Material parameters of Ottawa sand

$G_0 = 2750kPa$	$v = 0.29$	$e_{cr0} = 0.74$	$\varphi_{cv} = 30°$
$h_l = 426.8MPa$	$n_l = 0.43$	$a = 0.004$	$\beta = 2.3$
$h_{cr} = 2867MPa$	$n_{cr} = 0.232$	$m = 5.3$	$k = 0.065$
$d = 1$	$\Omega = 0.25$	$e_0 = 0.59$	

As shown in Table 4.2, the proposed stress-strain model involve a total number of 15 model parameter. The first ten parameters for Ottawa sand, (G_0, v, e_{cr0}, φ_{cv}, h_l, n_l, a, β, h_{cr}, n_{cr}), are the same as those determined by Guo (2000) based on laboratory results. The following three parameters (m, k, d), which mainly control the dilatancy properties of the sand, are determined using test results from test Series A (Table 3.2) in this study. The initial degree of anisotropy Ω, which is defined as $\Omega = \frac{2}{3}\sqrt{3J_2^F}$, is determined by fitting measured data from test Series A. The initial void ratio e_0 is taken as the average measured values for different specimens via standard laboratory tests.

4.5.2 Comparison of calculated and measured results

Series A tests with $b = \sin^2 \alpha$

Figure 4.13 compares the experimental stress-strain curves from Series A tests in Chapter 3 and the corresponding simulation results using the proposed stress-strain model. In general, the proposed stress-strain model reasonably reproduces the stress-strain responses obtained from Tests A1 to A5, in which the intermediate principal stress coefficient b and the major principal stress directions are different. In particular, the deviator stress at the peak of the stress-strain curves decreases from A1 to A5. The highest deviator stress value is obtained in test A1 with $b = 0$ and $\alpha = 0°$. The lowest peak deviator stress is obtained in test A5 with $b = 1$ and $\alpha = 90°$. For test A3 with $b = 0.5$ and $\alpha = 15°$, however, the simulation shows higher peak deviatoric stress than laboratory measurement. In all cases, the critical states at large shear strain are correctly captured.

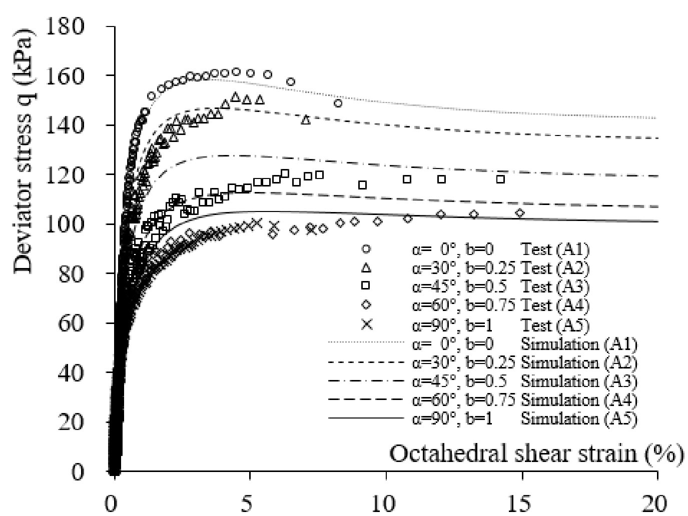

Figure 4.13: Stress-strain curves from series A (tests and simulations)

Figure 4.14 compares the theoretical and experimental volumetric strain responses

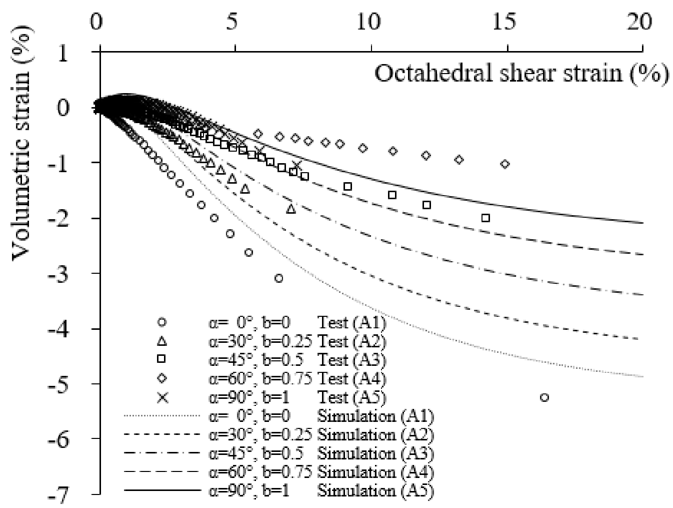

Figure 4.14: Volumetric strain against octahedral strain curves from series A (tests and simulations)

under different loading conditions. The test results clearly show that dilatancy of the specimens tends to decrease with the increase of b and α (from test A1 to A5). This deformation trend is correctly reproduced by the proposed stress-strain model, even though some differences are observed between the experimental and simulation results for each individual test. While the critical deformation state is obtained at large shear strains, the volumetric strains are slightly different from the experimental results. This deviation is attributed to the function given in Equation (4.27) defining the void ratios at the critical state. In addition, potential measurement error in the laboratory tests also attributes to the differences between modelling and experimental results.

Series B tests with $b = 0$ and Series C tests with $b = 1$

In these two series of tests, since the intermediate principal stress coefficient b is kept constant, the effect of α (i.e., the principal stress direction) can be obtained directly.

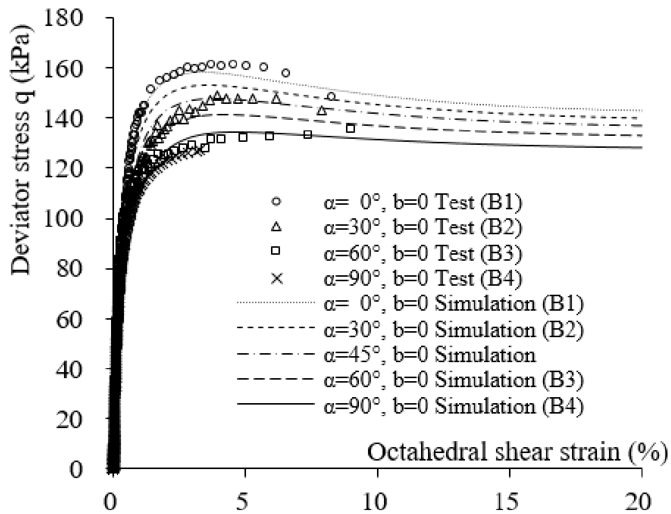

Figure 4.15: Stress-strain curves from series B (tests and simulations)

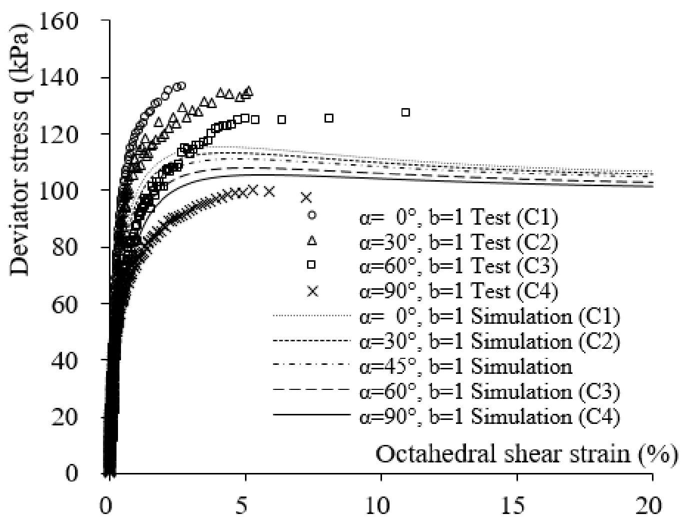

Figure 4.16: Stress-strain curves from series C (tests and simulations)

The stress-strain curves obtained from Series B and C tests are shown in Figures 4.15 and 4.16, respectively. In both series B ($b = 0$) and C ($b = 1$) tests, the peak deviator stress decreases as the principal stress direction makes a larger angle with the direction of the initial major principal direction of the material fabric. In particular, for tests with $b = 0$ in series B, the peak deviatoric stress drops from $148kPa$ at

$\alpha = 0°$ to $127kPa$ at $\alpha = 90°$; for tests with $b = 1$ in series C, the peak deviatoric stress decreases from $137kPa$ at $\alpha = 0°$ to $98kPa$ at $\alpha = 90°$. Figures 4.17 and 4.18 present the volumetric strain against the octahedral shear strain plots for tests in series B and C. Regardless of the $b-$value, there is a clear tendency that dilation is suppressed when α is increased. In other words, the specimen tends to dilate more when the major principal stress is perpendicular to the bedding plane.

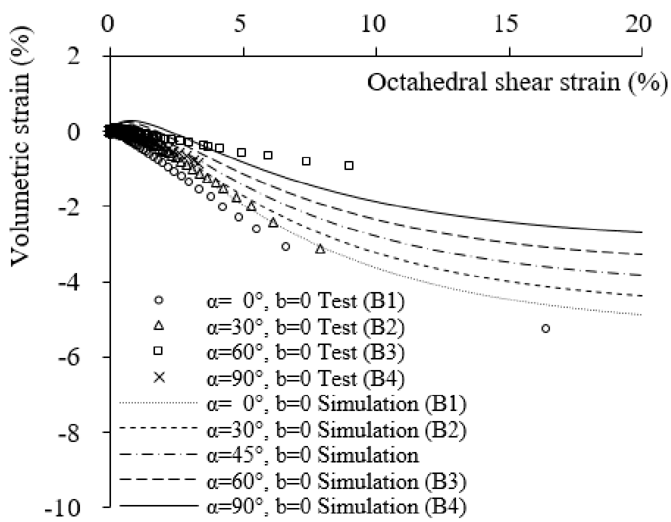

Figure 4.17: Volumetric strain against octahedral strain curves from series B (tests and simulations)

The comparisons between results from constitutive modelling and laboratory tests reveal that the proposed stress-strain model can reasonably reproduce the stress-strain responses in Series B tests (as can be observed in Figs. 4.15 and 4.17) with the influence of major principal stress direction on the peak stress states and dilatancy of the material. The critical states on both the stress-strain curves and the volume change curves are also captured. The model can satisfactorily describe the effect of principal stress direction on the stress-strain behaviour of granular soils, particularly when the intermediate principal stress coefficient is low (e.g., at $b = 0$). However,

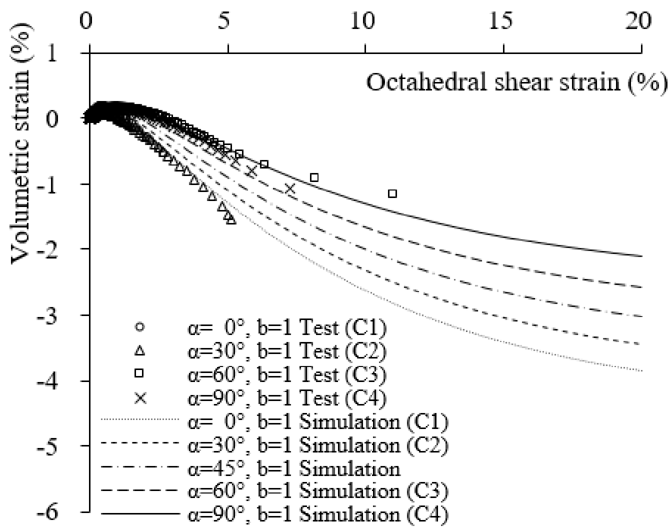

Figure 4.18: Volumetric strain against octahedral strain curves from series C (tests and simulations)

the model predictions for the stress-strain responses in series C tests ($b = 1$) have much lower peak deviatoric stresses than laboratory test results (Figure 4.16) while the volumetric strain responses are satisfactory (Figure 4.18). The inconsistency between the experimental and simulated stress-strain curves in Figure 4.16 could be attributed the non-uniformity of stress distribution in specimens during laboratory tests; as discussed in Section 3.1.3.

Figure 4.19b compares the peak failure surfaces on the octahedral plane predicted by the proposed model with the test results. The solid circulars represent the simulated failure stress states, and the four red lines represent the failure envelopes corresponding to $\alpha = 0°$, $\alpha = 30°$, $\alpha = 60°$ and $\alpha = 90°$, respectively, from the outside inwards. The proposed model successfully describes the influence of principal stress direction on the failure criterion as observed from laboratory tests. Similar experimental observations can be found in, for example, Pradhan *et al.* (1988) and Lade *et al.* (2013).

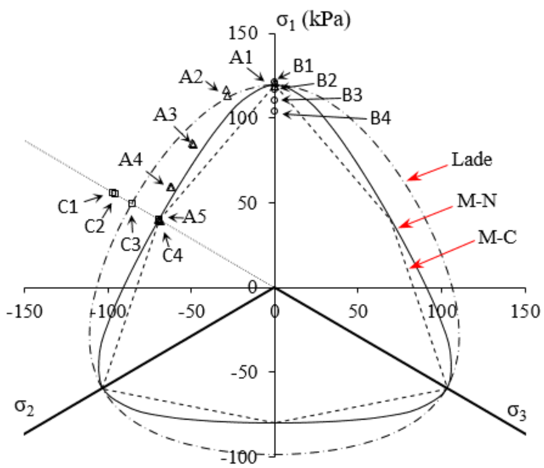

(a) failure states obtained from tests

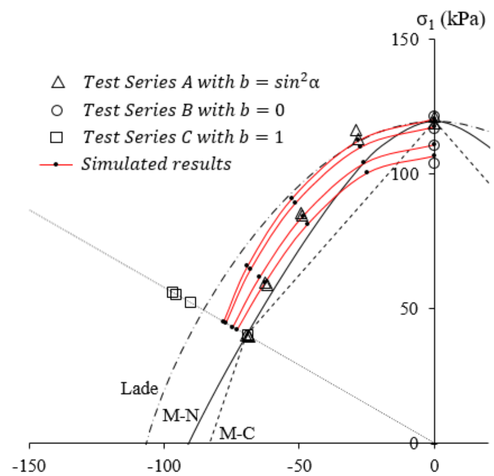

(b) simulated failure stresses

Figure 4.19: Failure states on the π-plane from series A, B and C (tests and simulations)

Figure 4.19a presents the peak stress states in test series A, B, and C on the octahedral plane. For comparison purposes, the benchmarked Lade-Duncan, Matsuoka-Nakai (M-N) and Mohr-Coulomb (M-C) failure surfaces are also plotted in the figure. Both the experimental data and the proposed model show that the Matsuoka-Nakai model is suitable for stress conditions in series A tests with $b = \sin^2 \alpha$. On the other hand, the Lade-Duncan model better matches the data of peak stress states in tests when α is relatively small; i.e., when the major principal stress direction marginally deviates from the direction of the major principal direction of fabric in Tests A1, B1 and C1 ($\alpha = 0°$), Test A2 ($\alpha = 30°$), Tests C2 and C3 ($\alpha = 30°$ and $45°$).

4.6 Conclusions

This chapter proposed a constitutive model for granular materials with the influence of fabric being properly considered. The fabric evolution law was developed based on the assumption that, during the loading process, the fabric state develops towards an ultimate state that is related to the critical state of deformation. A modified dilatancy formulation was proposed to address the effect of microstructure on shear-induced volume change characteristics in addition to the effect of density and stress level. A constitutive model was then developed based on the fabric evolution law and the fabric-dependent dilatancy formulation within the framework of elasto-plasticity. After the parameters in the model were calibrated using experimental results of hollow cylinder apparatus tests with $b = sin^2\alpha$, the model performance was verified with laboratory test results. By comparing the simulation results with the test results, the model was found to be capable of reflecting both directional and stress path dependency of granular material behaviours. Furthermore, the model's capacity of describing the peak deviator stresses was demonstrated by comparing with test results on the π-plane.

Chapter 5

Constitutive modelling of granular material behaviour under cyclic loading

5.1 Introduction

The constitutive models for cyclic behaviour of granular soils have been developed in two distinct directions, namely (a) phenomenological models based on continuum mechanics and the theory of plasticity, and (b) micromechanics-based models.

Among the plasticity based models, along with the kinematic hardening rules, the bounding surface (Dafalias and Popov, 1977; Dafalias, 1986b; McDowell, 1985; Ohno and Kachi, 1986; Bardet, 1986; Ellyin, 1989; Moosbrugger and McDowell, 1990) is probably the most popular concept adopted. But sometimes a bounding surface plasticity model may require numerous material parameters often lacking explicit physical meanings. The hypoplasticity models (Kolymbas, 1991; Wu *et al.*, 1996;

von Wolffersdorff, 1996; Wichtmann *et al.*, 2004; Niemunis *et al.*, 2005) are another class of models that conveniently describe geomaterial behaviour. Hypoplasticity is attractive for the development of stress-strain models in the cyclic regime, since it does not need to introduce a yield surface, which is often difficult to define for geomaterials. However, the lack of physical meaning of material parameters in the models and their determination greatly limit the application of this class of models.

The stress-strain model for granular material can also be developed based on micromechanical analysis. In this approach, the interaction of soil grains at the particle level is described by some simple contact laws, either linear or nonlinear. With the help of the principle of homogenization, the interaction forces and the relative displacements at particle contacts can be related to the average stresses and strain of a representative element volume (REV) (Chang and Hicher, 2005; Nicot *et al.*, 2005; Andrade and Tu, 2009). The spatial arrangement of particles and hence the internal structure (or fabric), as well as the effect of particle interaction can be taken into account, by introducing the distribution of contact normal and contact forces. Dilatancy is the natural consequence of internal constraints when particles rearrange themselves during deformation. The advantages of the micromechanics based stress-strain model include the relatively easy characterization of fabric and its evolution. In addition, there is no need for yield surfaces or plastic potentials. However, it is difficult for this type of models to describe an engineering soil or boundary-valued problems.

Even though there are reasonably good models for granular materials subjected to monotonic loading, when these models are used for cyclic loading, second-order inaccuracy tends to accumulate which may no longer be acceptable, particularly when the change of principal stress directions are involved. This is mainly because of the complexity of dilatancy and fabric evolution under cyclic loading.

This chapter develops a constitutive model for the cyclic behaviour of granular materials by considering critical state, stress-dilatancy, and fabric changes. In particular, plastic flow during loading and unloading is governed by a modification of the hardening rule developed in Chapter 4 with state parameters describing pyknotropy, barotropy and anisotropy. The dilatancy formulation with embedded fabric and the concept of critical fabric surface are extended to compute shear-induced volume changes during unloading. The proposed model used the concept of hypoplasticity, where the strain rate was associated to the stress rate. Finally, simulations of drained sand behaviour in cyclic loading regime are presented to demonstrate the capabilities of the model.

5.2 A kinematic hardening plasticity model with fabric effect

5.2.1 Loading surface and hardening law

For granular materials, there is a small purely elastic regime enclosed by a yield surface during a loading process as shown in Figures 5.1 and 5.2. This elastic core moves together with the current stress state in the stress space. During cyclic loading, the yield surface experiences both expansion (isotropic hardening) and translation (kinematic hardening). The loading surface of the shear mechanism takes the same form as that proposed in Equation (4.26) for monotonic loading:

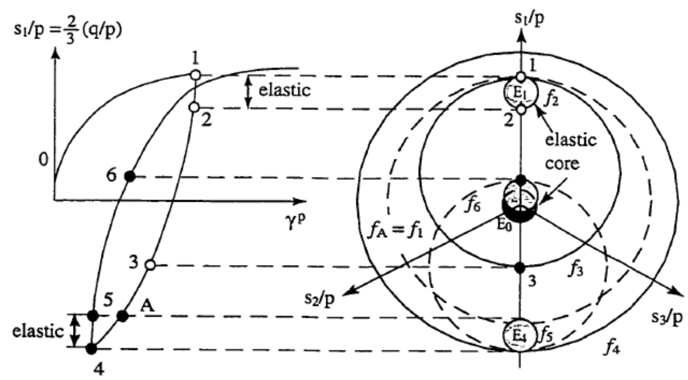

Figure 5.1: Evolution of loading and yield surfaces in cyclic loading (Guo 2000)

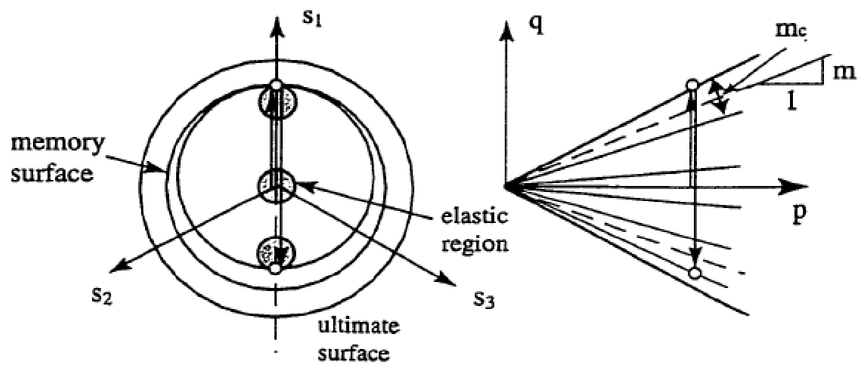

Figure 5.2: Mobilization of friction angle during initial loading and unloading (Guo 2000)

$$f_s = q - \bar{\eta}_m(\theta)p = q - \frac{\bar{\varepsilon}_q^p}{a + \bar{\varepsilon}_q^p}\left(\frac{e}{e_{cr}}\right)^{-\beta}\bar{\eta}_{cv}(\theta)p = 0 \tag{5.1}$$

in which $\bar{\eta}_m$ is the modified mobilized stress ratio and $\bar{\eta}_{cv}$ is its counterpart at the critical state which are defined as

$$\bar{\eta}_m = \eta_m(\theta) - C\eta^\star \tag{5.2}$$

$$\bar{\eta}_{cv} = \eta_{cv}(\theta) - C\eta^\star \tag{5.3}$$

where η_m is the current mobilized stress ratio, $\eta^\star$ is the stress ratio at the onset of loading (including initial loading and reloading) or unloading, and η_{cv} is the critical stress ratio corresponding to the current Lode angle. C is the loading index with $C = 1$ at loading/reloading and $C = -1$ at unloading. The stress surface and the fabric surface at the critical state are the same as those defined for monotonic loading in Chapter 4. To reflect the effect of deformation history as well as the differences between loading and unloading processes, the equivalent plastic shear strain $\bar{\varepsilon}_q^p$ in equation (5.1) is defined as

$$\bar{\varepsilon}_q^p = \varepsilon_q^p - C\varepsilon_{q(m)}^p \tag{5.4}$$

with $\varepsilon_{q(m)}^p$ being the plastic shear strain at the onset of unloading or reloading.

As for the deformation due to consolidation mechanism, a vertical cut-off surface similar to Equation (4.21) is used:

$$f_c = p - p_c$$

where p_c refers to the consolidation pressure as obtained from the virgin compression line at a given void ratio which reflects both hydrostatic and shear-induced volume changes. In this sense, it is clear that both the evolutions of the cap and shear yield surfaces are coupled.

5.2.2 Dilatancy formulation and plastic potential under cyclic loading

Similar to monotonic loading, a plastic potential function is needed to determine the plastic flow direction. The plastic potential function g_s is driven by the modified

Rowe's stress dilatancy formulation. In the $p - q$ space, the plastic potential g_s has the same functional form as Equation (4.29):

$$g_s = q - D(\theta)p$$

in which $D(\theta)$ is the dilatacy factor.

For the dilatancy formulation in cyclic loading regime, the parameter A in Equation (4.19) is modified to A' to reflect the change in the direction of stress increment. A' is defined as

$$A' = n_{ij}^F n_{ij}^{\dot{s}} \tag{5.5}$$

where n_{ij}^F and $n_{ij}^{\dot{s}}$ are unit-norm tensor-valued directions of the deviatoric fabric tensor and deviatoric incremental stress tensor defined as

$$n_{ij}^F = \frac{F_{ij}}{\sqrt{F_{kl}F_{kl}}}, \qquad n_{ij}^s = \frac{\dot{s}_{ij}}{\sqrt{\dot{s}_{kl}\dot{s}_{kl}}}$$

respectively. The dilatancy formulation in cyclic loading is then expressed as

$$D = -\frac{\dot{\varepsilon}_{v(s)}^p}{\dot{\varepsilon}_{q(s)}^p} = d[\eta - \bar{\eta}_{cv}(\theta)e^{m\zeta'}] \tag{5.6}$$

$$\zeta' = (e - e_{cr}) + k[1 - (\frac{s_{ij}F_{ij}}{K_c})A'] \tag{5.7}$$

where d, m, k are all positive material constants. $\bar{\eta}_{cv}$ is a function of the Lode angle, and is calculated from Equation (5.3). $\dot{\varepsilon}_{q(s)}^p$ is defined as $\dot{\varepsilon}_{q(s)}^p = \frac{2}{3}\sqrt{3J_2^{(\dot{\varepsilon}^p)}}$, where $J_2^{(\dot{\varepsilon}^p)}$ is the second deviator invariant of the incremental plastic strain $\dot{\varepsilon}^p$. Since A' reflects the non-coaxility angle between F_{ij} and $\dot{s}_{ij}$, change from loading to unloading will result in different rate of dilatancy, as shown in Equation 5.7.

5.2.3 Evolution of fabric during cyclic loading

Similar to monotonic loading, the evolution of fabric under cyclic loading depends on both the current stress and fabric states as well as the projections on the critical stress and fabric surfaces. More specifically, the fabric evolution law in cyclic loading is written as

$$\dot{F}_{ij} = \frac{\chi \dot{\eta}}{\left\| \eta_{kl}^{(cv)} - \eta_{kl} \right\|} (F_{ij}^{(cv)} - F_{ij}) \tag{5.8}$$

where F_{ij} and $F_{ij}^{(cv)}$ are the current and critical state deviatoric fabric tensors, η_{kl} and $\eta_{kl}^{(cv)}$ are the current and critical state deviatoric stress ratio tensors. $F_{ij}^{(cv)}$ and $\eta_{kl}^{(cv)}$ are determined using a linear projection rule with the same Lode angle $\theta_{\dot{\sigma}}$. χ is a constant that controls the rate of fabric change with variation of stresses during unloading. $\chi = 0.5$ is chosen in this study.

Let $\mu_{ij}^F = F_{ij}^{(cv)} - F_{ij}$ with $\mu_F = \left\|\mu_{ij}^F\right\|$, and $\mu_\sigma = \left\|\eta_{kl}^{(cv)} - \eta_{kl}\right\|$. Then the ratio μ_F/μ_σ reflects the rate of fabric change in Equation (5.8). μ_F and μ_σ are graphically expressed in Figure 5.3 during loading, unloading, reloading, as well as arbitrary loading conditions. "Stress state*" and "fabric state*" in the figures represent the stress and fabric state at the onset of unloading or reloading respectively. During unloading, the ratio μ_F/μ_σ is evidently larger than that in initial loading, thus the changing rate of fabric increases significantly upon unloading. Figure 5.3c shows μ_F and μ_σ during reloading, where the incremental stress is applied with the major principal incremental stress perpendicular to the direction of the major principal fabric component. Figure 5.3d shows μ_F and μ_σ during an arbitrary loading, where the initial fabric states can be anywhere within the fabric surface. The ultimate stress and fabric states are both determined using the Lode angle of the incremental stress tensor. A linear projection rule is used here together with the concept of ultimate fabric surface.

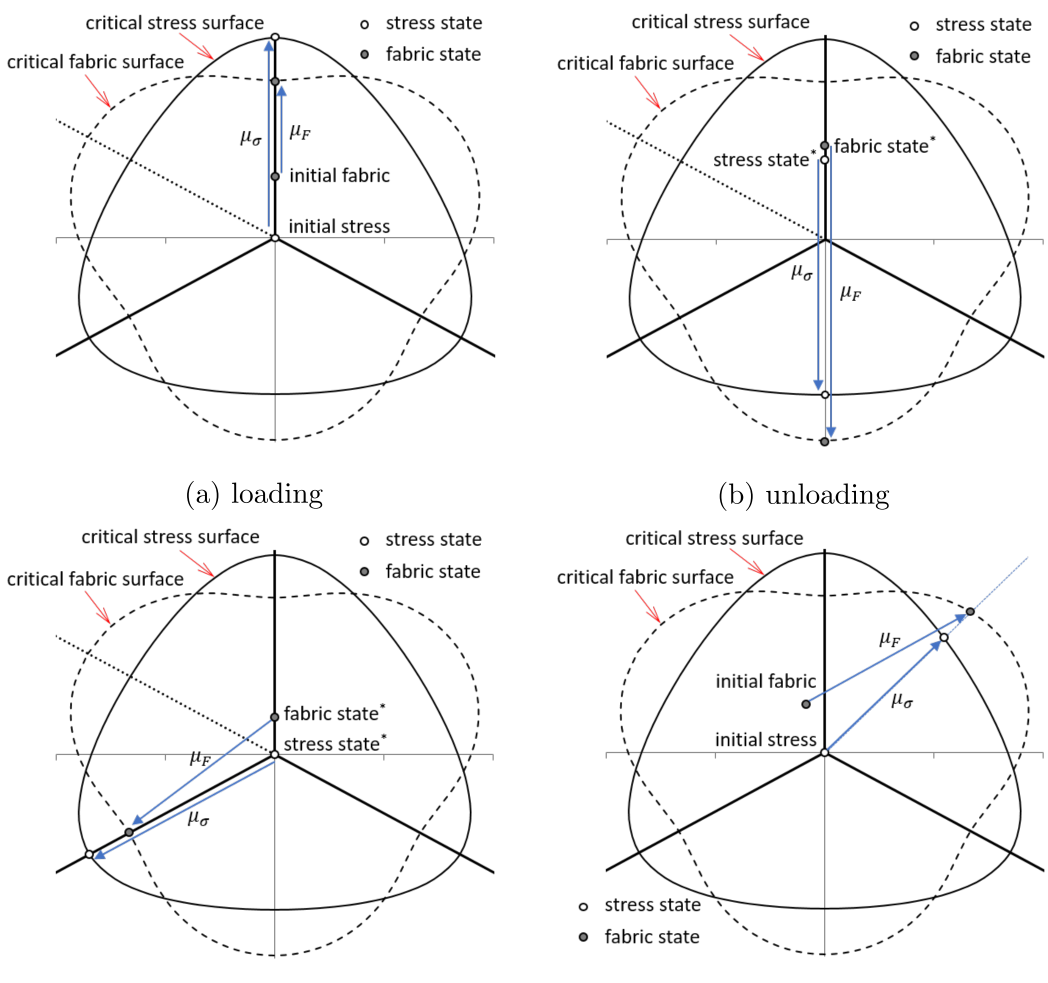

(a) loading (b) unloading

(c) reloading (d) arbitrary loading

Figure 5.3: Variation of μ_F and μ_σ for loading, unloading, reloading, and arbitrary stress paths

5.2.4 Incremental stress-strain relation

The explicit form of the incremental stress-strain relation for cyclic loading uses the general form as was given in Equation (4.37).

$$\dot{\sigma}_{ij} = D^{ep}_{ijkl}\dot{\varepsilon}_{kl}$$

with

$$D^{ep}_{ijkl} = D^{e}_{ijkl} - \frac{1}{H}(D^{e}_{ijpq}\frac{\partial g_s}{\partial \sigma_{pq}}\frac{\partial f_s}{\partial \sigma_{rs}}D^{e}_{rskl})$$

in which H, $\frac{\partial g_s}{\partial \sigma_{pq}}$, and $\frac{\partial f_s}{\partial \sigma_{rs}}$ were calculated as follows:

$$H = \frac{\partial f_s}{\partial \sigma_{pq}}D^{e}_{pqrs}\frac{\partial g_s}{\partial \sigma_{rs}} - \frac{\partial f_s}{\partial \bar{\varepsilon}^p_q}\frac{\partial g_s}{\partial q} + (1+e_0)\frac{\partial f_s}{\partial e}\frac{\partial g_s}{\partial p}$$

$$\frac{\partial f_s}{\partial \sigma_{ij}} = \frac{\partial q}{\partial \sigma_{ij}} - \frac{\bar{\varepsilon}^p_q}{a+\bar{\varepsilon}^p_q}(\frac{e}{e_{cr}})^{-\beta}\bar{\eta}_{cv}(\theta)\frac{\partial p}{\partial \sigma_{ij}} - \frac{\bar{\varepsilon}^p_q}{a+\bar{\varepsilon}^p_q}(\frac{e}{e_{cr}})^{-\beta}p\frac{\partial \bar{\eta}_{cv}(\theta)}{\partial \theta}\frac{\partial \theta}{\partial \sigma_{ij}}$$

$$\frac{\partial g_s}{\partial \sigma_{ij}} = \frac{\partial q}{\partial \sigma_{ij}} - D(\theta)\frac{\partial p}{\partial \sigma_{ij}} - p\frac{\partial D(\theta)}{\partial \theta}\frac{\partial \theta}{\partial \sigma_{ij}} - p\frac{\partial D(\theta)}{\partial \zeta'}\frac{\partial \zeta'}{\partial \sigma_{ij}}$$

with

$$D^{e}_{ijkl} = \frac{vE}{(1-2v)(1+v)}\delta_{ij}\delta_{kl} + \frac{E}{2(1+v)}(\delta_{ik}\delta_{jl}+\delta_{il}\delta_{jk})$$

$$\frac{\partial q}{\partial \sigma_{ij}} = \frac{3s_{ij}}{2q} \qquad \frac{\partial p}{\partial \sigma_{ij}} = \frac{1}{3}\delta_{ij}$$

$$\frac{\partial \theta}{\partial \sigma_{ij}} = \frac{\sqrt{3}}{2J_2^{3/2}cos3\theta}(\frac{3J_3}{2J_2}s_{ij} + \frac{2}{3}\delta_{ij}J_2 - s_{ik}s_{kj})$$

$$\frac{\partial \bar{\eta}_{cv}(\theta)}{\partial \theta} = \frac{\partial \eta_{cv}(\theta)}{\partial \theta} = \frac{3\omega cos3\theta cos(\frac{\pi - sin^{-1}(\omega sin3\theta)}{3})}{\sqrt{2}\lambda\sqrt{1-(\omega sin3\theta)^2}sin^2(\frac{\pi - sin^{-1}(\omega sin3\theta)}{3})}$$

$$\frac{\partial D(\theta)}{\partial \theta} = \frac{-3d\omega e^{m\zeta'}cos3\theta cos(\frac{\pi - sin^{-1}(\omega sin3\theta)}{3})}{\sqrt{2}\lambda\sqrt{1-(\omega sin3\theta)^2}sin^2(\frac{\pi - sin^{-1}(\omega sin3\theta)}{3})}$$

$$\frac{\partial D(\theta)}{\partial \zeta'} = -dm\eta_{cv}(\theta)e^{m\zeta'} \qquad \frac{\partial \zeta'}{\partial \sigma_{ij}} = -\frac{kA'}{K_c}F_{ij}$$

5.3 Constitutive modelling of granular soil behaviour under different cyclic loading conditions

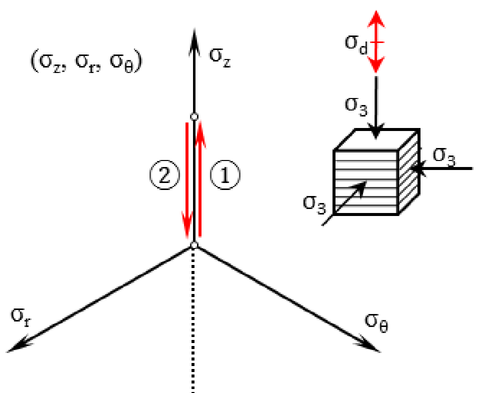

(a) Mode 1

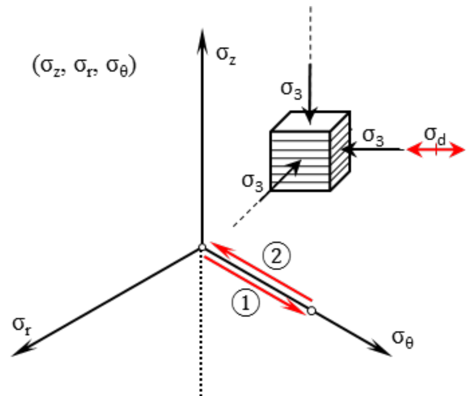

(b) Mode 2

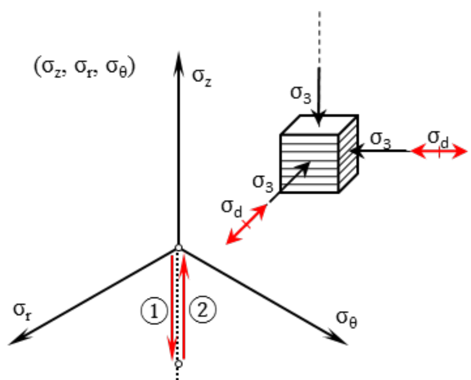

(c) Mode 3

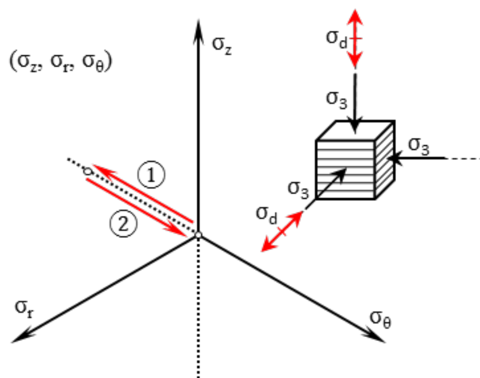

(d) Mode 4

Figure 5.4: Stress paths and soil elements demonstration

The performance of the proposed stress-strain model is demonstrated via simulating the behaviours of granular material in seven cyclic loading modes shown in Figure 5.4. The specimens were all consolidated initially under a hydrostatic confining pressure of $100kPa$. The confining pressure was kept constant throughout the

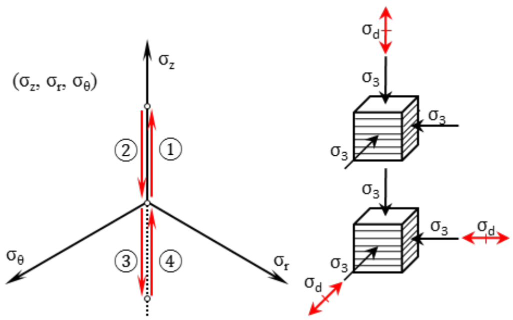

(e) Mode 5

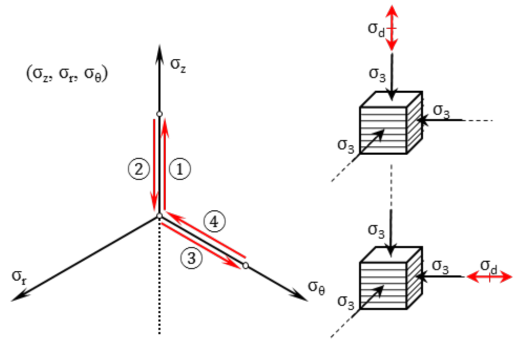

(f) Mode 6

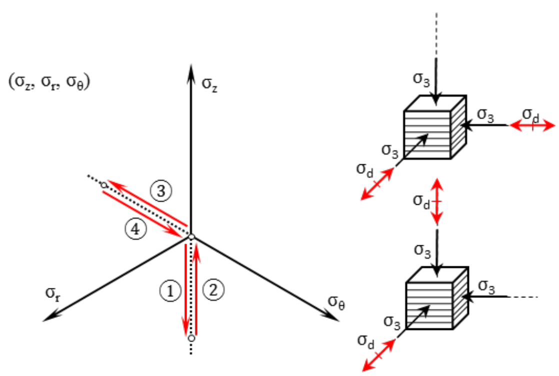

(g) Mode 7

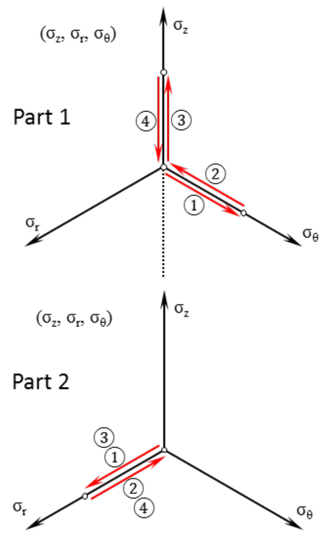

(h) Mode 7 decomposed

Figure 5.4: Stress paths and soil elements demonstration (Cont.)

subsequent shearing tests. The first four loading modes were one-way cyclic loading and the other three represented different two-way cyclic loading conditions. Results from loadings of the seven loading modes can demonstrate the capability of the proposed constitutive model in describing the effect of stress states and fabric on soil behaviour under cyclic loading.

Figures 5.4a to 5.4g present the stress paths and the corresponding stress states on soil elements for the seven select modes. For convenience, we hereby define $\alpha_{d\sigma}$ as the angle between the directions of the major principal incremental stress and the major principal fabric component, and $\theta_{d\sigma}$ is the Lode angle of the incremental deviatoric stress tensor. As shown in previous chapters, the Lode angle of the stress tensor can be related to the intermediate principal stress coefficient b that is defined as $b = (\sigma_2 - \sigma_3)/(\sigma_1 - \sigma_3)$. The specific loading conditions in different loading modes are as follows:

Modes 1 and 2 represent conventional one-way cyclic triaxial compression test with $b = 0$. In Mode 1, the cyclic stress was applied on the bedding plane. During the loading process, the major principal incremental stress was perpendicular to the bedding plane, with $\alpha_{d\sigma} = 0°$ and $\theta_{d\sigma} = 30°$. During the unloading process, however, a jump in the direction of the major principal incremental stress occurred (from the vertical to the horizontal) with $\alpha_{d\sigma} = 90°$ and $\theta_{d\sigma} = -30°$; as demonstrated in Figures 5.4a. However, there was no change in the principal stress directions. For example, the direction of major principal stress σ_1 was always perpendicular to the bedding plane, in both the loading and unloading processes. In Mode 2 loading, the cyclic stress was applied in the direction parallel to the bedding plane. Similar to Mode 1, the principal incremental stress direction jumped by 90° (from the horizontal to the vertical) and the principal stress directions did not change. Herein the bedding plane is considered to be horizontal, as in a cyclic triaxial compression test.

Modes 3 and 4 represent conventional one-way cyclic triaxial extension test with $b = 1$ corresponding to $\sigma_2 = \sigma_1$. As shown in Figure 5.4c, in Mode 3 loading, cyclic loading was applied in two orthogonal directions in the bedding plane. During a loading process, $\alpha_{d\sigma} = 90°$ and $\theta_{d\sigma} = -30°$. During the unloading process, however,

$\alpha_{d\sigma} = 0°$ and $\theta_{d\sigma} = 30°$ instead. The difference between Mode 4 and Mode 3 is that the cyclic loading was applied in two directions perpendicular and parallel to the bedding plane respectively, as shown in Figure 5.4d. In Mode 4 loading, we have $\alpha_{d\sigma_1} = 90°$, $\alpha_{d\sigma_2} = 0°$, and $\theta = -30°$ during loading while $\alpha_{d\sigma_1} = 0°$, $\alpha_{d\sigma_2} = 90°$ and $\theta = 30°$ during unloading. Similar to Modes 1 and 2 loading, a jump of principal incremental stress directions also occured in Modes 3 and 4 while the principal stress directions were fixed during the loading and unloading processes.

Mode 5 simulates the conventional cyclic triaxial compression test, which was a combination of Modes 1 and 3. In terms of the loading direction relative to the direction of the major principal fabric component, Mode 5 loading can be divided into four stages: Stage (1) corresponded to loading with $\alpha_{d\sigma} = 0°$ and $\theta_{d\sigma} = 30°$, followed by unloading in stage (2) in which $\alpha_{d\sigma} = 90°$ and $\theta_{d\sigma} = -30°$. In these two stages, the major principal stress direction was perpendicular to the bedding plane. In stage (3), loading continued with $\alpha_{d\sigma} = 90°$ and $\theta_{d\sigma} = -30°$. In this stage, the major principal directions of the stress and the incremental stress tensors were both parallel to the bedding plane; as demonstrated in Figure 5.4e. Finally, stage (4) took place under $\alpha_{d\sigma} = 0°$ and $\theta_{d\sigma} = 30°$ until the deviator stress reached zero. Different from Modes 1 to 4, Mode 5 cyclic loading involved a jump in both the major principal directions of the stress and the incremental stress tensors.

Mode 6 simulates a modified conventional one-way cyclic triaxial test in which $b = 0$ using the cyclic hollow cylinder apparatus. This mode of loading was a combination of Modes 1 and 2. In particular, the cyclic stress was applied to the specimen in the directions perpendicular and parallel to the bedding plane alternatively, as illustrated in Figure 5.4f. The cyclic loading process can be divided into four stages: stage (1) with $\alpha_{d\sigma} = 0°$ and $\theta_{d\sigma} = 30°$, followed by stage (2) with $\alpha_{d\sigma} = 90°$ and $\theta_{d\sigma} = -30°$. In these two stages, the major principal stress was perpendicular to the bedding plane. In stages 3 and 4, the major principal stress direction rotated 90° to the horizontal, with $\alpha_{d\sigma} = 90°$, $\theta_{d\sigma} = 30°$ in stage 3 and $\alpha_{d\sigma} = 0°$, $\theta_{d\sigma} = -30°$ in stage (4).

Mode 7 is a modified conventional one-way cyclic triaxial extension test in which $b = 1$ (i.e., $\sigma_2 = \sigma_1$). It can be considered as a combination of Modes 3 and 4. The four stages of Mode 7 are: stage (1) in which $\alpha_{d\sigma} = 90°$ and $\theta_{d\sigma} = -30°$; stage (2) with $\alpha_{d\sigma} = 0°$ and $\theta_{d\sigma} = 30°$; stage (3) with $\alpha_{d\sigma_1} = 90°$, $\alpha_{d\sigma_2} = 0°$, and $\theta_{d\sigma} = -30°$ and stage (4) in which $\alpha_{d\sigma_1} = 0°$, $\alpha_{d\sigma_2} = 90°$, and $\theta_{d\sigma} = 30°$. It is noted that Mode 7 is to Modes 3 and 4 as Mode 6 is to Modes 1 and 2. Similar to Mode 6, in Mode 7, the major principal stress direction rotated from the vertical to the horizonal, as shown in Figure 5.4g.

5.4 Results and discussions

Simulations for the responses of a granular material in the seven loading modes were carried out at select cyclic shear strain amplitudes, by mimicking the stress conditions in cyclic tests using hollow cylinder apparatus. The material constants were the same as those used in simulations for monotonic loading in Chapter 4 (see Table 4.2). Two series of simulations were performed. The first series of simulations intended to investigate the influence of cyclic strain amplitudes on the responses of the granular material with the initial void ratio and the initial degree of anisotropy being $e_0 = 0.59$

and $\Omega = (2/3)\sqrt{3J_2^F} = 0.2$, respectively. The material was assumed to be cross-anisotropy with an initial deviatoric fabric tensor

$$F_{ij} = \begin{bmatrix} 0.02 & 0 & 0 \\ 0 & -0.01 & 0 \\ 0 & 0 & -0.01 \end{bmatrix}$$

The second series was a parametric study for the effect of the initial void ratio, the initial degree of anisotropy and the variation of loading modes on the cyclic behaviour of granular materials.

In the figures of this section, the deviator stress is defined as $q^\star = \pm\sqrt{3J_2}$. Since all tests were performed at $b = 0$ or $b = 1$, $q^\star$ can be alternatively expressed as $q^\star = \sigma_z - \sigma_r$. As a result, $q^\star$ is referred as positive when $\sigma_a = \sigma_1$ (the major principal stress) and negative otherwise. A similar sign convention is adopted for the measure of shear strain $\gamma^\star$, which is defined as $\gamma^\star = \pm\sqrt{3J_2^\varepsilon}$ with $\gamma^\star$ being positive when $|\varepsilon_z| = \max(|\varepsilon_z|, |\varepsilon_r|, |\varepsilon_\theta|)$ and negetive otherwise. It should be noted, however, the strains may not be axisymmetric even for axisymmetric stress state owing to the inherent anisotropy of the material.

5.4.1 Effect of shear strain amplitude

(1) Stress-strain responses and volume change characteristics

Figure 5.5b presents the stress-strain responses in Mode 1 one-way cyclic loading tests at $b = 0$, $\theta_{d\sigma} = 30°$ and $\alpha_{d\sigma} = 0°$. For low strain amplitude (e.g., $\Delta\gamma^\star = 0.1\%$), the cyclic stress-strain curve was mostly linear. With the increase of shear strain amplitude, the hysteresis loops were generated. In each strain cycle, net volume compaction took place, as shown in the volumetric strain curves in Figures 5.5c and 5.5d. With an increasing number of strain cycles, the specimen became denser so that dilatancy built up progressively, which resulted in an escalation in the deviatoric stress. With increasing strain cycles, an ultimate stable deformation state was reached, corresponding to a shakedown condition with no further change in volume as well as the stress-strain response.

Figures 5.6b presents the stress-strain responses in Mode 2 one-way cyclic loading test at $b = 0$, $\theta_{d\sigma} = 30°$ and $\alpha_{d\sigma} = 90°$. In this case, the cyclic stress σ_d was applied in a direction parallel to the bedding plane. In general, the stress-strain responses and the volumetric strain curves in Mode 2 loading had the same trend of variation as those in Mode 1 test. Owing to the inherent anisotropy and the different loading directions (as reflected by $\alpha_{d\sigma}$), for the same strain amplitude, the specimen in Mode 2 cyclic loading showed lower shear resistance. For example, at the strain amplitude $\Delta\gamma^{\star} = 1\%$, the values of $|q^{\star}|_{\max}$ were $95.4kPa$ and $90.8kPa$ in Mode 1 and Mode 2 tests, respectively. The loading direction also affected the volume change responses. For the same cyclic strain amplitude, cyclic shearing induced more densification of the specimen in Mode 2 test than in Mode 1 test. For example, at the strain amplitude $\Delta\gamma^{\star} = 1\%$, the accumulative volumetric strain ε_v after 50 cycles of loading in Mode 1 was 0.44%, which was lower than $\varepsilon_v = 0.49\%$ in the Mode 2 test. It should be noted that a larger densification did not necessarily yield a higher shear resistance when the cyclic loading direction was different owing to the effect of internal structure. Similarly, for cyclic loading with the strain amplitude $\Delta\gamma^{\star} = 5\%$, the accumulative volumetric strains were 0.05% and 0.18% in modes 1 and 2 tests at N=50, respectively.

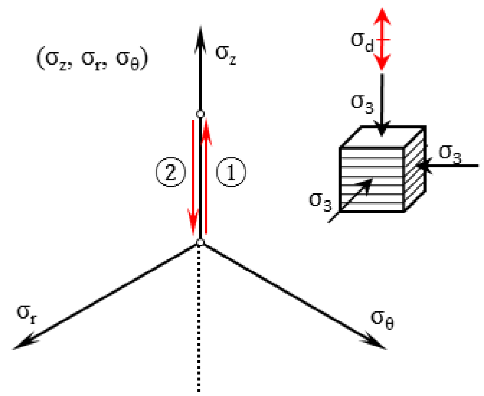

(a) Cyclic stress path of Mode 1

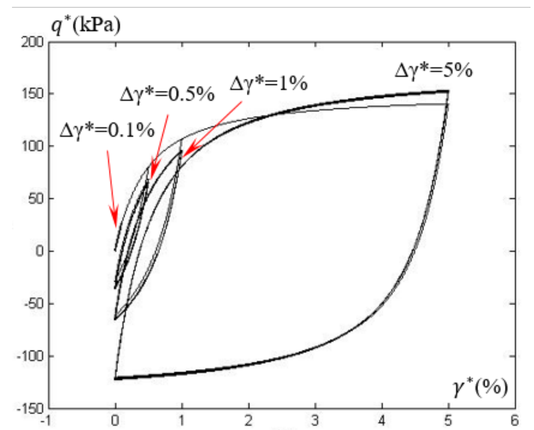

(b) Stress-strain curves

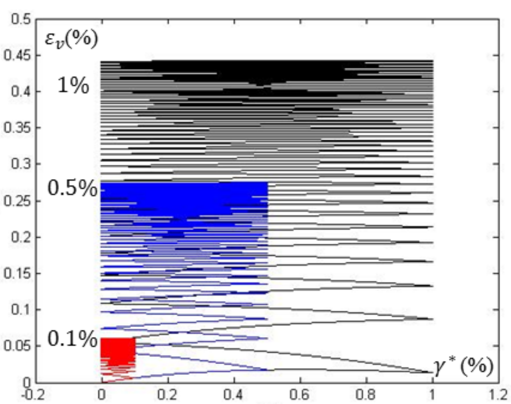

(c) Strain amplitudes: 0.1%, 0.5%, 1%

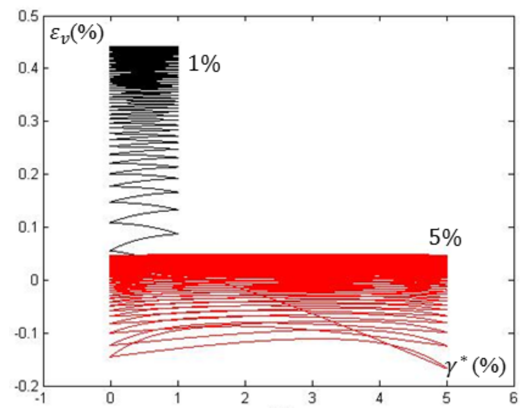

(d) Strain amplitudes: 1%, 5%

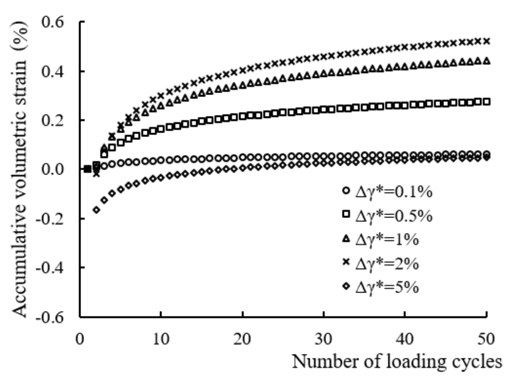

(e) Accumulative volumetric strains at different strain amplitudes

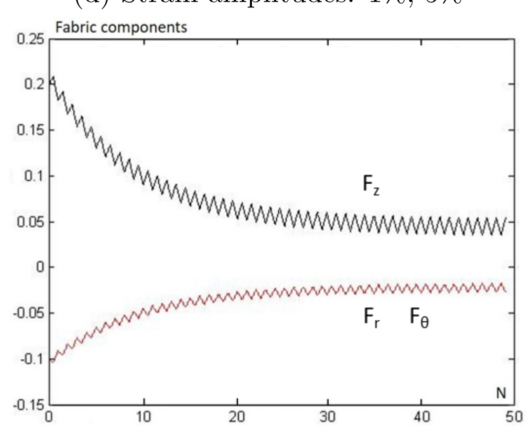

(f) Fabric evolution ($\Delta\gamma^{\star} = 0.1\%$)

Figure 5.5: Simulation results at strain amplitudes of 0.1%, 0.5%, 1% and 5% (Mode 1)

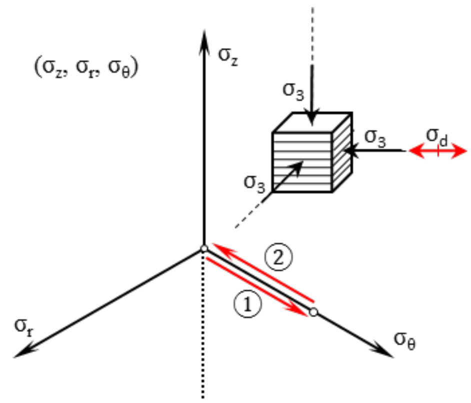

(a) Cyclic stress path of Mode 2

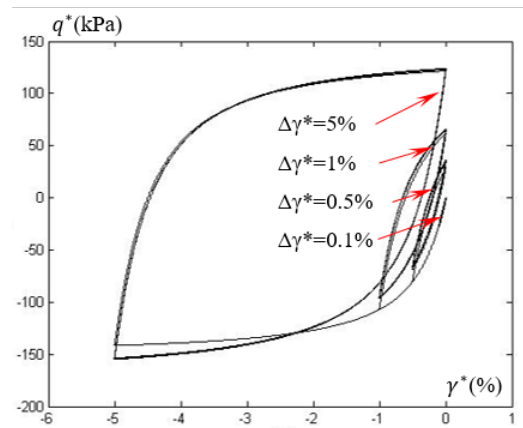

(b) Stress-strain curves

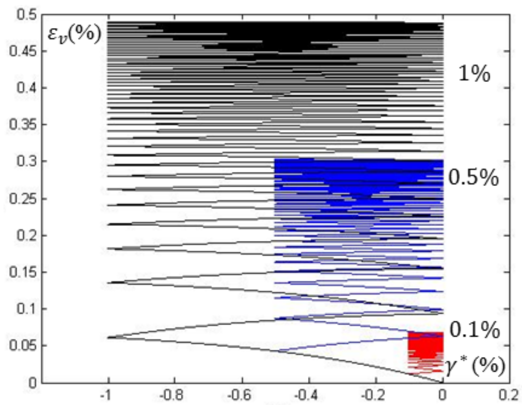

(c) Strain amplitudes: 0.1%, 0.5%, 1%

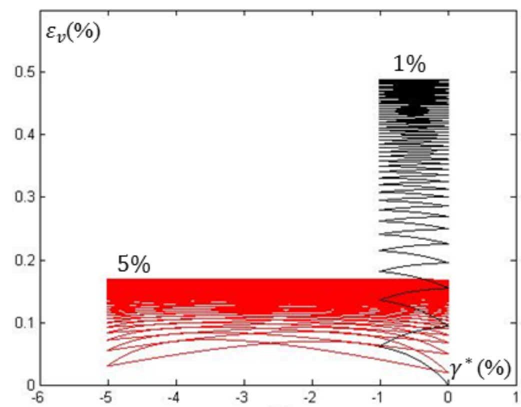

(d) Strain amplitudes: 1%, 5%

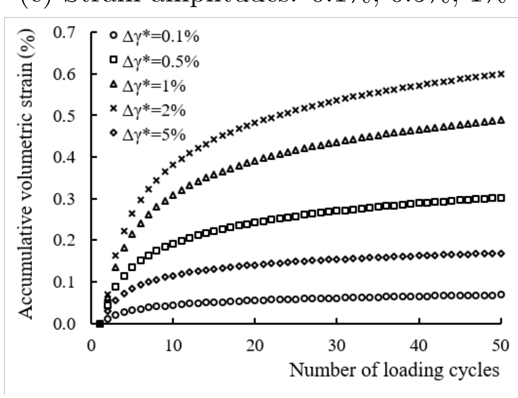

(e) Accumulative volumetric strains at different strain amplitudes

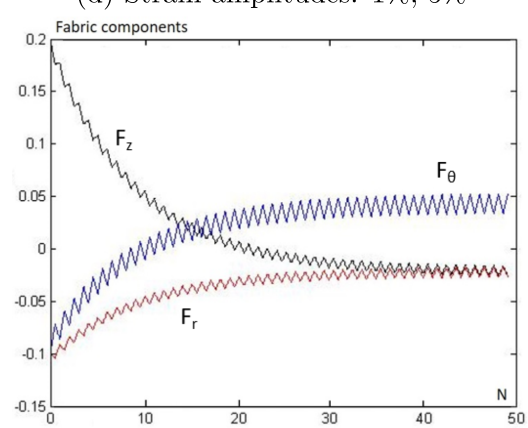

(f) Fabric evolution ($\Delta\gamma^\star = 0.1\%$)

Figure 5.6: Simulation results at strain amplitudes of 0.1%, 0.5%, 1% and 5% (Mode 2)

It should be noted that the deformation of the specimen in Mode 2 loading may not be axisymmetric when considering the evolution of induced fabric.

We next compare the material responses in Modes 2 and 3 tests. The difference between these two tests is whether cyclic loading was applied in one or two directions within the bedding plane while the axial stress was kept as the minimum principal stress (see Figure 5.4). Compared with Mode 2 loading, the specimen subjected to Mode 3 cyclic loading had noticeably larger volumetric compaction at the same strain amplitudes, as shown in Figures 5.6c-5.6d and Figures 5.7c-5.7d. For example, for the strain amplitude $\Delta\gamma^{\star} = 1\%$, the value of ε_v was 0.49% after 50 cycles of loading in Mode 2 and was $\varepsilon_v = 1.59\%$ after 50 strain cycles in Mode 3. The mobilized shear resistance in Mode 3 cyclic loading for a given strain amplitude was much lower than that in Mode 2 loading under the same conditions. For example, at $\Delta\gamma^{\star} = 1\%$, the value of $|q^{\star}|_{\max}$ was $90.8kPa$ in Mode 2, comparing with $|q^{\star}|_{\max} = 69.2kPa$ in Mode 3 at the same strain amplitude. The different behaviours in Modes 2 and 3 loading were related to the fabric change induced by different cyclic loading modes, either in one direction or two directions parallel to the bedding plane in Mode 2 and Mode 3, respectively. Regarding to the deformation pattern, different from Mode 2 loading, the deformation of the specimen in Mode 3 loading was axisymmetric.

Different from Mode 3 cyclic loading, in Mode 4 the specimen was subjected to cyclic loading in two directions that were parallel and perpendicular to the bedding plane, respectively. For the same cyclic strain amplitude, the specimen in Mode 4 had a little higher resistance to shearing than that in Mode 3 (see Figure 5.7b and Figure 5.8b). For example, the values of $|q^{\star}|_{\max}$ were $69.2kPa$ and $73.1kPa$ at $\Delta\gamma^{\star} = 1\%$ in Mode 3 and Mode 4, respectively. However, the corresponding

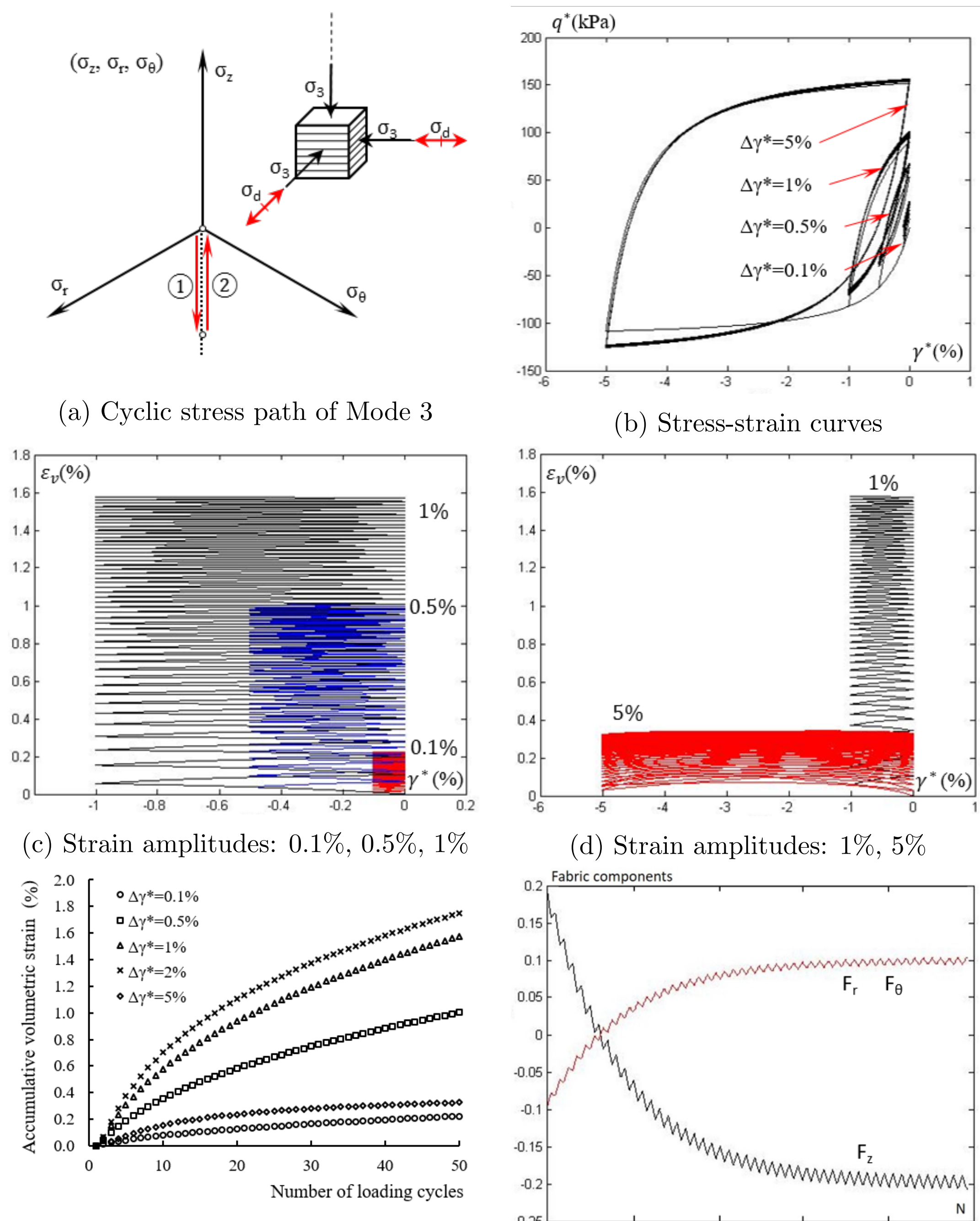

(a) Cyclic stress path of Mode 3

(b) Stress-strain curves

(c) Strain amplitudes: 0.1%, 0.5%, 1%

(d) Strain amplitudes: 1%, 5%

(e) Accumulative volumetric strains at different strain amplitudes

(f) Fabric evolution ($\Delta\gamma^{\star} = 0.1\%$)

Figure 5.7: Simulation results at strain amplitudes of 0.1%, 0.5%, 1% and 5% (Mode 3)

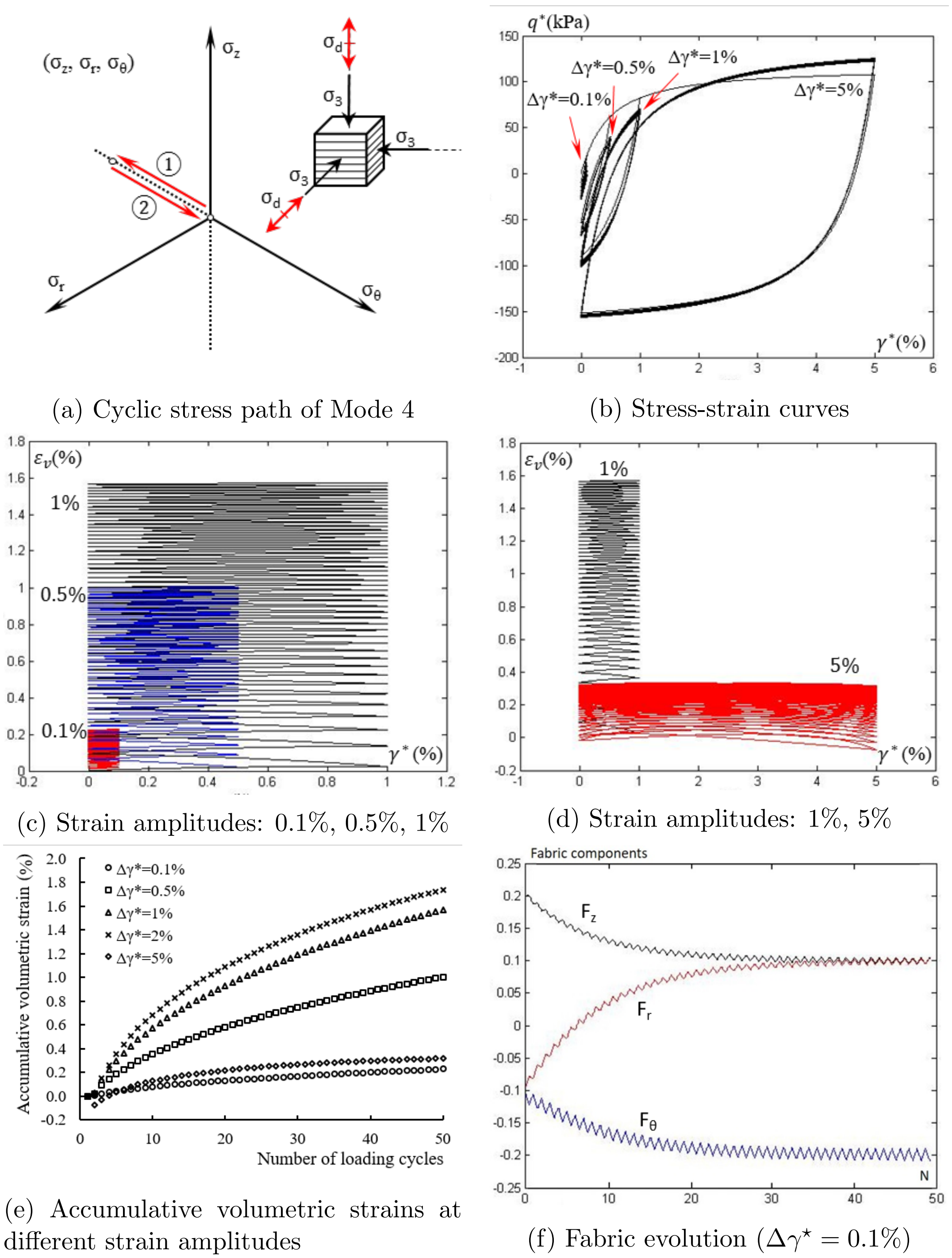

Figure 5.8: Simulation results at strain amplitudes of 0.1%, 0.5%, 1% and 5% (Mode 4)

accumulative volumetric compactions in these two modes of cyclic loading were almost identical (see Figure 5.7c-5.7d and Figure 5.8c-5.8d). When compared with shear-induced volume changes in the cyclic loading of Modes 1 and 2, the difference of volumetric compaction between Mode 3 and Mode 4 loading was much smaller than that between Mode 1 and Mode 2 cyclic loadings. It is noted that in Modes 3 and 4 loadings in which $\sigma_2 = \sigma_1$, one of the major principal incremental stress was always parallel to the bedding plane, while the other major principal incremental stress directions were $\alpha_{d\sigma} = 0°$ and $\alpha_{d\sigma} = 90°$, respectively. Recalling that the shear-induced volumetric compaction was more pronounced in Mode 2 than that in Model 1 in which the major principal incremental stress was perpendicular to the bedding plane. Therefore, it is likely that in Modes 3 and 4, the volume change characteristics were dominated by the principal incremental stress that was applied parallel to the bedding plane.

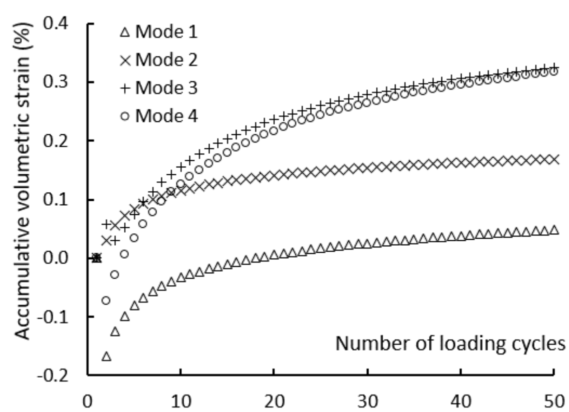

Figure 5.9: Accumulative volumetric strains from four one-way loading modes at $\Delta\gamma^{\star} = 5\%$

Figure 5.9 compares the evolution of accumulative volumetric strain with the number of cyclic strain cycles in different loading modes at the strain amplitude of

$\Delta\gamma^{\star} = 5\%$. In the first several strain cycles, dilation was observed in Mode 1 and Mode 4 loadings that both had cyclic stress applied perpendicular to the bedding plane. On the other hand, no accumulative dilation was observed in Modes 2 and 3 in which the cyclic loadings were all applied in the direction parallel to the bedding plane. The rates of accumulative volume compaction with respect to the number cyclic strain cycles in Mode 2 was higher than that in Mode 1. The results shown in Figure 5.9 confirmed that cyclic stresses in the bedding plane tended to induce more volumetric compaction and less dilation.

For the two-way cyclic loading modes, let us first examine the responses of specimen subjected to the cyclic loading of Mode 6. As illustrated in Figure 5.4f, in one strain cycle, the direction of $\alpha_{d\sigma}$ jumped from $0°$ to $90°$ when the direction of cyclic stress changed from the direction perpendicular to parallel to the bedding plane.

The stress-strain responses in Mode 6 cyclic loading are presented in Figure 5.11b. When the shear strain amplitude was less than 5%, the mobilized shear stress $|q^{\star}|_{\max}$ in each strain cycle tended to increase with the number of strain cycles, which implies that cyclic shearing induced hardening of the materials. At the shear strain amplitude $\Delta\gamma^{\star} = 5\%$, however, $|q^{\star}|_{\max}$ in each cycle decreased with the number of strain cycles. In particular, $|q^{\star}|_{\max} = 140.7kPa$ in the first cycle and it decreased to $130.0kPa$ in the second strain cycle. After that, continuous cyclic loading caused small reduction of $|q^{\star}|_{\max}$ continuously. The different variations of $|q^{\star}|_{\max}$ with the number of strain cycles at various shear strain amplitudes can be related to the accumulative volumetric strain and the evolution of fabric.

Figures 5.11c and 5.11d present the volume change curve of the specimen in Mode 6 cyclic loading. When the shear strain amplitudes $\Delta\gamma^{\star}$ were not larger than 1%,

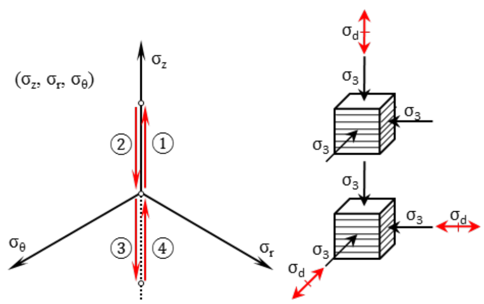

(a) Cyclic stress path of Mode 5

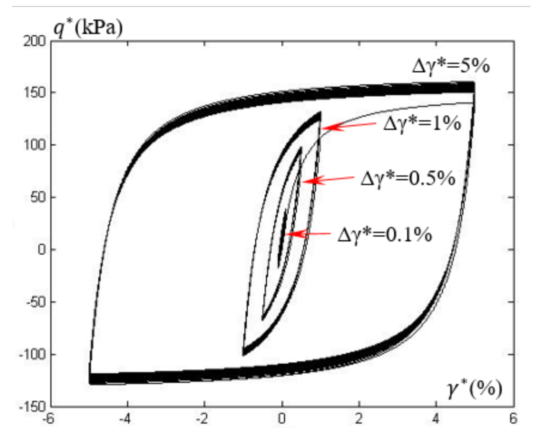

(b) Stress-strain curves

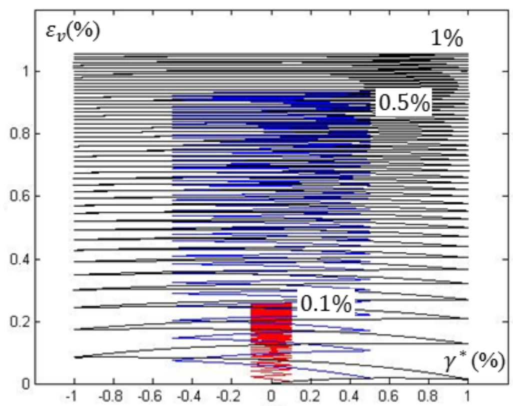

(c) Strain amplitudes: 0.1%, 0.5%, 1%

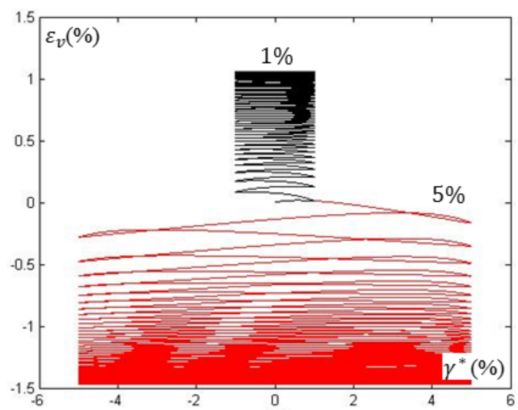

(d) Strain amplitudes: 1%, 5%

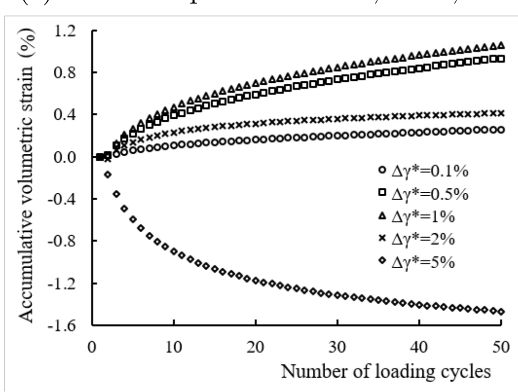

(e) Accumulative volumetric strains at different strain amplitudes

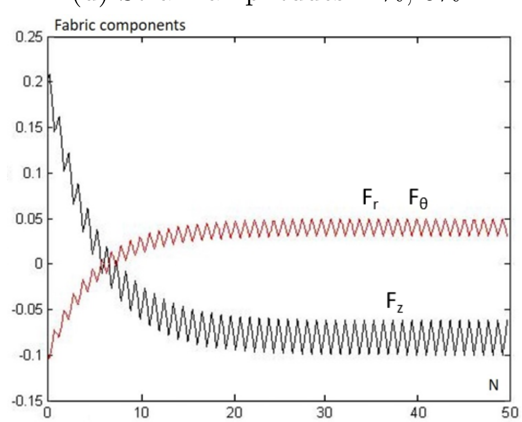

(f) Fabric evolution ($\Delta\gamma^{\star} = 0.1\%$)

Figure 5.10: Simulation results at strain amplitudes of 0.1%, 0.5%, 1% and 5% (Mode 5)

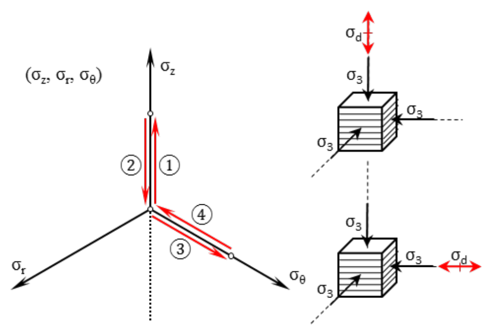

(a) Cyclic stress path of Mode 6

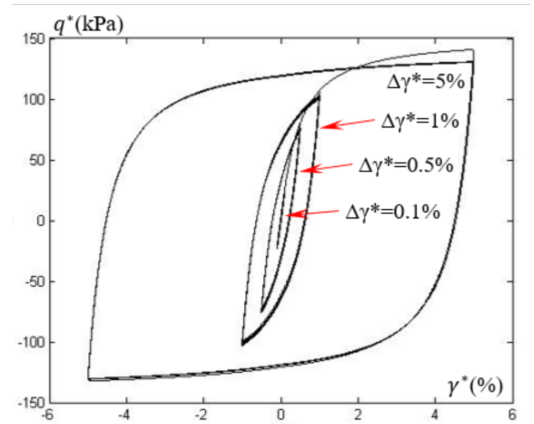

(b) Stress-strain curves

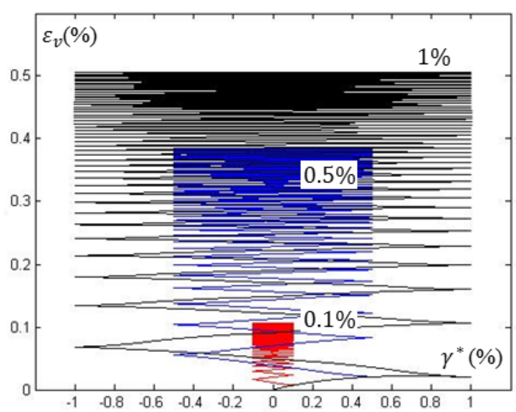

(c) Strain amplitudes: 0.1%, 0.5%, 1%

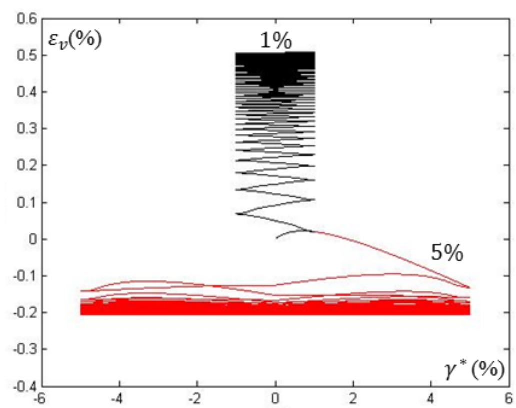

(d) Strain amplitudes: 1%, 5%

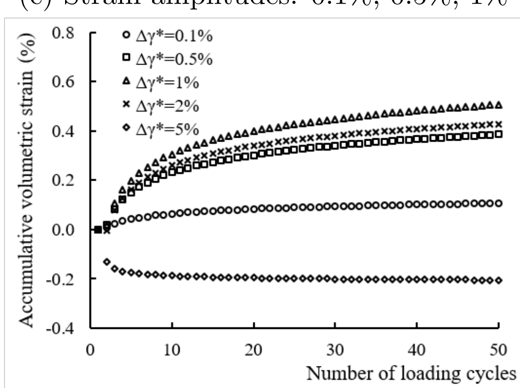

(e) Accumulative volumetric strains at different strain amplitudes

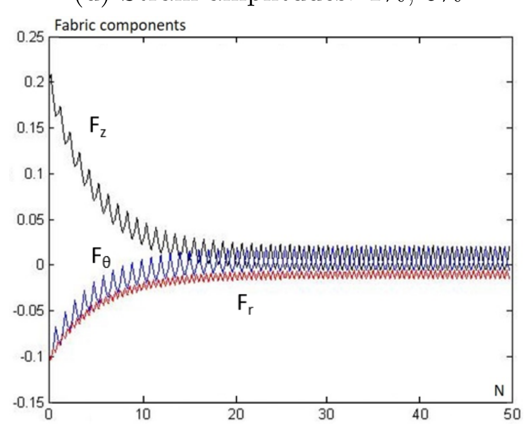

(f) Fabric evolution ($\Delta\gamma^\star = 0.1\%$)

Figure 5.11: Simulation results at strain amplitudes of 0.1%, 0.5%, 1% and 5% (Mode 6)

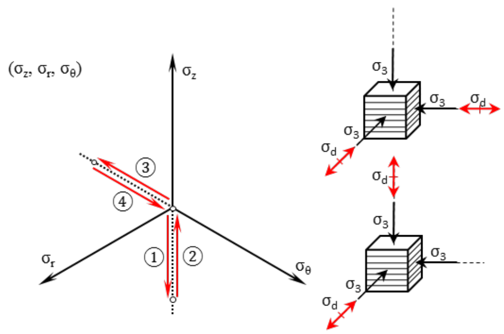

(a) Cyclic stress path of Mode 7

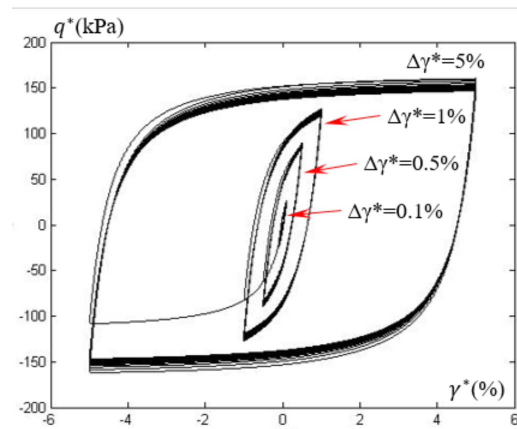

(b) Stress-strain curves

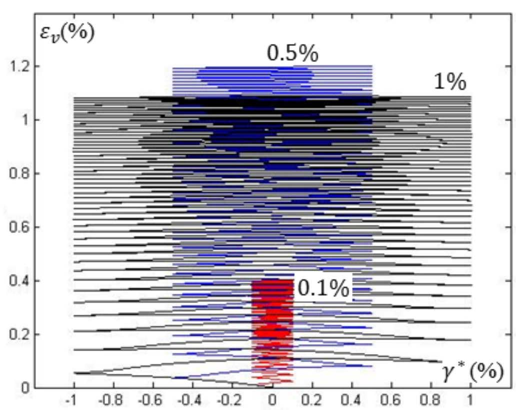

(c) Strain amplitudes: 0.1%, 0.5%, 1%

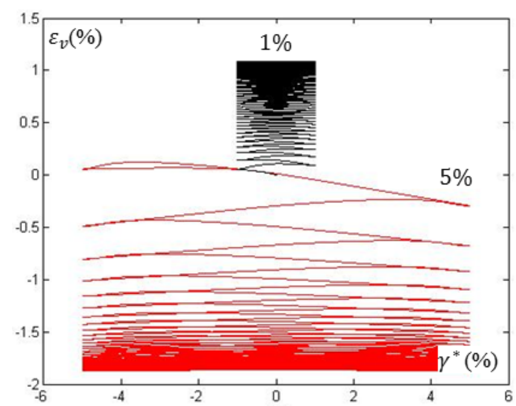

(d) Strain amplitudes: 1%, 5%

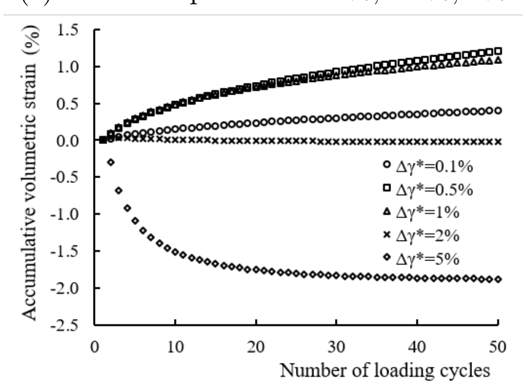

(e) Accumulative volumetric strains at different strain amplitudes

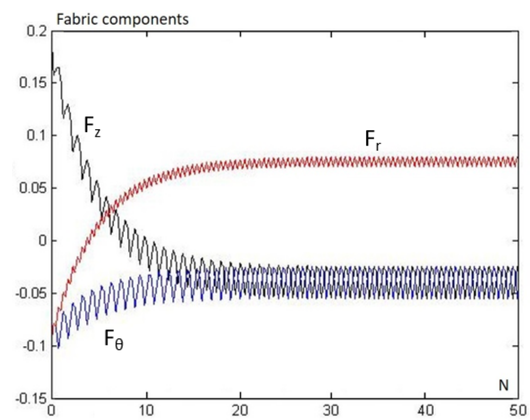

(f) Fabric evolution ($\Delta\gamma^{\star} = 0.1\%$)

Figure 5.12: Simulation results at strain amplitudes of 0.1%, 0.5%, 1% and 5% (Mode 7)

with an increase of strain cycles, accumulative volume compaction developed and tended to increase with an increase of the number of strain cycles. The volume tended to become stabilized and the accumulative volumetric strain after 50 cycles was affected by the shear strain amplitude. When the strain amplitude was increased to $\Delta\gamma^\star = 5\%$, net shear-induced dilation took place in each strain cycle. However, the amount of dilation in each strain cycle tended to decrease with the number of strain cycles and the accumulative volume change of the specimen eventually became stabilized. The significant dilation at $\Delta\gamma^\star = 5\%$ contributed to the decrease of $|q^\star|_{\max}$ with an increase of the number of strain cycles shown in Figure 5.11b.

The stress-strain responses in Mode 5 cyclic loading are presented in Figure 5.10b. The mobilized shear resistance in each strain cycle decreased as the number of strain cycles increased in all cases simulated. For the same cyclic shear strain amplitude, the specimen in Mode 5 loading had higher shear resistance than that in Mode 6. For example, at $\Delta\gamma^\star = 1\%$, $|q^\star|_{\max} = 130.77kPa$ and $101.7kPa$ in Mode 5 and Mode 6, respectively. In addition, when examining the volume change characteristics in Mode 6 loading (see Figure 5.11c), one observes that for small strain amplitude cyclic loading with $\Delta\gamma^\star \leq 1\%$, each cycle of Mode 5 loading caused larger net compaction of the specimen than that in Model 6 loading. However, in cyclic loading with $\Delta\gamma^\star = 5\%$, Mode 5 tended to induce higher dilation than Mode 6 loading.

The different deformation characteristics in Modes 5 and 6 loading can be attributed to the influence of fabric in the bedding plane. More specifically, in Mode 6, the cyclic loading in the bedding plane was in one direction, compared with two directions in Mode 5 loading. In other words, loading/unloading in multiple directions within the bedding plane tended to induce more volume change of the specimen, either compaction or dilation depending on the cyclic strain amplitude, and hence the different shear resistance. The conclusion is qualitatively in agreement with the laboratory test results by Tong *et al.* (2010).

Mode 7 of cyclic loading is different from Mode 6 in that when the periodic variation of σ_1 changed direction between $\alpha_{d\sigma_1} = 0°$ and $90°$, σ_r was kept to be a minor principal stress ($b = 0$) in Mode 6 loading but was kept to be a major principal stress in Mode 7 loading with $b = 1$, as illustrated in Figure 5.4. This explains why volume changes in Mode 7 loading were larger than those in Mode 6 loading, see Figures 5.11c, 5.11d, 5.12c and 5.12d. Mode 5 loading is different from Mode 7 in that the intermediate principal stress coefficient b jumped between $b = 0$ and $b = 1$ during each strain cycle. In general, both the stress-strain responses and the volume change characteristics of soil in Mode 7 were similar to those in Mode 5 loading, with even more shear-induced compaction by small amplitude ($\Delta\gamma^\star \leq 1\%$) strain cycles and higher dilation by large amplitude ($\Delta\gamma^\star = 5\%$) strain cycles. At the strain amplitude of $\Delta\gamma^\star = 0.5\%$, the value of ε_v was 0.93% after 50 cycles of loading in Mode 5 loading and was 1.20% in Mode 7 loading. When the strain amplitude became $\Delta\gamma^\star = 5\%$, the value of ε_v was -1.47% after 50 cycles of loading in Mode 5 loading and was -1.88% in Mode 7 loading. The results further confirmed that multiple direction cyclic loading tended to induce more significant volume change of the specimen for strain cycles of the same amplitude.

(2) Volume change in different loading modes

For comparison purposes, the accumulative volumetric strains after 50 cycles in the seven modes of cyclic loading are summarized for various strain amplitudes, as shown in Figure 5.13. The influence of different modes can be clearly seen from these figures.

Comparison between Modes 1 and 2 shows the influence of initial fabric anisotropy for $b = 0$. The tendency of compaction was always larger in Mode 2 with $\alpha_{d\sigma} = 90°$ than in Mode 1 with $\alpha_{d\sigma} = 0°$. This is consistent with observations from the monotonic loading tests. Different from Modes 1 and 2 in which $b = 0$, Modes 3 and 4 were simulated under $b = 1$. The volume compaction from these two modes was significantly higher than that from Modes 1 and 2.

Mode 5 can be seen as a medium mode of Modes 6 and 7 since half of this mode was under b=0 and the other half was under b=1. As a result, the material behaviour under Mode 5 fell into the range between those for Modes 6 and 7. By comparing Modes 6 and 7, the effect of b was identified. More specifically, a larger b value tended to induce a larger tendency of compaction at a small strain amplitude and a smaller tendency of dilation at a large strain amplitude. The cyclic experimental test results discussed in Chapter 3 were consistent with this observation under small strain amplitude. The results presented in Figure 3.33 were obtained from stress-controlled cyclic tests, with a stress amplitude of $\Delta q^{\star} = 80kPa$, which was close to the simulation at $\Delta\gamma^{\star} = 0.5\%$. Figures 5.13b and 3.33 show good agreement for which the accumulative strains were significantly higher in tests/simulations with $b = 1$ than those with $b = 0$.

Figure 5.14 shows the accumulative volumetric strain for each loading mode after 50 cycles. For Modes 1 to 4, the accumulative volumetric strains increased with an increase of shear strain amplitude and reached the maximum when $\Delta\gamma^{\star}$ was around 2%. This critical value of $\Delta\gamma^{\star}$ was about 1% for Modes 5 to 7, and was slightly larger for Mode 6 with b=0 than for Mode 7 with $b = 1$.

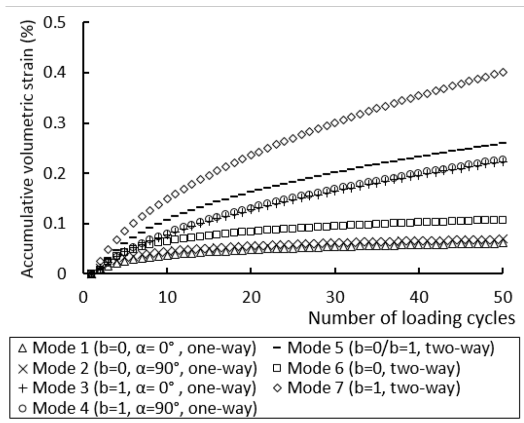

(a) $\Delta\gamma^{\star} = 0.1\%$

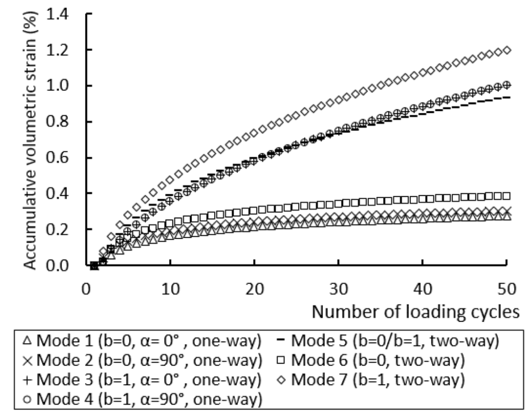

(b) $\Delta\gamma^{\star} = 0.5\%$

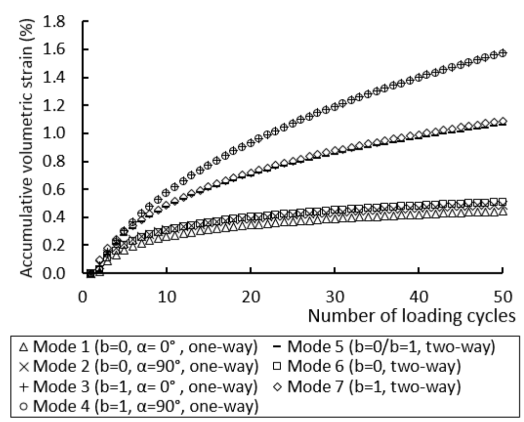

(c) $\Delta\gamma^{\star} = 1\%$

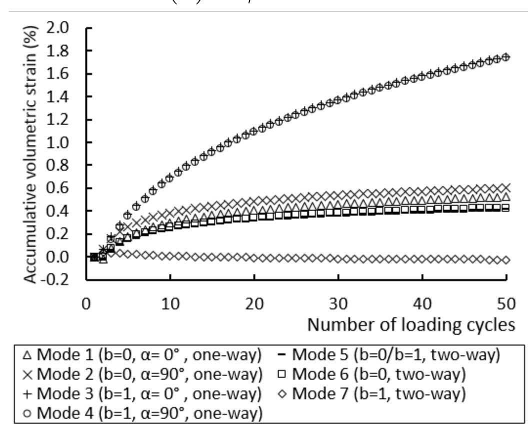

(d) $\Delta\gamma^{\star} = 2\%$

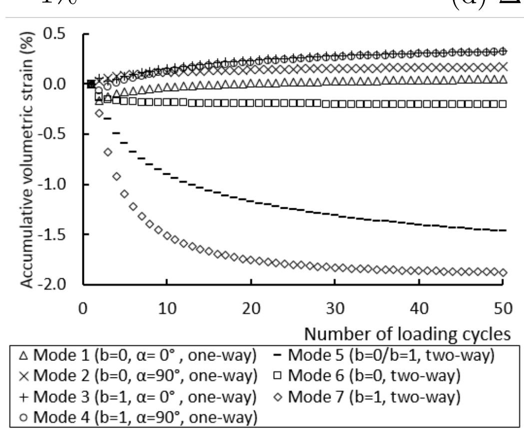

(e) $\Delta\gamma^{\star} = 5\%$

Figure 5.13: Accumulative volumetric strains in different loading modes at different strain amplitudes

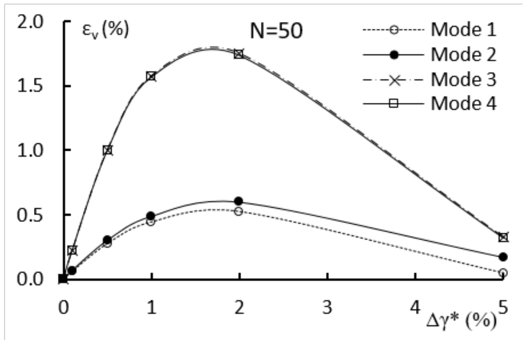

(a) Modes 1, 2, 3 and 4

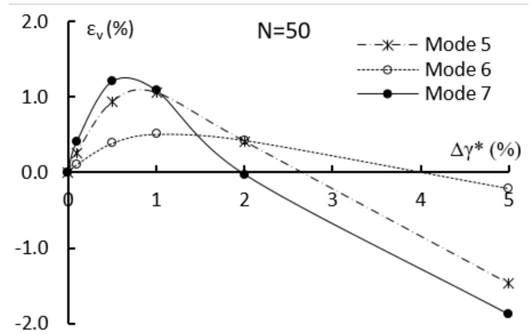

(b) Modes 5, 6 and 7

Figure 5.14: Accumulative volumetric strains under different loading modes after 50 cycles

(3) Fabric evolution induced by cyclic loading

To demonstrate the capability of the proposed stress-strain model in simulating fabric evolution of a granular material subjected to cyclic loading, the fabric evolutions in the seven cyclic loading modes at the cyclic strain amplitude $\Delta\gamma^\star = 0.1\%$ are presented in Figure 5.15. For other strain amplitudes, similar patterns of fabric evolution were observed with more significant variation of fabric components within the strain cycles.

We first examine the fabric evolution in loading Modes 1, 3, and 5, in which the stress states were axisymmetric and the specimens were cross-anisotropic with $F_r = F_\theta$ during the whole process of cyclic loading. It should be noted that the original cross-anisotropic fabric had the major principal component in the direction of the z-axis and the material was isotropic in the $r - \theta$ plane.

Figures 5.15a, 5.15c, and 5.15e show the variation of the three fabric components at $\Delta\gamma^\star = 0.1\%$ in Modes 1, 3, and 5, respectively. In all three loading modes, F_z started to increase as soon as the loading process started, and decreased upon unloading. On the contrary, F_r and F_θ decreased during loading and increased during unloading. The variations of all three fabric components F_z, F_r and F_θ were more significant during

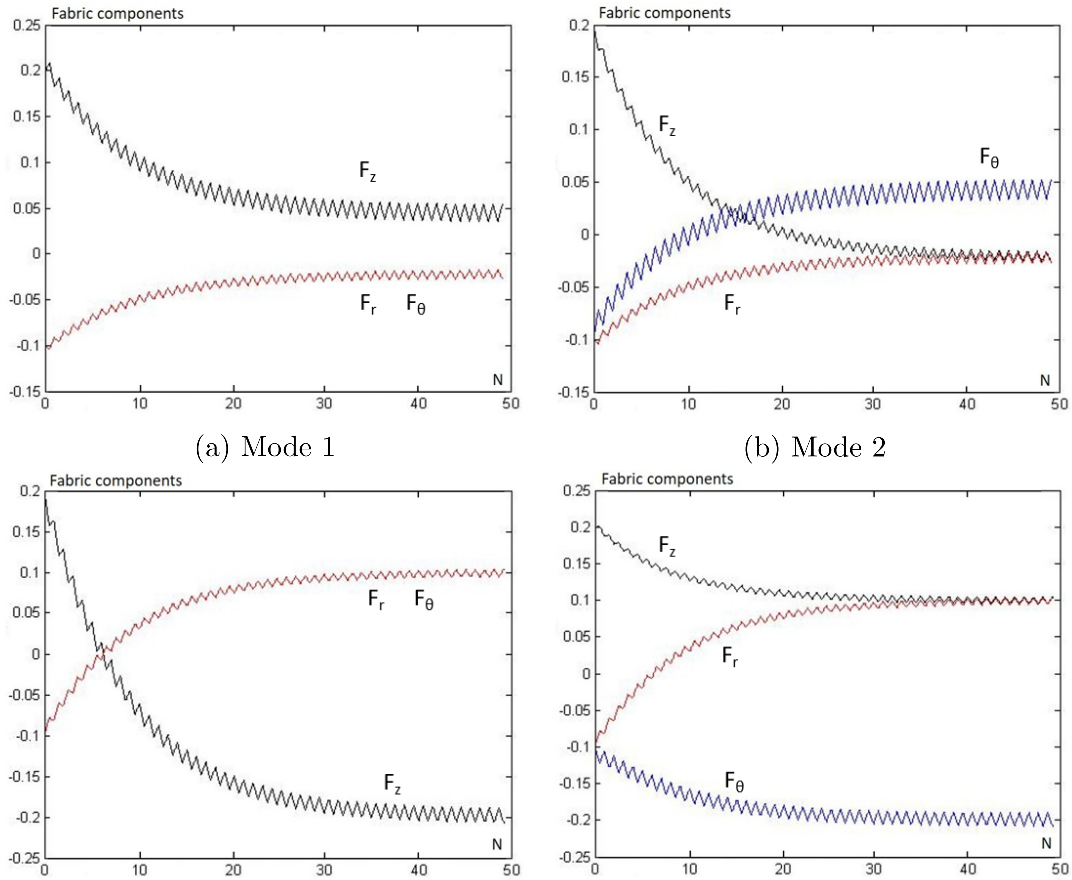

(a) Mode 1 (b) Mode 2

(c) Mode 3 (d) Mode 4

Figure 5.15: Fabric evolution during cyclic loading at strain amplitude of 0.1%

unloading than that during loading. This can be explained according to Figure 5.3 and the fabric evolution law in Equation (5.8). During unloading, the ratio μ_F/μ_σ was evidently larger than that in the preceding loading process. Thus the rate of fabric variation increased significantly upon unloading. As a result, the anisotropy of the structure decreased with the number of stress cycles. This is consistent with the results of DEM simulation; see, e.g., Sazzad and Suzuki (2010).

When comparing the fabric evolutions in Modes 1 and 3 loading, owing to the different cyclic loading directions with respect to the major principal direction of the fabric tensor, F_z decreased dramatically accompanied by increasing of F_r and F_θ with the number of stress/strain cycles in Mode 3. With an increase of the stress cycles, strong fabric built up within the bedding plane in which the cyclic stresses were applied. The initially strong fabric in the $z-$direction, however, was weakened and F_z evolved into the minor principal fabric component, with the average fabric components at $N = 50$ being $\bar{F}_z = -0.198$ and $\bar{F}_r = \bar{F}_\theta = 0.099$, respectively.

On the other hand, in Mode 1 loading, the cyclic stress in the $z-$direction caused a decrease of F_z as well as increases of F_r and F_θ. However, the decrease of F_z was relatively small so that F_z stayed as the major principal fabric component. The degree of anisotropy of the specimen decreased with the number of cyclic stress in Mode 1 loading, and eventually approached a steady fabric state. The general pattern of fabric evolution in Mode 5 loading, which can be considered as a combined Modes 1 and 3 loading, was the same as that in Mode 3 loading. At $N = 50$, the average fabric components were $\bar{F}_z = -0.078$ and $\bar{F}_r = \bar{F}_\theta = 0.039$, respectively.

For Modes 2 and 4 loading presented in Figures 5.15b and 5.15d, it is interesting to note that F_z and F_r became synchronous after around 45 cycles in both cases. Based on the loading paths presented in Figure 5.4, the incremental deviatoric stress components in directions of the z-axis and the r-axis were always identical in these two modes. According to the fabric evolution law, the induced fabric primarily depended on the stress increments. Even though the initial fabric components were different in the $z-$ and the $r-$directions, the same cyclic stress in these two directions resulted in a gradual decrease of the structural difference in these two directions, causing the convergence of F_z and F_r to the same ultimate value; as shown in the figures.

Figures 5.15f and 5.15g show the variation of fabric in Modes 6 and 7. These

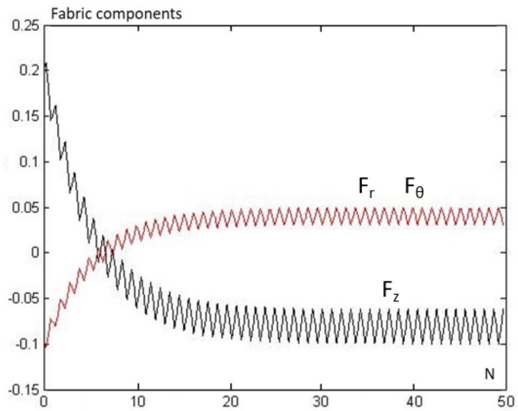

(e) Mode 5

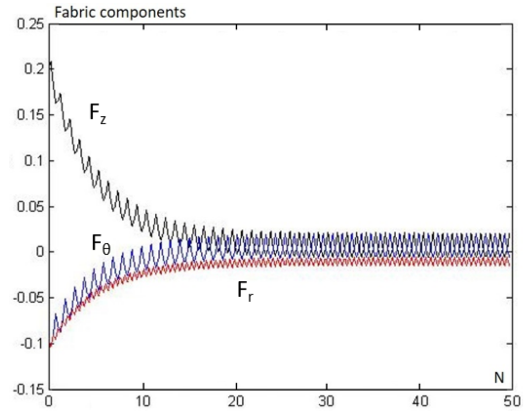

(f) Mode 6

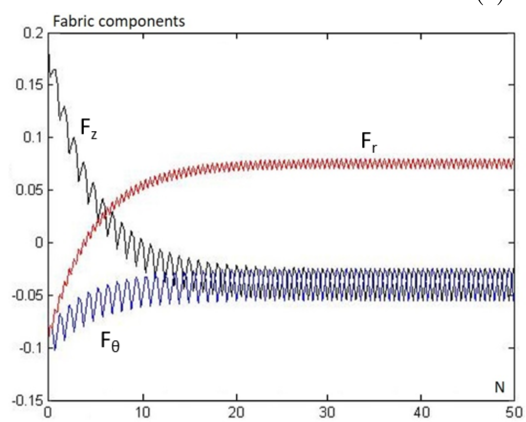

(g) Mode 7

Figure 5.15: Fabric evolution during cyclic loading at strain amplitude of 0.1% (cont.)

two modes both represented two-way cyclic loading. As discussed previously, loading Mode 6 can be decomposed into Modes 1 and 2, therefore the fabric evolution in loading at Mode 6 was qualitatively in agreement with the combination of fabric evolution in Modes 1 and 2, as shown in Figures 5.15a and 5.15b.

In the Mode 6 loading, the specimen was subjected to the same cyclic stress condition (one-way cyclic loading) in the $z-$ and $\theta-$axes alternately. Therefore the fabric components F_z and F_θ tended to evolve to the same average value during cyclic loading. After 50 cycles, $\bar{F}_r = -0.018$ and $\bar{F}_z = \bar{F}_\theta = 0.009$. Different from Modes 2 and 4 where F_z and F_r became synchronous, at the stabilized stage in Mode 6 loading, F_z and F_θ were asynchronous but with same average value as well as amplitude.

The difference between Figure 5.15f and Figure 5.15g was mainly in that the stabilized average value of F_r increases from 0.009 in Mode 6 to 0.075 in Mode 7, while F_z and F_θ increased from -0.025 to -0.011. This can be explained according to the decomposed Mode 7, as shown in Figure 5.4h. By this decomposition, Mode 7 loading can be considered as a Mode 6 loading with an additional Mode 1 loading applied in the r-direction. Referring to Figure 5.15a, the additional cyclic loading in the $r-$direction caused an increase of F_r as well as a decrease of F_z and F_θ.

5.4.2 Effect of initial void ratio

The stress-strain curves of sand specimens with different initial void ratios in Modes 1 and 4 loading are shown in Figures 5.16 and 5.17, respectively. Similar to simulations in the previous section, the specimens were assumed to have the same initial fabric and the applied cyclic shear strain amplitude was $\Delta\gamma^\star = 0.5\%$. With the increase of void ratio, the mobilized shear stresses, both the initial and the stabilized, decreased. For example, for specimens in Mode 1 cyclic loading (see Figure 5.16), the value of $|q^\star|_{\max}$ was 87.81 kPa at $e_0 = 0.55$, comparing to $|q^\star|_{\max} = 68.04$ kPa at $e_0 = 0.68$. For the stabilized strain cycles, the values of $|q^\star|_{\max}$ were 72.32 kPa and 54.86 kPa at $e_0 = 0.55$ and 0.68, respectively. The same pattern can also be found from Figure 5.17 in Mode 4 loading.

Figures 5.18 and 5.19 present the accumulative volumetric change of specimens with different initial void ratios in Modes 1 and 4 loading, respectively. In all cases, the accumulative volume compaction induced by cyclic shearing increased with the

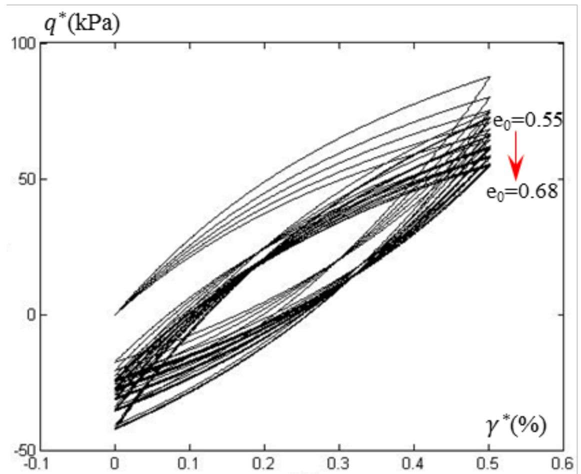

Figure 5.16: Stress-strain curves at different initial void ratios (Mode 1 with $\Delta\gamma^\star = 0.5\%$)

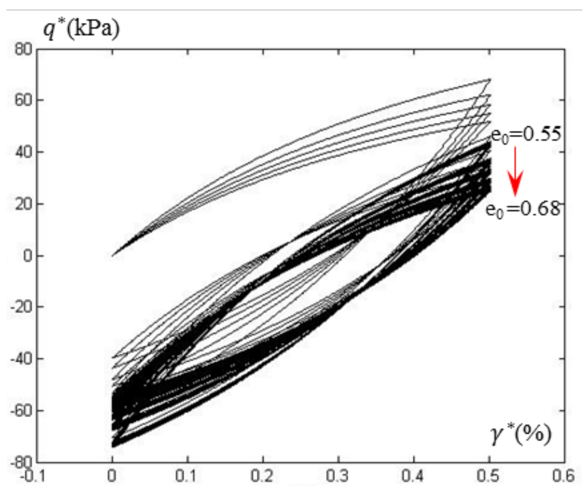

Figure 5.17: Stress-strain curves at different initial void ratios (Mode 4 with $\Delta\gamma^\star = 0.5\%$)

number of strain cycles. For an initially loose specimen, at a given number of strain cycles, the accumulative volumetric compaction was greater than that of a dense specimen. It should be noted that the accumulative volume change was also affected by the cyclic shear strain amplitude.

We next examine the effect of initial void ratio on the change of fabric in Modes

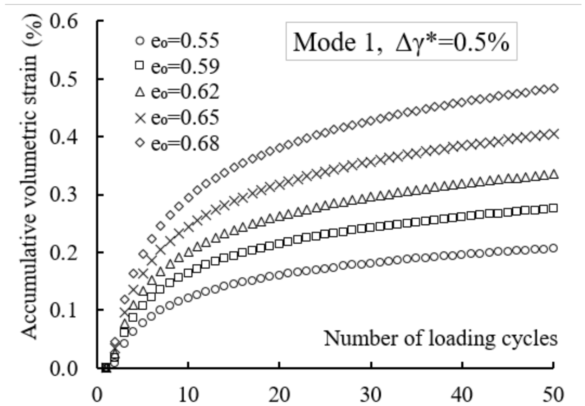

Figure 5.18: Accumulative volumetric strains at different initial void ratios (Mode 1)

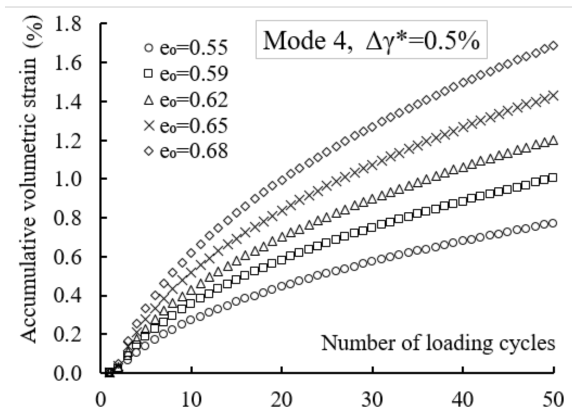

Figure 5.19: Accumulative volumetric strains at different initial void ratios (Mode 4)

1 and 4 loadings for specimens with $e_0 = 0.55$ and $e_0 = 0.68$. As shown in Figures 5.20a and 5.20b, regardless of the initial void ratio, cyclic loading reduced the inherent anisotropy of the specimens, similar to that shown in Figure 5.15a. The residual fabric anisotropy was marginally affected by the initial void ratio, even though the oscillation of fabric components or the instantaneous anisotropy was higher for the loose specimen, as shown in Figure 5.20b. Similar observations can be found in Figures 5.20c and 5.20d for Mode 4 loading. This is because that the fabric evolution was dominated by the change in stresses and the current stress state.

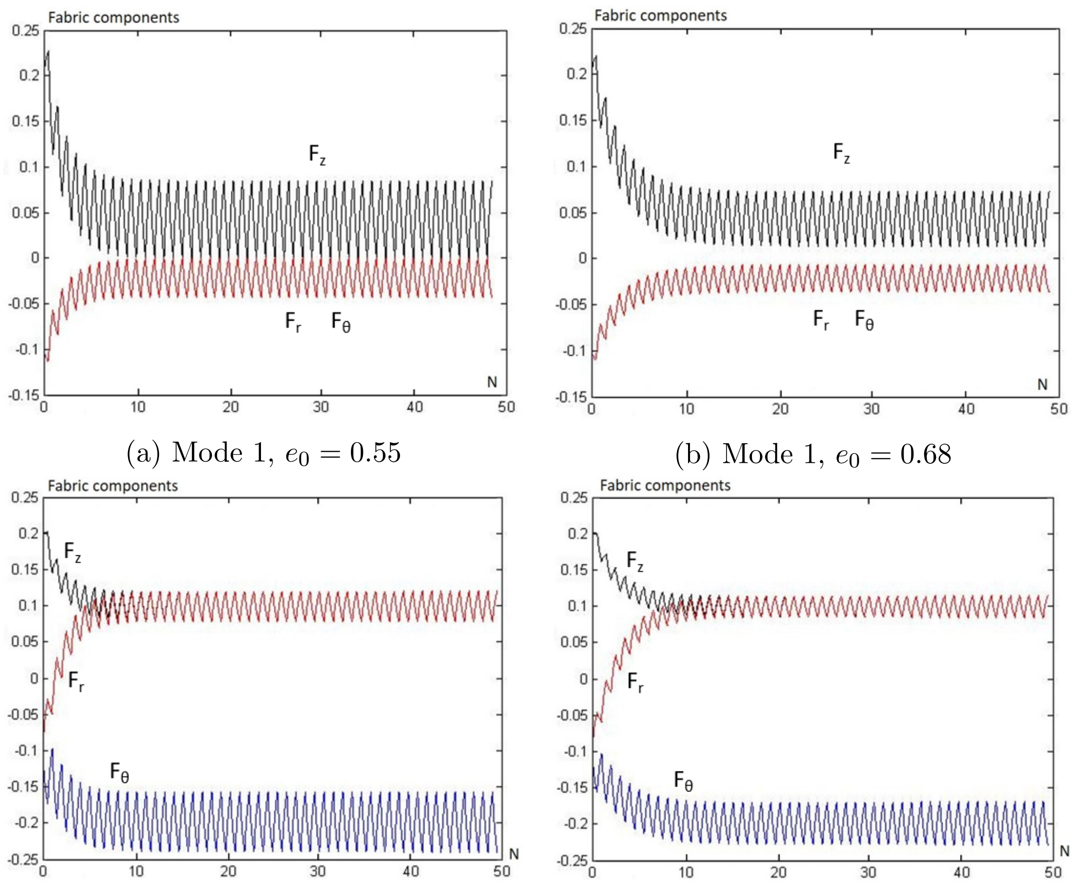

(a) Mode 1, $e_0 = 0.55$

(b) Mode 1, $e_0 = 0.68$

(c) Mode 4, $e_0 = 0.55$

(d) Mode 4, $e_0 = 0.68$

Figure 5.20: Fabric evolution during cyclic loading at different initial void ratios (Mode 1 and Mode 4 with $\Delta\gamma^\star = 0.5\%$)

5.4.3 Effect of initial degree of anisotropy

The effects of initial degree of anisotropy on the cyclic behaviours were investigated using Mode 1 ($\alpha_{d\sigma} = 0°$) and Mode 2 ($\alpha_{d\sigma} = 90°$), in which $b = 0$. Two groups of simulations were carried out with the initial void ratio being $e_0 = 0.59$ and 0.65, respectively. The initial value of the measure of anisotropy Ω, which is defined as $\Omega = \frac{2}{3}\sqrt{3J_2^F}$, varied between 0 and 0.4. The strain amplitude of $\Delta\gamma^\star = 0.5\%$ was used in these simulations. When $\Omega = 0$, the specimen was initially isotropic and

Mode 2 loading was the same as Mode 1 loading.

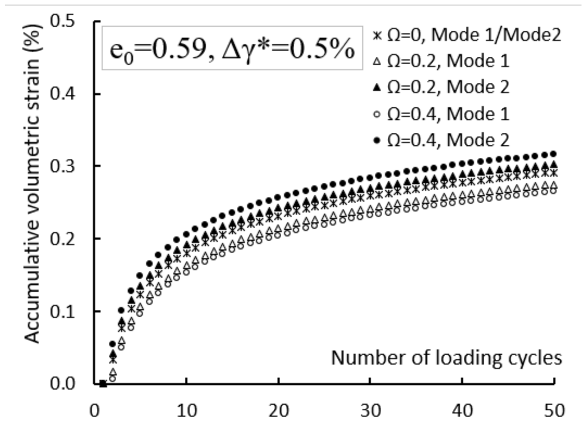

Figure 5.21: Accumulative volumetric strains at different initial degree of anisotropy ($e_0 = 0.59$)

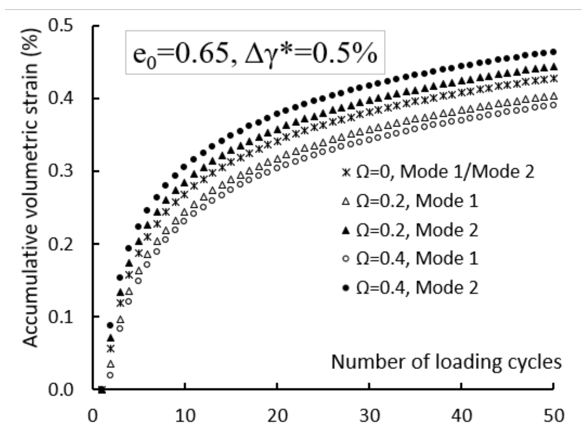

Figure 5.22: Accumulative volumetric strains at different initial degree of anisotropy ($e_0 = 0.65$)

Figure 5.21 presents the evolution of accumulative volumetric strains of specimens with $e_0 = 0.59$ in Modes 1 and 2 loadings at different initial values of Ω. Using the curve at $\Omega = 0$ as a reference, the curves at $\Omega = 0.2$ and 0.4 were located below and above the reference curve for Mode 1 and Mode 2 loading, respectively. In other words, the cyclic stress applied perpendicular to the bedding plane (i.e., $\alpha_{d\sigma} = 0°$)

generally caused less volumetric compaction than that applied in the bedding plane (i.e., $\alpha_{d\sigma} = 90°$). Moreover, for tests with $\alpha_{d\sigma} = 0°$, increased initial anisotropy tended to reduce the volumetric compaction during cyclic loading. On the contrary, in Mode 2 loading with $\alpha_{d\sigma} = 90°$, specimens with stronger inherent anisotropy tended to have higher volumetric compaction under cyclic loading. In particular, after 50 cycles of cyclic loading, the accumulative volumetric strains of the specimen with $\Omega = 0.2$ were $\varepsilon_v = 0.275\%$ and 0.303% in Mode 1 and Mode 2 loading respectively, comparing with $\varepsilon_v = 0.265\%$ in Mode 1 and $\varepsilon_v = 0.316\%$ in Mode 2 when $\Omega = 0.4$. For anisotropic granular materials, the direction of the cyclic stress tended to affect the development of accumulative volume change of a granular material. Cyclic loading in the direction of weak fabric component tended to cause higher volumetric compaction.

Simular patterns were found from the results of specimens with $e_0 = 0.65$ presented in Figure 5.22. Owing to the relative large initial void ratio, the differences in the volumetric compaction at different initial Ω values were more significant, with $\varepsilon_v = 0.404\%$ in Mode 1 and $\varepsilon_v = 0.444\%$ in Mode 2 at $\Omega = 0.2$, $\varepsilon_v = 0.390\%$ in Mode 1 and $\varepsilon_v = 0.464\%$ in Mode 2 at $\Omega = 0.4$, respectively.

The influence of the inherent anisotropy on the fabric change during cyclic loading is shown in Figure 5.23. Similar to the findings from Figures 5.20a to 5.20d, the evolution of fabric can be considered as independent of the initial void ratio. However, the direction of the cyclic stress with respect to the major principal fabric component, which was measured by $\alpha_{d\sigma}$, affected the evolution of the fabric. In all cases, the fabric component in the direction of the cyclic stress became stronger and the residual degree of anisotropy at $N = 50$ was independent of $\alpha_{d\sigma}$ and the initial value of Ω. The initial degree of anisotropy and $\alpha_{d\sigma}$ only affected the fabric states in the initial few cycles

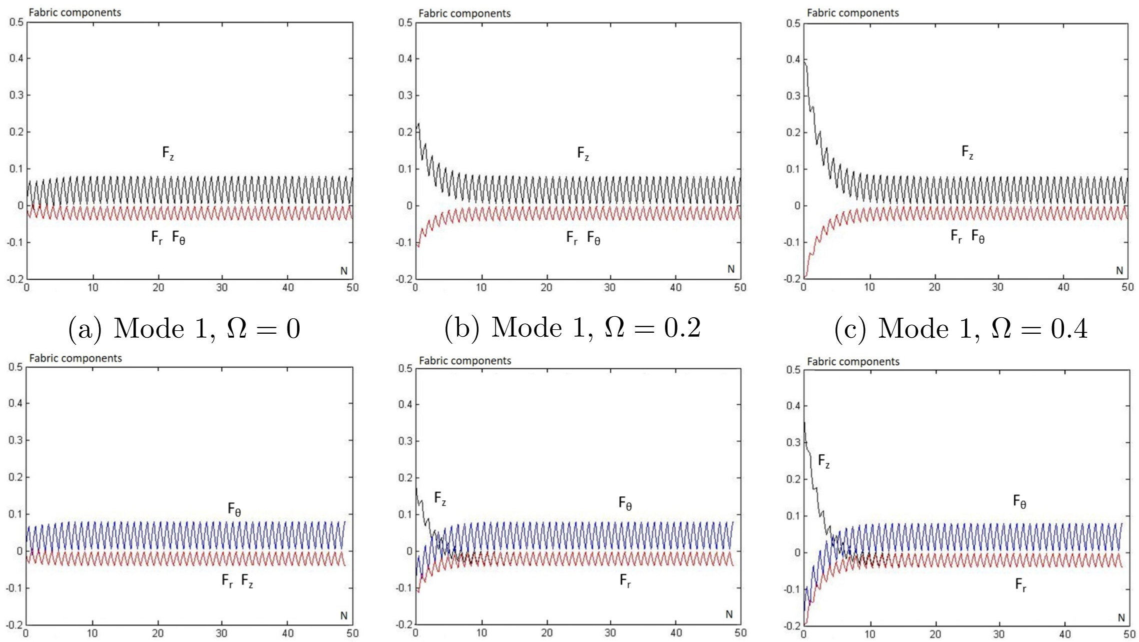

(a) Mode 1, $\Omega = 0$ (b) Mode 1, $\Omega = 0.2$ (c) Mode 1, $\Omega = 0.4$

(d) Mode 2, $\Omega = 0$ (e) Mode 2, $\Omega = 0.2$ (f) Mode 2, $\Omega = 0.4$

Figure 5.23: Fabric evolution during cyclic loading at different initial degree of anisotropy ($e_0 = 0.59$ and $\Delta\gamma^\star = 0.5\%$)

($N < 10$) upon cyclic loading; see Figures 5.21 and 5.22. Similarly, Figures 5.23e and 5.23f were different from Figure 5.23d mainly in the first 5-10 cycles.

5.5 Conclusions

This chapter presented a constitutive model for the cyclic behaviour of granular materials based on the framework proposed in chapter 4. In this model, a kinematic hardening law was adopted to consider the effects of plastic deformation. The concept of the critical state fabric surface was used to describe the evolution of fabric during cyclic loading, and the newly developed stress-dilatancy formulation was further extended to cyclic loading regime as well. As a result, the proposed model can take into account the influence of void ratio, stress level and fabric on cyclic soil behaviour in a consistent manner.

Seven different loading modes were designed to thoroughly investigate the performance of the proposed model under different conditions. By comparing the results obtained from various loading modes, it is demonstrated that the model can correctly describe the behaviours of inherently anisotropic granular materials subjected to cyclic loading in different directions with respect to the principal frame of the materials. More specifically, the model was able to describe the effects of the 3D general stress states, the major principal incremental stress direction and the fabric of the material.

A parametric study was carried out to examine the influence of initial void ratio as well as the degree of initial anisotropy on the behaviour of granular materials under cyclic loading. The accumulative volume compaction of a specimen was affected by both the initial density and the direction of the applied cyclic stress. A loose specimen with cyclic stress parallel to the bedding plane tended to have larger volumetric compaction. However, the evolution of fabric was marginally affected by the density of the material. The direction of cyclic stress had a significant influence on the evolution of fabric at the beginning of cyclic loading. However, the residual fabric anisotropy at a larger number of strain cycles was independent of the initial fabric.

Chapter 6

Numerical implementation of the proposed constitutive model

This chapter examines the performance of the stress-strain model developed in Chapter 4 in solving boundary-valued problems. The model was implemented into the commercial software package ABAQUS via the user-defined subroutine UMAT. The proposed stress-strain model and the developed algorithm are examined via FEM simulations for the following boundary value problems: (1) HCA test Series B on cubic specimens (constant b with different loading directions); (2) tests on cubic specimens with different initial void ratios; (3) tests on cubic specimens with different loading directions; (4) tests on cubic specimens along different stress paths; and (5) ground settlement on structured granular medium.

6.1 FEM simulations of element tests under different loading conditions

Six series of element tests on cubical specimens subjected to different loading conditions were simulated as boundary-valued problems using ABAQUS. A $10cm \times 10cm \times 10cm$ cubical specimen was modelled with $10 \times 10 \times 10$ eight-noded isoparametric elements (C3D8). The FEM mesh and boundary constraints are shown in Figure 6.1. The vertical displacement u_z of the bottom surface ($z = 0$) was constrained. $u_x = 0$ and $u_y = 0$ were reinforced on the central lines $x = 0$ and $y = 0$ of the bottom surface, respectively.

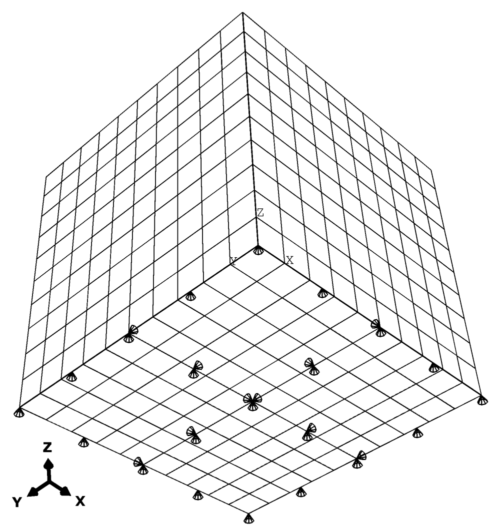

Figure 6.1: Mesh and boundary conditions of the initial step

For the initial step, in addition to the constraints, a confining pressure of 100kPa was applied by adding the following command line to the ABAQUS job file (*.inp). For the element tests, the gravity loads on the specimens were neglected.

initial conditions, type=stress, input=*.dat* where the data file ***.dat is written in the format of

Part-1-1.1,-100.00000,-100.00000,-100.00000,0.00000,0.00000,0.00000

Part-1-1.2,-100.00000,-100.00000,-100.00000,0.00000,0.00000,0.00000

Part-1-1.3,-100.00000,-100.00000,-100.00000,0.00000,0.00000,0.00000

...

In the loading step, different control methods may be used to control the loading process. For example, by using a stress-controlled loading method, the stress-strain behaviour of the specimen can only be modelled up to the peak deviatoric stress point. In other words, the softening part of the stress-strain curves would not be obtained. On the other hand, when using a displacement-controlled loading method, it would be possible to capture the post-peak behaviour of the material. However, to simulate certain stress conditions, e.g. tests under constant mean effective stress, the stress-controlled procedure is more convenient.

6.1.1 Model design and simulation matrix

Simulation of HCA tests Series B

To verify the proposed stress-strain model and the numerical algorithm, a series of simulations were carried out for the HCA tests (Series B as in Chapter 3) with $b = 0$ and α varying from $0°$ to $90°$. During the loading process, the mean effective stress was kept at $100kPa$. The simulation matrix is shown in Table 6.1, which is the same as that used in Chapter 3. The initial void ratio of the specimens was $e_0 = 0.59$ ($D_r = 72\%$), and the initial degree of anisotropy was $\Omega = 0.25$, with $\Omega = \frac{2}{3}\sqrt{3J_2^F}$.

For the initial step, a mean effective stress of 100kPa was applied to the specimen. During the loading step, the stress on the top surface (i.e., the vertical stress) of the

Table 6.1: Simulation matrix for HCA test Series B

Test No.	$\alpha(^\circ)$	b	$sin^2\alpha$	Lode angle $\theta(^\circ)$
B1	0	0	0	30
B2	30	0	0.25	30
B3	60	0	0.75	30
B4	90	0	1	30

model was increased while the stresses on all the four side surfaces (i.e., the horizontal stresses) were decreased at the same rate ($b = 0$). The stress rate on the top surface was two times of that on the side surfaces to keep $p = 100kPa$. By this load control method, the simulation was terminated when the deviatoric stress reached its peak point.

Series SE: influence of initial void ratio e_0

In this simulation series (SE), the inclination angle α between the major principal stress direction and the normal direction of the bedding plane was maintained at $\alpha = 0^\circ$, and the intermediate principal stress coefficient b was kept at $b = 0$. Different from Series B tests, the horizontal stress in Series SE tests was kept constant, as in conventional triaxial compression tests. The initial confining pressure was 100kPa, and the initial degree of anisotropy was $\Omega = 0.4$. The initial void ratio e_0 varied from 0.55 to 0.65, corresponding to tests SE1 to SE6, as presented in Table 6.2.

For the initial step, a mean effective stress of $100kPa$ was applied to the specimen. During the loading step, the horizontal confining pressure was kept at $100kPa$, while the displacement of the top surface was increased. Displacement control was chosen to capture the softening part of stress-strain curves.

Table 6.2: Simulation matrix for SE

Series No.	e (void ratio)	$D_r(\%)$	α	b
SE-1	0.55	85	0°	0
SE-2	0.57	78	0°	0
SE-3	0.59	72	0°	0
SE-4	0.61	65	0°	0
SE-5	0.63	59	0°	0
SE-6	0.65	52	0°	0

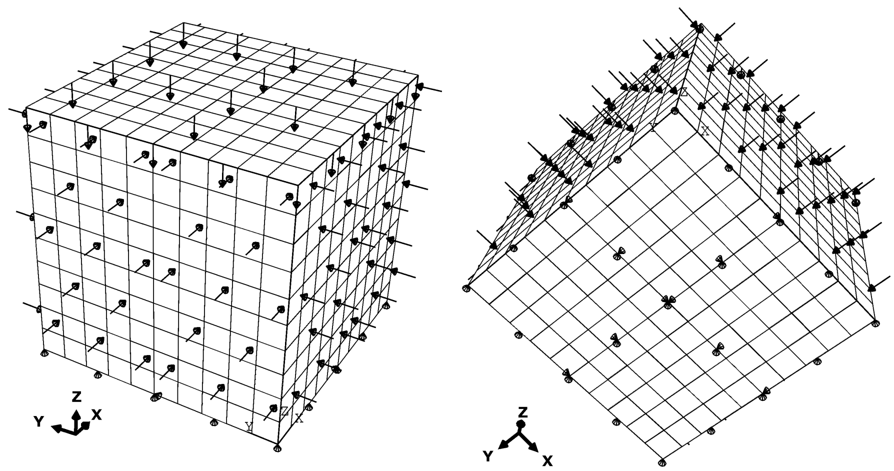

Figure 6.2: Boundary conditions for the simulations of SE, SA1, and SA2 at the loading step

Series SA1 and SA2: influence of loading direction α

For the next two series (SA1 and SA2) of simulations, the intermediate principal stress coefficient was kept at $b = 0$, while the inclination angle α varied from 0° to 90°. The initial confining pressure was $100kPa$, and the initial void ratio $e_0 = 0.59$. The initial degree of anisotropy measures were $\Omega = 0.4$ (SA1) and $\Omega = 0.2$ (SA2), respectively. The stress path for these two series of tests was the same as that of the conventional triaxial compression test. The simulation matrix is shown in Table 6.3. The boundary conditions for Series SA1 and SA2 are shown in Figure 6.2.

Table 6.3: Simulation matrix for SA1 and SA2

Series SA1	Ω	α	b	Series SA2	Ω
SA1-1	0.4	0°	0	SA2-1	0.2
SA1-2	0.4	30°	0	SA2-2	0.2
SA1-3	0.4	45°	0	SA2-3	0.2
SA1-4	0.4	60°	0	SA2-4	0.2
SA1-5	0.4	90°	0	SA2-5	0.2

Series SB1 and SB2: influence of multi-direction loading ratio $b^\star$

For this two series of tests (SB1 and SB2), the behaviour of cubical specimens subjected to mixed boundary conditions was simulated. Two control parameters, α and $b^\star = \varepsilon_2/\varepsilon_1$ were used to define different loading conditions.

The inclination angle α was kept at $\alpha = 0°$, while $b^\star$ varied from $b^\star = 0$ to $b^\star = 1$. The initial confining pressure was $100kPa$, and the initial void ratio $e_0 = 0.59$. The measures of the initial anisotropy were $\Omega = 0.4$ (SB1) and $\Omega = 0.2$ (SB2), respectively. During the loading process, a vertical displacement δ_u was applied on the top surface, while the left and right surfaces (x-z planes) were simutaneously moved by $\delta_u b^\star/2$. During this procedure, the pressures on the front and back surfaces (y-z planes) were kept at $100kPa$. As a result, the mean effective stress increased at different rates during the loading procedure for different $b^\star$. The simulation matrices are shown in Table 6.4. The boundary constraints of SB1 and SB2 are shown in Figure 6.3.

Table 6.4: Simulation matrix for SB1 and SB2

Series SB1	Ω	α	$b^\star$	Series SB2	Ω
SB1-1	0.4	0°	0	SB2-1	0.2
SB1-2	0.4	0°	0.25	SB2-2	0.2
SB1-3	0.4	0°	0.5	SB2-3	0.2
SB1-4	0.4	0°	0.75	SB2-4	0.2
SB1-5	0.4	0°	1	SB2-5	0.2

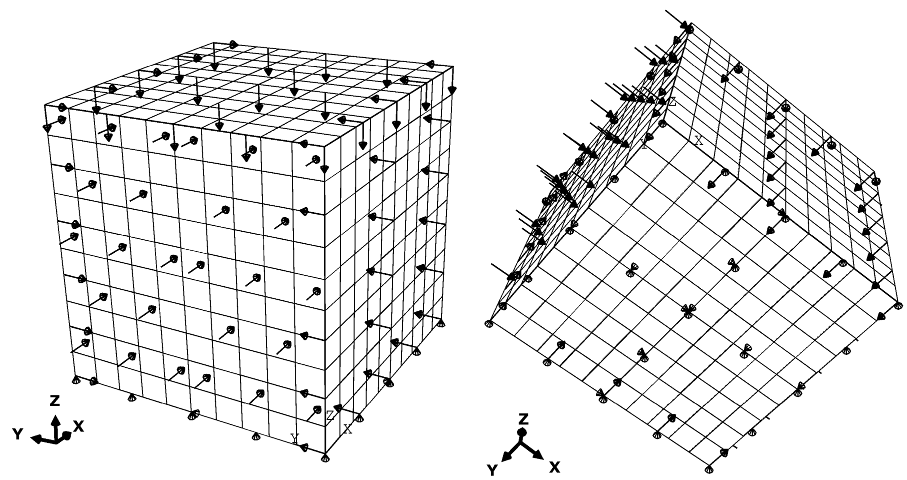

Figure 6.3: Mesh and boundary conditions for the simulations of SB1 and SB2

6.1.2 Simulation results

Simulation of HCA test Series B

The stress-strain curves from the FEM simulations are presented together with the test results as well as with the results from single-node simulations (as in Chapter 4) in Figures 6.4a and 6.4b, respectively. The results of FEM simulations agree well with single-node simulations, which were from the study in Chapter 4 using a Matlab code for the stress-strain relation of a single node.

As shown in Figure 6.4b, the FEM simulations stopped as soon as the peak value of deviatoric stress was attained. The peak deviatoric stress arrived earlier in the FEM simulations than in the single node simulations, while the values of the peak stresses were very close. For example, for Test B2 with $\alpha = 30°$ and $b = 0$, the FEM simulation stopped at an octahedral shear strain value of 2.28% with a maximum deviatoric stress of 151.83kPa, while in the single node simulation, the maximum deviatoric stress was 152.66kPa at the octahedral shear strain of 3.59%.

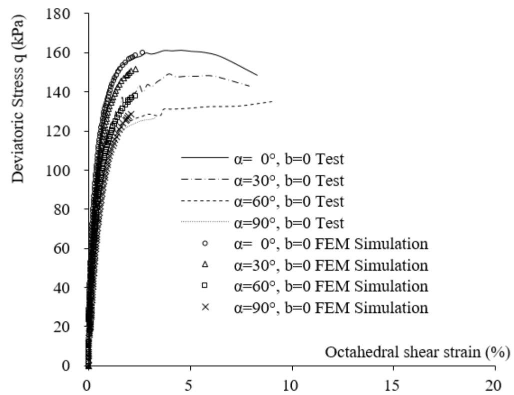

(a) Stress-strain curves from tests and FEM simulations

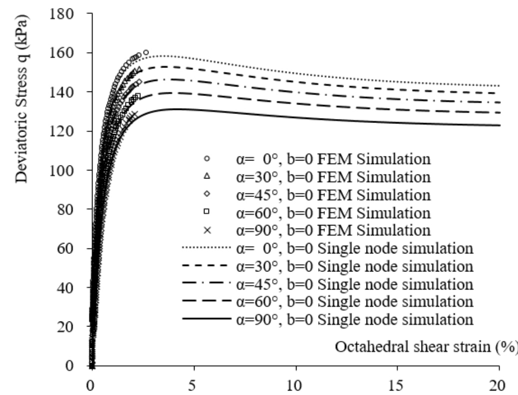

(b) Stress-strain curves from single node simulations and FEM simulations

Figure 6.4: Comparison of stress-strain curves for HCA test Series B

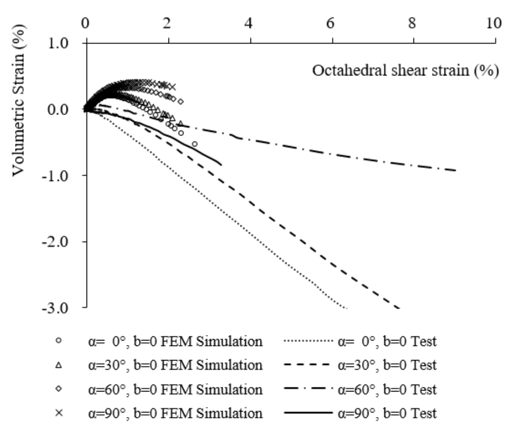

(a) Volumetric-shear strain curves from tests and FEM simulations

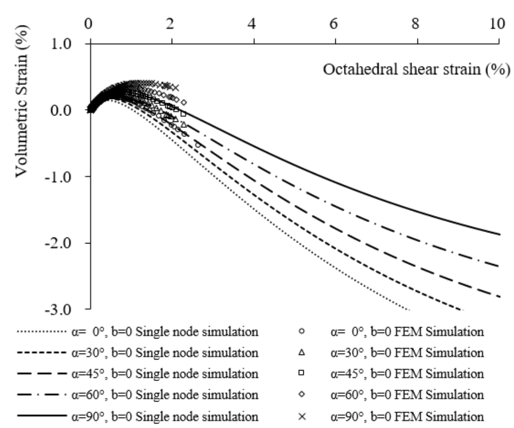

(b) Volumetric-shear strain curves from single node simulations and FEM simulations

Figure 6.5: Comparison of the volumetric deformation for HCA test Series B

Figures 6.5a and 6.5b compare the volumetric-shear strain curves from the FEM simulations, tests as well as single node simulations. Relatively large errors are observed in Figure 6.5a. However, as can be seen from Figure 4.17, better agreement between tests and simulations was obtained at larger shear strains. A good agreement was found between the FEM simulations and single node simulations, see Figure 6.5b.

In general, the dilatancy from FEM simulations was smaller than that from the single node simulations. The boundary condition of FEM simulations may have influenced the dilatancy properties. For example, in the FEM simulations, the displacement of two central lines on the bottom of the specimen was constrained to eliminate rigid body movement, which may decrease the potential of dilation. Moreover, the size and shape of the specimens used for FEM simulations may also have an influence on the dilatancy of the specimen.

Influence of initial void ratio e_0

Figures 6.6a and 6.6b present the stress-strain curves and volume change responses for specimens of different initial void ratios, respectively. The peak deviator stress decreased with an increase of the initial void ratio e_0. For $e_0 \leq 0.59$, a peak deviator stress was observed at approximately 3.5% octahedral strain. When $e_0 \geq 0.61$, no apparent peak stress was observed on the stress-strain curves.

The volumetric-shear strain curves showed that the dilatancy decreased significantly with an increase of the initial void ratio. For loose specimens with $e_0 = 0.65$, almost no dilation was observed during the whole shearing process. On the other hand, for dense sand with $e_0 = 0.55$, dilation occurred soon after the loading started.

Figure 6.7 presents the results from experimental studies under the same conditions as simulation Series SE by Kolymbas and Wu (1990). However, a different material, Karlsruhe sand, was used in their tests while the simulations were performed using the parameters of Ottawa sand. A qualitative agreement is found between Figure 6.6a and Figure 6.7a, as well as between Figure 6.6b and Figure 6.7b. Referring to Figure 6.6a, the failure deviatoric stress increased from $205.7kPa$ to $274.9kPa$ as the

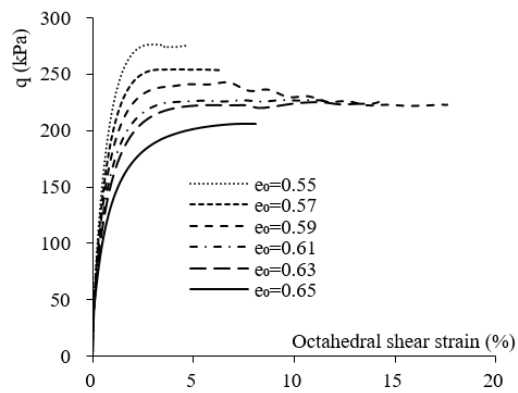

(a) Stress-strain curves

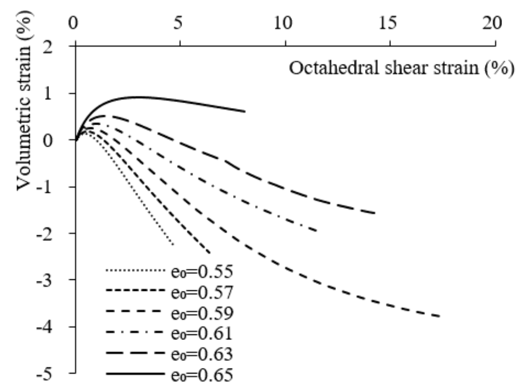

(b) Volumetric-shear strain curves

Figure 6.6: Results from simulations at different intial void ratios: Series SE

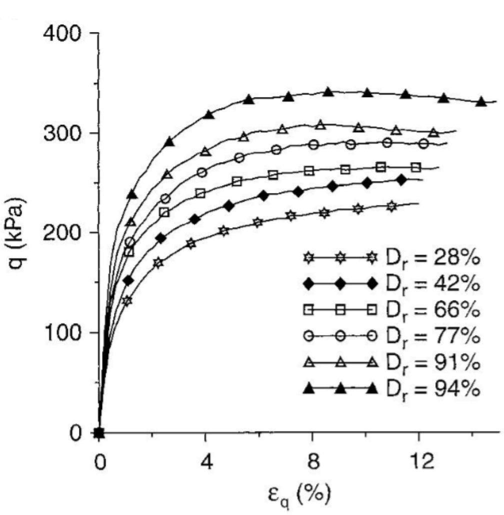

(a) Stress-strain curves

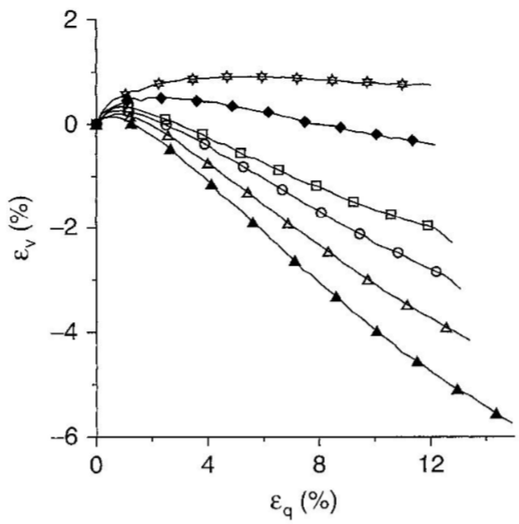

(b) Volumetric-shear strain curves

Figure 6.7: Results from triaxial compression tests on Karlsruhe sand at $p_0 = 100$ kPa (Kolymbas and Wu, 1990)

relative density increased from 52% ($e_0 = 0.65$) to 85% ($e_0 = 0.55$). With the same range of relative density (52%-85%), the maximum and minimum failure deviatoric stresses were $296.4kPa$ and $256.95kPa$, respectively, by interpolation of the results in Figure 6.7a.

Influence of loading direction α

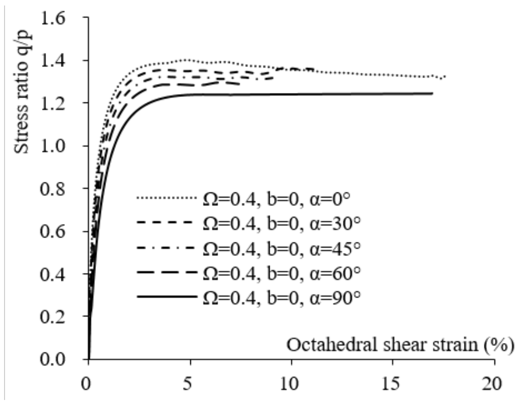

(a) Stress-strain curves: SA1 (Ω=0.4)

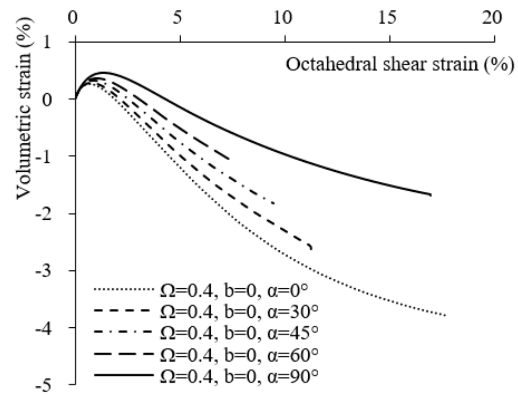

(b) Volumetric-shear strain curves: SA1

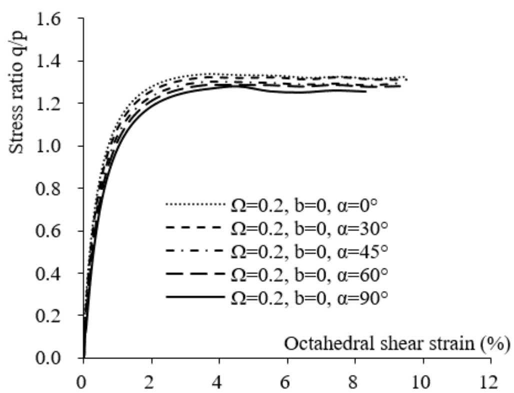

(c) Stress-strain curves: SA2 (Ω=0.2)

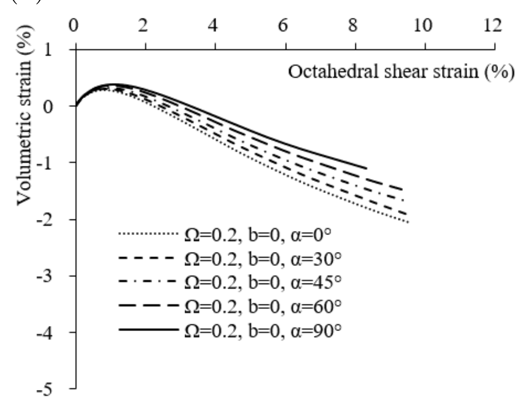

(d) Volumetric-shear strain curves: SA2

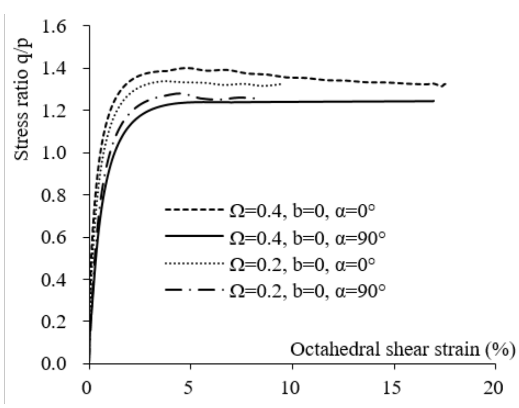

(e) Stress-strain curves: SA1 and SA2

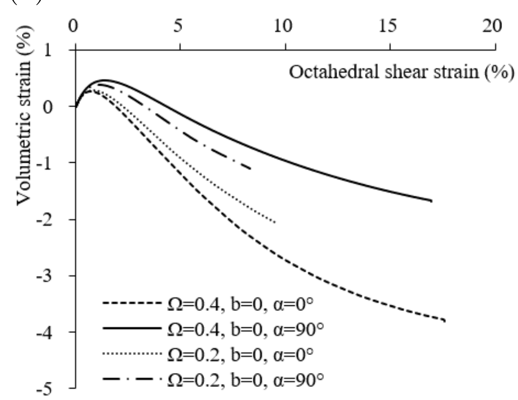

(f) Volumetric-shear strain curves: SA1 and SA2

Figure 6.8: Results from Series SA1 and SA2: influence of loading directions

Figure 6.8a presents the stress-strain curves from simulation Series SA1, in which α varied from $\alpha = 0°$ to $\alpha = 90°$. The volumetric-shear strain curves are shown in Figure 6.8b. The peak deviator stress tended to decrease with an increase of the inclination angle. As the strain level increased to approximately 10%, the difference between deviator stresses at different initial inclination angle tended to vanish. The volumetric-shear strain curves revealed that dilatancy decreased with an increase of the inclination angle. These observations were qualitatively in agreement with experimental results as well as with simulation results from the single-node model. It should be noted that the FEM simulations were carried out under conventional triaxial compression conditions, while the HCA experimental tests were performed under constant mean effective stress.

Figures 6.8c and 6.8d present the stress-strain curves and the volumetric-shear strain curves of Series SA2 simulations, respectively. By comparing the stress-strain curves with different initial anisotropy, as shown in Figures 6.8a and 6.8c, the peak deviator stress decreased with an increase of the inclination angle, particularly for simulations with higher initial anisotropy. By comparing the volumetric-shear strain curves with different initial anisotropy (6.8b and 6.8d), the dilatancy decreased with an increase of the inclination angle, which was similar to the experimental results. Again, the influence of the loading direction was more significant in simulations with higher initial anisotropy.

Figures 6.8e and 6.8f show the results at $\alpha = 0°$ and $\alpha = 90°$ only. With increased initial anisotropy, both the stress-strain curves and the volumetric-shear strain curves were more dispersed between $\alpha = 0°$ and $\alpha = 90°$ in Series SA1 than in Series SA2, which implies that the influence of loading direction was more significant for specimens with a higher degree of initial anisotropy.

Influence of multi-direction loading ratio $b^\star$

Figures 6.9a and 6.9b present the stress-strain curves and volumetric-shear strain curves for Series SB1 simulations with $b^\star$ varying from 0 to 1 and $\Omega = 0.4$. Both the peak deviator stress and the dilatancy decreased while the value of $b^\star$ increased. These observations were in agreement with the experimental results as well as simulation results from the single-node model.

The stress-strain curves of Series SB2 are shown in Figure 6.9c and the volumetric-shear strain curves are shown in Figure 6.9d. By comparing the stress-strain curves corresponding to different initial anisotropy presented in Figures 6.9a and 6.9c, it is observed that the peak deviator stress decreased with an increase of $b^\star$ in both series. By comparing the volumetric-shear strain curves at different initial anisotropy, presented in Figures 6.9b and 6.9d, one observes that the dilatancy decreased with an increase of $b^\star$, which agreed with the observations from the experimental study. However, unlike the influence of α, the influence of the loading path $b^\star$ was not significantly affected by increased initial anisotropy.

Figures 6.9e and 6.9f show the results with $b^\star = 0$ and $b^\star = 1$. The peak deviator stresses for both $b^\star = 0$ and $b^\star = 1$ increased slightly at higher initial anisotropy. The dilatancy in Series SB1 was larger than that in Series SB2 for each value of $b^\star$.

The results of simulations in Series SA1, SB1, SA2, and SB2 show that the proposed stress-strain model properly reflected the influence of initial anisotropy on granular soil behaviour. The effect of loading direction depended highly on the inherent anisotropy. The higher the initial degree of anisotropy, the more significant effect

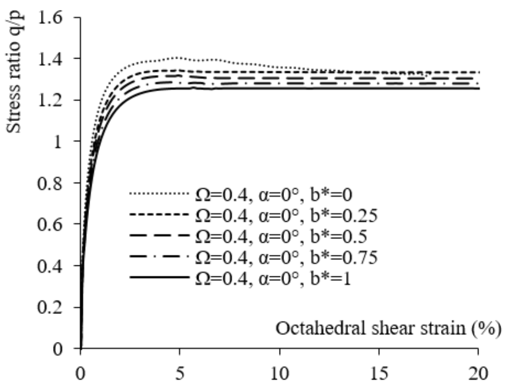

(a) Stress-strain curves: SB1 (Ω=0.4)

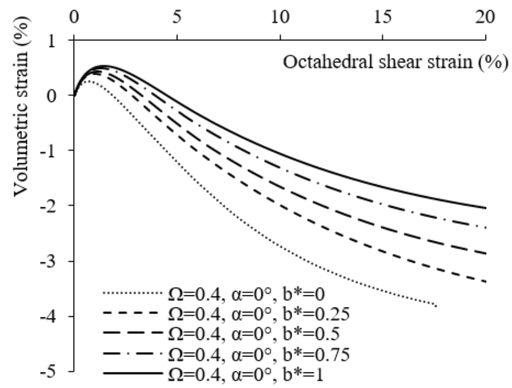

(b) Volumetric-shear strain curves: SB1

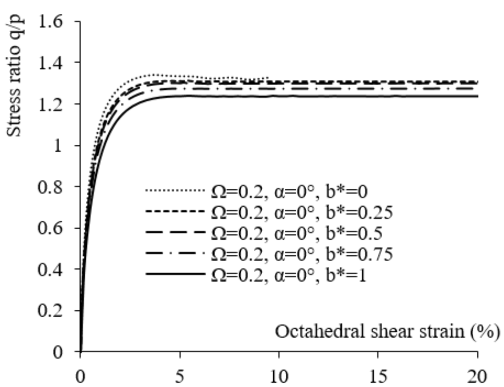

(c) Stress-strain curves: SB2 (Ω=0.2)

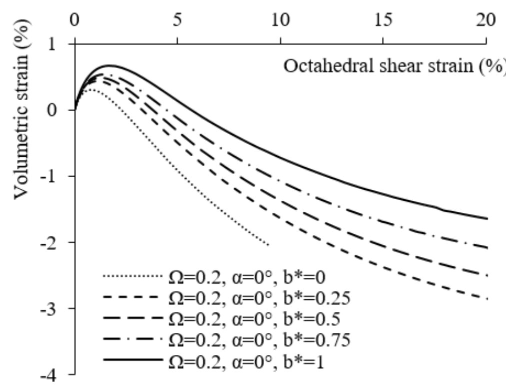

(d) Volumetric-shear strain curves: SB2

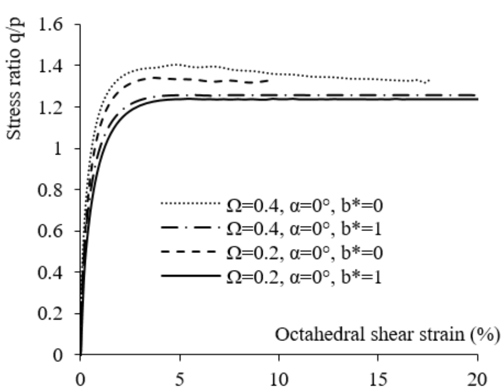

(e) Stress-strain curves: SB1 and SB2

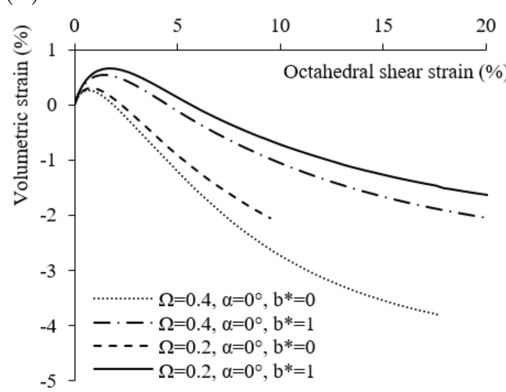

(f) Volumetric-shear strain curves: SB1 and SB2

Figure 6.9: Results from Series SB1 and SB2: influence of the multi-direction loading ratio $b^\star$

of the loading direction on the material's behaviour. The effect of loading path was mainly caused by the induced anisotropy, with the influence of initial anisotropy being limited.

Effect of loading direction on deformation in Series SA1 simulations

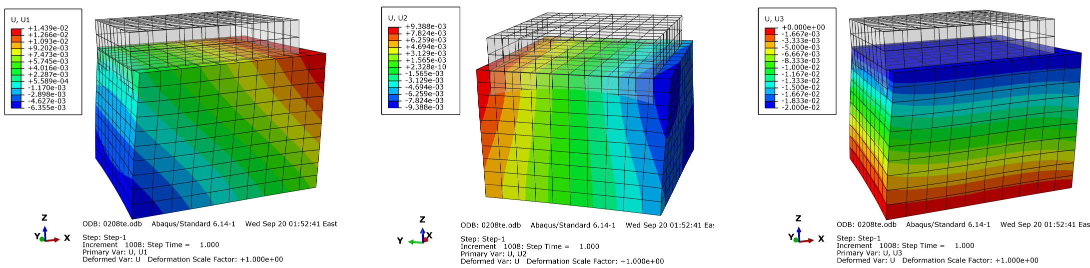

(a) x-displacement (b) y-displacement (c) z-displacement

Figure 6.10: Displacement components of SA1-2 ($\alpha = 30°$, $e_0 = 0.59$, $\gamma = 20\%$)

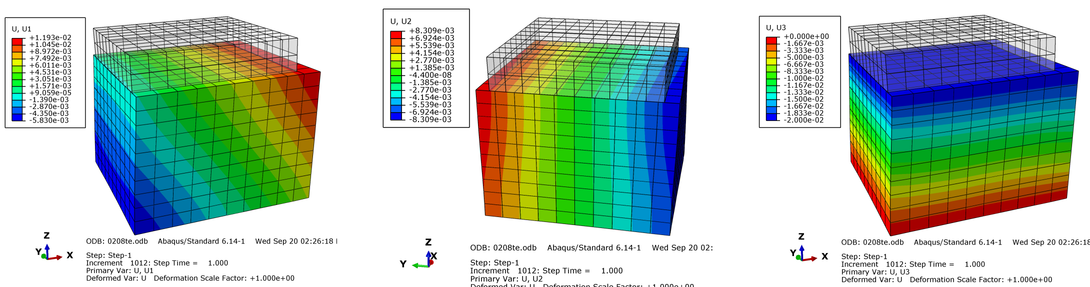

(a) x-displacement (b) y-displacement (c) z-displacement

Figure 6.11: Displacement components of SA1-3 ($\alpha = 45°$, $e_0 = 0.59$, $\gamma = 20\%$)

Figures 6.10 to 6.12 illustrate the distributions of u_x, u_y, and u_z at the shear strain level of 20% in Series SA1 simulations. In these simulations, b=0 with σ_2 parallel to the bedding plane and σ_1 making an inclination angle α with the normal of the bedding plane. As a result, the distribution of u_y was symmetric. The small non-uniformity in the distribution of u_y was related to the boundary constraint on

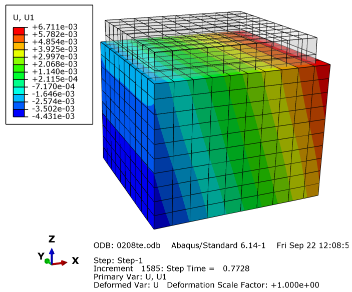

(a) x-displacement

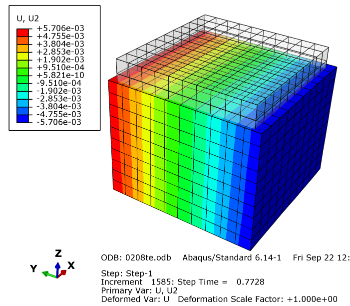

(b) y-displacement

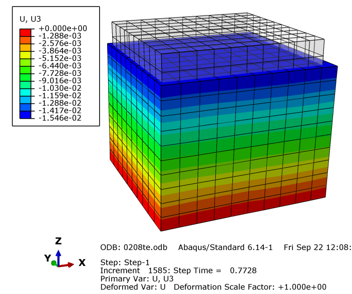

(c) z-displacement

Figure 6.12: Displacement components of SA1-4 ($\alpha = 60°$, $e_0 = 0.59$, $\gamma = 20\%$)

the bottom of the specimen. The distribution of u_x was significantly affected by the inclination angle α, with shear strain developing along the bedding plane. The results were consistent with laboratory observations.

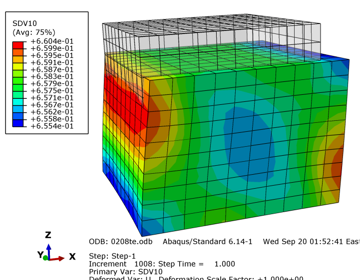

(a) SA1-2 ($\alpha = 30°$)

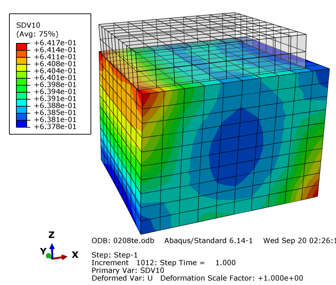

(b) SA1-3 ($\alpha = 45°$)

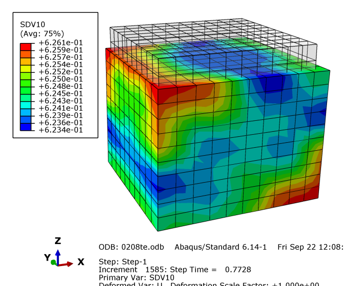

(c) SA1-4 ($\alpha = 60°$)

Figure 6.13: Distribution of void ratio e ($e_0 = 0.59$): influence of principal stress direction

Figure 6.13 presents the distribution of void ratio in specimens with different α at $\gamma = 20\%$. High void ratio zones induced by high local dilation were observed near the left upper corner and the lower right corner (the red areas), while a relative low-dilation zone was in the central domain of the specimens. If we connect these two red zones with locally high void ratios, an approximate shape of the original bedding plane can be observed. The local high-dilation zones were caused by local shear deformation parallel to the bedding plane. It is expected the shear band would initiate from these areas and would propagate nearly parallel to the bedding plane.

6.2 Numerical analysis of ground settlement on structured granular medium

This section presents FEM simulation results to investigate the capability of the proposed stress-strain model to determine the settlement of a cohesionless subgrade considering different bedding plane orientations induced by a uniformly distributed pressure on the ground surface.

6.2.1 FEM models

The discretizations and boundary conditions of the FE models are shown in Figure 6.14. The model was $3.2m$ in both length and width and $2m$ in depth. The surface load imprint was $0.4m \times 0.4m$. The bottom of the model (x-y plane) was constrained by the vertical displacement ($U3 = 0$), the left and right sides of the model (y-z planes) were constrained by the displacement in the x-direction ($U1 = 0$), and the front and back of the model (x-z planes) were constrained by the displacement in the y-direction ($U2 = 0$). The loading was applied at the center of the top surface (x-y plane), as shown in Figure 6.14b.

The unit weight of the material was $25kN/m^3$. It was assumed that the material's properties did not vary with depth. Other material properties are listed in Table 6.5, which were the same as those used in Chapter 4. The same material subroutine (UMAT) as that in the element study was used. The element type was C3D8 with full integration.

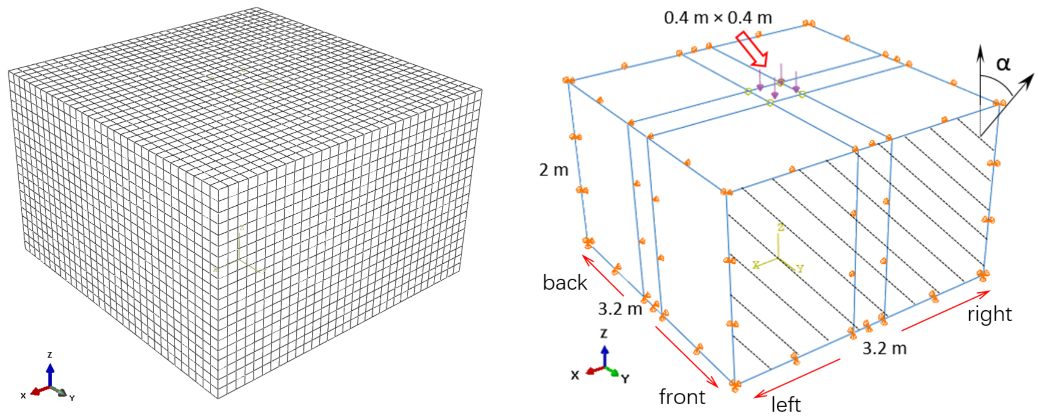

(a) (b)

Figure 6.14: Mesh and boundary conditions for the FEM model

Table 6.5: Material parameters of Ottawa sand

$G_0 = 2750kPa$	$v = 0.29$	$e_{cr0} = 0.74$	$\varphi_{cv} = 30°$
$h_l = 426.8MPa$	$n_l = 0.43$	$a = 0.004$	$\beta = 2.3$
$h_{cr} = 2867MPa$	$n_{cr} = 0.232$	$m = 5.3$	$k = 0.065$
$d = 1$	$\Omega = 0.25$	$e_0 = 0.59$	

Three series of simulations were performed with different pressures ($200kPa$ and $300kPa$) and different initial void ratios ($e_0 = 0.59$ and $e_0 = 0.61$), see Table 6.6. The bedding plane inclination angle α, as shown in Figure 6.14b, varied from 0° to 90°, with $\alpha = 0°$ corresponding to a horizontal bedding plane.

Different meshes were used to assess the sensitivity of the solution to element sizes, as shown in Figure 6.15. The element size and number of elements from the different meshes are shown in Table 6.7.

Table 6.6: FEM simulation matrix for ground settlement

Pressure: 200kPa						Pressure: 300kPa		
Series No.	α	e_0	Series No.	α	e_0	Series No.	α	e_0
BP1-1	0°	0.59	BP2-1	0°	0.61	BP3-1	0°	0.59
BP1-2	15°	0.59	-			BP3-2	15°	0.59
BP1-3	30°	0.59	BP2-2	30°	0.61	BP3-3	30°	0.59
BP1-4	45°	0.59	-			BP3-4	45°	0.59
BP1-5	60°	0.59	BP2-3	60°	0.61	BP3-5	60°	0.59
BP1-6	75°	0.59	-			BP3-6	75°	0.59
BP1-7	90°	0.59	BP2-4	90°	0.61	BP3-7	90°	0.59

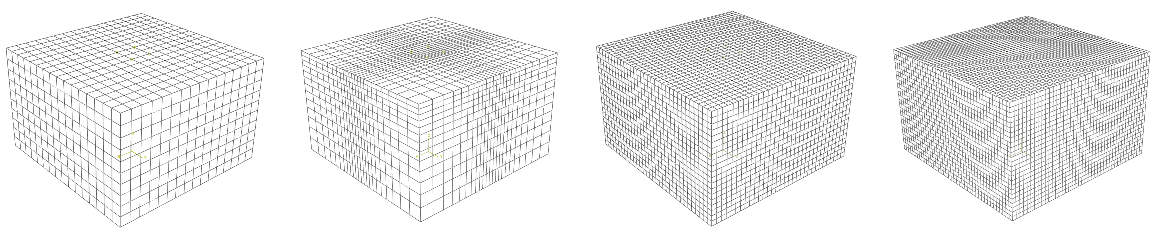

(a) Coarse (b) Partial densified (c) Fine (d) Very-fine

Figure 6.15: Finite element discretization with different mesh densities

6.2.2 Mesh sensitivity

Figure 6.16 presents the load-settlement curves obtained using different meshes when the pressure was gradually increased to $25kPa$ for $\alpha = 0°$. Except for the coarse mesh with $20cm \times 20cm \times 20cm$ elements, the results obtained using other three meshes were close to each other. In other words, even though increased element sizes caused numerical integration errors, owing to the nonlinearity of the model, the results were not very sensitive to mesh density. When assuming the results using the very-fine

Table 6.7: Element size and number of different meshes

Mesh type	Coarse	Partial densified	Fine	Very-fine
Element size (cm)	20×20×20	8×8×8∼25×25×25	10×10×10	8×8×8
Number of elements	2560	6877	20480	42025

mesh were the most reliable, relative errors of the results from the other three meshes (averaged from data at $5kPa$, $10kPa$, $15kPa$, $20kPa$, and $25kPa$) were given in Table 6.8. However, the CPU time of the very-fine mesh was almost 4 hours for one simulation (CPU: Intel Core i5-7400T, RAM: 12GB), compared with approximately one hour when using the fine mesh. It should be noted that the mesh with partial densification on the loading area was the most efficient. Using the result from the very-fine mesh for the comparison, the relative error from the partial densified mesh was only 0.5% larger than that from the fine mesh, but the CPU time of the former was seven times less.

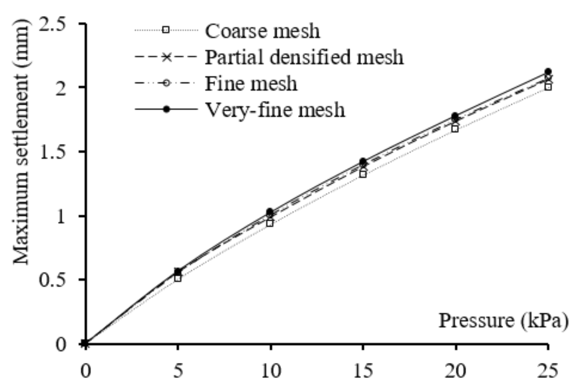

Figure 6.16: Comparison of the results from different meshes (25kPa)

Table 6.8: Sensitivity to mesh densities

Mesh	Number of elements	Relative error	CPU time (sec)
Coarse	2560	7.82%	177
Partial densified	6877	2.41%	402
Fine	20480	1.98%	3911
Very-fine	42025	-	13293

To further study the model's sensitivity to the mesh density, the coarse, fine, and very-fine meshes were all used to simulate case BP1-1. The load-settlement curves are shown in Figure 6.17. The maximum settlements at $200kPa$ from the simulations using the coarse, fine, and very-fine meshes were $10.26mm$, $10.95mm$, and $11.17mm$, respectively. The relative errors of the results when using the fine and coarse meshes were 1.96% and 8.14%, respectively. These results are similar to the errors shown in Table 6.8. It is concluded that the fine mesh in Figure 6.15 can provide reasonable accuracy ($< 2\%$) with relatively high efficiency.

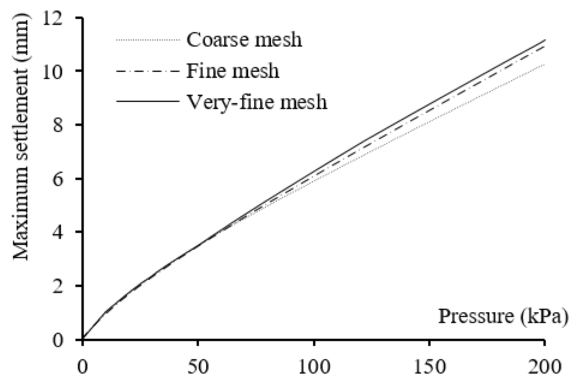

Figure 6.17: Comparison of the results from different meshes (200kPa)

6.2.3 Simulation results

For the FEM simulations, before applying the surface pressure, a geostatic step was used to generate the geostatic stress field in the ground. At the end of this step, the maximum displacement was in the order of $10^{-18}m$ (see Figure 6.18a), which was negligible. Figures 6.18b presents the displacement distributions after the loading step under loading of $200kPa$ at $\alpha = 30°$.

Figures 6.19a shows the variation of the maximum settlement from simulations BP1 at $e_0 = 0.59$ under the pressure level of $200kPa$. With an increase of α, the maximum settlement increased and reached the peak value at $\alpha = 90°$. In simulation

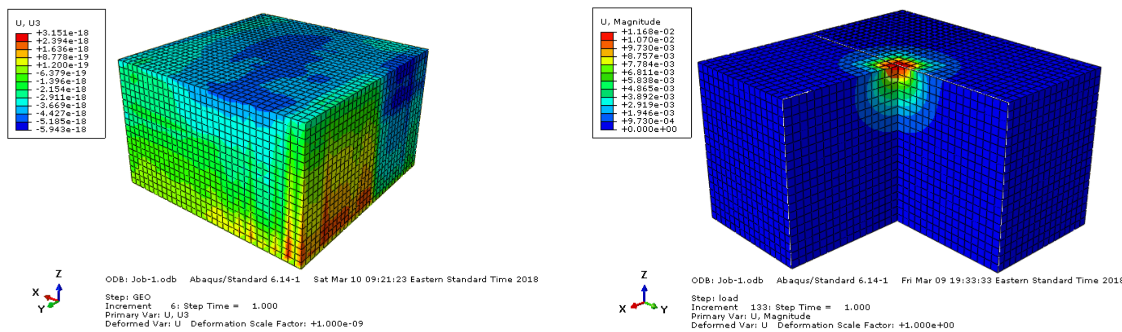

(a) after the geostatic step (b) after the loading step

Figure 6.18: Displacement distribution (U3) from the simulation BP1-3

with $\alpha = 90°$, the maximum settlement was $11.99mm$, 10.81% larger than the maximum settlement of $10.82mm$ at $\alpha = 0°$. More detailed results of the settlement can be found in Appendix (see Figure 6.25).

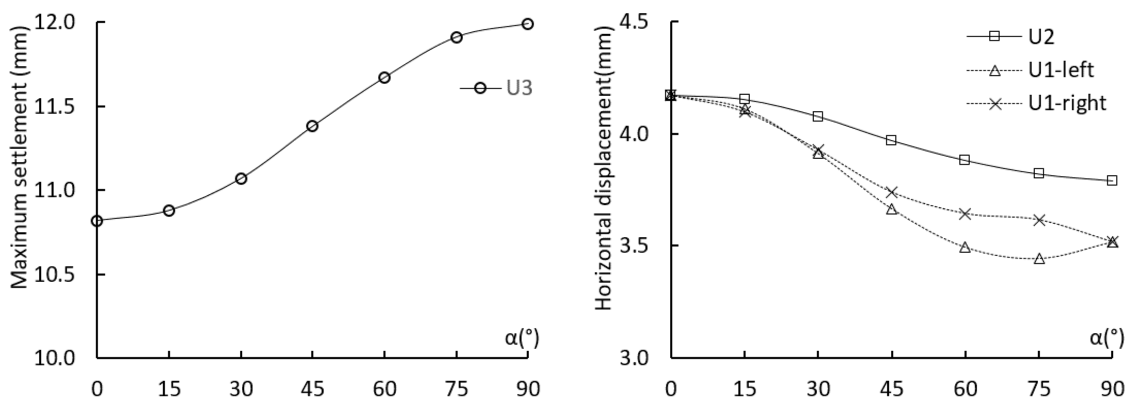

(a) Maximum settlement (b) Horizontal displacement

Figure 6.19: Variation of displacement with α from simulation Series BP1

Figures 6.19b shows the variations of the horizontal displacements U1 and U2 with different α from Series BP1 simulations. Since the bedding plane was inclined in the $x - z$ plane as shown in Figure 6.14b, the displacement in the $y-$dirction (U2) should be symmetrical about the $x - z$ plane. This is confirmed from Figures 6.24b, 6.24d, 6.24f, and 6.24h. However, U2 decreased from BP1-1 to BP1-7 with the increase of α as U3 increased. At $\alpha = 0°$, since the ground was cross-anisotropic, the displacement in the $x-$dirction (U1) was symmetrical, and the displacements U1 and U2 were idential, as shown in Figures 6.24a and 6.24b. When $0° < \alpha < 90°$, U1 was non-symmetrical about the $y-z$ plane. As α increased, U1 became larger in the right side than in the left side. Herein, the "left" and "right" sides were defined in Figure 6.14b. For $\alpha = 30°$, the difference was approximately 0.4%. This difference increased to 2.0% at $\alpha = 45°$, 4.3% at $\alpha = 60°$, and 5.0% at $\alpha = 75°$, respectively. At $\alpha = 90°$, the distribution of U1 became symmetrical again. However, a 7.8% difference was found between U1 and U2. These results revealed the influence of the bedding plane orientation on the horizontal displacement field. The detailed results of the horizontal displacement can be found in the Appendix (Figure 6.24). Results from Series BP2 simulations revealed similar responses at a higher initial void ratio of $e_0 = 0.61$, see Figures 6.20.

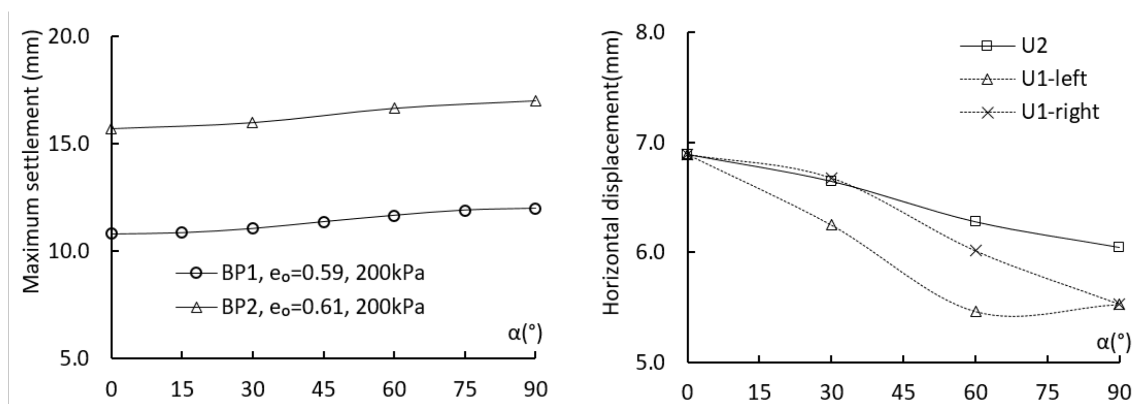

(a) Maximum settlement (BP1 and BP2) (b) Horizontal displacement (BP2)

Figure 6.20: Variation of displacement with α from simulation Series BP2

When the applied pressure was increased to 300kPa, as shown in Figure 6.21 for simulation Series BP3, the maximum settlement increased with α first and reached the peak at approximately $\alpha = 30°$, and decreased slightly afterward. The maximum settlement was 23.38mm at $\alpha = 30°$, 7.1% larger than that at $\alpha = 0°$, which was 21.83mm. At $\alpha = 90°$, the maximum settlement was 22.7mm, 4.0% larger than that at $\alpha = 0°$. At this pressure level, the range around the loading area has reached large strain levels (>5%). Therefore the displacement field was not entirely in agreement with the material response from the element tests. The formation of failure surfaces under the high pressure level may have attributed to the larger settlements in simulations with $\alpha = 30°$ to $\alpha = 60°$. This can also explain the large difference between the left and right sides of the U1 displacement. As shown in Figure 6.22a, the maximum displacement U1 on the right side was 20.5% larger than that on the left side when $\alpha = 45°$. From Figure 6.22b, heave was observed on the ground surface around the loading area, especially on the right side.

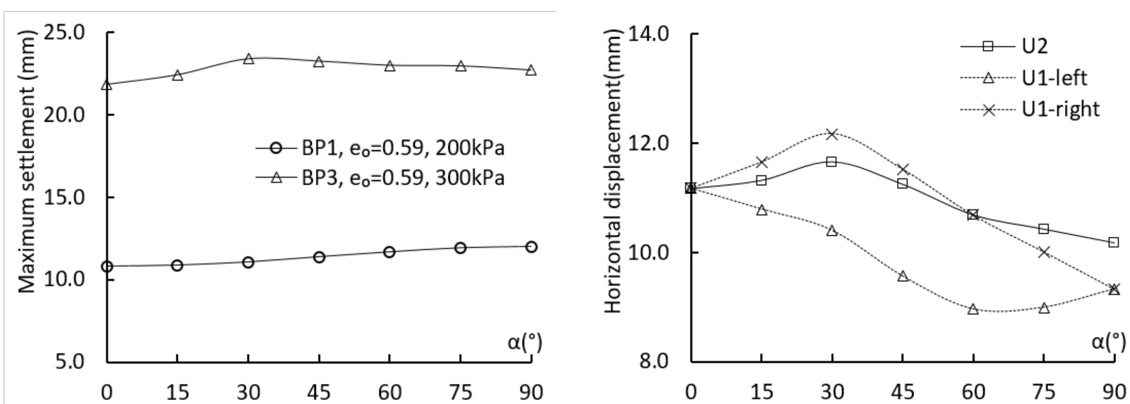

(a) Maximum settlement (BP1 and BP3) (b) Horizontal displacement (BP3)

Figure 6.21: Variation of displacement with α from simulation Series BP3

The influence of α on the stress distribution can be observed from Figures 6.26, 6.27 and 6.28 in the Appendix (for Series BP1). For $\alpha = 0°$ and $\alpha = 90°$, the fabric components in the ground were symmetric along each direction (x, y, and z) during

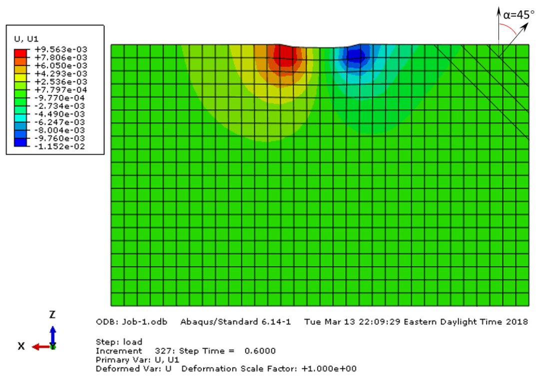

(a) Horizontal displacement (U1)

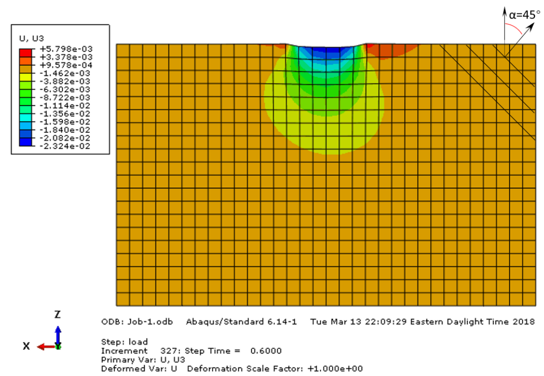

(b) Vertical displacement (U3)

Figure 6.22: Displacement fields from simulation BP3-4 (300kPa, $\alpha = 45°$)

loading. Thus the stress distributions were symmetric in each direction. For all other simulations from $\alpha = 15°$ to $\alpha = 75°$, unsymmetrical distributions of stress were observed in the $x-$direction (S1) as well as $z-$direction (S3). Similar to U2, the distribution of S2 was also symmetric about the $x - z$ plane. From the distribution of S1 and S3, it is also noted that the higher stresses were found on the right sides, where there were larger displacements (U1 and U3). It can be concluded that the model has properly reflected the general trends of stress and displacement responses of a sandy ground with different bedding plane orientations. However, verification for the accuracy of results from the numerical simulation is still necessary.

6.3 Conclusions

This chapter presents simulation results of boundary value problems based on the model developed in Chapter 4. A user-defined subroutine UMAT was developed for incorporating the stress-strain model into ABAQUS. In closing, the following remarks are made:

1. The comparison between the FEM simulation results and the laboratory test results (HCA test, Series B) in Chapter 4 confirm the appropriateness of the algorithm for implementation of the stress-strain model into ABAQUS.

2. The proposed model and the algorithm can properly simulate the density dependency of structured granular materials. In general with an increase of the void ratio, the peak deviator stress and the tendency of dilation both decreased. The results were consistent with experimental data.

3. The proposed stress-strain model and the developed numerical algorithm can simulate the directional dependency and stress path dependency of anisotropy granular materials. It was proven that the model could account for the anisotropy behaviour under generalized stress conditions. Different initial degrees of anisotropy were used. It was observed that an increase of initial anisotropy largely increases the directional dependency of material, which is dominated by inherent anisotropy, while the influence of higher initial anisotropy on the stress path dependency of material was limited. These results agreed with observations from laboratory tests.

4. FEM simulations were performed for the boundary value problem to determine pressure-induced ground settlement of sand with different bedding plane orientations. It was found that the settlements had a clear dependency on the inclination angle of the bedding plane in addition to the initial void ratio.

6.4 Appendix 1: Numerical integration of constitutive relations

When implementing a stress-strain model in ABAQUS through UMAT, the key is to determine the constitutive matrix at the current stress state. Starting from an equilibrium state at time t_0, ABAQUS performs an incremental loading and provides the subroutine UMAT with the initial 6-component stress vector $\boldsymbol{\sigma}(t_0)$ $[\sigma_{11}, \sigma_{22}, \sigma_{33}, \sigma_{12}, \sigma_{23}, \sigma_{13}]^T$, 6-component strain vector $\boldsymbol{\varepsilon}(t_0)$ $[\varepsilon_{11}, \varepsilon_{22}, \varepsilon_{33}, \varepsilon_{12}, \varepsilon_{23}, \varepsilon_{13}]^T$, void ratio $e(t_0)$, 9-component fabric vector $\boldsymbol{F}(t_0)$ $[F_{11}, F_{22}, F_{33}, F_{12}, F_{21}, F_{23}, F_{32}, F_{13}, F_{31}]^T$, and the strain increment vector $\Delta\boldsymbol{\varepsilon}(t_0)$ for time increment Δt. The strain increment vector is calculated by ABAQUS using the current Jobabian matrix. Based on the current stress state and the relevant state variables, the subroutine UMAT supplies ABAQUS with the updated stress vector $\boldsymbol{\sigma}(t_0 + \Delta t)$, which is updated according to the constitutive law as well as the derivative of $\boldsymbol{\sigma}$ with respect to the strain increment, known as the Jacobian (C_{Jac}). Following the determination of $\boldsymbol{\sigma}(t_0 + \Delta t)$, the fabric components are updated. Since the stress-strain relation depended on the fabric state, this process must be iterated according to the following steps for an initial state of $\boldsymbol{\sigma}(t_0)$, $\boldsymbol{\varepsilon}(t_0)$, $e(t_0)$, $\boldsymbol{F}(t_0)$ at time t_0 in step n:

1. Given the strain increment vector $\Delta\boldsymbol{\varepsilon}(t_0)$;

2. Based on the current Jacabian, an estimated $(\Delta\boldsymbol{\sigma})_0$ is obtained using

$$(\Delta\boldsymbol{\sigma})_0 = (\frac{\partial \Delta\boldsymbol{\sigma}}{\partial \Delta\boldsymbol{\varepsilon}})_n \Delta\boldsymbol{\varepsilon}(t_0) \tag{6.1}$$

3. Based on current stress increment $(\Delta\boldsymbol{\sigma})_0$, the fabric vector $\boldsymbol{F}$ and dilatancy factor D are updated.

4. The stress increment vector $(\Delta\boldsymbol{\sigma})_1$ is calculated using Equation (4.38),

$$(\Delta\boldsymbol{\sigma})_1 = [\boldsymbol{D}^{ep}]\Delta\boldsymbol{\varepsilon} \tag{6.2}$$

with

$$[\boldsymbol{D}^{ep}] = [\boldsymbol{D}^e] - \frac{1}{H}([\boldsymbol{D}^e]\frac{\partial g_s}{\partial\boldsymbol{\sigma}}(\frac{\partial f_s}{\partial\boldsymbol{\sigma}})^T[\boldsymbol{D}^e])$$

5. Steps 3 and 4 are repeated, using $(\Delta\boldsymbol{\sigma})_k$ instead of $(\Delta\boldsymbol{\sigma})_0$ with k being the iteration counter until the following convergence requirement is satisfied:

$$|\frac{(\Delta\boldsymbol{\sigma})_{k+1} - (\Delta\boldsymbol{\sigma})_k}{(\Delta\boldsymbol{\sigma})_k}| \leq 10^{-5}$$

The updated stress increment vector $\Delta\boldsymbol{\sigma}$ and $[\boldsymbol{D}^{ep}]$ are saved.

6. The stress vector, void ratio and the fabric vector are all updated as $\boldsymbol{\sigma}(t_0 + \Delta t) = \boldsymbol{\sigma}(t_0) + \Delta\boldsymbol{\sigma}$, $e(t_0 + \Delta t) = e(t_0) + \dot{\varepsilon}_v(1 + e_0)$, and $\boldsymbol{F}(t_0 + \Delta t) = \boldsymbol{F}(t_0) + \Delta\boldsymbol{F}$. It should be noted that $\Delta\boldsymbol{F}$ is calculated based on $\Delta\boldsymbol{\sigma}$ according to the fabric evolution law.

Figure 6.23 presents the flowchart of the UMAT subroutine. While the stress and strain components of an integration point are saved automatically by ABAQUS, the fabric components and void ratio must be saved as state variables. To achieve a higher rate of convergence, the Jacobian components are also stored as state variables, see Table 6.9.

Table 6.9: Quantities saved as state variables in UMAT

	Fabric components	Void ratio	Jacobian components
State variables	1-9	10	11-46

To call the UMAT subroutine, the following command lines must be added to the

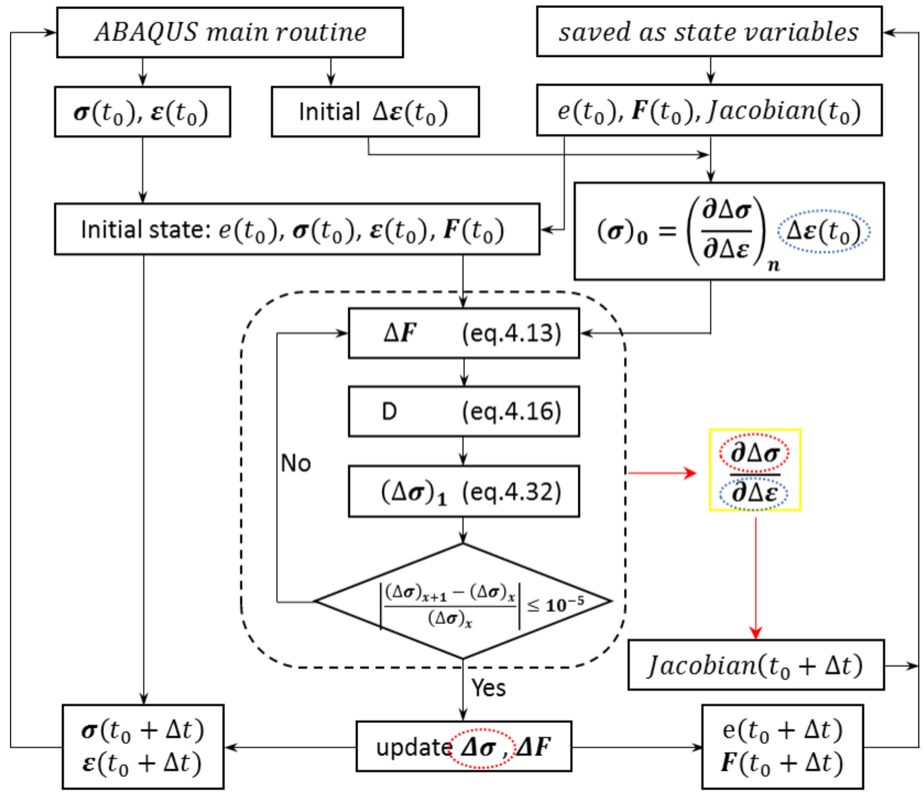

Figure 6.23: Flowchart for the UMAT procedure

ABAQUS job file (*.inp) to define the material. The material, denoted as 'Material-1', has 46 solution-dependent state variables and 10 input parameters.

*** MATERIALS*

**Material, name=Material-1*

**Depvar*

46,

**User Material, constants=10, unsymm*

2750., 0.29, 0.74, 30., 4268., 0.43, 2867., 0.232

0.59, 0.25

The UMAT subroutine shares 37 quantities with the ABAQUS main routine.

Using the following header, the information of stresses, strains and Jacobian are passed to UMAT from ABAQUS solver.

```
      subroutine umat(stress,statev,ddsdde,sse,spd,scd,rpl,
     & ddsddt,drplde,drpldt,stran,dstran,time,dtime,temp,
     & dtemp,predef,dpred,cmname,ndi,nshr,ntens,nstatv,
     & props,nprops,coords,drot,pnewdt,celent,dfgrd0,dfgrd1,
     & noel,npt,layer,kspt,kstep,kinc)
      implicit none
      character*8 cmname
```

6.5 Appendix 2: Simulation results from BP1

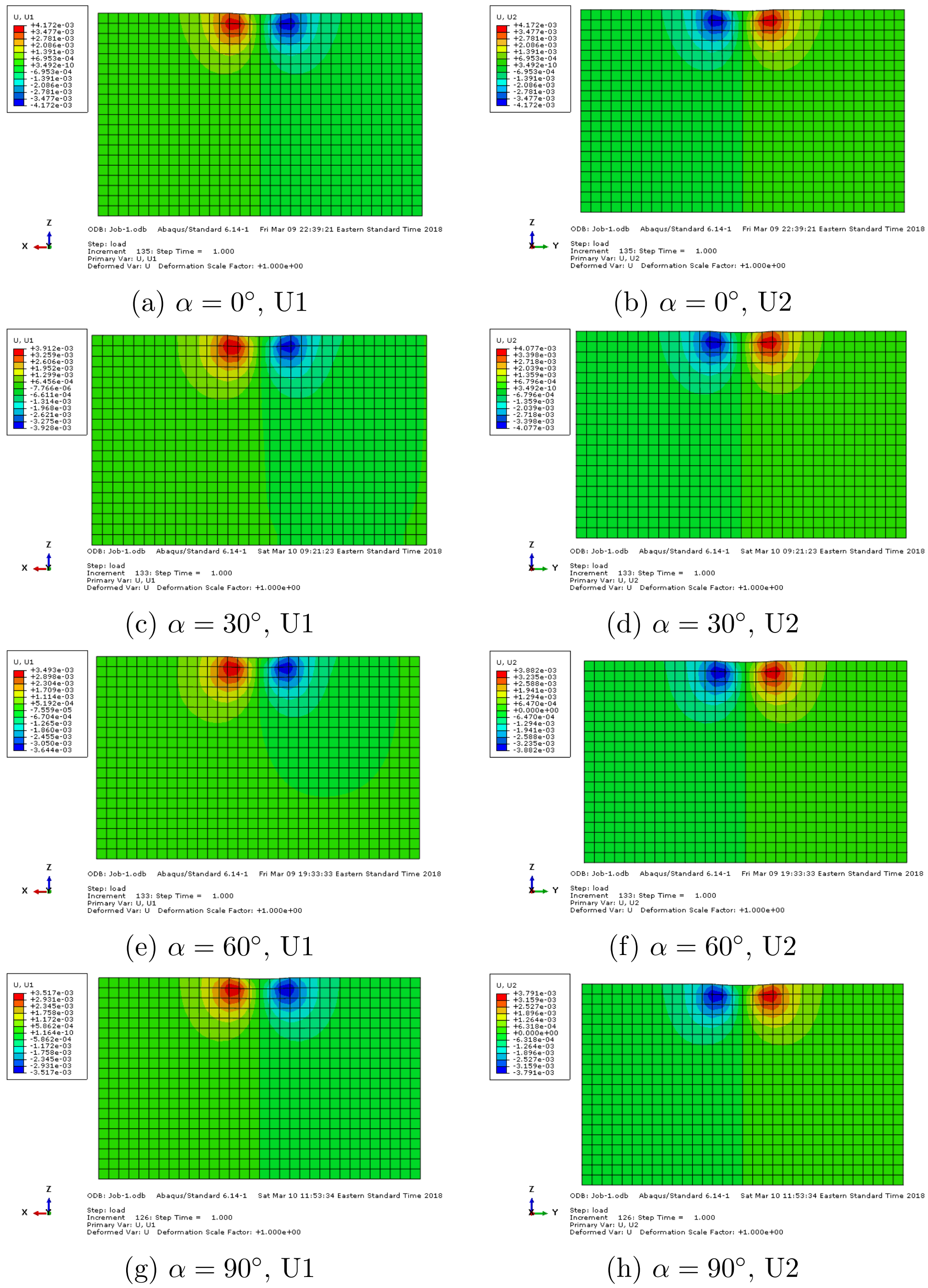

(a) $\alpha = 0°$, U1
(b) $\alpha = 0°$, U2
(c) $\alpha = 30°$, U1
(d) $\alpha = 30°$, U2
(e) $\alpha = 60°$, U1
(f) $\alpha = 60°$, U2
(g) $\alpha = 90°$, U1
(h) $\alpha = 90°$, U2

Figure 6.24: Displacement distributions (U1 and U2) from simulations BP1 ($200kPa$)

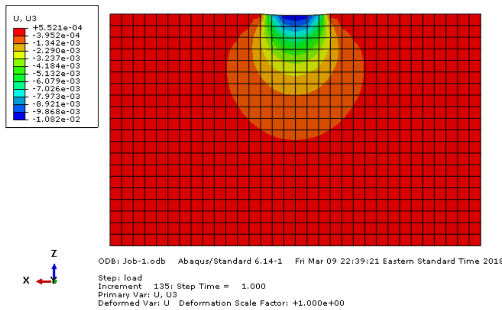

(a) $\alpha = 0°$, U3

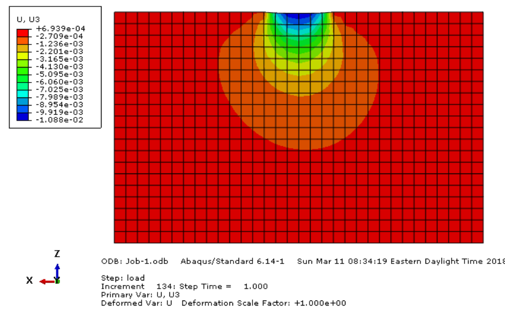

(b) $\alpha = 15°$, U3

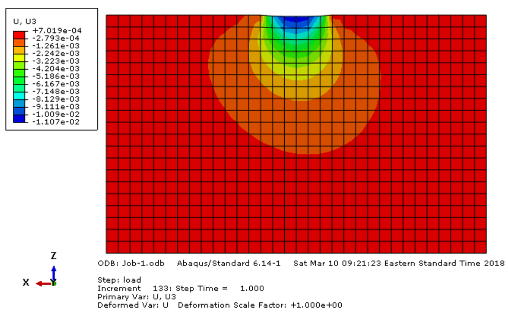

(c) $\alpha = 30°$, U3

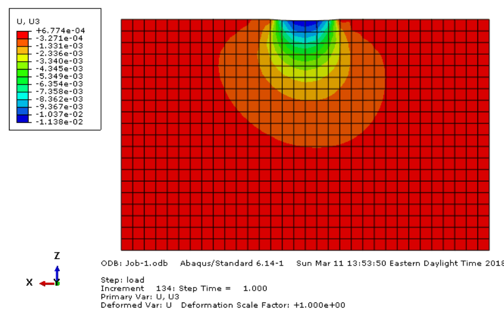

(d) $\alpha = 45°$, U3

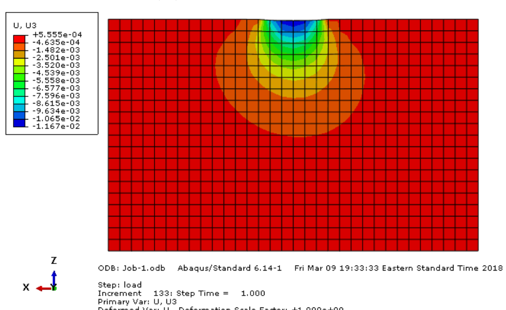

(e) $\alpha = 60°$, U3

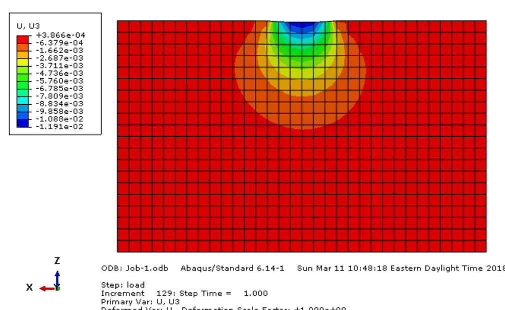

(f) $\alpha = 75°$, U3

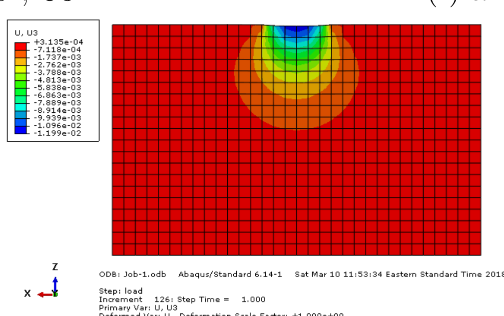

(g) $\alpha = 90°$, U3

Figure 6.25: Displacement distributions (U3) from simulations BP1 ($200kPa$)

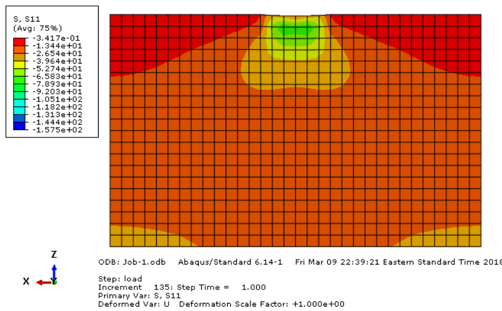

(a) $\alpha = 0°$, S1

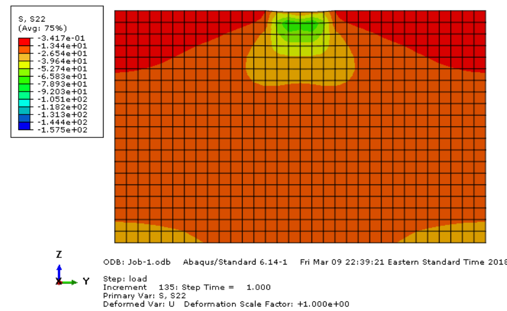

(b) $\alpha = 0°$, S2

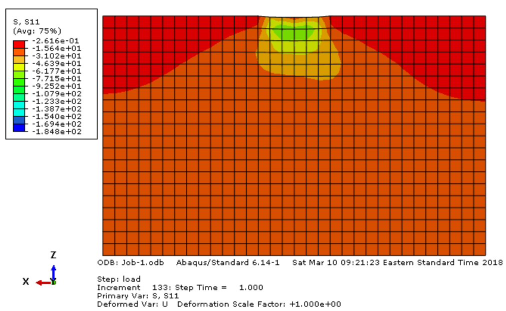

(c) $\alpha = 30°$, S1

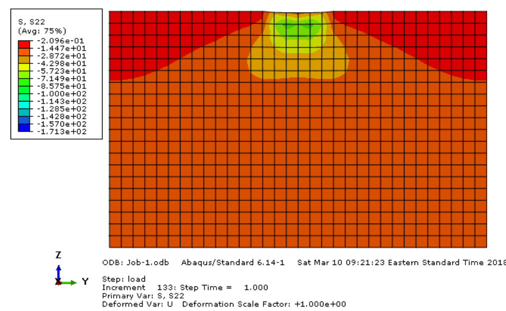

(d) $\alpha = 30°$, S2

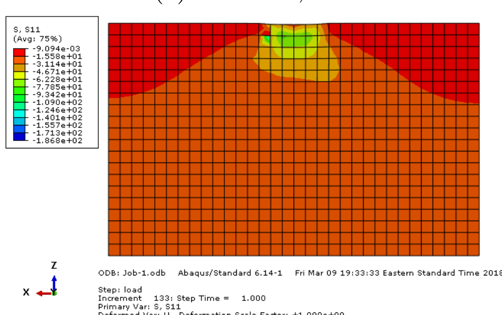

(e) $\alpha = 60°$, S1

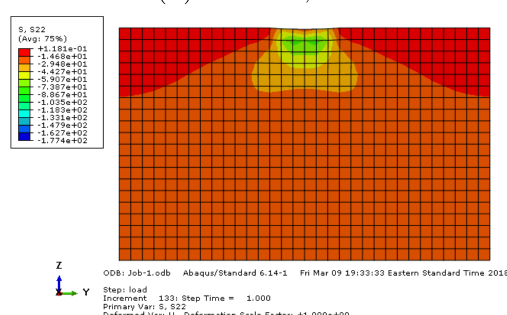

(f) $\alpha = 60°$, S2

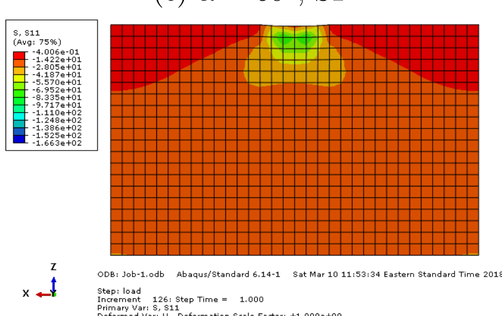

(g) $\alpha = 90°$, S1

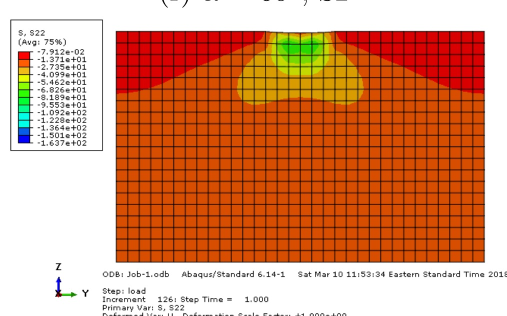

(h) $\alpha = 90°$, S2

Figure 6.26: Stress distributions (S1 and S2) from simulations BP1 ($200kPa$)

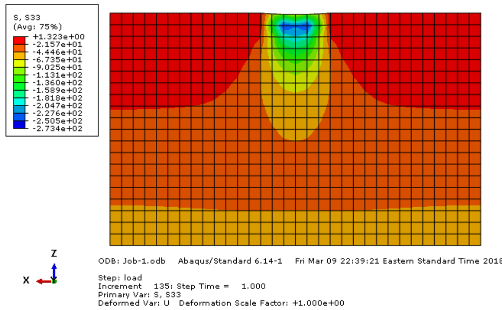

(a) $\alpha = 0°$, S3

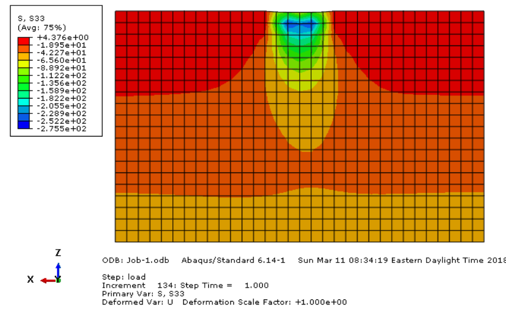

(b) $\alpha = 15°$, S3

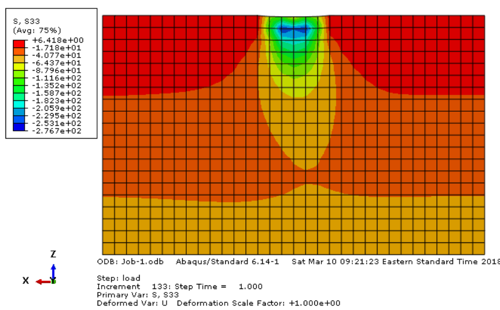

(c) $\alpha = 30°$, S3

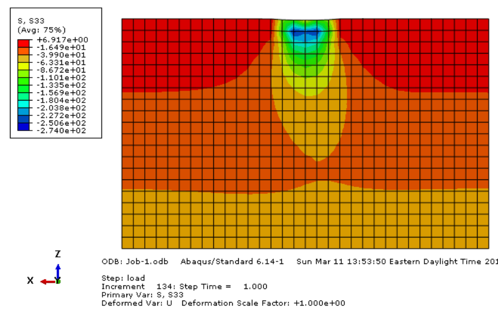

(d) $\alpha = 45°$, S3

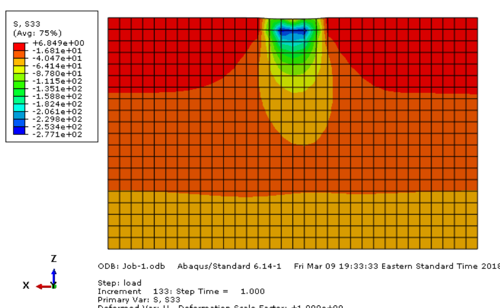

(e) $\alpha = 60°$, S3

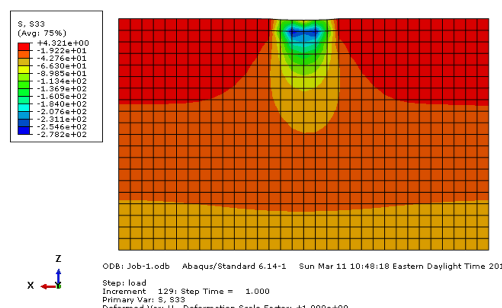

(f) $\alpha = 75°$, S3

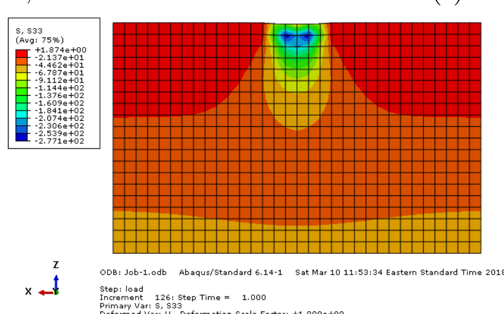

(g) $\alpha = 90°$, S3

Figure 6.27: Stress distributions (S3) from simulations BP1 ($200kPa$)

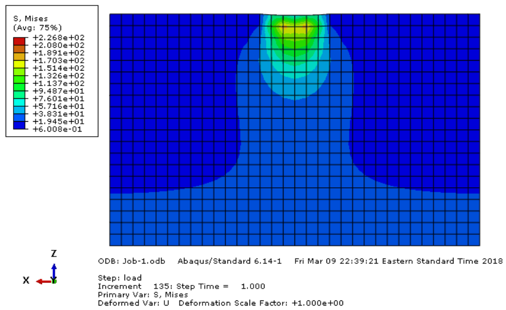

(a) $\alpha = 0°$

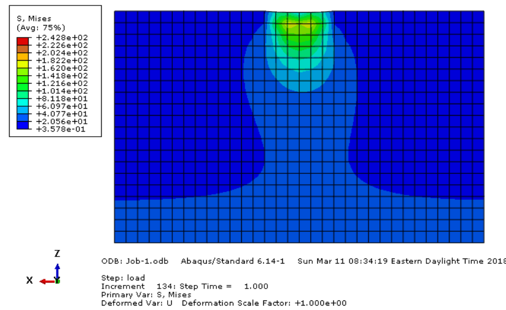

(b) $\alpha = 15°$

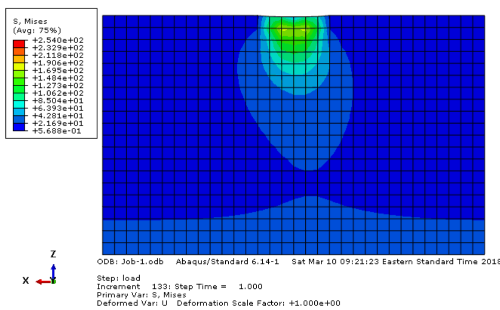

(c) $\alpha = 30°$

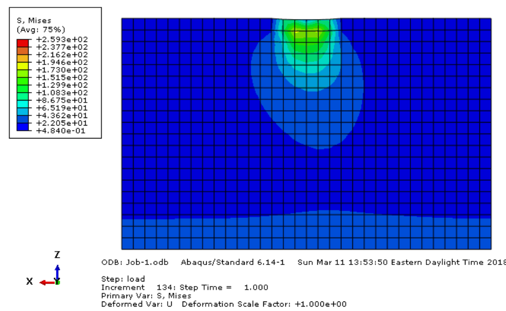

(d) $\alpha = 45°$

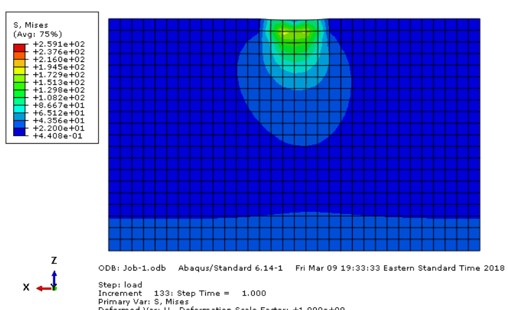

(e) $\alpha = 60°$

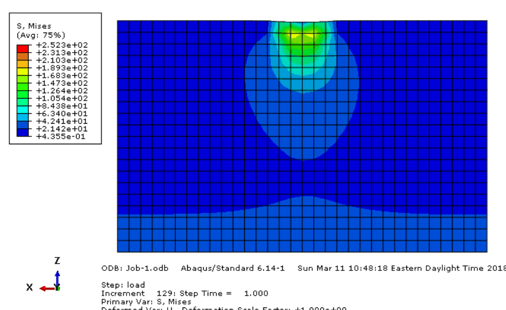

(f) $\alpha = 75°$

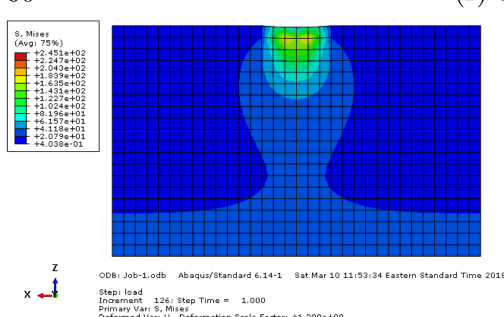

(g) $\alpha = 90°$

Figure 6.28: Mises stress distributions from simulations BP1 ($200kPa$)

Chapter 7

Summary and conclusions

This study focused on the development of a comprehensive constitutive model to describe the behaviour of structured granular soils under generalized stress conditions. The main contributions accomplished in this thesis are summarized as follows:

1. A comprehensive experimental study using a hollow cylinder apparatus was carried out to investigate the behaviour of Ottawa sand subjected to both monotonic and cyclic loading under general stress conditions. In the monotonic loading test, both the strength and dilatancy of sand was shown to decrease notably with an increase of the intermediate principal stress coefficient or the angle between the major principal directions of the stress and fabric tensors. At a select mean effective stress level, the highest shear resistance was found to be achieved when the major principal stress direction is perpendicular to the bedding plane.

2. The experimental data for the stress states at failure indicated that the benchmarked Matsuoka-Nakai and Lade failure criteria are only valid when the intermediate principal stress coefficient b and the angle α between the major principal directions of the stress and fabric tensors satisfy $b = sin^2\alpha$.

3. When subjected cyclic loading, in addition to the stress level and applied strain amplitudes, the accumulative volume change was observed to depend on the direction of cyclic loading relative to the direction of the bedding plane. For the same cyclic deviatoric stress amplitude, cyclic stresses perpendicular to the bedding plane tended to induce less accumulative volumetric compaction.

4. Under the same conditions, for a given cyclic deviatoric stress amplitude, multi-directional cyclic loading was found to cause larger accumulative volumetric compaction. Changes of the cyclic loading direction during cyclic loading induced immediate increases of volumetric compaction of a specimen.

5. The concept of the critical state fabric surface was proposed. On the π-plane, the critical fabric surface was assumed to take the shape of the inverted Lade's failure surface. A fabric evolution law was established based on this concept and the additional assumption that the incremental fabric change is proportional to the incremental stress tensor.

6. Based on the critical state fabric surface, a modified stress-dilatancy formulation was proposed to describe the effect of fabric and loading direction on shear-induced volume change of granular materials. A complete constitutive model was thus built within the framework of the theory of elasto-plasticity, in which the modified stress-dilatancy formulation was used as a flow rule.

7. The developed stress-strain model was verified using the laboratory test results. The capability of the model was further examined by simulating the behaviour of granular materials of different initial fabric and void ratio states along different stress paths. It was confirmed that the proposed model can reasonably reproduce the observed deformation feature of sand with the effect of inherent fabric, intermediate

principal stresses and the loading direction measured by the angle between the major principal directions of the stress and fabric tensors.

8. By implementing the concept of hypo-plasticity and adopting a kinematic hardening law, the constitutive model developed for monotonic loading was extended to describe the behaviour of granular material subjected to repeated loading with the influence of fabric being considered. The model was then used to simulate the behaviours of sand subjected to various modes of cyclic stress conditions, including one-way cyclic loading, multi-directional cyclic loading, cyclic loading with jump of cyclic loading directions.

9. After being verified using laboratory test results, the proposed constitutive model was implemented into the FEM software package ABAQUS to solve boundary-valued problems. In particular, the numerical implementation of the model was achieved by implementing the constitutive model into ABAQUS through a user-defined subroutine UMAT to determine pressure-induced ground settlement of sand with different bedding plane orientations. The FEM modelling results revealed the dependency of settlements on the inclination angle of the bedding plane in addition to the initial void ratio of the soil.

In addition to the theoretical aspects, the outcomes and findings of this research can be used to solve the practical engineering problems involving cyclic loading. For example, the developed stress-strain model can be used to simulate the performance of bridge approach embankment of integral abutment bridge (IAB), where the granular backfill is subject to cyclic loads from both vertical (traffic loads) and horizontal directions (induced by the movement of the abutment owing to thermal expansion of the structure). Similar circumstances can be found for coastal structures, the foundation of offshore wind power plants, machine foundations, etc. The compaction of granular soil under moving vibratory equipment can also be simulated by the developed approach since it is essentially a problem involving cyclic loading with continuous principal stress rotation.

It is recommended that the following work should be considered in the future.

1. Further DEM investigations on the fabric evolution of granular materials should be carried out to verify the assumption regarding the critical fabric state and to verify the fabric evolution law. The effects of particle shape, particle size as well as gradation on the ultimate fabric state surface should also be studied.

2. The proposed model should be used to solve additional boundary-valued problems involving cyclic loading. Proper measurement in reduced scale model tests or in-situ tests should be obtained to verify the performance of the model, particularly regarding its capability to model cyclic loading histories.

Bibliography

Abelev, A. V. and Lade, P. V. (2004). Characterization of failure in cross-anisotropic soils. *Journal of Engineering Mechanics*, **130**(5), 599–606.

Allersma, H. (1982). Photo-elastic stress analysis and strains in simple shear. In *IUTAM Conf. deformation and failure of granular materials, Delft*, pages 345–353.

Allersma, H. G. (1998). Using imaging technologies in experimental geotechnics. In *Imaging Technologies: Techniques and Applications in Civil Engineering. Second International Conference.*

Alshibli, K. A. and Sture, S. (2000). Shear band formation in plane strain experiments of sand. *Journal of Geotechnical and Geoenvironmental Engineering*, **126**(6), 495–503.

Andrade, J. E. and Tu, X. (2009). Multiscale framework for behavior prediction in granular media. *Mechanics of Materials*, **41**(6), 652–669.

Antony, S., Momoh, R., and Kuhn, M. (2004). Micromechanical modelling of oval particulates subjected to bi-axial compression. *Computational materials science*, **29**(4), 494–498.

Arthur, J. and Menzies, B. (1972). Inherent anisotropy in a sand. *Geotechnique*, **22**(1), 115–128.

Arthur, J., Chua, K., and Dunstan, T. (1977). Induced anisotropy in a sand. *Geotechnique*, **27**(1), 13–30.

Bagi, K. (1996). Stress and strain in granular assemblies. *Mechanics of materials*, **22**(3), 165–177.

Bardet, J. (1986). Bounding surface plasticity model for sands. *Journal of engineering mechanics*, **112**(11), 1198–1217.

Barreto, D. and O'Sullivan, C. (2012). The influence of inter-particle friction and the intermediate stress ratio on soil response under generalised stress conditions. *Granular Matter*, pages 1–17.

Been, K. and Jefferies, M. G. (1985). A state parameter for sands. *Géotechnique*, **35**(2), 99–112.

Bésuelle, P., Viggiani, G., Lenoir, N., Desrues, J., and Bornert, M. (2006). X-ray micro ct for studying strain localization in clay rocks under triaxial compression. In *GEOX 2006-2nd International Workshop on X-Ray CT for geomaterials*, pages 35–52. ISTE.

Biarez, J. and Wiendieck, K. (1963). La comparaison qualitative entre lanisotropie mécanique et lanisotropie de structure. *Comptes Rendus de lAcadémie des Sciences*, **254**, 2712–2714.

Bigoni, D. and Piccolroaz, A. (2004). Yield criteria for quasibrittle and frictional materials. *International journal of solids and structures*, **41**(11), 2855–2878.

Cai, Y., Yu, H.-S., Wanatowski, D., and Li, X. (2012). Noncoaxial behavior of sand under various stress paths. *Journal of Geotechnical and Geoenvironmental Engineering*, **139**(8), 1381–1395.

Callisto, L. and Calabresi, G. (1998). Mechanical behaviour of a natural soft clay. *Géotechnique*, **48**(4), 495–513.

Casagrande, A. and Carillo, N. (1944). Shear failure of anisotropic materials. *Journal of Boston Society of Civil Engineers*, **31**(4), 74–81.

Chang, C. and Hicher, P.-Y. (2005). An elasto-plastic model for granular materials with microstructural consideration. *International journal of solids and structures*, **42**(14), 4258–4277.

Chaudhary, S. K., Kuwano, J., Hashimoto, S., Hayano, Y., and Nakamura, Y. (2002). Effects of initial fabric and shearing direction on cyclic deformation characteristics of sand. *Soils and foundations*, **42**(1), 147–157.

Chen, H., Yu, T., Wang, X., and Liu, Z. (2005). *Elasticity and plasticity*. China Architecture & Building Press.

Chowdhury, E. and Nakai, T. (1998). Consequences of the tij-concept and a new modeling approach. *Computers and Geotechnics*, **23**(3), 131–164.

Coulomb, C. (1773). Test on the applications of the rules of maxima and minima to some problems of statics related to architecture. *Mem. Math. Phys*, **7**, 343–382.

Cresswell, A., Barton, M. E., and Brown, R. (1999). Determining the maximum density of sands by pluviation.

Cundall, P. and Strack, O. (1979). A discrete numerical model for granular assemblies. *Géotechnique*, **29**(1), 47–65.

Dafalias, Y. F. (1986a). An anisotropic critical state soil plasticity model. *Mechanics Research Communications*, **13**(6), 341–347.

Dafalias, Y. F. (1986b). Bounding surface plasticity. i: Mathematical foundation and hypoplasticity. *Journal of Engineering Mechanics*, **112**(9), 966–987.

Dafalias, Y. F. and Popov, E. P. (1977). Cyclic loading for materials with a vanishing elastic region. *Nuclear Engineering and Design*, **41**(2), 293–302.

Desrues, J., Lanier, J., and Stutz, P. (1985). Localization of the deformation in tests on sand sample. *Engineering fracture mechanics*, **21**(4), 909–921.

Drucker, D. C. and Prager, W. (1952). Soil mechanics and plastic analysis or limit design. *Quarterly of applied mathematics*, **10**(2), 157–165.

Ellyin, F. (1989). An anisotropic hardening rule for elastoplastic solids based on experimental observations. *Journal of applied mechanics*, **56**(3), 499–507.

Finge, Z., Doanh, T., and Dubujet, P. (2006). Undrained anisotropy of hostun rf loose sand: new experimental investigations. *Canadian geotechnical journal*, **43**(11), 1195–1212.

Gajo, A. and Wood, M. (1999). Severn–trent sand: a kinematic-hardening constitutive model: the q–p formulation. *Géotechnique*, **49**(5), 595–614.

Georgiannou, V., Tsomokos, A., and Stavrou, K. (2008). Monotonic and cyclic behaviour of sand under torsional loading. *Geotechnique*, **58**(2), 113–124.

Goddard, J. and Didwania, A. (1998). Computations of dilatancy and yield surfaces for assemblies of rigid frictional spheres. *Quarterly Journal of Mechanics & Applied Mathematics*, **51**(1).

Guo, P. (2000). *Modelling granular materials with respect to stress-dilatancy and fabric: A fundamental approach*. Ph.D. thesis, University of Calgary.

Guo, P. (2008). Modified direct shear test for anisotropic strength of sand. *Journal of geotechnical and geoenvironmental engineering*, **134**(9), 1311–1318.

Hardin, B. O. (1989). Low-stress dilation test. *Journal of Geotechnical Engineering*, **115**(6), 769–787.

Hareb, H. and Doanh, T. (2012). Probing into the strain induced anisotropy of hostun rf loose sand. *Granular Matter*, **14**(5), 589–605.

Haruyama, M. (1981). Anisotropic deformation-strength characteristics of an assembly of spherical particles under three dimensional stresses. *Soils and foundations*, **21**(4), 41–55.

Hight, D., Gens, A., and Symes, M. (1983). The development of a new hollow cylinder apparatus for investigating the effects of principal stress rotation in soils. *Geotechnique*, **33**(4), 355–383.

Ishihara, K. and Okada, S. (1978). Effects of stress history on cyclic behavior of sand. *Soils and Foundations*, **18**(4), 31–45.

Iskander, M. (1997). A transparent material to model the geotechnical properties of soils. In *Proc. XIV International Conference on Soil Mechanics and Foundation Engineering*. Balkema.

Iskander, M. G., Lai, J., Oswald, C. J., and Mannheimer, R. J. (1994). Development of a transparent material to model the geotechnical properties of soils.

Iwasaki, T., Tatsuoka, F., and Takagi, Y. (1978). Shear moduli of sands under cyclic torsional shear loading. *Soils and Foundations*, **18**(1), 39–56.

Kandasami, R. K. and Murthy, T. G. (2015). Experimental studies on the influence of intermediate principal stress and inclination on the mechanical behaviour of angular sands. *Granular Matter*, **17**(2), 217–230.

Ken-Ichi, K. (1984). Distribution of directional data and fabric tensors. *International Journal of Engineering Science*, **22**(2), 149–164.

Kirkgard, M. and Lade, P. V. (1993). Anisotropic three-dimensional behavior of a normally consolidated clay. *Canadian Geotechnical Journal*, **30**(5), 848–858.

Kolymbas, D. (1991). An outline of hypoplasticity. *Archive of applied mechanics*, **61**(3), 143–151.

Kolymbas, D. and Wu, W. (1990). Recent results of triaxial tests with granular materials. *Powder Technology*, **60**(2), 99–119.

Lade, P. V. (1977). Elasto-plastic stress-strain theory for cohesionless soil with curved yield surfaces. *International Journal of Solids and Structures*, **13**(11), 1019–1035.

Lade, P. V. and Duncan, J. M. (1975a). Cubical triaxial tests on cohesionless soil. *Journal of geotechnical and geoenvironmental engineering*, **101**(ASCE# 11269 Proceeding).

Lade, P. V. and Duncan, J. M. (1975b). Elastoplastic stress-strain theory for cohesionless soil. *Journal of Geotechnical and Geoenvironmental Engineering*, **101**(ASCE# 11670 Proceeding).

Lade, P. V. and Musante, H. M. (1978). Three-dimensional behavior of remolded clay. *Journal of the Geotechnical Engineering Division*, **104**(2), 193–209.

Lade, P. V., Rodriguez, N. M., and Van Dyck, E. J. (2013). Effects of principal stress directions on 3d failure conditions in cross-anisotropic sand. *Journal of Geotechnical and Geoenvironmental Engineering*, **140**(2), 04013001.

Lade, P. V., Rodriguez, N. M., and Van Dyck, E. J. (2014a). Effects of principal stress directions on 3d failure conditions in cross-anisotropic sand. *Journal of Geotechnical and Geoenvironmental Engineering*, **140**(2), 04013001.

Lade, P. V., Van Dyck, E., and Rodriguez, N. M. (2014b). Shear banding in torsion shear tests on cross-anisotropic deposits of fine nevada sand. *Soils and Foundations*, **54**(6), 1081–1093.

Lam, W.-K. and Tatsuoka, F. (1988). Effects of initial anisotropic fabric and $\sigma 2$ on strength and deformation characteristics of sand. *Soils and Foundations*, **28**(1), 89–106.

Leroueil, S. and Hight, D. (2003). Behaviour and properties of natural soils and soft rocks. *Characterisation and engineering properties of natural soils*, **1**, 29–254.

Li, X. and Dafalias, Y. F. (2000). Dilatancy for cohesionless soils. *Geotechnique*, **50**(4), 449–460.

Li, X. and Li, X.-S. (2009). Micro-macro quantification of the internal structure of granular materials. *Journal of engineering mechanics*, **135**(7), 641–656.

Li, X. S. and Dafalias, Y. F. (2012). Anisotropic critical state theory: role of fabric. *Journal of Engineering Mechanics*, **138**(3), 263–275.

Lions, J. L. and Duvaut, G. (1976). *Inequalities in mechanics and physics*. Springer.

Liu, M. D. and Indraratna, B. N. (2010). General strength criterion for geomaterials including anisotropic effect. *International Journal of Geomechanics*, **11**(3), 251–262.

Maeda, K., Hirabayashi, H., Ohmura, A., Hyodo, M., Murata, H., and Nakata, Y. (2006). Micromechanical influence of grain properties on deformationfailure behaviors of granular media by dem. *Proc. of Geomechnics and Geotechnics of Particulate Media*, pages 173–179.

Manzari, M. T. and Dafalias, Y. F. (1997). A critical state two-surface plasticity model for sands. *Geotechnique*, **47**(2), 255–272.

Masson, S. and Martinez, J. (2001). Micromechanical analysis of the shear behavior of a granular material. *Journal of Engineering Mechanics*, **127**(10), 1007–1016.

Matsuoka, H. (1974). Stress-strain relationships of sands based on the mobilized plane. *Soils and foundations*, **14**(2), 47–61.

Matsuoka, H. and Nakai, T. (1974). Stress-deformation and strength characteristics of soil under three different principal stresses. In *Proc. JSCE*, volume 232, pages 59–70.

Matsuoka, H. and Nakai, T. (1977). Stress-strain relationship of soil based on the smp. In *Proceedings of specialty session*, volume 9, pages 153–162.

McDowell, D. (1985). A two surface model for transient nonproportional cyclic plasticity. *ASME J. Appl. Mech*, **52**, 298–308.

Meyerhof, G. (1978). Bearing capacity of anisotropic cohesionless soils. *Canadian Geotechnical Journal*, **15**(4), 592–595.

Mises, R. v. (1913). Mechanik der festen krper im plastisch- deformablen zustand. *Nachrichten von der Gesellschaft der Wissenschaften zu Gttingen, Mathematisch-Physikalische Klasse*, **1913**, 582–592.

Miura, K., MiuRA, S., and TOKI, S. (1986). Deformation behavior of anisotropic dense sand under principal stress axes rotation. *Soils and Foundations*, **26**(1), 36–52.

Miura, S. and Toki, S. (1984a). Anisotropy in mechanical properties and its simulation of sands sampled from natural deposits. *Soils and foundations*, **24**(3), 69–84.

Miura, S. and Toki, S. (1984b). Elastoplastic stress-strain relationship for loose sands with anisotropic fabric under three-dimensional stress conditions. *Soils and foundations*, **24**(2), 43–57.

Mogi, K. (1971). Fracture and flow of rocks under high triaxial compression. *Journal of Geophysical Research*, **76**(5), 1255–1269.

Mohr, O. (1900). Welche umstände bedingen die elastizitätsgrenze und den bruch eines materials. *Zeitschrift des Vereins Deutscher Ingenieure*, **46**(1524-1530), 1572–1577.

Moosbrugger, J. and McDowell, D. (1990). A rate-dependent bounding surface model with a generalized image point for cyclic nonproportional viscoplasticity. *Journal of the Mechanics and Physics of Solids*, **38**(5), 627–656.

Ng, T.-T. (2004). Shear strength of assemblies of ellipsoidal particles. *Geotechnique*, **54**(10), 659–669.

Ng, T.-T. (2005). Behavior of gravity deposited granular material under different stress paths. *Canadian geotechnical journal*, **42**(6), 1644–1655.

Nicot, F., Darve, F., and Group, R. (2005). A multi-scale approach to granular materials. *Mechanics of materials*, **37**(9), 980–1006.

Niemunis, A., Wichtmann, T., and Triantafyllidis, T. (2005). A high-cycle accumulation model for sand. *Computers and geotechnics*, **32**(4), 245–263.

Ochiai, H. and Lade, P. V. (1983). Three-dimensional behavior of sand with anisotropic fabric. *Journal of Geotechnical Engineering*, **109**(10), 1313–1328.

Oda, M. (1972a). Initial fabrics and their relations to mechanical properties of granular material. *Soils and foundations*, **12**(1), 17–36.

Oda, M. (1972b). The mechanism of fabric changes during compressional deformation of sand. *Soils and foundations*, **12**(2), 1–18.

Oda, M. (1981). Anisotropic strength of cohesionless sands. *Journal of Geotechnical and Geoenvironmental Engineering*, **107**(ASCE 16491).

Oda, M. (1982). Fabric tensor for discontinuous geological materials. *Soils and Foundations*, **22**(4), 96–108.

Oda, M. (1993). Inherent and induced anisotropy in plasticity theory of granular soils. *Mechanics of Materials*, **16**(1), 35–45.

Oda, M. and Koishikawa, I. (1979). Effect of strength anisotropy on bearing capacity of shallow footing in a dense sand. *Soils and foundations*, **19**(3).

Oda, M. and Konishi, J. (1974a). Microscopic deformation mechanism of granular material in simple shear. *Soils and foundations*, **14**(4), 25–38.

Oda, M. and Konishi, J. (1974b). Rotation of principal stresses in granular material during simple shear. *Soils and foundations*, **14**(4), 39–53.

Oda, M., Koishikawa, I., and Higuchi, T. (1978). Experimental study of anisotropic shear strength of sand by plane strain test. *Soils and foundations*, **18**(1), 25–38.

Oda, M., Konishi, J., and Nemat-Nasser, S. (1980). Some experimentally based fundamental results on the mechanical behaviour of granular materials. *Geotechnique*, **30**(4), 479–495.

Oda, M., Nemat-Nasser, S., and Konishi, J. (1985). Stress-induced anisotropy in granular masses. *Soils and foundations*, **25**(3), 85–97.

Ohno, N. and Kachi, Y. (1986). A constitutive model of cyclic plasticity for nonlinear hardening materials. *Journal of Applied Mechanics*, **53**(2), 395–403.

Ouadfel, H. and Rothenburg, L. (2001). Stress–force–fabric'relationship for assemblies of ellipsoids. *Mechanics of Materials*, **33**(4), 201–221.

Park, C. and Tatsuoka, F. (1994). Anisotropic strength and deformation in sands in plane strain compression. In *Proc., 13th Int. Conf. on Soil Mechanics and Foundation Engineering*, volume 1, pages 1–4. CRC.

Pietruszczak, S. (2010). *Fundamentals of plasticity in geomechanics*. Crc Press.

Pietruszczak, S. and Krucinski, S. (1989). Description of anisotropic response of clays using a tensorial measure of structural disorder. *Mechanics of Materials*, **8**(2-3), 237–249.

Pradhan, T. B., TATSUOKA, F., and HORII, N. (1988). Strength and deformation characteristics of sand in torsional simple shear. *Soils and Foundations*, **28**(3), 131–148.

Reddy, K. R. and Saxena, S. K. (1993). Effects of cementation on stress-strain and strength characteristics of sands. *Soils and Foundations*, **33**(4), 121–134.

Roscoe, K. H., Schofield, A., and Wroth, C. (1958). On the yielding of soils. *Geotechnique*, **8**(1), 22–53.

Rowe, P. W. (1962). The stress-dilatancy relation for static equilibrium of an assembly of particles in contact. In *Proceedings of the royal society of London a: mathematical, physical and engineering sciences*, volume 269, pages 500–527. The Royal Society.

Saada, A., Zaman, M., Gioda, G., and Booker, J. (2000). Laboratory testing for the validation of constitutive models. *Modelling in geomechanics. Edited by M. Zaman, G. Gioda, and J. Booker. John Wiley and Sons Ltd., Chichester, New York*, pages 247–265.

Sadek, S., Iskander, M. G., and Liu, J. (2002). Geotechnical properties of transparent silica. *Canadian Geotechnical Journal*, **39**(1), 111–124.

Satake, M. (1982). Fabric tensor in granular materials. In *Proc., IUTAM Symp. on Deformation and Failure of Granular materials, Delft, The Netherlands.*

Sãyao, A. and Vaid, Y. (1991). A critical assessment of stress nonuniformities in hollow cylinder test specimens. *Soils and foundations*, **31**(1), 60–72.

Sãyao, A. and Vaid, Y. (1996). Effect of intermediate principal stress on the deformation response of sand. *Canadian Geotechnical Journal*, **33**(5), 822–828.

Sazzad, M. M. (2014). Micro-scale behavior of granular materials during cyclic loading. *Particuology*, **16**, 132–141.

Sazzad, M. M. and Suzuki, K. (2010). Micromechanical behavior of granular materials with inherent anisotropy under cyclic loading using 2d dem. *Granular Matter*, **12**(6), 597–605.

Schofield, A. and Wroth, P. (1968). Critical state soil mechanics.

Shibuya, S. and Hight, D. (1987). A bounding surface for granular materials. *Soils and Foundations*, **27**(4), 123–136.

Siddiquee, M., Tatsuoka, F., Tanaka, T., Tani, K., Yoshida, K., and Morimoto, T. (2001). Model tests and fem simulation of some factors affecting the bearing capacity of a footing on sand. *Soils and foundations*, **41**(2), 53–76.

Suzuki, K. and Kuhn, M. R. (2013). Discrete element simulations of cyclic biaxial shear of a granular material with oval particles. *International Journal of Geomechanics*, **14**(3), 06014005.

Symes, M., Gens, A., and Hight, D. (1984). Undrained anisotropy and principal stress rotation in saturated sand. *Geotechnique*, **34**(1), 11–27.

Symes, M., Gens, A., and Hight, D. (1988). Drained principal stress rotation in saturated sand. *Geotechnique*, **38**(1), 59–81.

Takemura, T., Takahashi, M., Oda, M., Hirai, H., Murakoshi, A., and Miura, M. (2007). Three-dimensional fabric analysis for anisotropic material using multi-directional scanning lineapplication to x-ray ct image. *Materials transactions*, **48**(6), 1173–1178.

Tatsuoka, F. (2000). Impacts on geotechnical engineering of several recent findings from laboratory stress-strain tests on geomaterials. *The Burmister Lecture*.

Tatsuoka, F. and Ishihara, K. (1974). Yielding of sand in triaxial compression. *Soils and Foundations*, **14**(2), 63–76.

Tatsuoka, F., Sonoda, S., Hara, K., Fukushima, S., and Pradhan, T. B. (1986). Failure and deformation of sand in torsional shear. *Soils and foundations*, **26**(4), 79–97.

Tatsuoka, F., Nakamura, S., Huang, C., and Tani, K. (1990). Strength anisotropy and shear band direction in plane strain tests of sand. *Soils and foundations*, **30**(1), 35–54.

Taylor, D. W. (1948). *Fundamentals of soil mechanics.*, volume 66. LWW.

Thornton, C. (2000). Numerical simulations of deviatoric shear deformation of granular media. *Géotechnique*, **50**(1), 43–53.

Thornton, C. and Zhang, L. (2010). On the evolution of stress and microstructure during general 3d deviatoric straining of granular media. *Géotechnique*, **60**(5), 333–341.

Tong, Z.-X., Zhang, J.-M., Yu, Y.-L., and Zhang, G. (2010). Drained deformation behavior of anisotropic sands during cyclic rotation of principal stress axes. *Journal of geotechnical and geoenvironmental engineering*, **136**(11), 1509–1518.

Toyota, H., Nakamura, K., and Sakai, N. (2003). Application of the elastic boundary induced by shear history on saturated cohesive soil. *Soils and foundations*, **43**(1), 93–100.

Tresca, H. (1864). Memoir on the flow of solid bodies under strong pressure. *Comptes-rendus de lacadémie des sciences*, **59**, 754–758.

Vaid, Y., Sãyao, A., Hou, E., and Negussey, D. (1990). Generalized stress-path-dependent soil behaviour with a new hollow cylinder torsional apparatus. *Canadian Geotechnical Journal*, **27**(5), 601–616.

Vaid, Y. P. and Negussey, D. (1984). Relative density of pluviated sand samples. *Soils and Foundations*, **24**(2), 101–105.

Vardoulakis, I. and Sulem, J. (1995). Bifurcation analysis in geomechanics. hapman & hall.

Vermeer, P. A. and De Borst, R. (1984). Non-associated plasticity for soils, concrete and rock. *HERON, 29 (3), 1984*.

von Wolffersdorff, P.-A. (1996). A hypoplastic relation for granular materials with a predefined limit state surface. *Mechanics of Cohesive-frictional Materials*, **1**(3), 251–271.

Wan, R. and Guo, P. (1997). Coupled dilatancy-compaction model for homogeneous and localized deformation of granular materials. *Numerical Methods in Geomechanics*, pages 3–8.

Wan, R. and Guo, P. (1998). A simple constitutive model for granular soils: modified stress-dilatancy approach. *Computers and Geotechnics*, **22**(2), 109–133.

Wan, R. and Guo, P. (2014). Microstructural formulation of stress dilatancy. *Comptes Rendus Mécanique*, **342**(3), 198–207.

Wan, R. G. and Guo, P. J. (2004). Stress dilatancy and fabric dependencies on sand behavior. *Journal of Engineering Mechanics*, **130**(6), 635–645.

Wanatowski, D. and Chu, J. (2006). Stress-strain behavior of a granular fill measured by a new plane-strain apparatus. *Geotechnical Testing Journal*, **29**(2), 149–157.

Wichtmann, T., Niemunis, A., and Triantafyllidis, T. (2004). The effect of volumetric and out-of-phase cyclic loading on strain accumulation. *Cyclic Behaviour of Soils and Liquefaction Phenomena*, pages 247–256.

Wong, R. and Arthur, J. (1985). Induced and inherent anisotropy in sand. *Geotechnique*, **35**(4), 471–481.

Wroth, C. and Bassett, R. (1965). A stress–strain relationship for the shearing behaviour of a sand. *Geotechnique*, **15**(1), 32–56.

Wu, W., Bauer, E., and Kolymbas, D. (1996). Hypoplastic constitutive model with critical state for granular materials. *Mechanics of materials*, **23**(1), 45–69.

Yamada, Y. and Ishihara, K. (1979). Anisotropic deformation characteristics of sand under three dimensional stress conditions. *Soils and foundations*, **19**(2), 79–94.

Yang, L.-T., Li, X., Yu, H.-S., and Wanatowski, D. (2016). A laboratory study of anisotropic geomaterials incorporating recent micromechanical understanding. *Acta Geotechnica*, **11**, 1111–1129.

Yimsiri, S. and Soga, K. (2010). Dem analysis of soil fabric effects on behaviour of sand. *Géotechnique*, **60**(6), 483–495.

Yoshimine, M. and Ishihara, K. (1998). Flow potential of sand during liquefaction. *Soils and Foundations*, **38**(3), 189–198.

Zdravkovic, L. and Jardine, R. (1997). Some anisotropic stiffness characteristics of a silt under general stress conditions. *Géotechnique*, **47**(3), 407–437.

Zhao, J. and Guo, N. (2013). Unique critical state characteristics in granular media considering fabric anisotropy. *Géotechnique*, **63**(8), 695–704.